F/G 13/8

1 OF 2
AD A
102154

Material Science and Component Technology Directorate

(11) (12) 179

(16) RR00 0268
RR0 02 11

(14) NRL-MR-4527

(17) RR00 0844

REPORT DOCUMENTATION PAGE		READ INSTRUCTIONS BEFORE COMPLETING FORM
1. REPORT NUMBER NRL Memorandum Report 4527	2. GOVT ACCESSION NO. AD-A102154	3. RECIPIENT'S CATALOG NUMBER
4. TITLE (and Subtitle) THE USE OF ION IMPLANTATION FOR MATERIALS PROCESSING — SEMIANNUAL PROGRESS REPORT FOR THE PERIOD 1 APRIL 1980 - 30 SEPTEMBER 1980		5. TYPE OF REPORT & PERIOD COVERED Progress report for the period 1 April 1980 - 30 September 1980
		6. PERFORMING ORG. REPORT NUMBER
7. AUTHOR(s) F. A. Smidt, Coordinator		8. CONTRACT OR GRANT NUMBER(s)
9. PERFORMING ORGANIZATION NAME AND ADDRESS Naval Research Laboratory Washington, D.C. 20375		10. PROGRAM ELEMENT, PROJECT, TASK AREA & WORK UNIT NUMBERS Complete list follows on next page
11. CONTROLLING OFFICE NAME AND ADDRESS Office of Naval Research Arlington, VA 22217		12. REPORT DATE June 24, 1981
		13. NUMBER OF PAGES 188
14. MONITORING AGENCY NAME & ADDRESS(if different from Controlling Office)		15. SECURITY CLASS. (of this report) UNCLASSIFIED
		15a. DECLASSIFICATION/DOWNGRADING SCHEDULE

16. DISTRIBUTION STATEMENT (of this Report)

Approved for public release; distribution unlimited.

17. DISTRIBUTION STATEMENT (of the abstract entered in Block 20, if different from Report)

18. SUPPLEMENTARY NOTES

19. KEY WORDS (Continue on reverse side if necessary and identify by block number)

Auger electron spectroscopy	Ion implantation	Ti-6Al-4V	Friction
Corrosion	Materials processing	M50	
Fatigue	Wear	Bearings	
Rutherford backscattering	Sputtering	H permeation	
Index of refraction	AISI 52100	Electron beam annealing	

20. ABSTRACT (Continue on reverse side if necessary and identify by block number)

An interdisciplinary program on the use of ion implantation for materials processing is being conducted at NRL. This report describes the important factors in ion implantation science and technology and reports progress in the use of ion implantation to modify friction, wear, fatigue, corrosion, and optical properties of materials.

DD FORM 1473 EDITION OF 1 NOV 65 IS OBSOLETE
1 JAN 73
S/N 0102-014-6601

i

10. Program Element, Project, Task Area & Work Unit Numbers

66-0300-0-0	62761N NavMat	ZF 61-544-007
66-0424-0-0	RR022-08-44 ONR	
66-0424-A-0	62376 NAPC/NavAir	
66-0424-B-0	61101E DARPA Order 3577	
66-0425-0-0	RR022-08-44 ONR	
66-0420-0-0	RR022-11-41 ONR	
63-1019-0-0	RR022-08-44 ONR	
63-1020-0-0	RR022-01-47 ONR	
61-0037-0-0	RR013-01-43 ONR	
66-0425-A-0	61153N22	WR022-01-001
66-0446-0-0	RR012-02-41	
66-0447-0-0	RR012-02-41	
66-0423-0-0	RR022-11-41	
66-0418-0-0	RR012-01-41	

Accession For	
NTIS GRA&I	X
DTIC TAB	☐
Unannounced	☐
Justification	
By	
Distribution/	
Availability Codes	
Dist	Avail and/or Special
A	

CONTENTS

THE USE OF ION IMPLANTATION FOR MATERIALS PROCESSING

Preface - F. A. Smidt

This report is the second in a series of Semi-annual Progress Reports of work conducted at the Naval Research Laboratory (NRL) on the use of ion implantation for materials processing. The objective of the programs is to develop ion implantation for materials processing applications and to provide the fundamental understanding of the implantation processes and the changes produced in the surface so as to confidently utilize the technology.

The work reported here represents a coordinated effort in three divisions at NRL, the Condensed Matter and Radiation Sciences Division (Code 6600), the Chemistry Division (Code 6100) and the Material Science and Technology Division (Code 6300). The work is coordinated through the Ion Implantation Steering Committee consisting of Dr. J. K. Hirvonen (Code 6670), Dr. J. N. Butler (Code 6670), Dr. N. L. Jarvis (Code 6170), Dr. B. B. Rath (Code 6320), and Dr. F. A. Smidt (Code 6004), Chairman. The work includes both in-house basic research conducted under the auspices of the Office of Naval Research and applied research performed for several Navy and DOD sponsors (NAVAIR, DARPA, NAVMAT, AFML, SSPO, NAVSEA).

The purpose of this report is to make available in one source the results from all studies at NRL related to the use of ion implatation for materials processing so as to provide a more comprehensive picture of the scope and interrelationship of the research. The report consists of four sections describing the research and a cumulative bibliography of published papers and reports.

THE USE OF ION IMPLANTATION FOR
MATERIALS PROCESSING

SEMI-ANNUAL PROGRESS REPORT FOR THE PERIOD
1 APRIL 1980 - 30 SEPTEMBER 1980

SUMMARY

I. ION IMPLANTATION SCIENCE AND TECHNOLOGY

Research reported in this section contributes to our general understanding of the ion implantation process and the development and refinement of techniques for ion implantation processing.

A.   Production of High Current Metal Ion Beams

J. K. Hirvonen, C. A. Carosella and G. K. Hubler

A sputter-type ion source is sometimes used for production of ion beams with metal ions that do not form gaseous compounds and which require very high temperatures for volatilization.   This contribution reports the experience with the internal chlorination technique with a Freeman-type source on the NRL Varian/Extrion Model 200-20 A2F ion implanter.   This technique has the advanage of producing generally higher currents than sputter sources but has the disadvantage of corrosion produced by the chlorine gas.   The procedure used at NRL consists of placing finely divided pieces of the ion source feedstock metal into a chlorination chamber made from graphite and admitting chlorine gas to a pressure of about 2×10^{-6} torr.   The chlorine gas forms a plasma discharge under the action of a filament and an electric field.   The chlorine then reacts with the hot metal feedstock to form volatile chlorides, which are in turn ionized in the plasma.   The technique allows the production of a variety of metal ions (i.e., Al, Ti, Cr, Ni, Cu, Mo, Ta), spanning a wide range of melting points and chemical reactivities, with current intensities of hundreds of microamperes.

B.   Sputtering Observations During Binary Alloy Production by Ion Implantation

G. William Reynolds, A. R. Knudson and C. R. Gossett

Surface sputtering during ion implantation was monitored by measuring the intensity of optical photon emission from the excited neutrals leaving the surface of the sample.   Emission from both the implanted species and the substrate species was monitored throughout the implantation and has been compared with the change in the surface atomic fraction for each species predicted by a model of the sputtering process.   Profile measurements of the implanted species were made after implantations and the profiles were compared with predictions of the model.   The binary systems Cr implanted into Fe and Cu implanted into Al were the subject of the investigation.   The observations show a strong correlation between intensity of the optical emission from the sputtered species and surface atomic fraction and confirm that a surface layer of approximately twice the mean range of the implanted species

needs to be sputtered from the surface to reach a steady state condition during ion implantation.

C.   Sputter Distortion of Implantation Profiles

I. Manning

Distortion of the implanted ion profile due to the sputter erosion of the target surface was examined. This effect is expected to be the dominant factor in high fluence implantations. The effect was investigated by considering the distortion of the Gaussian range distribution for implanted ions as a function of various sputtering parameters.

D.   Computer Simulations of Ion Implantations

M. Rosen and G. P. Mueller

Two phenomena are under investigation using computer simulations of ion implantations, ion beam interface mixing and sputtering. The mechanism of ion beam interface mixing in which a thin surface film is mixed into the substrate by ion implantation is being investigated as a means to circumvent the concentration limit imposed by sputtering for direct implantation. The role of recoil implantation and diffusion in the mixing process are under investigation. The sputtering investigation involves the use of the binary simulation code MARLOWE to study parameters which influence sputtering and the comparison of these results with experimental data obtained by another NRL research group.

II. WEAR AND FATIGUE

Research reported in this section involves the application of ion implantation processing to the improvement of wear and fatigue properties of surfaces and fundamental investigations conducted to improve our understanding of the effects.

A.   Abrasive Wear Resistance of Titanium and Nitrogen-Implanted 52100 Steel Surfaces

I. L. Singer, R. N. Bolster and C. A. Carosella

The wear resistance of titanium- and nitrogen-implanted 52100 bearing steels was measured by an abrasive wear technique with a depth resolution of 20-30 nm. Titanium-implanted surfaces were extremely resistant to wear against fine (1-5 μ m) diamond abrasion, which suggests a very hard surface layer. Nitrogen-implanted surfaces, by contrast, wore at the same rate as non-implanted surfaces. Wear resistance versus depth profiles of titanium-implanted surfaces followed the concentration versus depth profile of the implanted titanium. Auger depth profiles indicated a large concentration of carbon ($\approx$20 at.% maximum) distributed with a diffusion-like profile from the titanium-implanted surface into the bulk. The carbon was identified by Auger line shape analysis as a titanium carbide, and the wear resistance of the surface was attributed in part to its presence.

B.   Friction Behavior of 52100 Steel Modified by Ion Implanted Ti

I. L. Singer, C. A. Carosella and J. R. Reed

Friction measurements (low speed, dry sliding) were performed on 52100 steel implanted with Ti to fluences between 5 and 50 x 10^{16} cm^{-2}. Auger analysis and transmission electron microscopy (TEM) were used to identify the composition and microstructure of the implanted surfaces. At highest fluence, implanted disk/non-implanted couples had a friction coefficient of $u_k = 0.38$, compared to $u_k = 0.62$ for nonimplanted couples; moreover, the implanted surface resisted scarring. The surface contained, in addition to Fe and Ti, an excess quantity of a carbide form of C (8 x 10^{16} C/cm^2) which extended 150 nm into the surface with a diffusion-like profile. TEM detected only non-crystalline material in a thinned implanted foil, suggesting the surface layer was amorphous. At lower fluences, 16 x 10^{16} Ti/cm^2, the implanted steel displayed extremely high friction ($u_k = 0.9$) before the surface wore through and the friction returned to its nonimplanted value. Excess carbon concentrations were 2 x 10^{16} C/cm^2 and 0.2 x 10^{16} C/cm^2, respectively. The near surface Ti and C concentrations were nearly equal at the metal/metal oxide interface for higher fluence implants. A model for C gettering by exposed surface Ti is supported by these results.

C. Surface Morphologies Produced by Ion Milling on Ion-Implanted 18Cr8Ni Steels

I. L. Singer

Microstructures of ion-implanted 18Cr8Ni steel surfaces were examined using a metallographic approach i.e., etching and optical microscopy. Polished surfaces were implanted with selected ions (Ti$^+$, N$^+$, Ar$^+$, Ne$^+$) to high doses (10^{17}/cm^2), then Ar ion milled stepwise to beyond the implantation depth. Michelson interferograms showed that the implanted surfaces were etched at the same rate as non-implanted surfaces. Several implanted surfaces, nonetheless, developed unique etch features. On most surfaces, large (50-100 u m) austenitic grains became visible after etching to a depth of about 60 nm. Ti-implanted surfaces, however, showed no grain relief until a depth of 240 nm, well beyond the implanted ion range ($R_p \sim 60$ nm). Individual grains on nonimplanted as well as Ne$^+$ and Ar$^+$ implanted surfaces etched with a rough texture. On the N-implanted surfaces, however, grains remained smooth until etched to a depth well beyond the implanted region. The absence of grain relief on etching a Ti-implanted surface is ascribed to isotropic sputtering from an amorphous surface. The absence of grain roughness on etching N-implanted surfaces may be due to locally isotropic sputtering from a reacted, e.g., nitrided, surface layer, or from a more stable microstructure, e.g., nitrogen-stabilized austenite.

D. The Effect of Ion Implantation on Fatigue Life in Ti-6Al-4V

R. G. Vardiman and R. A. Kant

Ion implantation of the alloy Ti-6Al-4V with carbon and nitrogen ions has been found to produce a microstructure which contains fine precipitates of TiC and TiN respectively. Rotating beam fatigue tests show improved fatigue life for both implants. The superior carbon implantation gives a 20% increase in endurance limit and a factor of four to five increase in lifetime over unimplanted material at higher stresses. A dose of 1 x 10^{17} atoms/cm^2 is required to obtain the maximum effect. Fatigue cracks have been observed to originate up to 150 u m below the surface, indicating a complex interaction between the implanted layer and the fatigue failure process.

III. CORROSION

Research reported in this section involves the application of ion implantation

3

processing to improvement of the corrosion resistance of surfaces and fundamental investigaions conducted to improve our understanding of the effects.

A. Ion Implantation of Bearings for Improvement of Corrosion Resistance

R. Valori and G. K. Hubler

The results of a program to use ion implantation to improve the tribological and corrosion characteristics of load bearing surfaces in both rolling element bearings and gears used in aircraft propulsion systems are reported. This contribution describes that aspect of the program concerned with the use of ion implantation for surface alloying of bearing components in order to alleviate the problem of corrosion in costly M50 steel mainshaft aircraft engine bearings. Results to date indicate that implantation of selected ion species can significantly improve resistance to both generalized and localized (pitting) corrosion without adversely affecting bearing performance or fatigue endurance life.

B. The Corrosion Behavior and Rutherford Back-Scattering Analysis of Palladium-Implanted Titanium

G. K. Hubler and E. McCafferty

The corrosion behavior of Pd-implanted Ti in boiling 1M H_2SO_4 has been investigated by means of high resolution Rutherford backscattering (RBS) profiles of the Pd concentration as a function of corrosion time, and by electrochemical methods consisting of corrosion potential vs time curves and potentiostatic polarization data. Employing ion-implanted Xe as a surface 'marker', absolute corrosion rates were determined by RBS analysis and compared to corrosion rates determined from the polarization curves. The rate of Ti dissolution is found to be reduced by about three orders of magnitude for Pd-implanted samples. The corrosion potential-time curves and high resolution RBS data both show that soon after immersion, the Pd surface contentration rises at 20 at.% because of preferential dissolution of Ti and that the Pd is retained in the surface for corrosion times of up to 9 h. The steady state corrosion potential of implanted samples is close to that of pure Pd and 800 mV anodic with respect to the corrosion potential of pure Ti. The protection is explained by the fact that the mixed electrode potential is more noble than the critical potential for passivity of Ti, resulting in a markedly reduced dissolution rate.

C. Effect of Helium, Iron, and Platinum Implantation on the Absorption of Hydrogen by Iron

M. Zamanzadeh, A. Allam, H. W. Pickering and G. K. Hubler

A preliminary study was made of the effect of certain elements implanted in iron on the absorption of hydrogen by Ferrovac-E iron. Using the permeation technique it was found that the location of implanted Pt, as modified by selective dissolution of iron from the surface, affects the kinetics of the hydrogen evolution reaction and, hence, of the hydrogen absorption process. The rate of hydrogen absorption decreased with increase in Pt concentration on the surface in both 0.1N NaOH and 0.1N H_2SO_4. A catalytic mechanism is proposed to explain the marked reduction in hydrogen permeation. There are no significant differences in the permeation behavior of unimplanted and helium- or iron-implanted iron membrances in 0.1N NaOH. The experimentally observed Tafel slope, the permeation- (charging) potential relationship, and the permeation- (charging) current relationship indicate a

coupled discharge-recombination mechanism of hydrogen evolution on He-, or Pt-implanted iron. At higher cathodic overpotentials in 0.1N NaOH, corresponding to potentials more negative than -1.0V (SHE), another mechanism of hydrogen evolution is indicated. Selective dissolution of iron from the Pt-implanted Fe surface layer may involve some platinum and iron interdiffusion according to Rutherford backscattering analyses.

D. Corrosion Resistant AISI 52100 Bearing Surfaces by Implantation

G. K. Hubler, J. K. Hirvonen, C. R. Clayton, Y. F. Wang, J. Budnick and H. Hayden

This contribution describes the use of ion implantation for surface alloying of bearing components in order to alleviate the problem of corrosion in 52100 steel aircraft engine bearings. Potentiodynamic polarization measurements on 0.01M buffered (pH=6) NaCl solutions were carried out on AISI 52100 specimens polished to a mirror finish. Implantations of Ta and Cr+P were carried out to promote the formation of an amorphous stainless steel surface alloy; with Cr to form stainless steel; and Cr+Mo to enhance the pitting resistance of the stainless steel. The improvement as measured from the absolute change in the pitting potential (E_b) was in order of improvement Ta (+935 mV), Cr+P (+785 mV) Cr+Mo (+630 mV, and Cr (+560 mV). These large changes in the pitting potential are unprecendented in attempts to improve pitting resistance by conventional alloying procedures and can only be produced by gross compositional changes in the surface layers. Auger depth profiles and nuclear reaction profiles were measured for Cr, Cr+P, and Ta implantation and the concentration of implanted ions was shown to range from 12 to 30 atomic % in a layer approximately 80 nm in thickness, more than sufficient to produce the noble pitting potentials observed. Environmental simulation tests of Cr and Cr+Mo implanted specimens showed no pitting or rusting while control samples had rusted severely.

Ion beam intermixed coatings were produced by vacuum evaporating 25 nm of Cr on AISI 52100 samples and implanting with 400 keV Xe ion to a fluence of 3 x 10^{16} ions/cm^2. A surface alloy with 100% Cr gradually diminishing to 0% Cr over depth of about 80 nm was produced. The Xe implant eliminates the sharp interface between the Cr coating and the bulk material so that the Cr coating is very adherent. Corrosion tests on samples prepared in this manner showed pitting potentials that compared favorably with the Cr implanted samples. An advantage of this method is that the corrosion protection can be achieved for an ion dose that is an order of magnitude less than by straight ion implantation of the chromium. Further studies of this promising technique are underway.

IV. OTHER EXPLORATORY RESEARCH AREAS

Research reported in this section includes exploratory investigations of the application of ion implantation in areas other than wear/fatigue and corrosion.

A. Optical Effects Resulting From Deep Implants of Silicon with Nitrogen and Phorphorus

G. H. Hubler, P. R. Malmberg, C. A. Carosella, T. P. Smith, III, W. G. Spitzer, C. N. Waddell and C. N. Phillippi

Single crystal silicon has been implanted with nitrogen and phorphorus ions at MeV energies to fluences between 10^{16} and 1.6 x 10^{18} ions/cm^2. Infrared transmission

and reflection spectra in the range of 1.25 to 40 μm were measured for as-implanted samples and after various annealing treatments. Interference fringes were observed in the IR spectra which are produced by the interference of light which has been multiply reflected between the front surface and the buried layers. By detailed theoretical analyses of the interference fringe structure, we obtained refractive index profiles, which, under suitable interpretation, provide accurate measurements and several quantities of interest. These quantities are the range and straggling of the implanted ions, the depth of disordered layers, and the width of the order-disorder transition. Mechanisms for the refractive index changes which have been identified include amorphization of the implanted silicon, bulk compositonal change in the buried layer, localized vibrational mode dispersion, and free electron dispersion. Experimental results and theoretical predictions are presented, demonstrating each of these mechanisms.

B.   Pulsed Electron Beam Irradiation of Ion-Implanted Copper Single Crystals

J. K. Hirvonen, J. M. Poate, A. Greenwald and R. Little

The effect of an intense, pulsed electron beam on high-dose implanted Cu single crystals has been studied. Rutherford backscattering and channeling have been used to obtain the depth concentration profiles and lattice locations of the implanted species (Au, Ag, and Ta) before and after pulsed electron beam irradiation. Channeling and secondary electron microscopy measurements show that the Cu surface melts during pulsed irradiation followed by an epitaxial lattice growth resulting in (i) a redistribution of the implanted species, (ii) some species (e.g., Au and Ag) remaining on lattice sites, and (iii) Ta leaving substitutional sites.

Section I.A

PRODUCTION OF HIGH CURRENT METAL ION BEAMS

J. K. Hirvonen, C. A. Carosella and G. K Hubler

Materials Modification and Analysis Branch
Condensed Matter and Radiation Technology Division
Naval Research Laboratory

Production of High Current Metal Ion Beams

J. K. Hirvonen, C. A. Carosella, and G. K. Hubler
U.S. Naval Research Laboratory
Washington, DC 20375

Ion implantation is becoming increasingly used for the modification of surface sensitive mechanical and chemical properties [1,2]. These relatively new applications often require the use of a wide variety of unconventional ion species whose production is not always as convenient as simple gaseous charge materials. For example, NRL is involved in research programs to test the feasibility of improving the corrosion and wear resistance of aircraft bearing surfaces by implantation of elements such as Cr, Ta, and Ti [3]. These involve implantation of $1-5 \times 10^{17}$ ions/cm^2 and areas up to 500 cm^2. These high fluences and areas have prompted experimentation with several methods of maximizing ion currents of these and other metal ion beams.

This paper reports on the adaptation of a well established technique [4] (i.e., internal chlorination) for producing moderately high beam currents of several metal species from a Freeman-type ion source used in the NRL modified Varian/Extrion Model 200-20 A2F Ion Implanter shown schematically in Fig. 1. Internal chlorination refers to the technique of passing a chlorine (containing) gas over the hot surface of the element of interest to produce in-situ chlorides which subsequently decompose and ionize in the plasma discharge. The temperatures necessary to vaporize many metals are higher than can be conveniently reached in a hot filament ion source. The advantage in chlorination is that a volatile chloride of the pure metal will form at the internal source operating temperature so that the need for a high temperature source oven is eliminated.

The use of a vaporizer or oven to sublimate either the elemental or a chemical compound (often halides) of the required element can have problems, especially if the chemical compound has an affinity for water or requires temperature control outside the range of the oven (typically 150°C to 900°C). It is well known that the presence of a small amount of water in the charge material can seriously degrade the beam quality when using CCl_4 or halide source materials [5]. The use of internal chlorination avoids the problems associated with loading anhydrous salts and can significantly reduce the time required for outgassing of the ion source prior to use. The in-situ production of chlorides has also been found to significantly reduce the corrosion problems associated with handling certain charge materials previously used (i.e., $TiCl_4$). Basically, the approach taken has been to either (i) use as a source material, a foil liner [6] on the inside of the cylindrically shaped anode arc chamber, or (ii) use an internal graphite chlorination chamber introduced into the rear of the ion source assembly as shown in Figure 2. In both geometries the filament and arc discharge provide the required heating. The lack of precise temperature control requires two types of graphite chamber arrangements—one for maximum temperatures, and one for lower temperatures for those elements (e.g., Al) whose vapor pressures are too high at the operating temperature inside the source (approximately 800°C). In the lower

8
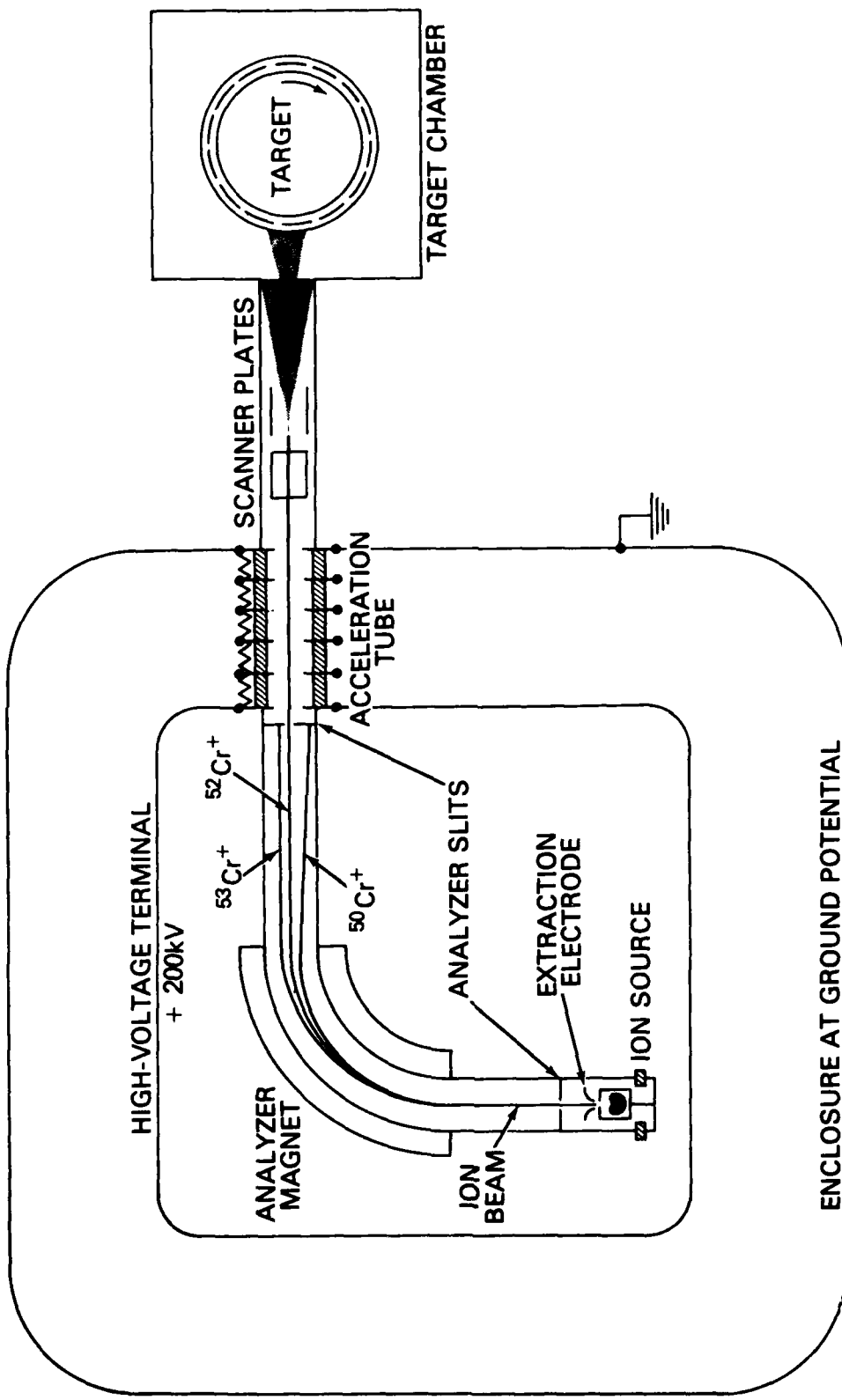
Fig. 1 — Schematic drawing of ion implantation system modified for nonsemiconductor materials research

ANALYZER SLIT

ION BEAM

0V

−2kV

+25kV

EXTRACTION ELECTRODE

LOCAL GROUND

ELECTRON REFLECTOR

PLASMA

HOT FILAMENT

+ 25kV

GAS FEED

INSULATOR
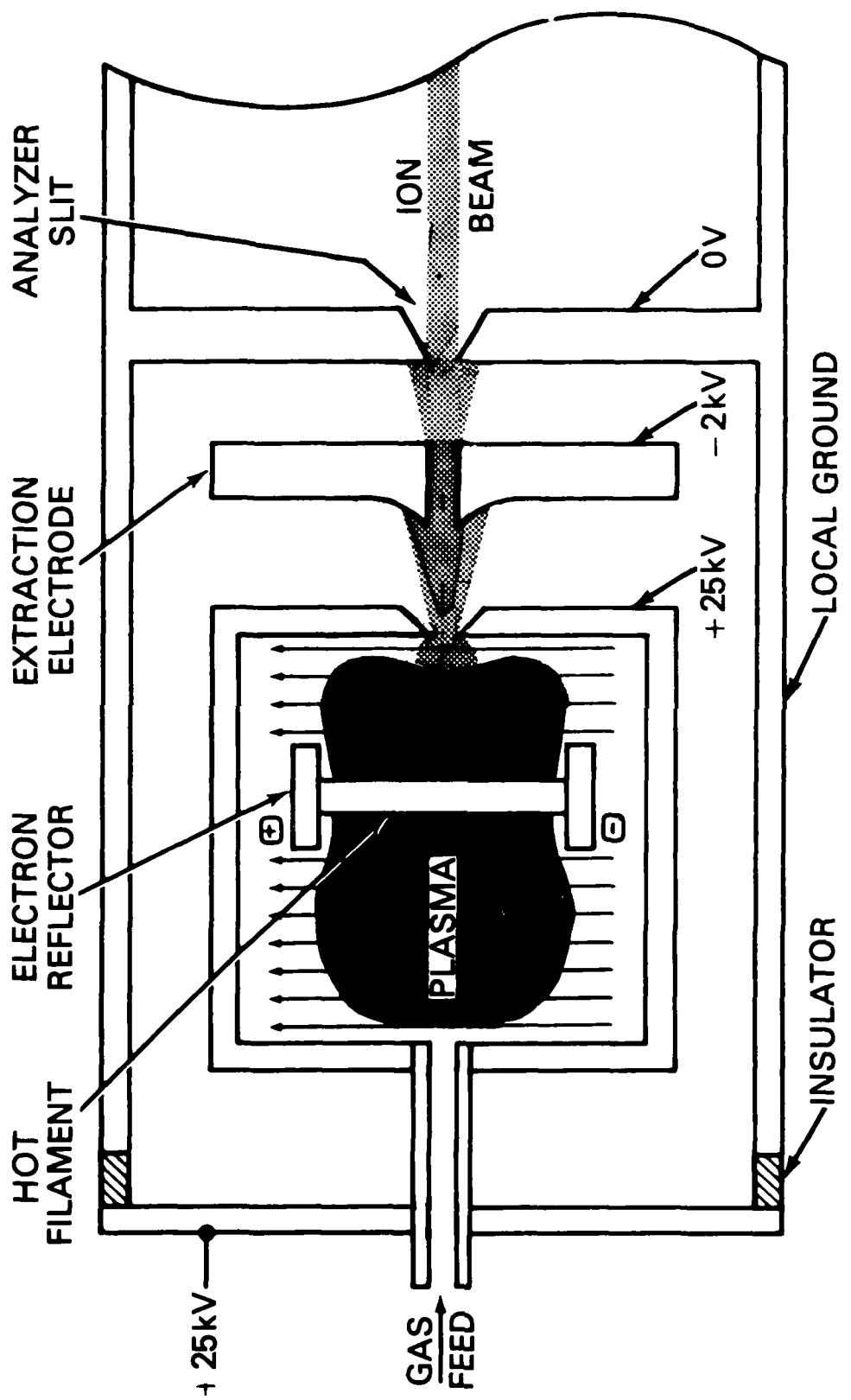
Fig. 2 — Schematic drawing of Freeman-type ion source containing an added internal graphite chlorination chamber

10

temperature configuration, the graphite chamber is doubled in length so that the charge is external to the anode and operates at a considerably lower temperature than $800^{\circ}C$. The tendency of graphite components to outgas slowly has been alleviated by heating of the entire ion source anode assembly with a torch just prior to insertion and pumpdown. Control over the source output is possible by varying power to the source through the arc voltage and arc current, by installing additional Ta heat shields around the anode, and finally, by varying the gas flow.

The use of a foil liner is satisfactory providing it doesn't deform and short to the biased filament. Our experience has indicated that a scale will form on the surface of the liner with use and will eventually spall leading to an electrical short to the filament. Generally this doesn't happen for an uninterrupted run of 8-10 hrs. Initially, a BF_3 support was used along with additional CCl_4 vapor but more recently pure Cl_2 been used by itself. Use of pure Cl_2 results in relatively clean mass spectra (see fig. 3 for example) and lower arc currents for a given beam current, presumably leading to longer source lifetimes.

The separate in-situ chlorination chamber allows the use of metal shavings, chunks, etc. as well as powder sources which have larger active areas, and the chamber has eliminated the shorting out of the filament by reaction by-products. In particular, whereas shorting of the filament to ground (anode) often resulted upon restarting a liner-charged source, sources using a chamber have been run for 2-3 consecutive days (15-25 hrs) and restarted two or three times without shorting.

A tungsten filament rod is used in all cases except Ta. For a W beam, no charge is required since ample beam is obtained by using Cl_2 as the support gas which undergoes a chlorination reaction with the hot filament. For Ta, a Mo filament must be used since Ta and W overlap in the mass spectra. Table I lists the metal ion beams and typical beam currents thus far produced by this technique. Generally the obtained beam currents are in the hundred microampere intensity range with filament lifetimes of 15-20 hrs.

Source poisoning effects have also been seen. For example, it has been observed that the presence of a Cr buildup on either the Mo arc chamber or graphite electron reflectors which retain the filament can result in many orders of magnitude reduction of a Mo^+ beam when a Mo liner and BF_3 plus CCl_4 gas is used. For this reason we attempt to dedicate chlorination chambers and graphite reflectors for specific elements, and to thoroughly clean the anode arc chamber upon changing ion species.

No attempt has been made to optimize the ion source parameters such as gas flow but it has been found that Cl_2 pressures of 1-3 x 10^{-6} torr above the minimum operating pressure (monitored above the ion source diffusion pump) results in satisfactory beam currents and filament lifetimes with no evidence of filament deactivation as sometimes seen when using higher pressures of CCl_4.

Normally after a two-day source operation it is found that there is a fair amount of deposited material (usually hygroscopic or deliquescent chlorides) on the source housing walls and accel/decel element and their thorough removal is critical to subsequent pumpdowns and spark free operation. When the source supply gas is Cl_2, BF_3, or CCl_4, the oil is changed twice weekly in the corrosion resistant mechanical pump which backs the ion source diffusion pump in order to further reduce corrosion problems. A more general maintenance period is scheduled twice yearly when the entire inside walls of the implanter are cleaned of deposited chlorides, etc...

11
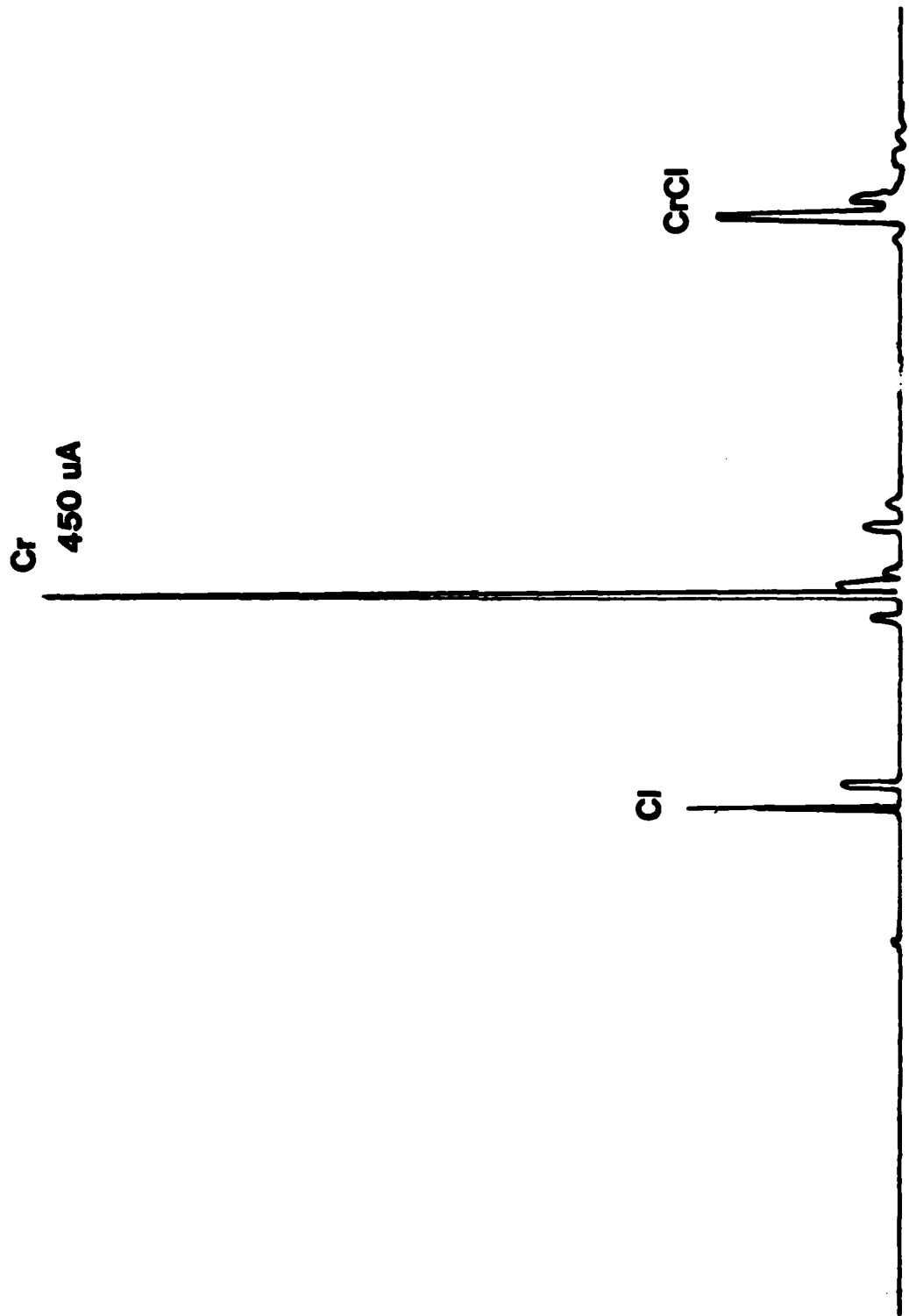
Fig. 3 — Ion beam mass spectrum obtained with a chlorine gas feed and with chromium in the chlorination chamber. The most abundant chromium isotope has an intensity of 450 microamperes in this example.

12

TABLE I

	Charge Material				
Species	Foil Liner	Graphite Chamber	Gas	$I(\mu\alpha)$	Comments
^{9}Be	2 mil foil		BF_3+CCl_4	80	Extended graphite chamber used
^{27}Al		5 mil foil	Cl_2	540	
^{48}Ti	1 mil foil		CCl_4+N_2	100	No BF_3 because of mass interference
^{48}Ti		Powder	Cl_2	500	
^{52}Cr	5 mil nichrome		BF_3+CCl_4	270	
^{52}Cr		Chunks	Cl_2	700	
^{58}Ni	5 mil foil		BF_3+CCl_4	70	Less than 10 μA Ni with nichrome foil
^{63}Cu		Shavings	Cl_2	85	
^{89}Y		Shavings	Cl_2	>20	
^{98}Mo	Anode alone		CCl_4	40	Filament deactivated
^{98}Mo	5 mil foil		Cl_2	100	Hotter Mo with liner
^{98}Mo		Powder	Cl_2	50	
^{106}Pd	2 mil foil		BF_3+Cl_2	5	
^{181}Ta	5 mil foil		BF_3+Cl_2	100	Mo filament to avoid W/Ta mass interference
^{184}W			BF_3	30	W filament only
^{196}Pt	6 mil foil		Arsine/BF_3	3 steady/ 30 short-time	Arsine on initially to attack Pt

In summary, we have adapted internal chlorination techniques that are compatible with use in a Varian/Extrion Model 200-20 A2F Ion Implanter. The techniques allow us to produce ions of a variety of metals spanning a wide range of melting points and chemical reactivities, with current intensities in the range of hundreds of microamperes. The technique should be usable with a wide variety of elemental species, facilitating the use of ion implantation for materials research requiring high fluences.

We wish to acknowledge many fruitful discussions on ion sources with our late friend and colleague, R. Bastide.

REFERENCES

[1] J. K. Hirvonen, J. Vac. Sci. Technol. 15 (1978) 1662.

[2] C. A. Carosella, I. L. Singer, R. C. Bowers, and C. R. Gossett in Ion Implantation Metallurgy (ed. C. M. Preece and J. K. Hirvonen, TMS-AIME, New York, 1980).

[3] Y. F. Wang, C. R. Clayton, G. K. Hubler, W. H. Lucke, and J. K. Hirvonen, Thin Solid Films 63 (1979) 11.

[4] G. Sidenius and O. Skilbreid in Electromagnetic Separation of Radioactive Isotopes (ed. M. J. Higatsberger and F. P. Viehbock, Springer Verlag, Vienna, 1961) p. 234.

[5] G. Dearnaley, J. K. Freeman, R. S. Nelson, and J. Stevens in Ion Implantation (North Holland, Amsterdam, 1973) p. 383.

[6] This technique of using a Pt foil liner was suggested to us by C. W. White (ORNL).

Section I.B

SPUTTERING OBSERVATIONS DURING BINARY ALLOY PRODUCTION BY ION IMPLANTATION

G. William Reynolds*, A. R. Knudson and C. R. Gossett[1]
Condensed Matter and Materials Modification and Analysis Branch
Radiation Technology Division
Naval Research Laboratory

*On leave from the Physics Department, SUNY at Albany, Albany, NY.

Sputtering Observations During Binary Alloy Production
by Ion Implantation

G. William Reynolds*, A. R. Knudson, C. R. Gossett
Naval Research Laboratory
Washington, DC 20375

ABSTRACT

As thin layer binary alloys were being prepared by ion implantation, the surface sputtering was monitored by measuring the intensity of optical photon emission from the excited neutrals leaving the surface of the sample. Emission from both the implanted species and the substrate species was monitored throughout the implantation and has been compared with the change in the surface atomic fraction for each species monitored as predicted by a model of the sputtering process. Following the implantation the samples were profiled for the implanted species and the profiles were compared with predictions of the model. The two binary systems studied here are Cr implanted into Fe and Cu implanted into Al, both done at a beam energy of 90 keV. The observations strongly support the idea that the optical emission of these sputtered species parallels the surface atomic fractions during the preparation of the binary alloy by ion implantation. The observations confirm that to reach steady state conditions during ion implantation, a surface layer of approximately twice the mean range of the implanted species needs to be sputtered from the surface. This study reinforces the need for more extensive measurements of sputtering yields.

INTRODUCTION

The success of ion implantation technology in the production of semiconductor devices has fostered the application of the same technology to the modification of the surface properties of metals and alloys. Surface hardening, wear resistance, corrosion resistance and metal fatigue are areas where this technology is currently being applied [1]. The fluences required for the desired surface modification are calculated using published sputtering yields [2] and depth distributions for the implanted species calculated from existing theories [3,4]. Following implantation the samples are profiled using ion beam analytical techniques and compared with the theory. The samples are then subjected to testing for the enhanced surface characteristic. Since high concentrations of the implanted atoms are generally desired and since the concentration of implanted atoms attainable by implantation is limited by the sputtering process, an understanding of the sputtering behavior of the surface during the implantation process is important.

*On leave from the Physics Department, SUNY at Albany, Albany, NY.
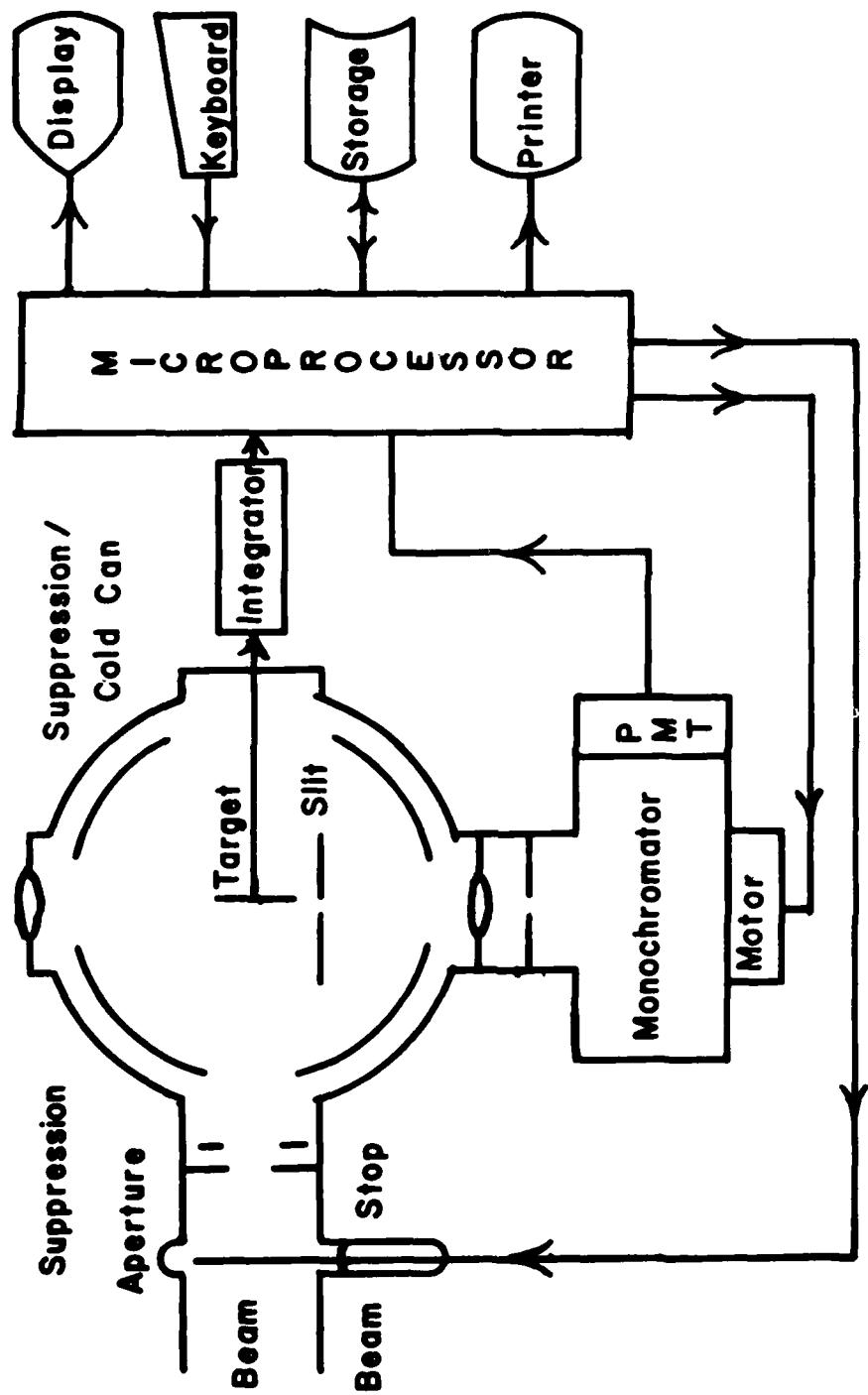
Fig. 1 — Equipment arrangement (not to scale)

In this paper we report the results of monitoring surface composition during implantation by measurements of the intensity of optical emission lines from sputtered neutral substrate and implanted beam atoms. After implantation composition versus depth profiles were determined by Rutherford backscattering and nuclear reaction analysis. The optical emission and depth profile data were then compared with the predictions of a model of the sputtering process during implantation.

EXPERIMENT

The experimental arrangement is shown in Figure 1. The target materials were elemental polycrystalline samples of high purity and were mounted perpendicular to the axis of the ion beam. The ion beam was raster scanned across the aperture to insure uniformity of the implanted region on the target. Both high and low dose rate implants were performed. Average scanned current for the low dose rate samples was 2 microamperes with peak instantaneous currents ranging from 8 to 25 microamperes on different days. The scanned current for the high dose rate samples was 6 to 8 microamperes with peak instantaneous currents of 80 microamperes. The scanning rate, i.e., dwell time on the target, was selected to reduce the overall heating of the sample being implanted. The energy of the ion beam for all samples in this series was 90 keV. The target chamber pressure was maintained at 3×10^{-7} torr during the low dose rate implantations and at 1×10^{-6} torr for the high dose rate implantations. The targets were surrounded by a liquid nitrogen cold shield during implantation. The optical emission was monitored in the direction perpendicular to the beam axis.

During the implantation the optical emission of selected lines for both the target element and the beam element was monitored. The sampling intervals, data acquisition, and the spectrometer wavelength setting were under the control of a dedicated microprocessor system. The microprocessor program assured that each optical emission data acquisition period corresponded to the same amount of accumulated charge on the target. Each data cycle included measurements of substrate line intensity, implanted atom line intensity, and background count rate. As each raw data point was collected, the program calculated the background correction and subtracted the correction from the raw data. The program then calculated the number of photons per arbitrary integrated charge unit and stored the result in a data matrix. The number of data intervals occurring during an implantation was determined by the total fluence desired divided by the product of the average incident flux and the time data interval. After the desired charge had been collected by the current integrator, the beam was interrupted and the microprocessor program then normalized the implanted data points against data from a reference sample (pure Cr or Cu as appropriate) and also normalized the substrate data points against the mean of the first two percent of the substrate data points. The data so normalized were stored in additional matrix elements followed by the storage of the data matrix on magnetic media for later analysis. The entire matrix was printed out for examination.

Initial estimates of sputtering yields for the binary system were determined from the literature [2] and the fluences required to reach the steady state condition for the implanted species were calculated. The calculated fluence was then doubled to insure that the steady state condition was reached during the implantation. These calculations were made to facilitate scheduling the time required to accomplish the implantations. Following the implantation the samples were removed and the surface concentration and implanted profiles were determined by Rutherford backscattering and nuclear reaction analysis.

18

From the surface concentration information the self sputtering yield for the implanted species was determined using equation [5]:

$$S_1 = 1/n_1 \qquad (1)$$

where n_1 is the surface atomic fraction at the steady state condition, S_1 is the self sputtering yield, and the subscript 1 refers to the implanted species.

In this study samples were implanted with different fluences to obtain profiles of the implanted atoms at various surface concentrations. Eight Fe samples were implanted with Cr at an energy of 90 keV with fluences ranging from 1.7×10^{17} ions/cm^2 to 8.1×10^{17} ions/cm^2 and nine Al samples were implanted with Cu at 90 keV with fluences ranging from 6.9×10^{16} to 3.3×10^{17} ions/cm^2.

RESULTS

The figures illustrate the typical behavior of the optical signals during implantation. Figures 2a and 2b show the behavior of the Cr and Fe signals respectively as 90-kev Cr ions are implanted into Fe. Figures 3a and 3b show the behavior of the Cu and Al signals as 90-keV Cu ions are implanted into Al. In deriving the results shown in these figures we have assumed that:
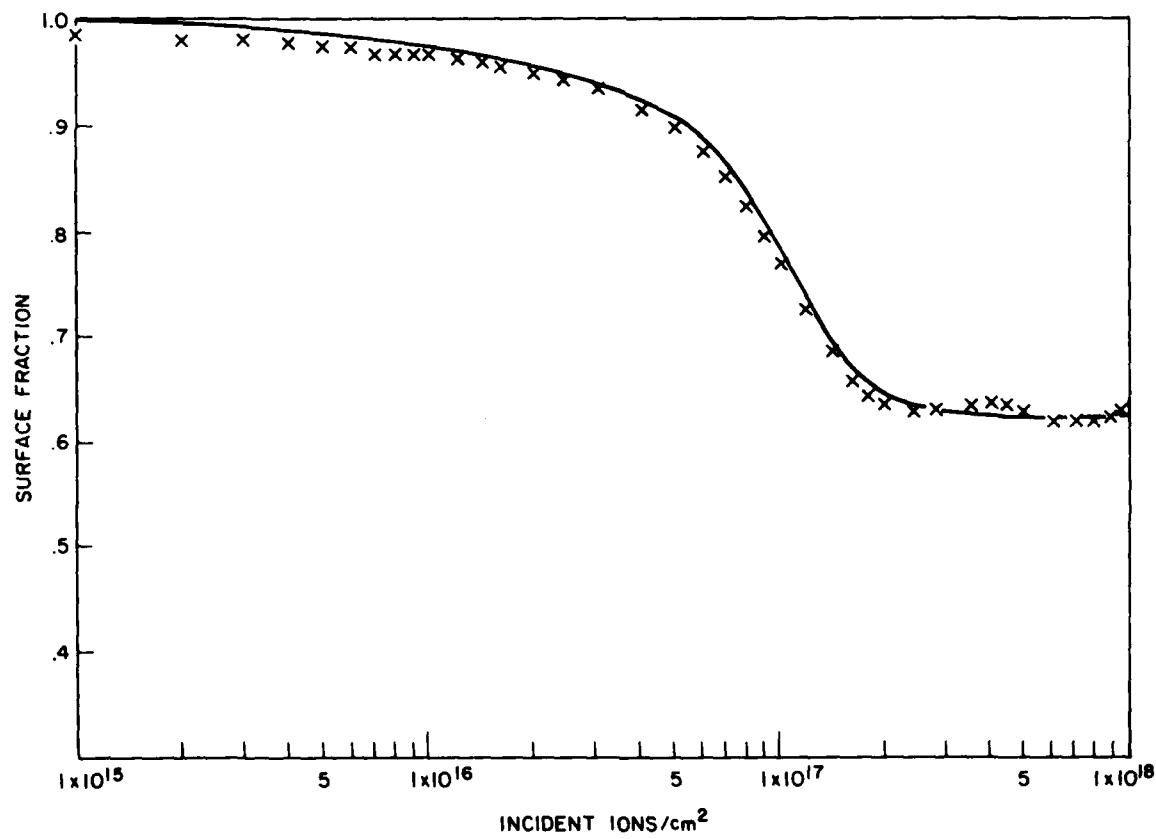
$$I_i = k_i \, \Phi \, n_i \, S_i \qquad (2)$$

where I_i is the intensity of the optical signal observed, k_i is a proportionality constant, Φ is the incident flux, n_i is the surface atomic fraction, and S_i is the sputtering yield for the "i" th species.

Figures 4 and 5 show the implanted profiles for Cr into Fe and Cu into Al. The Cr profile was measured independently by three different techniques, Rutherford backscattering (RBS), nuclear reaction analysis (NRA), and optical emission sputtering (OES). The RBS profile was obtained by taking an RBS spectrum of the implanted Fe sample and subtracting the RBS spectrum for pure Fe. The resulting data was fitted by adjusting the Cr profile input to the RBS computer program developed by Ziegler [6]. The NRA profile was measure using a (p,γ) resonance reaction technique developed by Gossett [7]. The OES profile was prepared from data obtained by sputtering the sample with an Ar beam [8]. It should be noted that the three profiles are in good agreement within the uncertainties inherent in each technique. The Cu profile was measured only by RBS.

ANALYSIS

In order to fit the observed data we have developed a computer model of the implantation process. Much effort has previously been devoted to the calculation [9-13] of the distribution of implanted ions including the effect of sputtering. Additional effects, such as radiation enhanced diffusion, [14] changes in the stopping power of the substrate, [15] and preferential sputtering [14,15] have also been incorporated into this calculation. Since high fluence implants are generally used to modify the surface properties of metals and alloys, it seemed worthwhile to take into account in our model the "widening" of the target by the build-up of implanted ions. To the best of our knowledge, this effect has been previously considered only by Krautle [15].

19
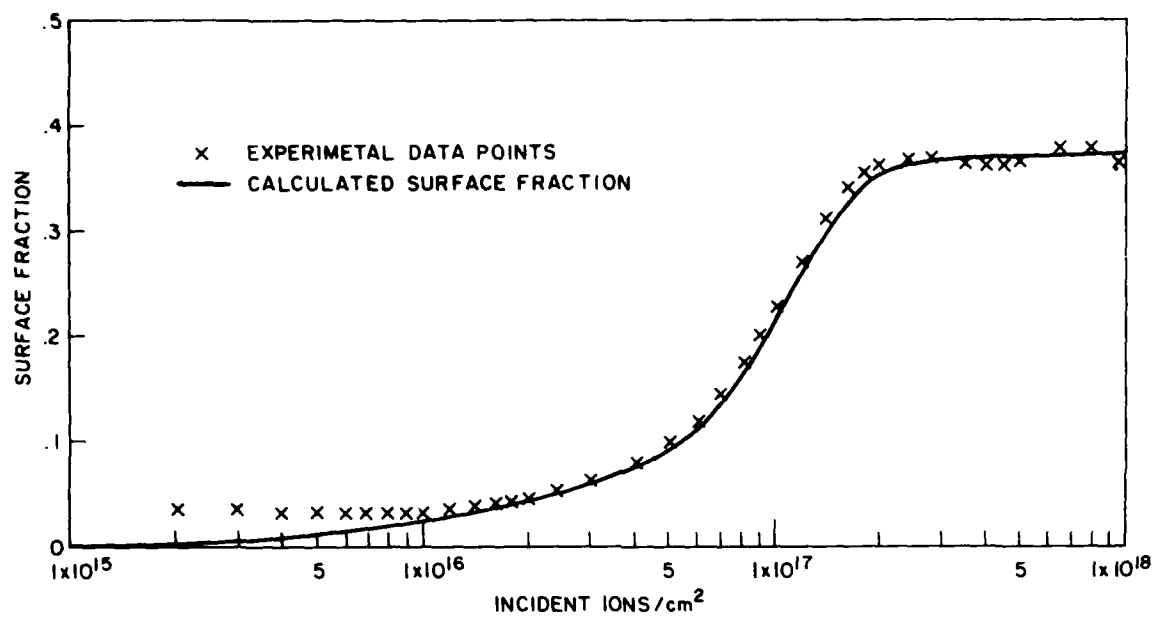
Fig. 2a — Normalized intensity of Cr optical signal at 357.5 nm during
implantation of 90-keV Cr into Fe

Fig. 2b — Normalized intensity of Fe optical signal at 373.4 nm during
implantation of 90-keV Cr into Fe

20
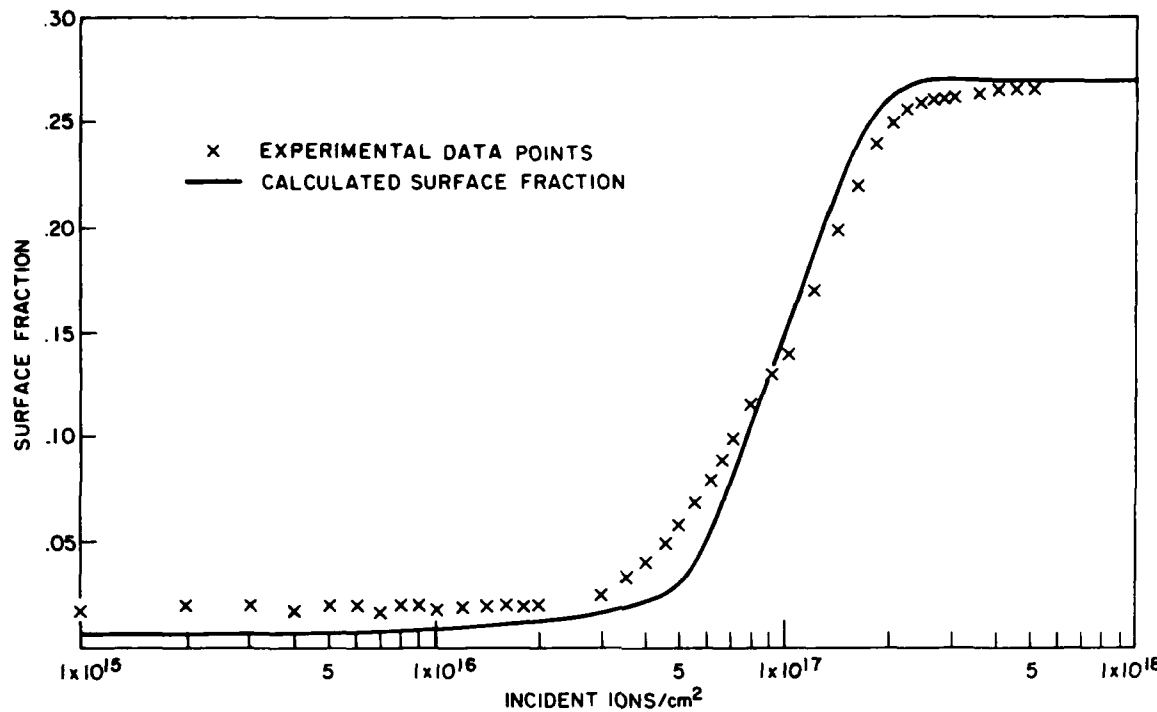
Fig. 3a — Normalized intensity of Cu optical signal at 324.7 nm during
implantation of 90-keV Cu into Al
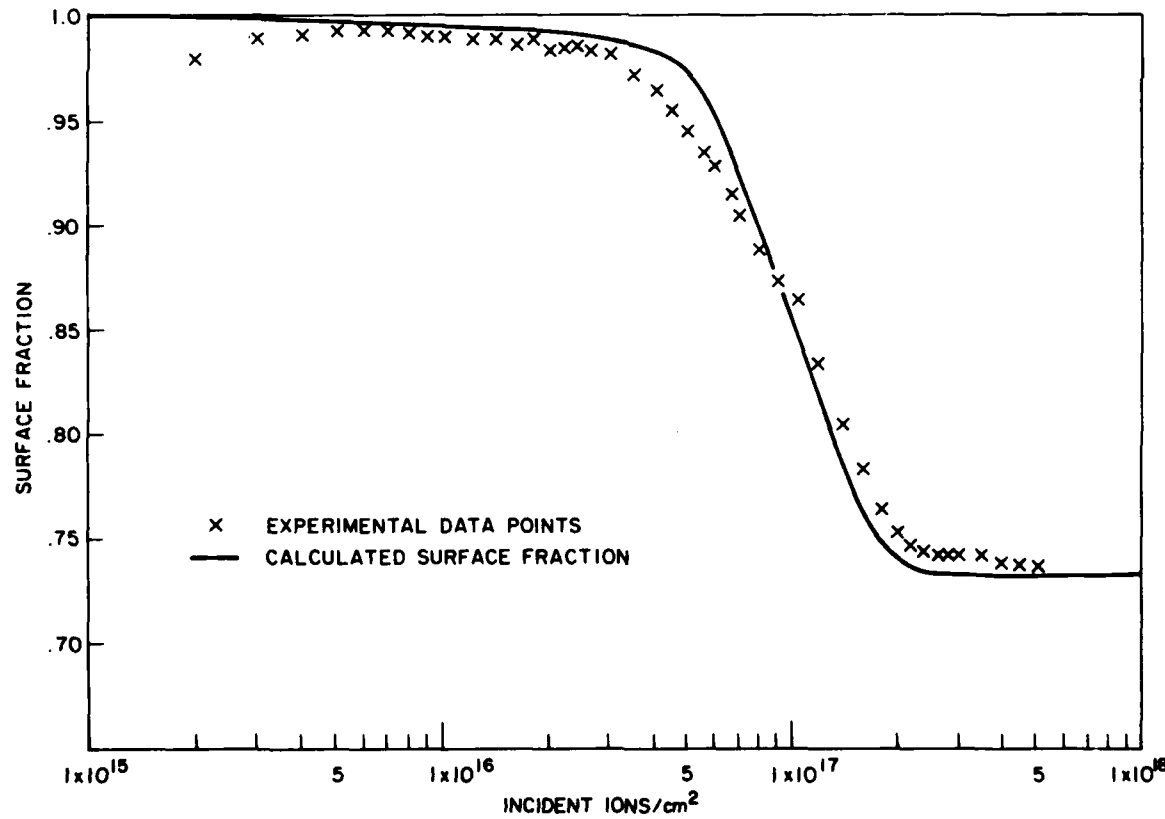
Fig. 3b — Normalized intensity of Al optical signal at 309.2 nm during
implantation of 90-keV Cu into Al

21
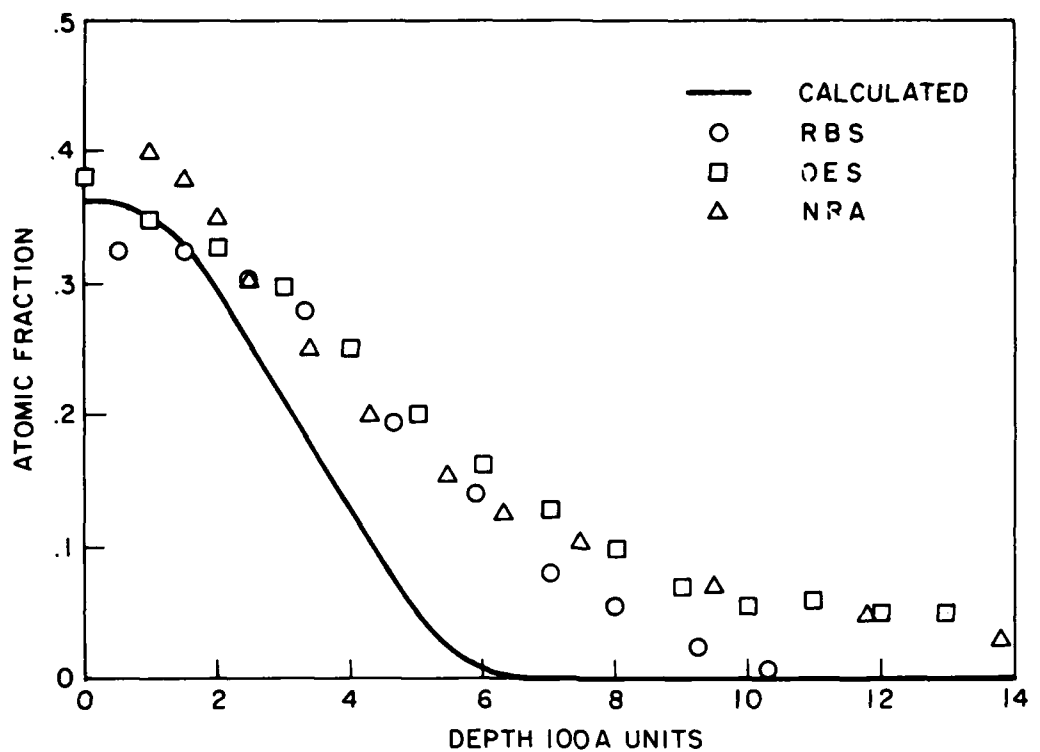
Fig. 4 — Steady state implanted Cr profile. This profile corresponds
to a fluence of 4.1×10^{17} atoms/cm^2
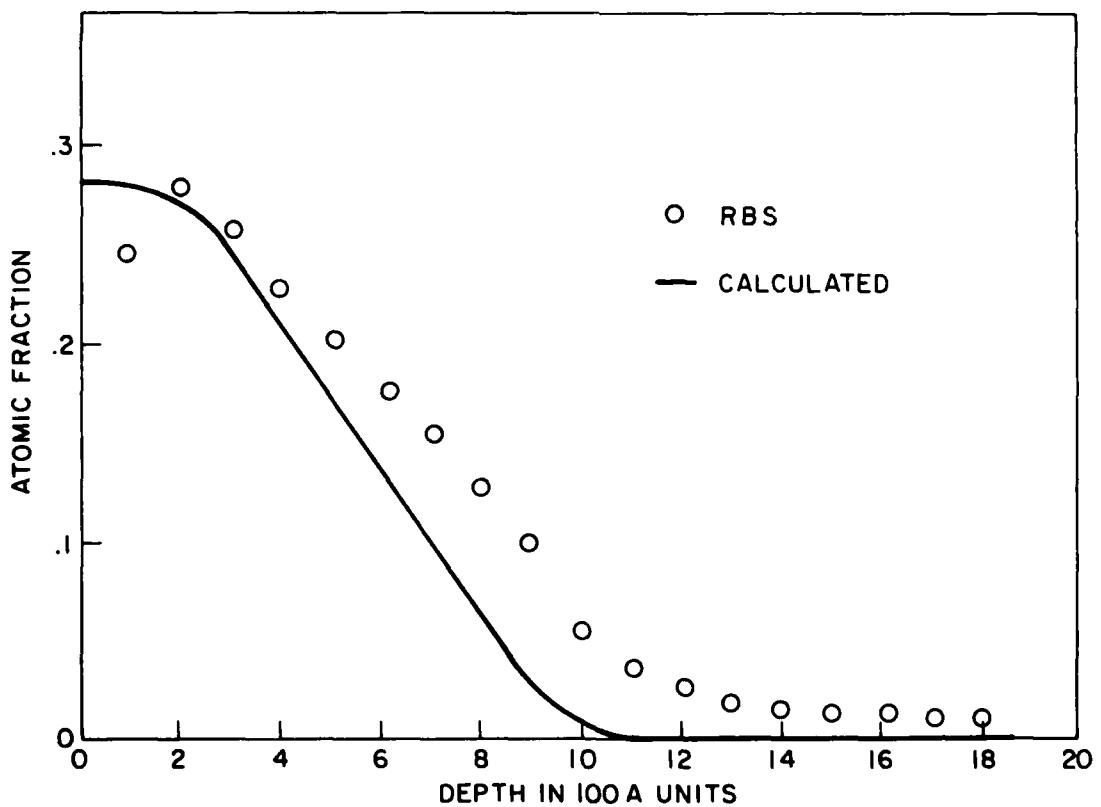
Fig. 5 — Steady state implanted Cu profile. This profile corresponds
to a fluence of 3.3×10^{17} atoms/cm^2

22

Our model is similar to Krautle's in including the effect of implanted ion build-up in widening the target and in neglecting radiation enhanced diffusion, but it differs in that it does not include the effect of the implanted ions on the stopping power of the substrate and preferential sputtering has been treated in a different manner. In our model the substrate is divided into layers parallel to the surface. Two arrays are used to describe the layers with one array containing information on the number of substrate atoms per cm^2 in each layer and the second array containing information on the number of implanted atoms per cm^2 in each layer. Each layer contains the same total number of atoms per cm^2. The range distribution of the implanted atoms is assumed to be an asymmetric Gaussian with parameters obtained from references 3 and 4. The fraction of beam ions which come to rest in each layer can then be calculated from this information.

It is assumed that the number of implanted atoms sputtered from the first layer is Nn_1S_1 and the number of substrate atoms sputtered from the first layer is Nn_2S_2 where n_1 and n_2 are the atomic fractions of implanted and substrate atoms in the first layer and S_1 and S_2 are the sputtering yields of the implanted and substrate atoms. N is the number of ions incident on the substrate in one iteration and is equal to the total number of atoms per layer divided by the larger of S_1 or S_2. A total of N implanted atoms are added to the various layers in accord with the calculated range distribution. The boundaries between layers are then readjusted so that each layer again contains the same number of atoms. N incident ions are sufficient to sputter away all of the higher sputtering yield element in the first layer, but only a portion of the lower sputtering yield element. The remainder of the lower sputtering yield element is then added into the second layer and the first layer is discarded. The N implanted atoms are again added to the various layers and the cycle is repeated for the desired number of iterations. The assumption of uniform mixing of material to a depth equal to the range of the incident ions could readily be incorporated into the model, but was not used for the calculations shown here.

DISCUSSION

Cr-Fe

In modeling the implantation of Cr into Fe, it was assumed that the sputtering yields of Cr and Fe were equal since the two elements are similar in mass and charge. The peak of the range distribution was calculated [3,4] to occur at a depth of 1.77×10^{17} atoms/cm^2 with the standard deviation of the half Gaussian nearest the surface being 7.32×10^{16} atoms/cm^2 and that of the other half Gaussian being 1.38×10^{17} atoms/cm^2. In order to fit the surface atomic fraction of Cr in the steady state a sputtering yield of 2.8 was used.

It was observed in Figures 2a and 2b the experimental surface concentration of Fe and Cr change more rapidly than the calculated concentrations. In addition the depth distribution of the Cr shown in Figure 4 extends to considerably greater depths than predicted. Measurements [7] of the depth profile of 150-keV Cr implanted into Fe are in good agreement with values determined from references 3 and 4, so it is unlikely that the predictions are greatly in error at 90 keV. Some possibility exists that heating of the target occurred during implantation, so thermal or radiation enhanced diffusion together with some recoil mixing may account for the discrepancies between theory and experiment.

From equation (2) it may be seen that the agreement between the atomic fraction of Cr determined by photon counting during the steady state phase of the implantation and that measured later by other techniques indicates that the product $k_i S_i$ for Cr in Fe is not significantly different than for an elemental Cr target which was used to calibrate the photon counting system. Also the fact that the Fe and Cr atomic fractions in the steady state add up to approximately 1 indicates that $k_i S_i$ for Fe does not change significantly when it is diluted with 38% Cr. It appears that k_i and S_i for both Cr and Fe are individually relatively insensitive to matrix effects, since no reason is known for them to vary in such a manner as to keep the product $k_i S_i$ invariant.

Cu-Al

In modeling the implantation of Cu into Al the sputtering yields for both Al and Cu were varied independently to fit the atomic fraction versus fluence data in Figures 3a and 3b. A Cu sputtering yield of 4.0 and an Al sputtering yield of 3.1 produced a good fit to the data. Although it is more common for the lighter element of a binary target to have the higher sputtering yield, numerous examples of the reverse situation exist. In addition the calculations of Sigmund in ref. 2 indicate that the sputtering yields for rare gas ions incident on elemental Al at these energies are lower than the corresponding sputtering yields of elemental Cu.

The measured depth profile of Cu in Al, shown in Figure 5, exhibits to a somewhat lesser degree the same sort of disagreement with the calculated distribution that was seen for Cr in Fe in Figure 4. References 3 and 4 predict that the peak of the range distribution should occur at a depth of 2.41×10^{17} atoms/cm^2 with the standard deviation of the half Gaussian nearest the surface being 6.71×10^{16} atoms/cm^2 and that of the other half Gaussian being 1.51×10^{17} atoms/cm^2. The dip seen in the data point closest to the surface is due to the energy resolution of the particle detector used for the RBS measurement. Possible causes of the disagreement between the measured and calculated distributions are expected to be the same as those mentioned for the Cr in Fe case.

Again the consistency of the surface atomic fractions derived from the RBS and the photon emission measurements seems to indicate that the products $k_i S_i$ for the constituents of the binary surface alloy are very similar to those of the corresponding pure elements. No evidence was seen of the phenomenon reported by Arminen et al[16] in which the amount of implanted Cu retained in Al plotted as a function of dose rises to a peak and then decreases to its steady state value.

SUMMARY

In summary the following points should be emphasized:

(1) The ability to predict the atomic fraction at the surface, the peak atomic fraction in the implanted layer, and the profile for any given fluence is severely limited by the precision with which the sputtering yields for the implanted species are known. The elemental sputtering yields interpolated from the literature [2] for Cr and Cu are larger by a factor of two than those determined by this study using the steady state condition for the implanted species.

24

(2)   The monitoring of the optical emission intensity of the sputtered implanted species produces a profile of the changing surface fractions during the implantation process.

(3)   The optical emission data indicate that the steady state condition is obtained when a surface layer approximately twice the mean range for the implanted species has been removed by sputtering.

(4)   The optical emission information that is collected during implantation concerning surface atomic fractions compares very well with the surface atomic fractions as measured by other techniques.

The binary systems studied here were selected to determine the feasibility of examining the sputtering behavior of both system components during the fabrication of a binary alloy by ion implantation. Although this study has not examined all the possible parameters which influence the sputtering behavior of these alloy surfaces, the technique appears to be a very useful tool for observing the surface behavior.

Further study in these systems and other binary systems should provide additional data on surface behavior during the implantation process.

REFERENCES

[1]   Treatise on Materials Science and Technology, J. K. Hirvonen, editor (Academic Press, New York, 1980).

[2]   H. H. Anderson and H. L. Bay, Chapter 4, Sputtering by Ion Bombardment (edited by R. Behrisch) (Springer-Verlay, Berlin, 1980).

[3]   J. F. Gibbons, W. S. Johnson, and S. W. Mylroie, Projected Range Statistics in Semiconductors and Related Materials, 2nd ed. (Dowden, Hutchinson and Ross, Inc., Stroudsberg, Penn., 1975).

[4]   K. B. Winterbon, Ion Implantation Range and Energy Distributions: Low Incident Ion Energies, Vol. II (Plenum, New York, 1975).

[5]   Z. L. Liau and J. W. Mayer, Chapter 2, Treatise on Materials Science and Technology (edited by J. K. Hirvonen) (Academic Press, New York, 1980).

[6]   J. F. Ziegler, private communication.

[7]   C. R. Gossett, Nucl. Instr. and Meth. 168 (1980) 217.

[8]   M. Braun, B. Emmoth, and R. Buchta, Rad. Effects 28 (1976) 77.

[9]   E. F. Krimmel and H. Pfleiderer, Rad. Effects 19 (1973) 83.

[10]   J. C. C. Tsai and J. M. Morabito, Surface Sci. 44 (1974) 247.

[11]   F. Schulz and K. Wittmaack, Rad. Effects 29 (1976) 31.

[12]   J. Biersack, Rad. Effects 19 (1973) 249.

[13]   R. Collins and G. Carter, Rad. Effects 26 (1975) 181.

[14]   G. Carter and R. Webb, Rad. Effects Lett. 43 (1979) 125.

[15]   H. Krautle, Nucl. Instr. and Meth. 134 (1976) 167.

[16]   E. Arminen, A. Fontell, and V. K. Lindroos, Phys. Stat. Sol. (a) 4 (1971) 663.

Section I.C

SPUTTER DISTORTION OF IMPLANTATION PROFILES

Irwin Manning

Materials Modification and Analysis Branch
Condensed Matter and Radiation Sciences Division
Naval Research Laboratory

Sputter Distortion of Implantation Profiles*

Irwin Manning
Materials Modification and Analysis Branch
Condensed Matter and Radiation Sciences Division

I. INTRODUCTION

The theory of preferential sputtering of binary alloys with diffusion is being studied. The starting point is the formalism of Collins, [1] but the approach is different in that the aim is to analyze experimental results to uncover details about the role of radiation-enhanced diffusion in perferential sputtering. (It may well be that other ion-beam mixing mechanisms, such as that of Haff and Switkowski, [2] will have to be considered.)

The sputter-induced erosion of the target surface affects ion implantation profiles. The present work examines only this isolated effect; we shall see that the sputter-induced distortion of profiles is significant for large-fluence implantations. The distortion of the profile of energy deposition is expected to be particularly significant for theories of preferential sputtering.

In order to better examine this one effect, we will assume that there is no diffusion or atomic mixing. We also assume that the penetrating ion beam is unaffected by the implanted atoms or effects caused by ion bombardment, such as target damage. This work is therefore didactic: an unrealistic model (no atomic migration or damage effects) is invoked in order to bring into clear relief the specific effects of sputter erosion of the target surface.

II. COORDINATE FRAMES

In addition to the laboratory frame x_L of figure 1, we consider a target frame x which has its origin fixed to the target surfaces. Let u be the x_L-value of the target surface. This distance is a function of the fluence τ: The target surface recedes with velocity $U(\tau)$ (whose units are distance per unit bombarding fluence):

$$U(\tau) = \frac{du}{d\tau} \tag{1}$$

$$u(\tau) = \int_0^\tau d\tau' \, U(\tau)$$

---

*Note added in proof: Since submitting this article, I have noticed that these results are contained in the work of F. Schulz and K. Wittmaack, "Model Calculation of Ion Collection in this Presence of Sputtering," Radiat. Eff. **29**, 31 (1976).
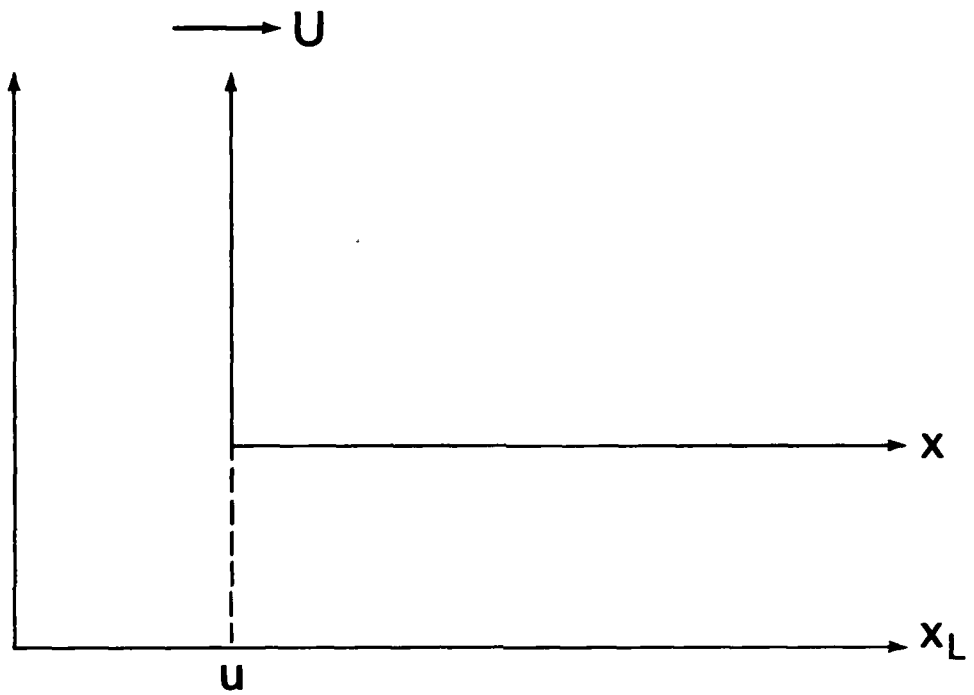
Fig. 1 — Laboratory and target coordinate frames. The target frame has its origin fixed to the target surface, which recedes with velocity U (units: distance per unit bombarding fluence).

III. RANGE PROFILES

A. Profile Evolution

Consider a monatomic target of B-atoms bombarded by a beam of A-ions. Let

$$f(x) \, dx \, d\tau = \text{number of beam ions coming to rest in } dx$$
$$\text{about about } x \text{ after fluence } d\tau, \tag{2}$$

This distribution has the property

$$\int_0^\infty f(x) \, dx = c$$

with

$$0 < c \leq 1. \tag{3}$$

One gets $c = 1$ when there are not reflected beam atoms (no albedo).

Also let

$$N_A(x,\tau) = \text{number density of beam ions at rest at } x \text{ after}$$
$$\text{bombarding fluence } \tau \tag{4}$$

We have

$$\lim_{\tau \to 0} N_A(x,\tau) = \tau f(x). \tag{5}$$

The steady state range profile is

$$N_A^S(x) = \lim_{\tau \to \infty} N_A(x,\tau). \tag{6}$$

For an increase of fluence from τ to $\tau + d\tau$ we have

$$dN_A(x,\tau) = f(x_L) \, d\tau$$

with

$$x_L = x + u(\tau). \tag{7}$$

Thus

$$N_A(x,\tau) = \int_0^\tau d\tau' \, f(x + u(\tau')). \tag{8}$$

Using $du = U(\tau) d\tau$,

$$N_A(x,\tau) = \int_0^{u(\tau)} du' \, \frac{1}{U(\tau')} \, f(x + u'). \tag{9}$$

The main result of this work is the analogue of equation (9) for energy deposition profiles.

B. Example: Gaussian Range Profile

Let

$$f(x) = \frac{1}{\sqrt{2\pi}\,\sigma}\; e^{-\frac{1}{2}\left(\frac{x-\bar{x}}{\sigma}\right)^2} \tag{10}$$

Assume that $\bar{x}/\sigma \gg 1$, so that there is no albedo. Assume also that $U(\tau)$ is a constant independent of fluence.

Introducing the dimensionless variable

$$\xi = \frac{x}{\sqrt{2}\,\sigma}\;, \tag{11}$$

we have

$$f(x) = \frac{1}{\sqrt{2\pi}\,\sigma}\; e^{-(\xi-\bar{\xi})^2}\;. \tag{12}$$

Equation (9) becomes

$$N_A(x,\tau) = \frac{1}{\sqrt{\pi}\,U}\int_0^{u(\tau)} du'\; e^{-(\xi-\bar{\xi}+u')^2}\;, \tag{13}$$

where

$$\mu = \frac{u(\tau)}{\sqrt{2}\,\sigma} = \frac{V\,\tau}{\sqrt{2}\,\sigma} \tag{14}$$

is a dimensionless parameter for the depth of target material sputtered off after fluence τ.

In terms of the complementary error function, [3] the distorted implantation profile (13) can be written:

$$N_A(x,\tau) = \begin{cases} \dfrac{1}{2u}\left\{\, \text{erfc}\,(\bar{\xi}+\mu-\xi) - \text{erfc}\,(\bar{\xi}-\xi)\,\right\}, & \xi < \bar{\xi}-\mu \\[2ex] \dfrac{1}{2u}\left\{\, 2 - \text{erfc}\,(\bar{\xi}-\xi) - \text{erfc}\,(\xi-\bar{\xi}+\mu)\,\right\}, & \bar{\xi}-\mu < \xi < \bar{\xi} \\[2ex] \dfrac{1}{2u}\left\{\, \text{erfc}\,(\xi-\bar{\xi}) - \text{erfc}\,(\xi-\bar{\xi}+\mu)\,\right\}, & \xi > \bar{\xi} \end{cases} \tag{15}$$

The steady state distribution is obtained by taking the limit $\tau \to \infty$:

$$N_A^S(x) = \begin{cases} \dfrac{1}{2u} \left\{ 2 - \text{erfc} \, (\bar{\xi} - \xi) \right\}, & \xi < \bar{\xi} \\[3mm] \dfrac{1}{2u} & , \; \xi = \bar{\xi} \\[3mm] \dfrac{1}{2u} \, \text{erfc} \, (\xi - \bar{\xi}) & , \; \bar{\xi} - \xi \end{cases} \qquad (16)$$

Figure 2 depicts the initial distribution $f(x)$ and the steady state distribution N_A^S (x) for the case $\bar{\xi} = 6$, while figure 3 depicts the evolution of f to N_A^S for several values of u (or, equivalently, several values of fluence).

C. Saturation Density

For the example of section IIIB above, the saturation density is

$$N_A^S \, (o) = \frac{1}{U} \qquad (17)$$

Let S_A and S_B be the sputtering coefficients for A and B atoms (atoms sputtered per incident ion), and let N_A and N_B be the respective atomic volumes ($N_B \equiv N_B^{-1}$). We have

$$U = S_A \, v_B + S_B \, v_B. \qquad (18)$$

Now assume that

$$v_A = v_B \equiv v$$

so that

$$N \equiv N_A + N_B$$

remains constant during the implantation. Then equation (18) becomes

$$U = v \, (S_A + S_B) \equiv v \, S. \qquad (19)$$

Using

$$v = \frac{1}{N_A + N_B} \, , \qquad (20)$$

the relation (17) can be recast into the familiar result [4]

$$\frac{N_A}{N_A + N_B} = \frac{1}{S} \, , \qquad (21)$$

where the quantities N_A and N_B are (saturation) steady-state values at the target surface.
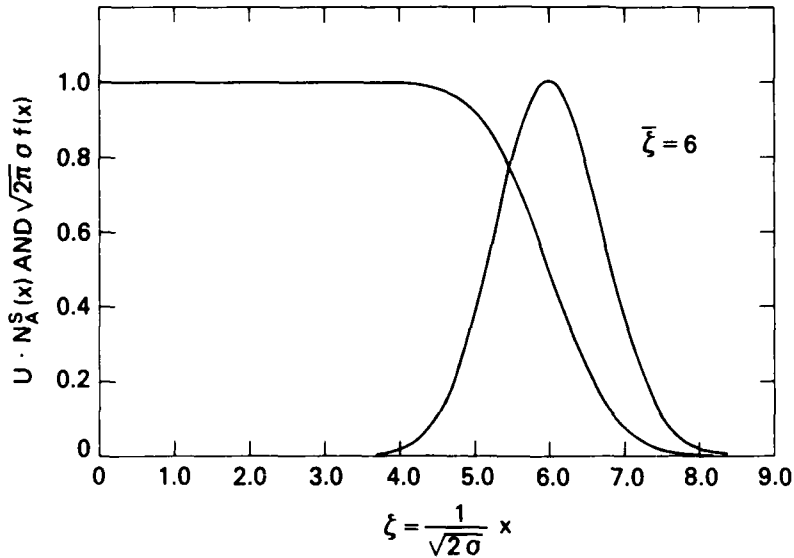
Fig. 2 — Range distributions for the two extremes of infinite and zero fluence. In both cases the ordinates are dimensionless, as is the abscissa.
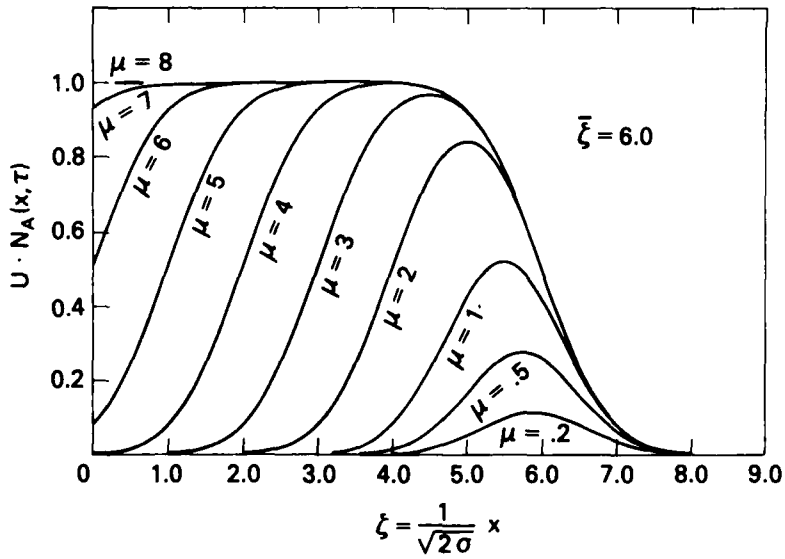

Fig. 3 — The evolution of the distribution f to N_A^S for several fluences, determined by the dimensionless parameter μ of equation (14), which measures the amount of target material sputtered away.

IV. ENERGY DEPOSITION PROFILE

The density of Frenkel defects initiated by ion bombardment is proportional to the damage energy S_D deposited into the target, [5] where

$$S_D(x) dx d_\tau = \text{damage energy density deposited into dx about x}$$
$$\text{during fluence } d\tau. \tag{22}$$

The total damage energy per incident ion (for small fluences) is

$$E_D = \int_0^\infty S_D(x) \, dx. \tag{23}$$

In analogy with section IIIA, let

$$G(x,\tau) \, dx = \text{damage energy deposited into dx about x after}$$
$$\text{fluence } \tau \tag{24}$$

We have

$$\lim_{\tau \to 0} G(x,\tau) = \tau \, S_D(x), \tag{25}$$

and the steady state distribution is

$$G^S(x) = \lim_{\tau \to \infty} G(x,z). \tag{26}$$

Corresponding to equation (9), we have the main result

$$G(x,\tau) = \int_0^{u(\tau)} du' \, \frac{1}{u(\tau')} \quad S_D(x + u'). \tag{27}$$

The example of section IIIB indicates that, independent of the detailed shape of $S_D(x)$, we can expect a steady-state (saturation) energy deposition profile which, for $x/\bar{x} \ll 1$, has the constant value

$$G^S(x) = \frac{E_o}{U}, \quad o \le x \le \bar{x} \quad - \partial. \tag{28}$$

V. CONCLUSION

In high-fluence bombardments, the sputtering erosion of the target surface causes significant alterations of implantation profiles. This is expected to be an important effect for the profiles of energy deposition and implanted ions.

REFERENCES

1. R. Collins, "Preferential Sputtering of Binary Alloys with Diffusion," Radiat. Eff., Vol. **37**, pp. 13 (1978).

2. P. K. Haff and Z. Switkowski, "Ion-Beam Induced Atomic Mixing," J. Appl. Phys., Vol. **48**, pp. 3383 (1977).

3. M. Abramowitz and I. A. Stegun, Handbook of Mathematical Functions (National Bureau of Standards, 1964), section 7.] .

4. See, for example, the article by Z. L. Liau and J. W. Mayer, "Ion Bombardment Effects on Material Composition," in Treatise on Materials Science and Technology, edited by J. K. Hirvonen (Academic Press, 1980).

5. The notation is that of I. Manning and G. P. Mueller, "Depth Distribution of Energy Deposition in Ion Bombardment," Computer Phys. Commun., Vol. **7**, pp. 85 (1974).

Section I.D

COMPUTER SIMULATIONS OF ION IMPLANTATIONS

Mervine Rosen, George P. Mueller

Radiation-Matter Interactions Branch
Condensed Matter and Radiation Sciences Division
Naval Research Laboratory

COMPUTER SIMULATIONS OF ION IMPLANTATIONS

Mervine Rosen, George P. Mueller

Radiation-Matter Interactions Branch
Condensed Matter And Radiation Sciences Division

ION BEAM MIXING

INTRODUCTION

We are carrying out an investigation of possible mechanisms in ion beam interface mixing. The restriction placed by sputtering on the percentage of atoms that may be implanted into a surface can be circumvented by placing a thin film of the material to be implanted on the surface of the substrate and then bombarding the system with a beam of atoms whose range is at least equal to the film thickness. For high incident fluence all of the thin film is incorporated into the substrate.

PROGRESS

Simulation calculations with MARLOWE allow us to determine directly the role played by recoil implantation in this process and yield the distribution (density and concentration gradients) of vacancies and interstitals produced during the irradiation. This latter information is necessary to study the subsequent role of diffusion processes in the system. Both phenomena contribute to the disruption of the interface between film and substrate. Because much experimental information is available for the case of a palladium coated silicon substrate exposed to a beam of energetic xenon atoms, we have concentrated our calculations on this system. The computations are well under way and preliminary results indicate that recoil implantation is not responsible for the bulk of the palladum-silicon mixing. It is know, however, that the diffusion processes do not occur at room temperature without being initiated by an irradiation.

CONCLUSION

Because the results of our calculations will form the initial conditions for the various competing diffusion processes, we are looking into the possbility of performing (simple) diffusion calculations on the palladium-silicon system.

SPUTTERING

INTRODUCTION

As part of a collaboration with the experimental ion sputtering group of Code 6670, we have started a program of simulating ion sputtering using the binary-collision simulation code MARLOWE of Robinson and Torrens.[1] (The code was described briefly in the last review of the group.[2]) This is a preliminary report in which we indicate the kind of information that is readily obtainable from MARLOWE, and then outline how we plan to use the code to fit several of the phenomenological parameters associated with sputtering.

PROGRESS

We have investigated copper self sputtering, which is one of the first experiments planned by Code 6670, and show typical results for the case of a bombardment by 100 copper ions, with energy 90 keV, normally incident on a polycrystalline copper surface. In order to minimize computer time, we take the target to be a thin film of copper of thickness about ten atomic layers. This is adequate because virtually no sputtered atoms originate deeper in the target.

The results shown assume a surface binding energy of 4.5 eV. The code examines any ion that is about to leave the surface and prohibits its escape if the "normal component" of its energy is less than the surface binding energy.

In Fig. 1 we show the depth distribution of the original sites of the sputtered atoms. The results justify the thin film model. We see that almost all of the sputtered atoms originate within one to three atomic layers of the surface. Less than one per cent start as deep as the eighth layer.

The angular distribution of sputtered particles is shown in Fig. 2. We see that within the statistical errors, the yield per unit solid angle varies linearly with the cosine of the outgoing direction theta, where theat is measured from the surface normal. This is the expected relationship based on a simple model of the sputtering process.[3] The slope of this line depends on the value of the surface binding energy.

In Fig. 3 we display the frequency of occurrence that n atoms are sputtered by an incident atom, as a function of n. The average number of sputtered atoms is 4.2, indicated by the arrow in the drawing. But we note that 40% of the time no atoms are sputtered and 5% of the time more than 20 are sputtered. This is a good example of what one often finds in these simulation studies, namely that the average result is not necessarily a typical or insightful result.

In Fig. 4 we show the energy distribution of the sputtered particles. We see that over 30% leave the surface with less than 10 eV and that few leave with more than 40–50 eV. The shaded portion of the figure indicates the additional particles that would have been sputtered if we had not imposed a surface binding energy. We see that the overall sputtering rate is sensitive to the value of the surface binding energy.

Members of the Materials Modifications Branch are planning a series of self-sputtering experiments, ranging from light to heavy metals. We plan to use their results as a data base that will allow us to set values (or ranges) of several phenomenological parameters in our theoretical model, e.g., the surface binding energy, which will enable us to make reasonably good predictions of the sputtering properties of other species by running MARLOWE with these (fitted) parameters.

CONCLUSION

In order to give us greater flexibility, we will impose a zero surface binding energy on future MARLOW runs. Each sputtered atom and its energy direction and other characteristics will be stored. Then a simple auxiliary program that we are writing will be used to study how the distribution of sputtered ions varies as the binding energy is changed. In addition, the auxiliary program will allow a variety of tabular and graphical displays of the results.
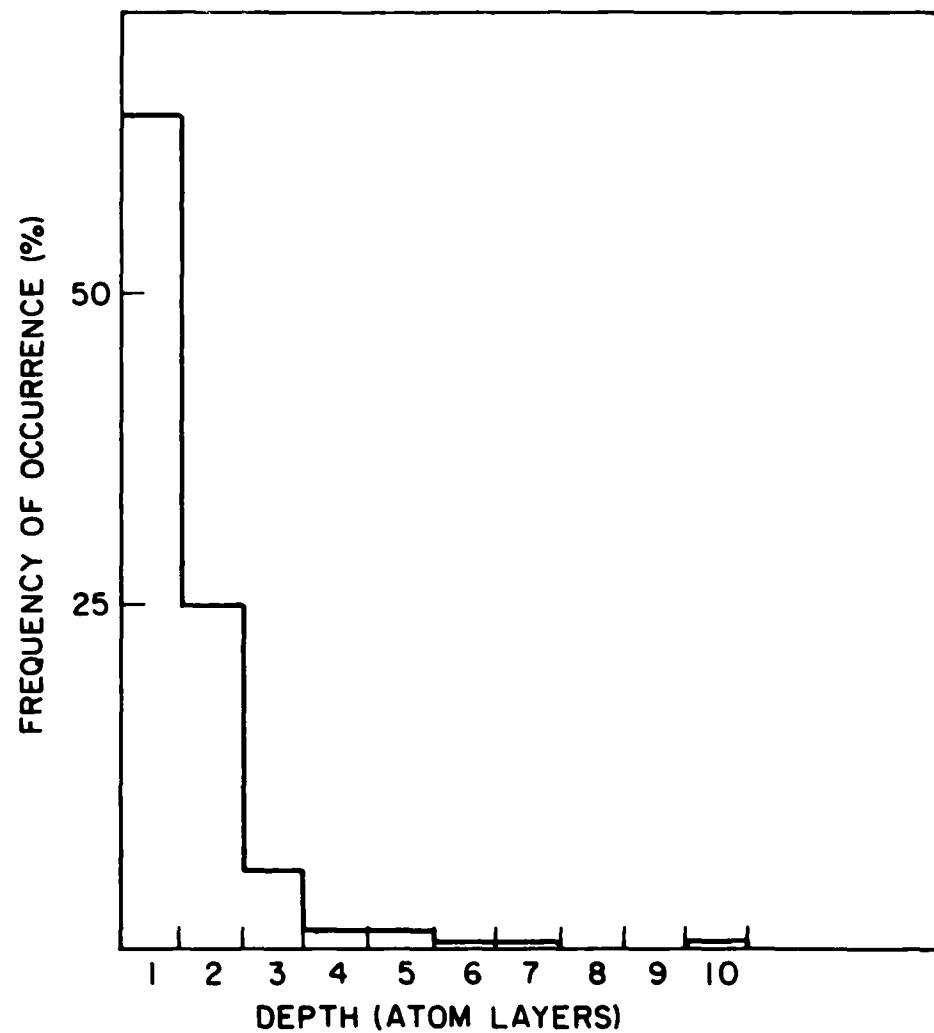
Fig. 1 — Depth distribution of original site of sputtered atoms
for the case of 90 keV copper self sputtering
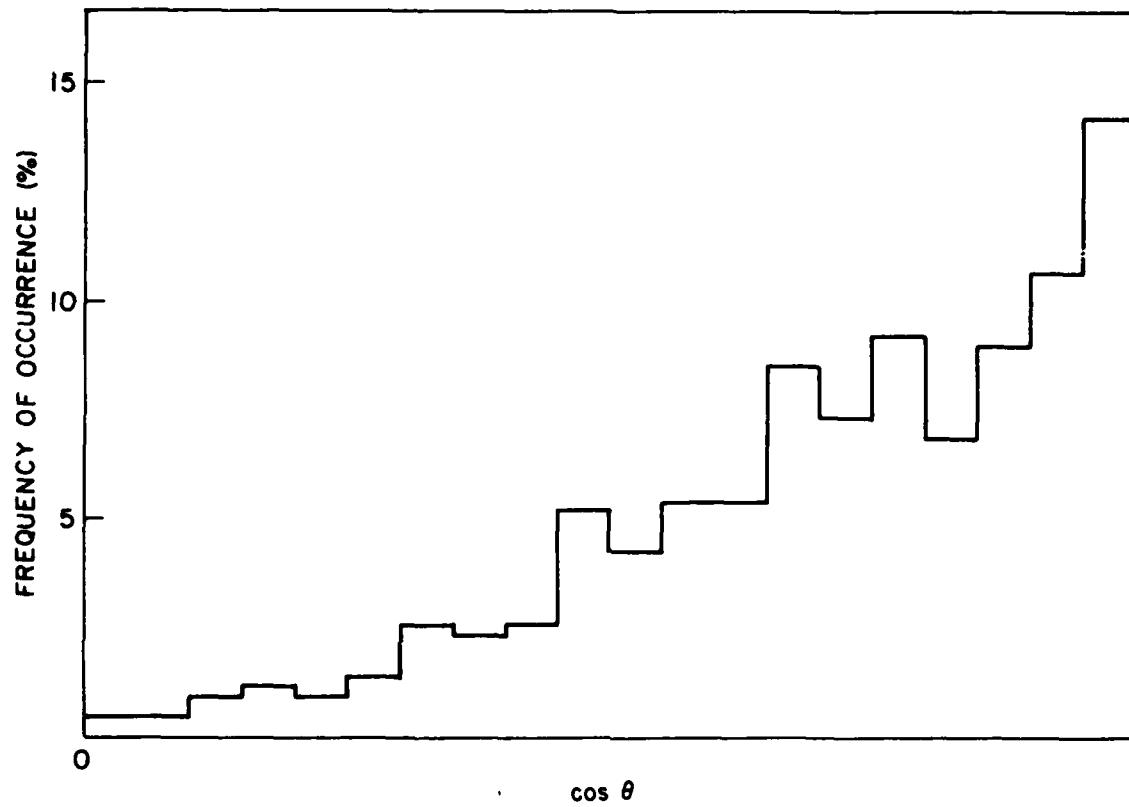
Fig. 2 — Angular distribution of sputtered particles

41
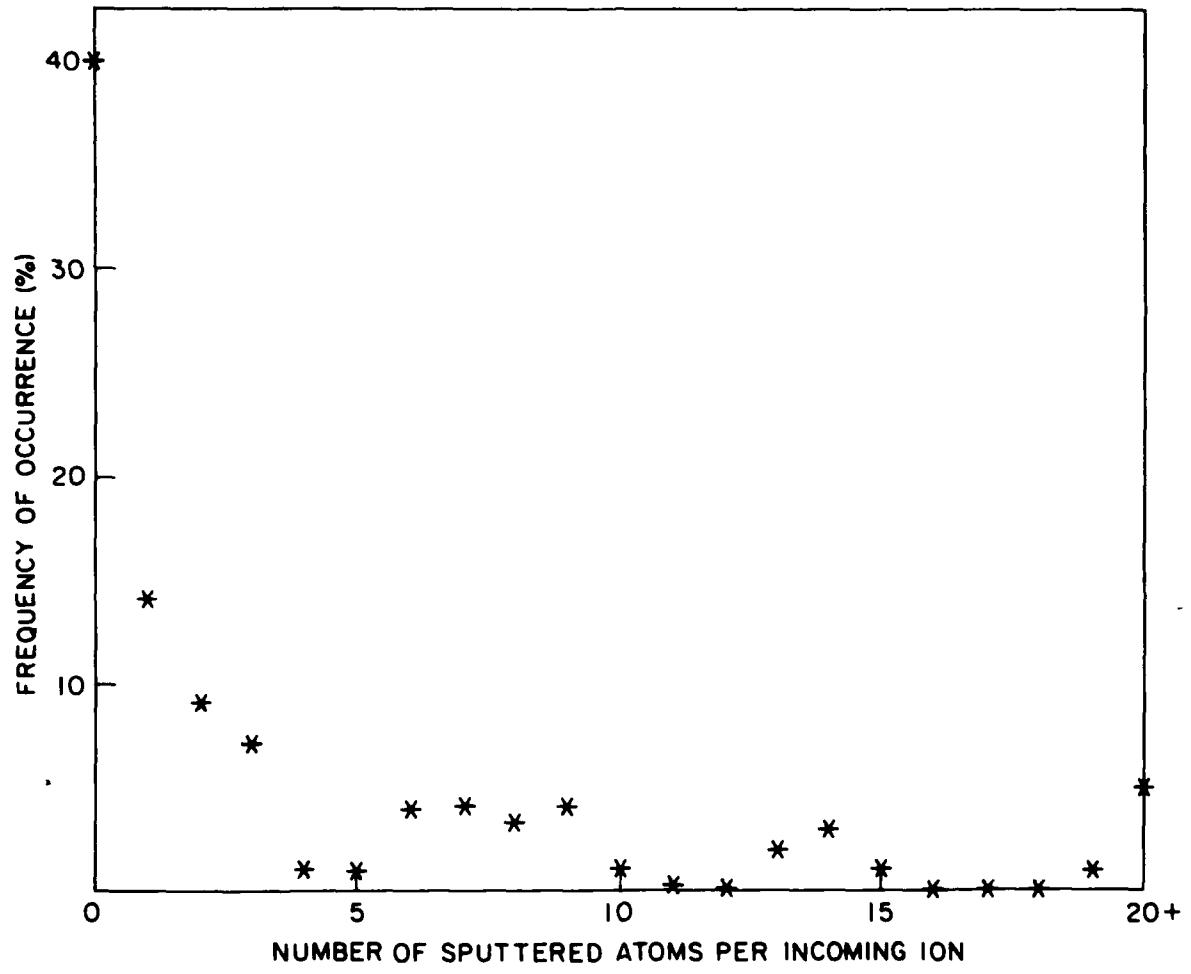
Fig. 3 — Yield of sputtered particles: the frequency of occurrence of the
number of sputtered particles per incoming ion
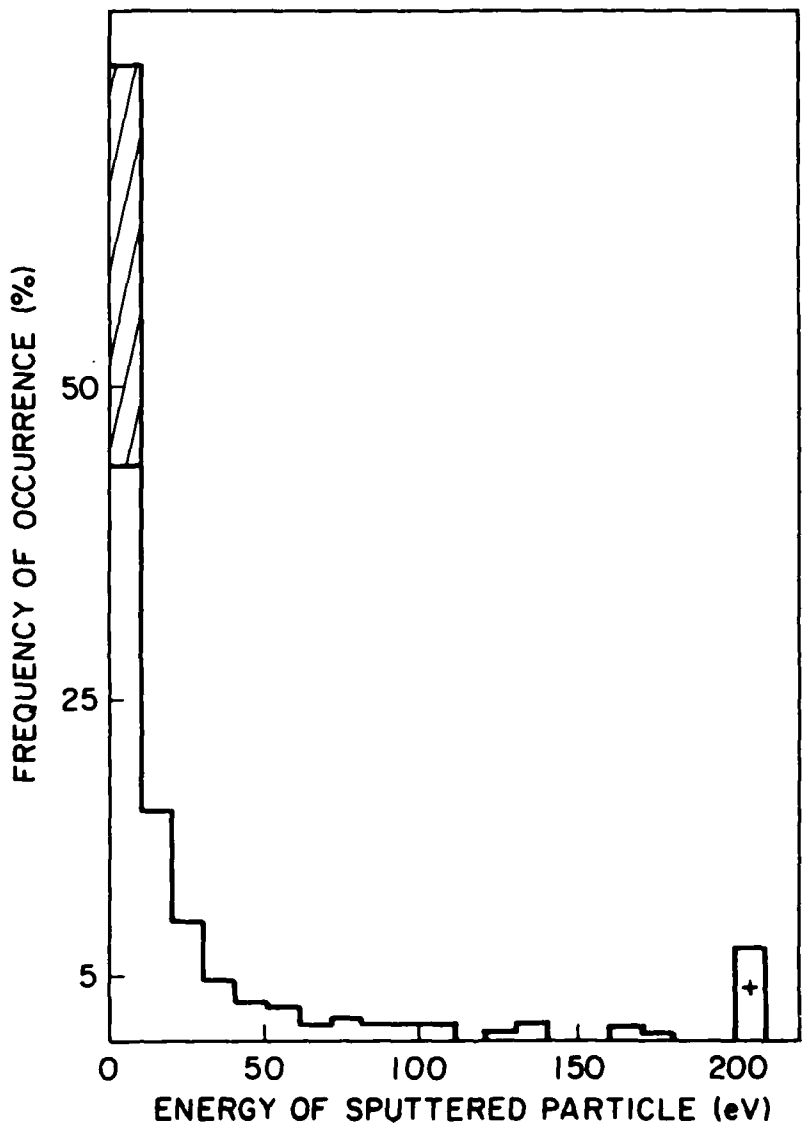
Fig. 4 — Energy distribution of sputtered particles. The shaded region in the 10 eV bin indicates the additional atoms that would have been sputtered if the surface binding energy were zero.

REFERENCES

1.   M. T. Robinson and I. M. Torrens, "Computer Simulation of Atomic-Displacement
      Cascades in Solids in the Binary-Collusion Approximation," Phys. Rev. B9, pp.
      5008-5024 (1974).

2.   G. P. Muller and M. Rosen, "Ion Implantation Simulations with MARLOWE," pp.
      29-32, in The Use of Ion Implantation for Materials Processing (Semi-annual
      Report), F. A. Smidt, Coordinator, NRL Memorandum Report 4341, October 1980.

3.   M. W. Thompson, "The Energy Spectrum of Ejected Atoms During the High
      Energy Sputtering of Gold," Phil. Mag. 18. pp. 377-4] 5 (1968).

Section II.A

ABRASIVE WEAR RESISTANCE OF TITANIUM – AND NITROGEN-IMPLANTED 52100 STEEL SURFACES

I. L. Singer[1], R. N. Bolster[1] and C. A. Carosella[2]

[1]Surface Chemistry Branch
Chemistry Division

[2]Materials Modification and Analysis Branch
Condensed Matter and Radiation Technology Division
Naval Research Laboratory
(Currently on assignment at Office of Naval Research, Arlington, VA)

ABRASIVE WEAR RESISTANCE OF TITANIUM- AND NITROGEN-IMPLANTED 52100 STEEL SURFACES*

I. L. SINGER, R. N. BOLSTER AND C. A. CAROSELLA

Naval Research Laboratory, Code 6170, Washington, D.C., 20375 (U.S.A.)

The wear resistance of titanium- and nitrogen-implanted 52100 bearing steels was measured by an abrasive wear technique with a depth resolution of 20 30 nm. Titanium-implanted surfaces were extremely resistant to wear against fine (1 5 μm) diamond abrasion, which suggests a very hard surface layer. Nitrogen-implanted surfaces, by contrast, wore at the same rate as non-implanted surfaces. Wear resistance *versus* depth profiles of titanium-implanted surfaces followed the concentration *versus* depth profile of the implanted titanium. Auger depth profiles indicated a large concentration of carbon (≈ 20 at.%, maximum) distributed with a diffusion-like profile from the titanium-implanted surface into the bulk. The carbon was identified by Auger line shape analysis as a titanium carbide, and the wear resistance of the surface was attributed in part to its presence.

1. INTRODUCTION

Ion implantation is a surface treatment which has shown great promise for improving the sliding wear resistance of steels[1-4]. One class of steels which forever need improving are the "work-horse" steels of the bearing industry   52100, 440C and M50. Wear studies were performed recently on 52100 steel implanted with various ion species[5]. One species, titanium, caused spectacular improvements in both the friction and the wear behavior, whereas nitrogen, which had previously been shown to improve sliding wear in softer steels[1-4], appeared ineffective.

In the present study, wear *versus* depth profiles of titanium- and nitrogen-implanted 52100 steel surfaces were measured with a depth resolution of about 20 30 nm. An abrasive wear technique was used which we[6,7] and others[8-10] have previously shown to be sensitive to the hardness of steels. Here, correlations of wear resistance *versus* depth and composition *versus* depth profiles are also shown.

2. EXPERIMENTAL TECHNIQUES

2.1. Sample preparation

AISI 52100, a steel widely used in bearing applications, has the composition Fe 1C 1.5Cr 0.3Mn 0.2Si in weight per cent. Three 52100 steel discs were quench

hardened* to produce a martensitic structure. In addition, nine carbon steel discs were prepared from a low alloy carbon tool steel (composition Fe 1C 0.3Mn 0.2Si) whose carbon concentration was near that of the 52100s. Two sets of these discs were heat treated and a third was thermally nitrided[7]. The Knoop hardness values of all the discs examined are given in Table 1.

TABLE 1

RELATIVE ABRASION RESISTANCE OF NITROGEN-IMPLANTED STEELS

Material and treatment	Hardness HK_{2kg} (kg mm^{-2})	Relative wear rates	
		Non-implanted	Nitrogen-implanted[a]
Carbon steel			
Quenched and tempered	400	1	1.5 ± 0.2
Quenched	800	1.2 ± 0.2	1.2 ± 0.1
Nitrided		1.5 ± 0.1	
52100			
Quenched and tempered	720	1.1 ± 0.1	1.1 ± 0.1

[a] Average values from the first 50 nm of wear.

2.2. Abrasive wear studies

Wear resistance *versus* depth profiles of implanted layers were obtained by repeatedly abrading and weighing implanted and non-implanted discs[6]. Nine discs, six implanted and three reference, were abraded in a vibratory polisher charged with diamond powder (1 5 μm) in paraffin oil. The atmosphere was air dried to a frost point of 200 K. After each wear period, the discs were ultrasonically cleaned, rinsed and dried, and their mass losses were determined by weighing them with microgram precision. The relative wear resistance (RWR) of an implanted disc was calculated as the inverse of the wear depth of the implanted disc normalized to that of the reference disc. Carbon steel discs, quenched and then tempered to a hardness of $HK_{2kg} = 400$ kg mm^{-2}, served as reference discs. Since each microgram loss of steel corresponded approximately to a depth of 1 nm and mass losses could be measured to ± 3 μg, RWRs could be determined with depth uncertainties of a few nanometers for layers as thin as 15 nm.

Wear depths Δd for each wear period were calculated from the mass loss Δm, area A and density ρ, as $\Delta d = \Delta m / \rho A$. For non-implanted and nitrogen-implanted discs, wear depths were calculated using the measured density of the disc. For titanium-implanted discs a depth-dependent density $\rho(d)$ was used to account for the mass of titanium in the steel surface. $\rho(d)$ was calculated as

$$\rho(d) = \rho_{steel}\left(1 - \frac{[Ti]}{100}\right) + \rho_{Ti}\frac{[Ti]}{100}$$

in which the titanium concentration [Ti] was determined from composition *versus* depth profiles of the titanium-implanted 52100 steel, and densities of $\rho_{steel} = 7.8$ g cm^{-3} and $\rho_{Ti} = 4.5$ g cm^{-3} were assumed.

* Austenitized at 1520 F for 10 min; oil quenched at 120 F for 3 min; subcooled to −120 F for 2.5 h; tempered at 375 F for 5 h.

2.3. Implantation

The surface finish on the discs before implantation was that achieved by lengthy polishing in 1–5 µm diamond. Polished discs were then implanted with a model 200–20A2F Varian/Extrion ion implanter equipped with a hot cathode arc discharge source and a rasterable ion beam. The titanium beam energy was 190 keV and the average current density 5 µA cm^{-2}. The N$_2$ molecular ion beam energy was 80 keV (i.e. 40 keV (nitrogen ion)$^{-1}$) and the average current density was 4 µA cm^{-2} The samples were mounted on a water-cooled substrate holder and the chamber pressure was kept below 10^{-7} Torr during implantation. Implantation fluences were 4.6 × 10^{17} ions cm^{-2} and 2 × 10^{17} ions cm^{-2} for titanium and nitrogen respectively.

2.4. Auger analysis

Auger analysis was performed with a scanning Auger microprobe system (Perkin-Elmer PHI Model 545). The UHV chamber was equipped with a CMA Auger analyzer, a rasterable ion gun, a titanium sublimator and liquid-nitrogen-cooled cryopanels. The electron gun was operated at 2 kV at a current of about 0.6 µA and was rastered over a spot size of 50 µm to reduce the intensity. Auger derivative spectra were recorded either directly, with a modulation amplitude of 3 eV, or by a peak-height-recording multiplexer with a 6 eV modulation amplitude.

The ion gun was operated at 2 kV in an argon atmosphere ($p \approx 5 \times 10^{-5}$ Torr) with a rastered beam at a current density of about 30 µA cm^{-2}. Auger depth profiles were recorded during ion milling with titanium sublimators operating and cryopanels cooled to the liquid nitrogen temperature. These procedures reduced the contamination of ion-milled surfaces by residual gas vapors to below detectable levels.

Composition analysis of titanium-implanted steel was achieved by combining nuclear reaction profile data with Auger reference data. Relative sensitivity factors for Ti$_{385 \text{ eV}}$ to Fe$_{650 \text{ eV}}$ Auger lines were determined from a ^{48}Ti(p,γ)^{49}V resonance reaction; for C$_{272 \text{ eV}}$ to Ti$_{385 \text{ eV}}$. Auger spectra of TiC powders were measured[5]. The sensitivity factors were similar to those found in ref. 11, except for carbon, which had been established for a graphite-type carbon line shape and not a carbide-type line shape.

The depth scale for the Auger profiles was established by Michelson interferometry. Auger depth profiles were taken near the edges of partially masked steel surfaces. The depth of an ion-milled step was later measured with an interference microscope to an accuracy of about ±5 nm. This procedure gave the depths at which several composition profiles had been terminated. Since no differences were observed in the milling rates of implanted and non-implanted steels the depth was assumed to be proportional to milling time.

3. RESULTS AND DISCUSSION

3.1. Titanium-implanted 52100 steel

Abrasive wear data on titanium-implanted 52100 steel are shown in Fig. 1. The RWR increased to a value of about 6 at a depth of 60 nm, then fell off gradually from 100 to 600 nm. Beyond 600 nm the RWR value 1.1 ± 0.1 was that of the non-implanted 52100 (see Table I). The broken line indicates the trend in the data. The

48

RWR values are markedly higher than values obtained for the nitrided carbon steel; this indicates extreme surface hardening. An almost identical curve was obtained for the hardened carbon steel implanted with titanium ions.
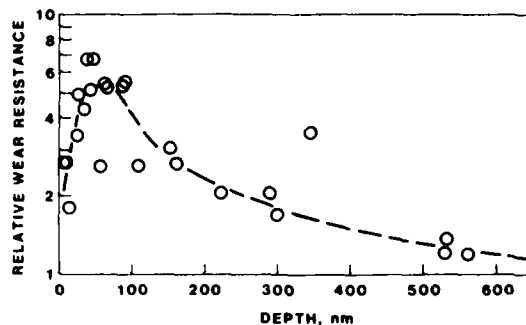

Fig. 1. Relative wear resistance of titanium-implanted 52100 steel vs. depth.
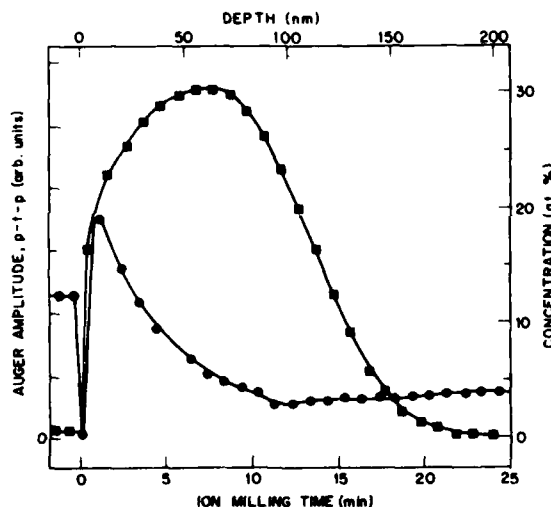
Fig. 2. Concentration vs. depth profile of titanium and carbon in titanium-implanted 52100 steel by Auger analysis with ion beam milling: Auger lines (■) $Ti_{385\,eV}$ and (●) $C_{272\,eV}$.
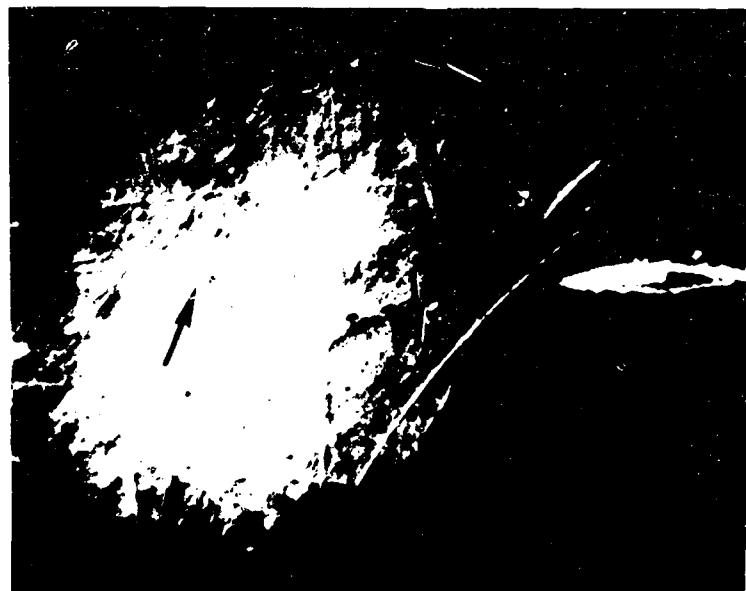
The shape of the RWR versus depth curve within the first 150 nm of the surface follows the composition versus depth curve (Fig. 2) of a titanium-implanted 52100 steel disc. The similarity of the two curves is evidence that abrasive wear responds to hardness at the surface with very good depth resolution. Nomarski photo-micrographs of worn surfaces support this contention. Medium-sized scratches produced during one abrasion period, shown in Fig. 3(a), virtually disappeared after about 15 nm of material had been removed (Fig. 3(b)). The true depth sensitivity of the hardness profiles might well be 20 or 30 nm, even though the abrasive particle size is 1–5 μm diamond. Below the implanted surface (≈ 150 nm) the wear resistance fell off slowly over a depth of about 600 nm. Its persistence beyond the implanted layer possibly indicates non-uniform cutting; that is, as one area of the "hardened"

49

layer was worn away, softer substrate material beneath it was removed much more rapidly than were the remaining patches of hard material.

Fig. 3. Nomarski photomicrographs of abrasion scratch marks on the titanium-implanted 52100 surface: (a) after implantation but before wear; (b) after about 15 nm of wear by abrasion. Medium-sized scratch marks in (a) are barely visible in (b).

In addition to titanium, the composition profile showed a large unexpected concentration of subsurface carbon. Appearing directly below the oxide layer, the carbon first reached a maximum concentration of about five times the bulk value of 4 at.%. The concentration then fell off, with a diffusion-like tail, to almost the bulk value at a depth of about 100 nm. The carbon profile actually appeared to dip to a minimum before leveling off. We do not yet know whether this dip reflects a gradient in the carbon concentration or is an Auger artifact associated with ion milling through a rapidly changing interface. Carbon profiles similar to that shown in Fig. 2 have also been observed in low carbon AISI 304 stainless steel (Fe 18Cr 8Ni) and in pure iron (< 20 ppm C). The latter observation suggests that the subsurface carbon (above background) in titanium-implanted 52100 steel diffused in from the surface via the vacuum system during implantation. Knapp et al.[12] also observed subsurface carbon in pure iron samples implanted with titanium and likewise have attributed it to diffusion from the surface.

Auger line shape analysis was used to infer the chemical identity of titanium and carbon in the implanted 52100 steel. The carbon, which virtually disappeared in the oxide layer, reappeared below it in the form of titanium carbide, as identified by the $C_{272 eV}$ line shape. Titanium carbide was also identified from the $Ti_{385 eV}$ and $Ti_{420 eV}$ line shapes[13]. As the carbide disappeared, the titanium line shapes became more like those of metals.

The titanium carbide phase may be very fine. Since Auger electrons detect the local electronic states of atoms, Auger spectra cannot easily be used to distinguish a single TiC molecule from a TiC precipitate. Knapp et al.[12] performed transmission electron microscopy on their titanium-implanted iron samples and observed no TiC crystallites; in fact they saw no crystalline features at all. The surface of titanium-implanted iron was amorphous.

The wear resistance of the titanium-implanted steel surface is presumed to be due, in part, to the presence of a fine carbide phase (of unknown origin) within the surface. It might also be due to an amorphous microstructure. Disordered alloys may be both harder and more resistant to mild wear than ordered alloys, as a wear study by Sheasby[14] of an Fe Co V alloy has shown. In either case, the increased resistance to sliding wear of titanium-implanted 52100 bearing steel, reported by Carosella et al.[5], can be attributed to a hardened surface layer.

3.2. Nitrogen-implanted 52100 steel

Nitrogen implantation did not affect the abrasive wear resistance of either 52100 or hardened carbon steel. The nitrogen-implanted discs wore at the same rate as non-implanted discs at depths to 300 nm. RWR values listed in Table I are averages of the first 50 nm of wear. Apparently nitrogen implantation does not "harden" a carbon steel already quenched. This result is consistent with the recent finding of Carosella et al.[5] that nitrogen-implanted 52100 bearing steel wore no better than non-implanted 52100.

Nitrogen implantation did, however, harden the tempered carbon steel. Its RWR value, given in Table I, is equal to the RWR value of nitrided carbon steel. In fact the RWR versus depth profile of the tempered steel showed that the RWR value reached about 1.8 after 10 nm of wear but fell rapidly to the bulk value after 100 nm of wear[6,7]. The different responses of the tempered and hardened steels to nitrogen

implantation may be related to the stability of their microstructures; the tempered steel has an equilibrium microstructure whereas the hardened steels have a metastable microstructure (martensite). We are presently pursuing this possibility with hardness and electron microscopy studies on several microstructures.

4. SUMMARIZING REMARKS

The implantation of titanium ions into hardened (AISI 52100) bearing steel was found to increase its resistance to fine particle (1-5 µm diamond) abrasion. The dramatic increase in abrasion resistance indicates a greatly hardened surface layer. This hardness is attributed to the presence of a fine titanium carbide phase (of unknown origin) in an amorphous Fe–Ti alloy surface layer. The implantation of nitrogen ions into 52100 steel did not increase its resistance to fine particle abrasion.

ACKNOWLEDGMENT

We should like to thank J. K. Hirvonen and B. B. Rath for their continuing assistance and advice.

REFERENCES

1 N. W. W. Hartley, *Wear, 34* (1975) 427.
2 G. Dearnaley and N. E. W. Hartley, *Thin Solid Films, 54* (1978) 215.
3 J. K. Hirvonen, *J. Vac. Sci. Technol., 15* (1978) 1662.
4 N. E. W. Hartley, *Thin Solid Films, 64* (1979) 177.
5 C. A. Carosella, I. L. Singer, R. C. Bowers and C. R. Gossett, in C. M. Preece and J. K. Hirvonen (eds.), *Ion Implantation Metallurgy*, Metallurgical Society of the American Institute of Mechanical Engineers, Warrendale, Pennsylvania, 1980.
6 R. N. Bolster and I. L. Singer, *Appl. Phys. Lett., 36* (1980) 208.
7 I. L. Singer and R. N. Bolster, in C. M. Preece and J. K. Hirvonen (eds.), *Ion Implantation Metallurgy*, Metallurgical Society of the American Institute of Mechanical Engineers, Warrendale, Pennsylvania, 1980.
8 M. M. Khruschov, *Wear, 28* (1974) 69.
9 R. C. D. Richardson, *Wear, 10* (1967) 353.
10 E. Rabinowicz, *Lubr. Eng., 33* (1977) 378.
11 L. E. Davis (ed.), *Handbook of Auger Electron Spectroscopy*, Physical Electronics Industries, Eden Prairie, Michigan, 2nd edn., 1976, p. 13.
12 J. A. Knapp, D. M. Follstaedt and S. T. Picraux, in C. M. Preece and J. K. Hirvonen (eds.), *Ion Implantation Metallurgy*, Metallurgical Society of the American Institute of Mechanical Engineers, Warrendale, Pennsylvania, 1980.
13 N. K. Sharma and W. S. Williams, *Thin Solid Films, 54* (1978) 75.
14 J. S. Sheasby, *Wear, 55* (1974) 345.

Section II.B

FRICTION BEHAVIOR OF 52100 STEEL MODIFIED BY ION IMPLANTED TI

I. L. Singer[1], C. A. Carosella[2] and J. R. Reed[3]

[1]Surface Chemistry Branch
Chemistry Division

[2]Materials Modification and Analysis Branch
Condensed Matter and Radiation Technology Division

[3]Thermostructural Materials Branch
Material Science and Technology Division
Naval Research Laboratory

Friction Behavior of 52100 Steel Modified by Ion Implanted Ti

I. L. Singer, C. A. Carosella, and J. R. Reed
Naval Research Laboratory
Washington, DC 20375

ABSTRACT

Friction measurements (low speed, dry sliding) were performed on 52100 steel implanted with Ti to fluences between 5 and 50 x 10^{16}/cm^2. Auger analysis and transmission electron microscopy (TEM) were used to identify the composition and microstructure of the implanted surfaces. At the highest fluence, implanted disk/nonimplanted couples had a friction coefficient of $\mu_k = 0.38$, compared to $\mu_k = 0.62$ for nonimplanted couples; moreover, the implanted surface resisted scarring. The surface contained, in addition to Fe and Ti, an excess quantity of a carbide form of C (8 x 10^{16} C/cm^2) which extended 150 nm into the surface with a diffusion-like profile. TEM detected only non-cyrstalline material in a thinned implanted foil, suggesting the surface layer was amorphous. At lower fluences, 16 x 10^{16} and 5 x 10^{16} Ti/cm^2, the implanted steel displayed extremely high friction ($\mu_k = 0.9$) before the surface wore through and the friction returned to its nonimplanted value. Excess carbon concentrations were 2 x 10^{16} C/cm^2 and 0.2 x 10^{16} C/cm^2, respectively. The near surface Ti and C concentrations were nearly equal at the metal/metal oxide interface for higher fluence implants. A model for C gettering by exposed surface Ti is presented and supported by these results.

INTRODUCTION

The tribological behavior of materials is often controlled by the chemistry of the surface layers [1]. It is therefore not surprising that ion implanation can markedly affect the friction and wear of metals and alloys [2,3]. Ion implantation can produce rather unique surface alloys which cannot be formed by conventional metallurgical techniques, e.g., metastable alloy phases and even amorphous structures [4,5]. It is therefore necessary to determine the chemical and structural modifications produced in implanted surfaces in order to understand how implantation controls tribological behavior.

Recent investigations [6,7] of AISI-52100 steel (a martensitic bearing alloy of Fe-1.5Cr-1C by weight) implanted with Ti to a high fluence (46 x 10^{16} Ti/cm^2) illustrate the need for such an approach. Ti implantation produced a highly wear resistant surface. Composition analyses of the surface showed, in addition to Ti, a large

concentration of C (20 at.% max) which had not been anticipated from the implantation process. The wear resistance could therefore be attributed to the presence of a ternary Fe-Ti-C surface layer. Knapp, et al. [8] generated further interest in Ti-implanted Fe surfaces. They detected large amounts of C in Ti-implanted pure Fe samples and found that the Fe-Ti-C layers were completely amorphous.

In the present study, we have examined the tribological behavior, chemistry, and microstructure of 52100 steel implanted with Ti to fluences between 5 and 50 x 10^{16} Ti/cm^2. Friction coefficient measurements and wear scar analyses are used to evaluate the dry sliding behavior of implanted surfaces. Results are compared to friction studies on conventionally prepared Fe-based alloys. Auger spectroscopy in conjunction with ion milling provides composition profiles and chemical analysis of the implanted surface. Composition vs Ti fluence data are used to support a proposed model for the incorporation of C into the implanted surface. Transmission electron microscopy is used to examine the microstructure of 52100 steel implanted to 50 x 10^{16} Ti/cm^2. The role of C in forming this unique surface layer is discussed.

EXPERIMENTAL PROCEDURES AND DATA ANALYSIS

Implantation

Implantation of the AISI-52100 steel samples was done with a modified Model 200-20A2F Varian/Extrion ion implanter. The ion source is a hot filament (cathode) arc discharge type. An internal chlorination technique was employed to produce Ti ion beams. Chlorine gas is passed through fine titanium powder contained in a graphite chamber mounted within the source, near the filament, producing titanium chlorides. The chlorides volatilize at the high source temperature (800°C) and are subsequently ionized. Ion beam intensities of about 200 μA of ^{48}Ti$^+$ are routinely obtained.

The AISI-52100 steel samples, disks 0.95 cm in diameter and 0.32 cm thick, were heat-sunk onto a water-cool holder and were kept near room temperature (< 40°C) during the implantation. Six samples were implanted simultaneously with 190 keV ^{48}Ti$^+$ in a target chamber that was cryogenically pumped to pressures of about 5 x 10^{-7} torr. The ion beam was scanned electrostatically over the sample holder to give a uniform current density of 15 to 20 μA/cm^2. The implantation was stopped when the lowest fluence (5 x 10^{16}/cm^2) was reached. The samples were removed from the vacuum, two were placed in a dessicator, and the remaining four were returned to the target chamber for further implantation. This process was repeated after 16 x 10^{16}/cm^2 and finally 50 x 10^{16}/cm^2, which gave two samples each at three doses.

Kinetic Coefficient of Friction

The apparatus used to measure the kinetic coefficient of friction was a "stick-slip" machine. It utilized a sphere sliding on a plane surface (disk). AISI-52100 steel disks were rough polished with 9-25 μm alumina paste in water. Final polishing was with 0.25 μm diamond paste in water on a pitched lap. Surfaces had a mirror finish with a surface roughness less than 0.025 μm. After being polished these samples were stored in a dessiccator. Just prior to friction measurements the disks were wiped clean with benzene and 2-propanol. The sliders were 1.27 cm diameter spheres of AISI-52100 steel with a surface roughness of 0.025 μm. These sliders were cleaned by refluxing benzene in a Soxhlet extractor. Sliders and disks had bulk hardness of about R_c = 60. The slider in the "stick-slip" apparatus is attached to an elastically restrained friction

arm, and the disk is clamped to a sliding table so that the disk moves under the steel slider. Two pairs of resistance strain gauges bonded to the arm measure the normal and tangential forces (load and friction).

The kinetic coefficient of friction μ_k was measured in air at $23^{\circ}C$ at a sliding velocity of 0.01 cm/sec. Neither surface was intentionally lubricated. A normal force of 9.8N was used, producing a peak Hertzian pressure of 0.57 GPa. Multiple unilateral traverses were made over the disks. The first traverse was 5 mm in length and subsequent traverses were made over the center 3 mm of the first traverse without rotating the slider. Tracks produced on the discs were photographed with a Michelson interference microscopy. Monochromatic (yellow) light produced interference bands with a fringe spacing of 294 nm.

Auger Analysis

Auger analysis was performed in a UHV chamber equipped with a Perkin-Elmer (PHI) model 545 Auger microprobe, a rasterable ion gun, a Ti sublimator and liquid nitrogen cooled cryopanels. The electron gun was operated at 2 kV, with a 1 μA beam current, rastered over a spot size of 50 μm to reduce the intensity. Auger derivative spectra were recorded either directly or by a peak-height recording multiplexer with a 3 eV modulation amplitude. The ion gun was operated in an Ar atmosphere (about 5 x 10^{-5} Torr) with a rastered beam of 2 keV Ar^+ ions, at selected current densities between 2 and 30 $\mu A/cm^2$. Depth profiles were recorded during ion milling with Ti sublimators operating and cryopanels cooled to liquid nitrogen temperature. These procedures reduced contamination of ion-milled surfaces by residual gas vapor to below detectable levels.

Quantitative analysis was performed with the standard normalizing formalism [9].

$$X_i = \frac{I_i/S_i}{\sum_j I_j/S_j} ,$$

where X_i is the atomic concentration of element i, I is the Auger peak-to-peak intensity, and S is the Auger sensitivity factor for a given Auger peak. S values were determined from Auger analysis of reference samples of known composition. These values are listed in Table 1 for the principal Auger peaks used to characterize each species (note the shorthand notation, e.g., Ti_{420}, meaning the peak-to-peak intensity of the spectrum around 420 eV from a Ti Auger electron). The value for Cr_{530} (relative to Fe_{650}) was obtained from FeCr alloys (Fe25Cr, 304 steel, 440C steel, and 52100 steel); the value for C_{270} (relative to Cr_{530}) from $Cr_{23}C_6$, Cr_7C_3 and Cr_3C_2 powders. The value for Ti_{420} was obtained from a Ti-implanted 52100 steel whose concentration profile was established by a resonant nuclear reaction analysis [6].

Table 1. Sensitivity factors for Auger peak-to-peak intensities acquired at a modulation amplitude of 3 eV

Auger Peak	Fe_{650}	Cr_{530}	Ti_{420}	C_{270}
S	0.17	0.36	0.48	0.47

56

This normalization procedure was used to calculate atom concentrations from Auger depth profile data. Two types of errors arise in this analysis. One type is associated with the systematic errors in Auger intensity measurements. These errors will be given with concentration values in Table 2 since our concern here is with the relative concentrations of Ti and C as a function of Ti ion fluence. A second error has to do with the accuracy of sensitivity factors and therefore the absolute accuracy of these atom concentrations. Concentrations obtained with S values in Table 1 are probably accurate ± 20%, with the exception of Ti concentration for Ti/0 or Ti/C ratios ≤ 1. At these ratios values, the Ti lineshape changes and therefore its S value also changes. Thus absolute values of the concentrations in Table 2 may be no better than 20% or even worse for Ti. Values of the excess C content were obtained by integrating the area under the C_{270} profile vs. depth curve.

Table 2. Measured concentrations of C* and Ti at metal oxide/metal interface, $(C^*)_s$ and $(Ti)_s$ respectively, and doses of C* in Ti-implanted 52100 steel

Fluence (10^{16} Ti/cm^2)	$(C^*)_s$ (at.%)	$(Ti)_s$ (at.%)	C* dose (10^{16} atoms/cm^2)
5	5 ± 0.5	1 ± 0.1	≤ 0.2
16	9 ± 1	7 ± 1	1.9
50	16 ± 1	23 ± 3	8.3

The depth scale for the Auger profiles was established by Michelson interferometry. Auger depth profiles were taken near the edges of partially masked steel surfaces. The depth of an ion-milled step was later measured with a Michelson interferometer to an accuracy of about ± 5 nm. This procedure gave the depths at which several composition profiles had been terminated. Since no differences were observed in the sputter rates of Ti-implanted and nonimplanted steels, the depth scale was taken to be proportional to milling time.

Transmission Electron Microscopy

Specimens were prepared for ion implantation by cutting a 250 μm thick slice from a 52100 disk with a low-speed diamond wheel. 3 mm diameter disks were punched from this slice, then fine-ground to approximately 100 μm thickness. One surface of each disk was given a short electropolish. The polished surface was implanted in the manner described in section 2a to a fluence of 50 x 10^{16} Ti/cm^2. Following implantation, the specimen was thinned from the back surface with a dual-jet electropolisher (implanted surface masked) using an electrolyte of 250 ml methyl alcohol, 150 ml n-butyl alcohol, and 30 ml perchloric acid at a voltage of 90 V, current of 30 mA, and temperature of -60°C.

Transmission electron microscopy and selected-area diffraction were performed on two instruments: a JEM-200A and a JEM-200CX, both operating at 200 kV. Because of its higher resolution (0.5 nm point), the JEM 200CX was used for dark field investigations of the sizes of coherently scattering regions in the implanted layer. Values of S for the diffuse diffraction rings were measured by microdensitometry, and agreed within 1% for patterns recorded on the two instruments.

RESULTS

Friction and Wear

Fig. 1 summarized the kinetic coefficient of friction (μ_k) data measured for a 52100 ball sliding on Ti-implanted 52100 disks. Data points represent average values of μ_k for each pass; vertical bars indicte high and low values of μ_k where stick-slip was observed. A disk implanted to fluence of 50×10^{16} Ti/cm^2 quickly reached steady state $\mu_k = 0.38$. This value is considerably smaller than $\mu_k = 0.62$, the steady-state value obtained with nonimplanted 52100 disks.

The friction coefficients for disks implanted at lower fluences of Ti were markedly different, as illustrated also in Fig. 1. A disk implanted to 16×10^{16} Ti/cm^2 initially had low average μ_k values, with large stick-slip behavior. But after ten passes, μ_k rose to a value of 0.88, then fell to the steady state value of the nonimplanted disc, $\mu_k = 0.62$. A disk implanted to the lowest fluence investigated (5×10^{16} Ti/cm^2) had a large value of $\mu_k = 0.94$ on the first pass, which gradually fell to the steady state value of the nonimplanted disk after 7 passes.

Wear tracks produced during friction tests are shown in Fig. 2. The disk implanted to 50×10^{16} Ti/cm^2 (Fig. 2a) was virtually scar free, unlike the two discs implanted to the lower fluences (Figs. 2b-2d). Interferograms in Figs. 2b-2d indicate the depths of the tracks on the scarred surfaces. Wear tracks on the disk implanted to 16×10^{16} Ti/cm^2 changed considerably from the tenth to the twentieth pass, as did the μ_k values. After ten passes ($\mu_k = 0.94$), the track was uniformly depressed about 40 nm below the original surface (Fig. 2b). By the twentieth pass ($\mu_k = 0.62$), deep (≥ 300 nm) plow marks were also visible (Fig. 2c). Plow marks were also observed after 7 passes on the disk implanted to 5×10^{16} Ti/cm^2 (Fig. 2d). This disk also showed evidence of adhesion even with no sliding. A scar was produced on the disk after contacting with the ball at a 9.8N load. No such mark was observed on the disks implanted at the two higher fluences.

Auger Analysis

Auger depth profiles were obtained from 52100 disks implanted at the same time *as those used in the friction experiments.* Auger peak-to-peak intensities as well as selected derivative spectra are shown in Fig. 3 for a disk implanted to a fluence of 50×10^{16} Ti/cm^2. The outermost surface (about 6 nm) was ion milled at a slower rate than the remaining 200 nm, giving the expanded scale of the oxide layer seen on the left-hand side of Fig. 3.

The chemical state of C, Fe and Ti in the surface layer could be identified from spectra taken before ion milling began. A hydrocarbon-like overlayer covered the oxide layer, which consisted of Fe oxide on top of Ti oxide. The Fe oxide was probably Fe_2O_3, identified by the Fe MVV spectral lineshape [10] (not shown); the Ti oxide was probably TiO_2, identified by the Ti LMM lineshape [11]. The carbon overlayer and Fe oxide layer were very thin. Once ion millling had commenced, the carbon disappeared rapidly (1/2 minutes of exposure at about 3 $\mu A/cm^2$), and the Fe became metal-like, according to the Fe MVV lineshape [10]. Meanwhile the O_{515} and Ti_{420} intensities grew simultaneously. At its maximum in the oxide layer, the Ti LMM spectrum (shown in Fig. 3) was that of TiO_2 [10]. As the oxide disappeared, a C_{270} carbide signal appeared, reaching a maximum intensity at what we arbitrarily define as the metal oxide/metal interface.
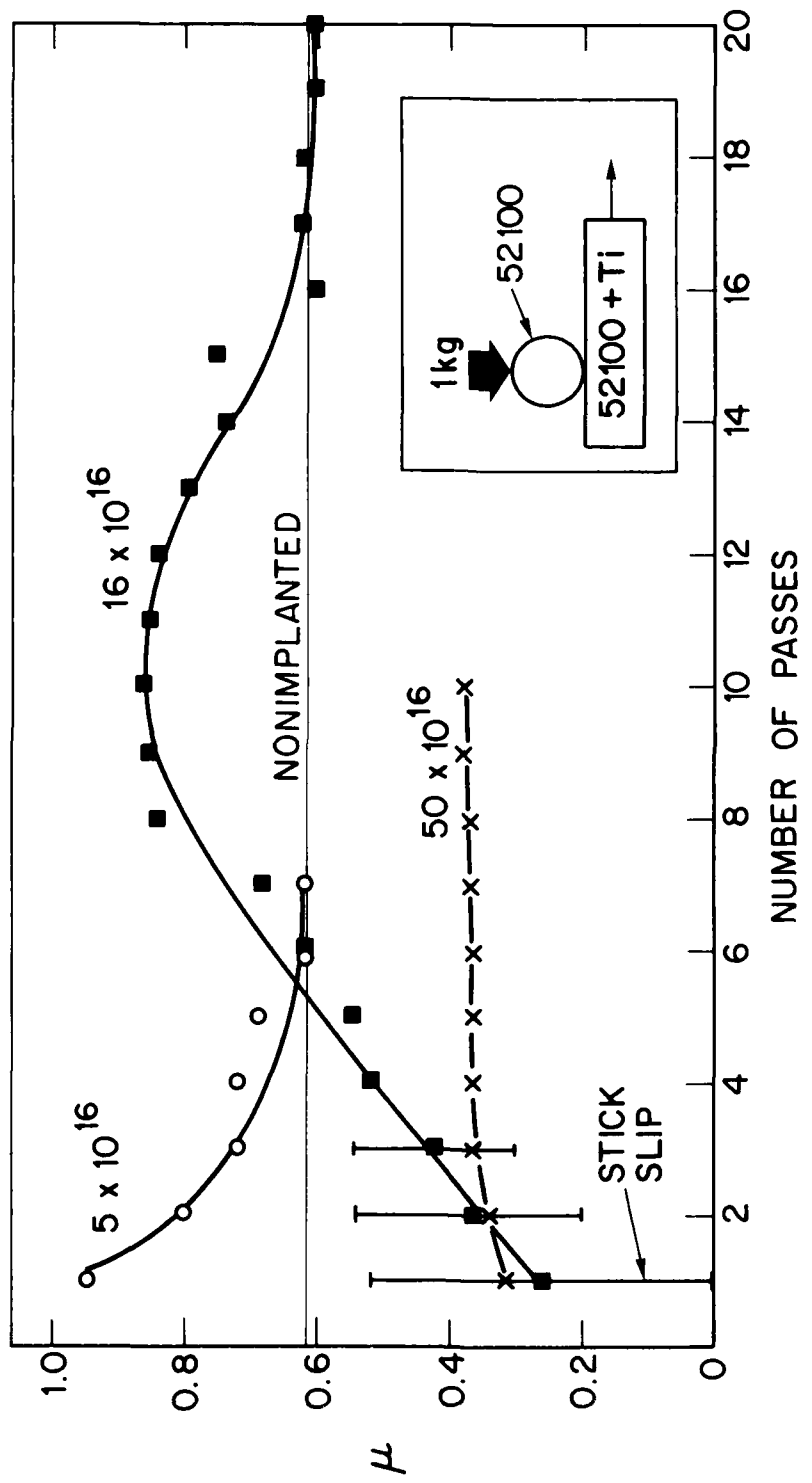
Fig. 1 — Friction coefficient of 52100 steel on Ti-implanted 52100 steel
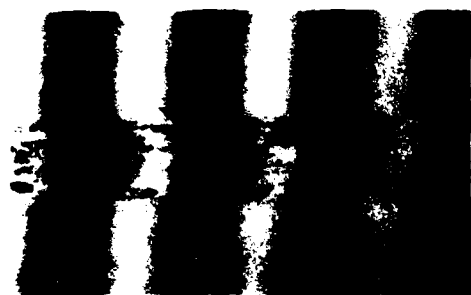
16 × 10^{16} Ti/cm^2
10 PASSES
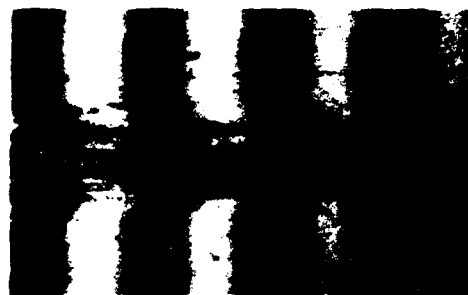
16 × 10^{16} Ti/cm^2
20 PASSES

200μm

50 × 10^{16} Ti/cm^2
10 PASSES
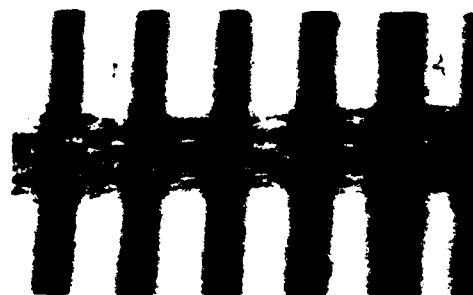
5 × 10^{16} Ti/cm^2
7 PASSES

R-056

Fig. 2 — Interference micrograph of wear scars on Ti-implanted 52100 steel
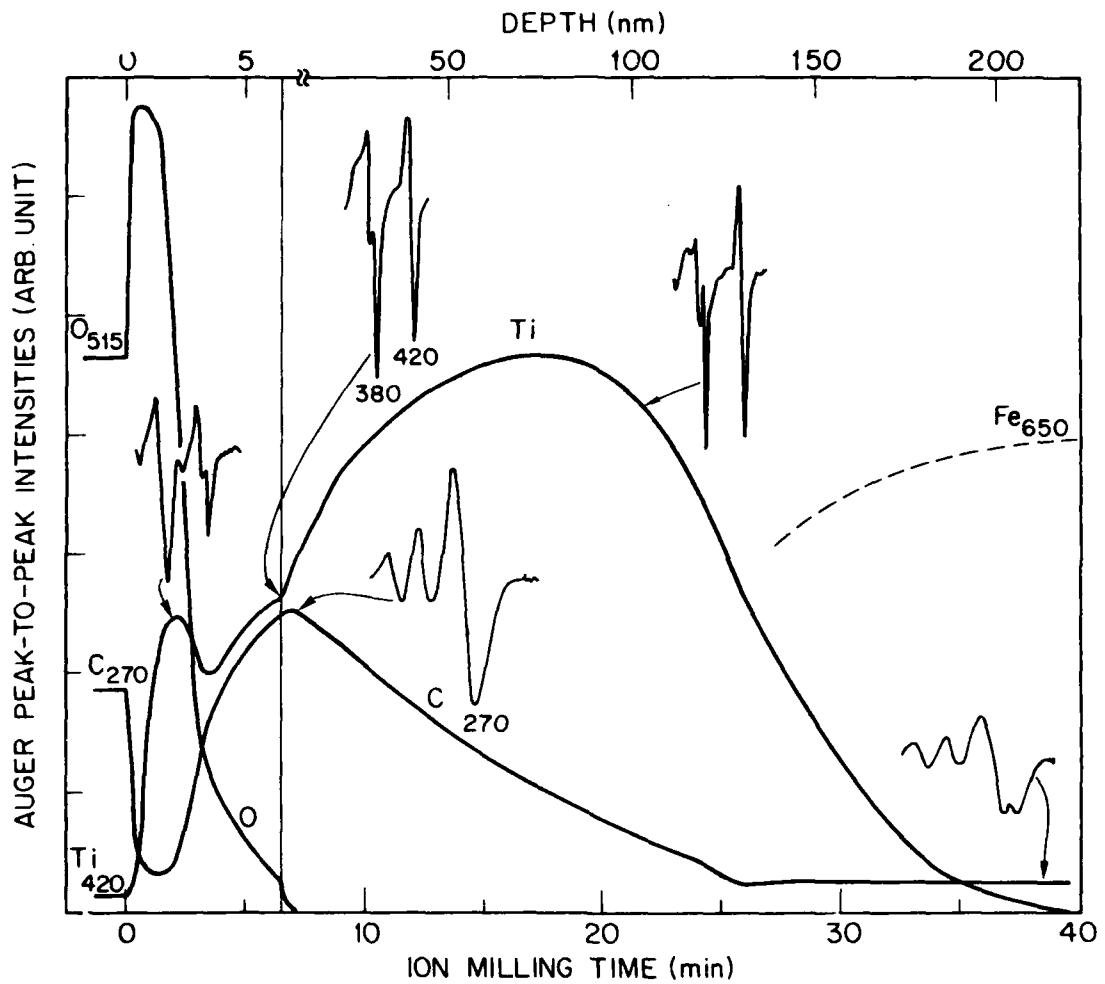
Fig. 3 — Auger depth profile of Ti-implanted 52100 steel (50×10^{16} Ti/cm^2 at 190 keV). Oxide layer, shown with expanded depth scale on left, was profiled at a low ion milling rate (J $\sim$ 3-5 μA/cm^2). Implant region, on right, was profiled at J $\sim$ 25 μA/cm^2. Portions of Ti LMM spectra (360-430 eV) were obtained with modulation amplitude of 3 eV; and those of the C KLL spectra (250-280 eV) with 1 eV.

The lineshape of the C_{270} spectrum at the interface (shown in Fig. 3) is identical to that observed for C_{270} in TiC [12]. It can be easily distinguished from other forms of carbon [13] and even the other form of carbide present in the 52100 steel (note the C_{270} spectral lineshape at a depth of about 200 nm). The Ti spectrum at the metal oxide/metal interface also showed a lineshape nearly identical to that observed in TiC [12]. These lineshape identifications suggest that C atoms are bonded preferentially to Ti atoms.

Beyond the metal oxide/metal interface, the C_{270} intensity fell to bulk value (aobut 4 at.%) for 52100 steel. The Ti_{420} intensity continued to grow, reached maximum value between 60 and 70 nm, then disappeared by 200 nm. As the Ti_{420} intensity fell to zero, the Ti spectral lineshape (see Fig. 3) became more metal-like [11]. The Ti_{420} curve follows the depth profile expected for a surface subjected to sputter erosion during implantation: a broadened Gaussian profile with a significant concentration of Ti at the surface [14].

Many of the same features were observed in Auger depth profiles of 52100 disks implanted at the two lower Ti fluences. A thin Fe_2O_3 layer covered a TiO_2 layer. The C_{270} carbide peaked at the metal oxide/metal interface, then fell off; its intensity fell to bulk value at a depth of 50 nm on the disk implanted to 16×10^{16} Ti/cm^2, and at 15 nm on the disk implanted to 5×10^{16} Ti/cm^2. The Ti_{420} depth profiles were a Gaussian. There was, of course, proportionately less Ti at lower Ti fluences.

Atom concentrations have been calculated from the Auger data using the semiquantitative normalization procedures discussed in Section 2. Table 2 lists the concentrations of excess C and Ti at the metal oxide/metal interface, $(C^*)_s$ and $(Ti)_s$ respectively. The excess C was computed by subtracting $(C^{bulk}) = 4\%$ from the normalized C concentration. Also listed in Table 2, under a column headed C* dose, are *values for the excess C content at the three fluences examined.* Results in Table 2 are pertinent to the discussion in Section 4b on how C enters the implanted surface layer. Finally, the Ti + C content accounted for nearly 50% of the atoms in the first 100 nm of the 52100 steel implanted to a fluence of 50×10^{16} Ti/cm^2.

Transmission Electron Microscopy

A thinned foil of 52100 disk implanted to a fluence of 50×10^{16} Ti/cm^2 was examined by transmission electron microscopy. A diffraction pattern from a thin layer (about 60 nm) is shown in Fig. 4. At least four diffuse rings were observed. The wave number $s(s = 4\pi/\sin\theta = 2\pi/d$, where d is the atomic spacing) for the first ring and wave number ratios for the last three rings are listed in Table 3. The wave numbers are about the same (maybe a few percent smaller) as values for amorphous Fe [15]; moreover their ratios also agree to better than one percent with those from amorphous Fe. Dark field micrographs apertured on the first diffuse ring showed no crystallites (i.e., coherently scattering regions) with diameters greater than 0.5 nm, the resolving power of the microscope. Bright field micrographs of thin sections also showed what appear to be "ghosts" of carbides, i.e., weak contrast features the size of carbides observed in non-implanted 52100 steel foils. Diffraction patterns of these "ghosts" also showed no evidence of crystallinity. These results suggest that Ti implanted to a fluence of 50×10^{16} Ti/cm^2 produced an amorphous layer in this multiphased hardened steel.
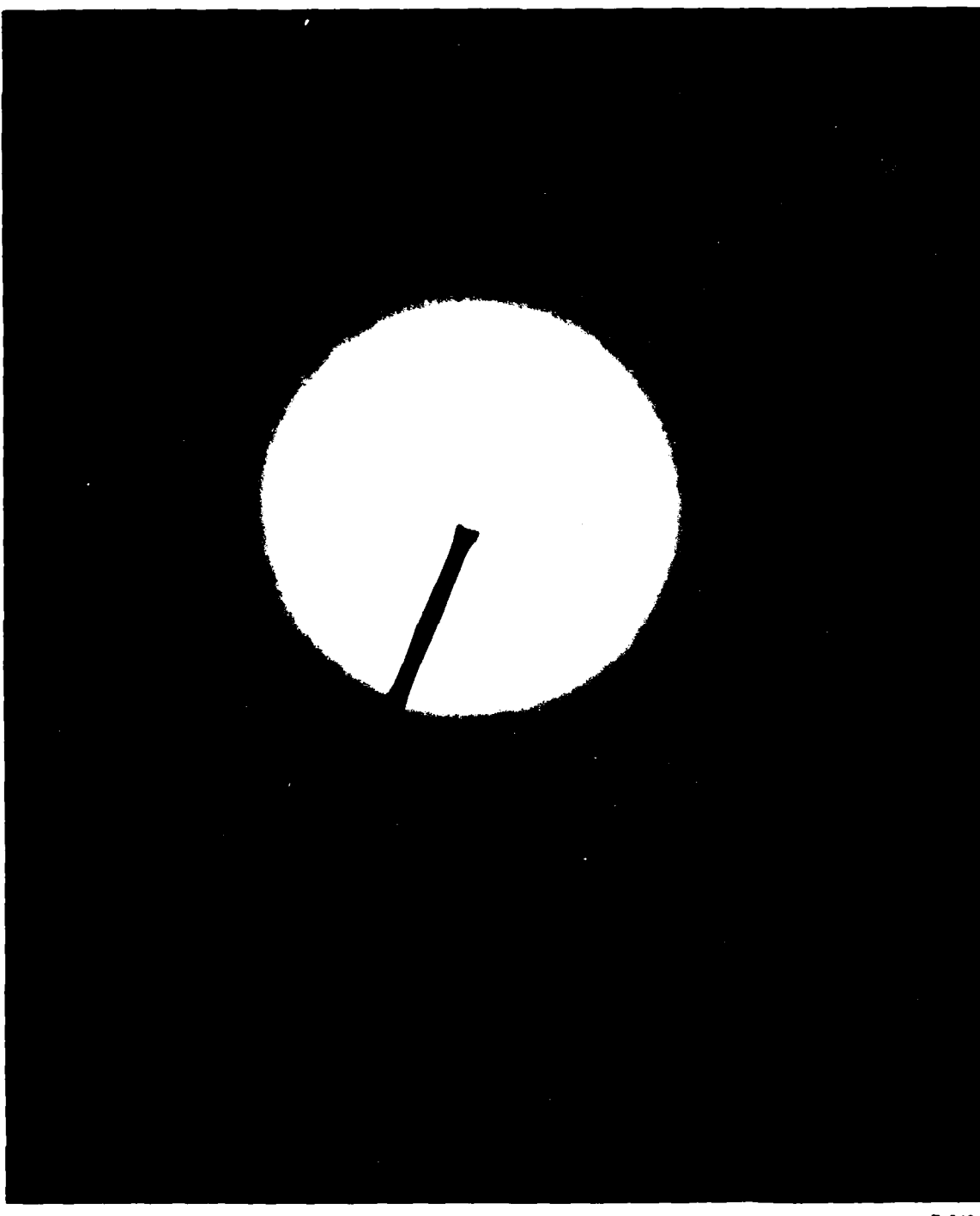
R-049

Fig. 4 — Transmission electron diffraction pattern from a thinned foil of 52100 steel implanted with 50×10^{16} Ti/cm^2.

Table 3. Positions of diffraction peaks from thin foils of Ti-implanted 52100 steel

Peak Position	Peak Ratios		
$s_1(\overset{o}{A}^{-1})$	s_2/s_1	s_3/s_1	s_4/s_1
3.01 ± 0.02	1.6(8)	2.0(4)	2.5(8)

DISCUSSION

Tribological Behavior

In the two previous reports on the friction and wear of 52100-steel implanted to high fluences of Ti (4.6 x 10^{17} Ti/cm^2) [6,7], we speculated that the excess C, in combination with Ti, improved the tribological properties of the implanted surface. In the present study, the friction and wear results (Figs. 1 and 2) not only suggest that C is an important ingredient but that without C, Ti may adversely affect the tribological behavior of steel. According to Table 2, very little excess C (0.2 x 10^{16} C/cm^2) was present in the disk implanted to 5 x 10^{16} Ti/cm^2. The friction coefficient on this predominantly Fe-Ti alloy surface was initially μ_k = 0.9, approximately 50% greater than the nonimplanted 52100 steel couples. Considerably more excess C (1.9 x 10^{16} C/cm^2) was present in the disk implanted to 16 x 10^{16} Ti/cm^2, most of it concentrated within the outermost 50 nm of the surface. This disk showed reduced friction on the first few passes. By the tenth pass, however, sliding action had worn away the outermost 40 nm of the surface (Fig. 2b), where most of the excess carbon resided. The friction coefficient against this subsurface Fe-Ti alloy layer measured about μ_k = 0.9. Thus in both lower fluence disks, a high μ_k value occurred when 52100 steel was rubbed against an Fe-Ti alloy surface. The steady state nonimplanted value of μ_k = 0.6 was reached only after the implanted layer (about 200 nm) was penetrated.

Several Fe-based alloys have larger friction coefficients than Fe itself. Miyoshi and Buckley [16] found increased μ_k values on Fe alloyed with Ti, W, Mn, Ni, and Rh in tests performed at high vacuum with a SiC slider. Buckley [17] has also showed that an Fe slider on Fe-Al alloys produced increases in μ_k. Iwaki et al. [18] reported that both Ni and Cu implants produced increased μ_k values in implanted Fe/Fe couples tested in air. Therefore, Fe-based binary alloy surfaces formed by ion implantation appear to have similar high-friction behavior as their bulk alloyed counterparts.

Miyoshi and Buckley [16] also found that the chemical activity of an alloying element was an important parameter in controlling the friction of Fe-based alloys. One way that chemically active elements may affect friction is by modifying the oxide layer. Buckley [19] has demonstrated quite convincingly that the coefficient of friction between 52100 steel couples depends strongly on the chemistry of the oxide layer formed during sliding. Results of friction experiments performed in controllable vacuum showed that reduced iron oxide layers (i.e., mainly FeO) had lower μ_k values than the principally Fe_2O_3 layers formed at atmospheric pressure. Neither of these oxide layers, however, can develop to full thickness on Fe alloys containing a chemically active metal, such as Ti. As the Auger analysis has shown, oxide layers on Ti-implanted 52100 steel have a TiO_2 layer sandwiched between a thin outer Fe_2O_3 layer and the metallic substrate. Thus, chemically active implant species may prevent lubricating Fe oxide layers from forming during wear.

Steels implanted to high fluences (ca. 50 x 10^{16} Ti/cm^2), by contrast, have superior tribological sufaces. Sliding [6] and abrasive [7] wear studies suggest that the surface is extremely hard. The inability of a loaded 52100 ball slider to "scratch" this surface also attests to its hardness. Hard, wear resistant surfaces with low friction are often obtained with refractory carbide coatings, such as TiC. The implanted layer is, however, unlike conventional hard coatings. Auger analysis (Section 3b) and transmission electron microscopy (Section 3c) identified the surface as an amorphous nonstoichiometric Fe-Ti-C alloy, with C extending to a depth of about 150 nm and Ti, to about 200 nm. Auger lineshape analysis indicated that C bonded preferentially to Ti atoms. However these "TiC" species are probably just molecular in size and not a precipitated phase since TEM micrographs failed to show any coherent phases larger than 0.5 nm.

It is clear from earlier discussion on the lower fluence implants that C plays a crucial role in the formation of this superior tribological surface. Carbon by itself is not responsible for the friction or wear reduction; implantation of C into 52100 steel did not significantly affect friction or wear behavior [6]. Carbon may, however, have stabilized the amorphous state in the Fe-Ti surface alloy as it has been shown to do in sputter-deposited films of 18Cr8Ni steel [20]. At present the wear behavior of amorphous steels has not been established. However, amorphous steel layers have been shown to have superior corrosion resistance [21] and therefore may be expected to resist mild oxidative wear.

Carbon may also affect the residual stress retained in the implanted steel. The Ti-implanted surface is subjected to large stresses both from the implanted ions as well as the excess C. C atoms tend to strain the host lattice in proportion to their concentration even in rapidly quenched alloys [22]. Based on the C concentration profile (Fig. 3), one would expect a large strain gradient from the surface inward. Normally, an Fe lattice could accommodate the C-induced strain by transforming to martensite. This transformation, however, requires that the C atoms move to selected interstitial sites. But in a Ti-implanted surface, C atoms are bound to Ti atoms and are therefore immobile. Thus stresses are frozen into the surface. High stresses can strengthen and harden surfaces and, in fact, wear resistant coatings are often tailored to achieve large stress gradients near the surface. Therefore, C may contribute to improving the resistance of the Ti-implanted surface to both chemical and mechanical wear.

Origin of Excess Carbon

Knapp et al. [8] have speculated that excess C enters the Ti-implanted surface from the vacuum system. According to their model, a C layer forms on the surface due to breakdown of residual hydrocarbon molecules by the ion beam. Above some minimum Ti fluence, the C layer reaches a constant steady-state concentration while the C duffuses inward. The C_{270} Auger intensity vs depth profile in Fig. 3 appears to be some type of diffusion curve originating at the surface. However, the shape of the C_{270} profile does not fit the well-known diffusion profile, K(d), expected for a constant source concentration, K_0 [23]:

$$K(d,t) = K_0 \text{ erfc } \left(\frac{d}{2(Dt)^{1/2}}\right) , \tag{1}$$

where d is depth from the surface, t is the exposure time, and D is a diffusion constant. The experimental Auger curves (at all fluences) were more peaked at the surface than the theoretical curve of equation (1). Moreover, the amount of diffusion carbon $M(t)$ which enters the subsurface would according to Knapp's model increase as

$$M(t) \propto \sqrt{t} , \qquad\qquad (2)$$

whereas the C^* dose vs. fluence data in Table 2 clearly increase faster than $\sqrt{t}$. (Time and fluence are proportional, in the present context, since the samples were implanted at approximately a constant beam current density.)

In the remaining paragraphs we present a slightly different model for the entry of C into Fe. Although the model is addressed specifically to the problem of Ti implanted in Fe, it may also be applicable to implantation of any strong carbide formers such as Nb, V, ... The model presented here is, like Knapp's [8], a diffusion model. It differs, specifically on the mechanism by which a C layer is absorbed by the Ti-implanted surface. The two models, therefore, have different dependences of excess C buildup on the surface and, hence, different time (fluence) dependences of the subsurface C content.

The principal assumption of the proposed model is that the C atoms which diffuse into the bulk originate as TiC molecules on the surface. TiC molecules are presumed to be formed at free Ti sites by dissociative chemisorption of carbonaceous gas molecules; the latter molecules (e.g., CO, CO_2 . . .) are abundant during implantation in a vacuum chamber whose "vacuum" is typically no better than 5×10^{-7} Torr. These TiC molecules act as a source of C for "carburizing" the subsurface. The process is analogous to gaseous carburizing whereby C atoms from the gas phase dissolve in the surface, then diffuse into the bulk. One major difference between the two processes is that, in gaseous carburizing, the surface concentration is kept constant, whereas in the present model, the concentration increases proportional to the surface Ti concentration.

The buildup of C on the surface and, therefore, in the bulk is governed by $(Ti)_s$, the concentration of Ti on the surface. $(Ti)_s$ depends on the Ti fluence as well as the sputtering rate of the surface. At low fluences, all of the Ti is embedded below the surface and therefore $(Ti)_s \approx 0$. But as the impinging ions sputter erode the original surface, an increasing fraction of the embedded Ti is uncovered and becomes part of the receding surface. Table 2 shows the expected build up of $(Ti)_s$ with increasing fluence. $(C^*)_s$ and C^* dose values also increased with increasing $(Ti)_s$ in agreement with the present model. $(C^*)_s$ was roughly proportional to $(Ti)_s$, except at the lowest fluence. This value of $(C^*)_s = 5\%$ is probably due mostly to native surface contaminants, suggesting that a fluence of 5×10^{16} Ti/cm^2 was unable to sputter remove this layer. The excess C^* content appears to have built up rapidly at fluences $>$ 5×10^{16} Ti/cm^2, i.e., only after the native oxide was removed and the implanted Ti reached the surface [24].

In summary, Ti implantation modified the chemistry, structure and the tribological behavior of 52100 bearing steel surfaces. These modifications have been attributed not only to implanted Ti atoms but also to excess C atoms introduced into the surface during implantation. We have described a process by which C can be absorbed from residual gases in the vacuum chamber by the carbide-forming implant species. The C then diffuses into the subsurface, preferentially bonding with Ti atoms. When the C content is sufficiently large, a portion of the Fe-Ti-C layer becomes

66

amorphous. This surface of high C content appears to have extremely good tribological properties against steel including reduced friction and high wear resistance. Surfaces with insufficient carbon, by contrast, have increased frictional coupling and lower wear resistance.

ACKNOWLEDGMENTS

REFERENCES

[1] D. H. Buckley, Fundamentals of Tribology (Eds. N. P. Suh and N. Saka, MIT Press, Cambridge, 1980) p. 173.

[2] N. E. W. Hartley, Thin Solid Films 64, 177 (1979).

[3] N. E. W. Hartley, Ion Implantation (Ed. J. K. Hirvonen, Academic Press, New York, 1980) p. 321.

[4] Chapters 2-4 in Ion Implantation, Ibid.

[5] Ion Implantation Metallurgy (Eds. C. M. Preece and J. K. Hirvonen, Metallurgical Society of AIME, Warrendale, PA 1980).

[6] C. A. Carosella, I. L. Singer, R. C. Bowers, and C. R. Gossett, Ion Implantation Metallurgy, Ibid., p. 103.

[7] I. L. Singer, R. N. Bolster, and C. A. Carosella, Thin Solid Films 73, 283 (1980).

[8] J. A. Knapp, D. M. Follstaedt, and S. T. Picraux, Ion Implantation Metallurgy, Op. Cit., p. 152.

[9] C. C. Chang, Surf. Sci., 48, 9 (1975).

[10] M. Seo, J. B. Lunsden, and R. W. Staehle, Surf. Sci. 50, 541 (1975).

[11] J. S. Solomon and W. L. Baun, Surf. Sci. 51, 228 (1975).

[12] N. K. Sharma and W. S. Williams, Thin Solid Films 54, 75 (1978).

[13] M. P. Hooker and J. T. Grant, Surf. Sci. 62, 21 (1977).

[14] F. Schulz and K. Wittmaack, Radiat. Eff. 29, 31 (1976).

[15] P. J. Grundy and J. M. Marsh, J. Mater. Sci. 13, 677 (1978); A. Ali, W. A. Grant, and P. J. Grundy, Philos. Mag. B 37, 353 (1978).

[16] K. Myoshi and D. H. Buckley, NASA TP-1604 (1980).

[17] D. H. Buckley, NASA TND-6359 (1971); J. Vac. Sci. Technol. 13, 88 (1976).

[18] M. Iwaki, H. Hayashi, A. Kohno, S. Namba, K. Yoshida, and N. Soda (1979) Proc. Int. Conf. Ion Beam Modif. Mater., September 1978, Budapest Hungary, Eds. J. Gyulai, T. Lohner, and E. Pasztor, (Hungarian Acad. of Sciences, Budapest, 1979) p. 3.

[19] D. H. Buckley, Friction, Wear, and Lubrication in Vacuum (NASA SP-277, 1972) p. 47.

[20] T. W. Barbee, Jr., B. E. Jacobson, and D. L. Keith, Thin Solid Films 63, 143 (1979).

[21] K. Hashimoto and T. Musumoto, Mater. Sci. Eng. 23, 285 (1976).

[22] J. V. Wood and R. W. K. Honeycombe, Mater. Sci. Eng. <u>23</u>, 107 (1976).

[23] J. Crank, <u>The Mathematics of Diffusion</u>, (Clarendon Press, Oxford, 1975) Chapter 3.

[24] From this discussion, it should be clear why we have chosen to measure surface concentrations of Ti and C* at the metal oxide/metal interface. After the native oxide is removed by sputtering, the receding surface is metal-like, except for absorbed species. The outermost 6 nm or so of the implanted disks grows immediately after the implantation is halted. The surface during implantation is actually at the present metal oxide/metal interface.

Section II.C

SURFACE MORPHOLOGIES PRODUCED BY ION MILLING
ON ION-IMPLANTED 18CR8NI STEELS

I. L. Singer

Surface Chemistry Branch
Chemistry Division
Naval Research Laboratory

SURFACE MORPHOLOGIES PRODUCED BY ION MILLING ON ION-IMPLANTED

18Cr8Ni STEELS

I.L. Singer
Naval Research Laboratory
Washington, D.C.   20375

ABSTRACT

Microstructures of ion-implanted 18Cr8Ni steel surfaces were examined using a metallographic approach i.e., etching and optical microscopy. Polished surfaces were implanted with selected ions (Ti^+, N^+, Ar^+, Ne^+) to high doses ($>10^{17}/cm^2$), then Ar ion milled stepwise to beyond the implantation depth. Michelson interferograms showed that the implanted surfaces were etched at the same rate as non-implanted surfaces. Several implanted surfaces, nonetheless, developed unique etch features. On most surfaces, large (50-100 μm) austenitic grains became visible after etching to a depth of about 60 nm. Ti-implanted surfaces, however, showed no grain relief until a depth of 240 nm, well beyond the implanted ion range ($R_p \sim 60$ nm). Individual grains on nonimplanted as well as Ne^+ and Ar^+ implanted surfaces etched with a rough texture. On the N-implanted surfaces, however, grains remained smooth until etched to a depth well beyond the implanted region. The absence of grain relief on etching a Ti-implanted surface is ascribed to isotropic sputtering from an amorphous surface. The absence of grain roughness on etching N-implanted surfaces may be due to locally isotropic sputtering from a reacted, e.g., nitrided, surface layer, or from a more stable microstructure, e.g., nitrogen-stabilized austenite.

1. INTRODUCTION

Detailed microstructures of ion-implanted materials are difficult to obtain because of the shallowness of the implant layer (often 0.1 - 0.2 μm). Yet this information is necessary to understand the mechanisms by which ion implantation improves their resistance to wear, fatigue, and corrosion (1,2). A common, but laborious, method of examining microstructures is by transmission electron microscopy studies of thinned, implanted surfaces. An alternative method, explored here, is metallographic analysis of ion-beam etched surfaces (3). The method is particularly profitable when ion beam sputtering is required for surface chemical analysis e.g., SIMS or ISS or in conjunction with another surface sensitive spectroscopy, e.g., Auger or XPS (4).

This paper presents results of a metallographic analysis of ion-implanted, 18Cr8Ni steels. Four implant species were chosen based on recent studies of the wear resistance of implanted steels. Two (N and Ti) produced dramatic changes in the wear resistance of steels (5-8), while two others (Ne and Ar) had little or no effect (9,10). Steel surfaces were etched by Ar ion bombardment, performed usually in conjunction with Auger analysis of the implanted steels (11). Etched surfaces were examined with several highly surface sensitive optical microscopes, capable of discerning surface features no higher than 1 nm (12). Textures of etched surfaces are discussed in terms of mechanisms of ion sputtering, and microstructures are inferred from surface analytical results and the wear behavior of the steels.

2. EXPERIMENTAL

AISI 302 and AISI 304 steels are commonly used austenitic stainless steels, often called by their nominal alloy composition (weight percent) 18Cr8Ni steels. Substrates of these steels were polished to a metallographic finish by standard grinding and polishing methods for austenitic steels (240, 320, 400 and 600 grit papers; 9-, 3-, or 1-diamond paste; finally 0.05 γ-alumina paste). Several samples were electropolished to remove the polishing damage layer, while some others were repolished on coarse diamond compounds to damage the surfaces.

Ion implantation of N, Ar, Ne and Ti was performed with one of several high current implantation machines available at NRL. Ion implantation of N and Ti was performed with substrates mounted on a water-cooled surface which insured that the temperature remained below 50°C. Substrate temperatures for Ar and Ne implantations were probably below 100°C. Ion energies were chosen so that the Gaussian range distribution would have a peak concentration at a depth between 50 and 70 nm and not exceed 200 nm. Fluences were chosen to achieve peak concentrations of about 10 or 20 at.%, except for N and Ti. N was

implanted over a range of fluences up to and including near
sputter-limited fluences ($10^{18}N/cm^2$); Ti was implanted to near
sputter-limited fluences, as well. Implanted ions and implanta-
tion conditions are given in Table 1. Concentration profiles
of N and Ti ions were obtained by Auger depth profile analysis
and found to agree with theory. The presence of Ar or Ne could
not be observed by Auger depth profile analysis, but Ar was
detected by X-ray emission spectroscopy (EDAX).

Substrates were subjected to low energy (1 or 2 keV) inert
ion milling, either Ne or, in most cases, Ar. Two ion milling
guns were used: a commercial ion milling device (Millatron II,
Commonwealth Scientific Corp.) and a PHI 0.5 to 5 keV ion gun,
inserted in a PHI Model 545 scanning Auger microprobe. Ion
milling was usually performed with the substrate at a fixed
angle (from 30 to 60°) to the ion gun. In several cases,
substrates were rotated during oblique angle ion bombardment.
Ion currents were measured with an unbiased Faraday cup.
Metallographic features of ion milled surfaces were examined
with three optical microscopes: a metallographic microscope,
whose light source could be apertured to produce oblique
incidence illumination; a microscope with Nomarski (differential
interference contrast) lenses; and a Michelson interferometer.
Depths of ion milled craters were also determined from Michelson
interferograms. Surface profiles were measured on a Sloan Dektak.

3. RESULTS

Substrates of 302 and 304 steel were polished, masked, then
subjected to low energy inert ion bombardment. After several
tens of nanometers had been removed, the eroded surface looked
somewhat speckled. What appeared speckled to the naked eye was
readily identified by optical microscopy as grain relief. Grains
(i.e., crystallite projections) became visible after ion milling
40-60 nm into the polish steel surface, and grain relief
continued to evolve as the substrate was milled further. An
ion-milled crater in 304 steel is shown in the micrograph of
Fig. 1. The grains of this austenitic steel were clearly
defined by the time 150 nm had been removed.

Grain relief resulted from ion milling a polycrystalline
substrate at a fixed bombardment angle. Height differences,
from grain to grain, produced the observed relief. Inter-
granular height variations are readily distinguished by dis-
jointed dark bands across the crater in the Michelson inter-
ferogram of Fig. 1a and by a height profile trace of the crater
also shown in Fig. 1b. The grain relief illustrated in Fig. 1
was found on N-, Ne-, and Ar-implanted as well as nonimplanted
substrates; furthermore, relief emerged at the same rate in all
four cases.

Erosion rates of the steel substrates ion milled in the PHI
system have been determined. Michelson interferograms were
taken on craters milled for a known time and at a known current
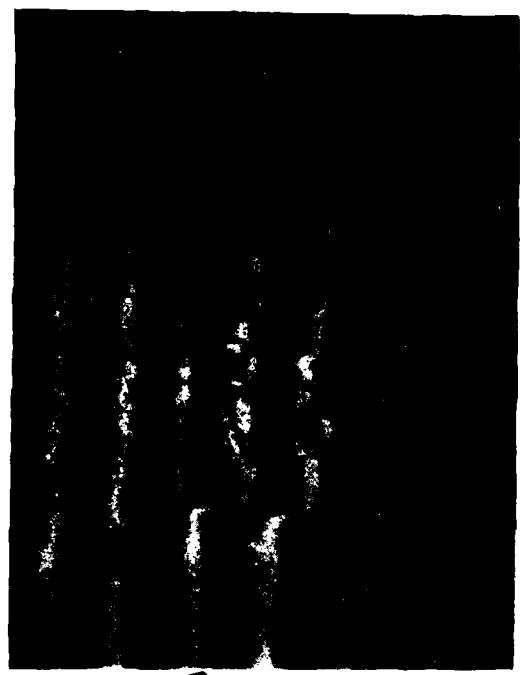
(a) INTERFEROGRAM

(b) STYLUS TRACE
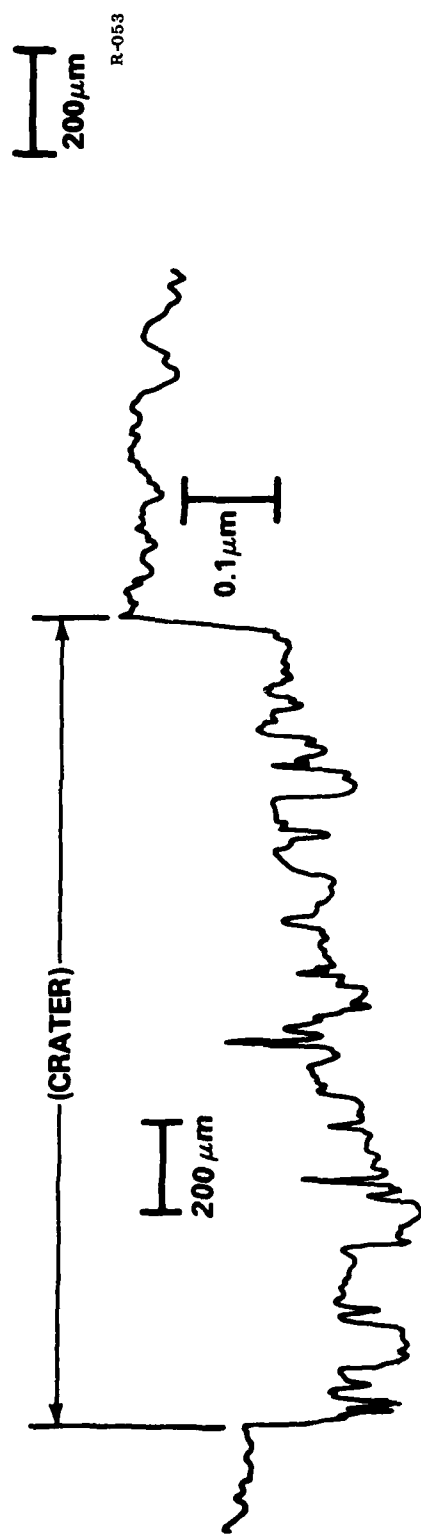
Fig. 1 — Ion-milled crater in 304 steel. (a) Optical interferogram showing Michelson interference lines (taken with yellow filter λ = 587 nm) and (b) Stylus trace across crater

density. Within measurement errors ($\pm 10\%$), the rates for implanted and nonimplanted substrates were found to be the same. The results for average erosion rates were determined from average depth measurements; values were 0.17 ± 0.02 and 0.25 ± 0.02 nm/μA-min/cm^2 for Ar ions of nominal energies 1 keV and 2 keV, respectively, incident at 45° to the substrates. These average rates, however, must be used with caution when performing surface analysis with high spacial resolution, because grain heights varied by 20 to 40% of the average erosion depth.

Although similar grain relief was seen on both the N-implanted and nonimplanted substrates, roughening of the implanted grains by ion-etching was inhibited. For example, in the non-implanted half of a 302 steel substrate, many grains developed roughly-textured surfaces after being milled to depths of 120 nm (see Fig. 2). After 180 nm, most surface grains appeared roughened. In contrast, grains in the N-implanted half retained smooth surfaces (except for polishing "ghosts" common to both sides) until almost 180 nm of surface had been removed. This inhibition period against ion-beam roughening was observed on 302 and 304 steel substrates implanted with N to fluences of about 10^{17} atoms/cm^2 or greater.

Substrates implanted with Ne or Ar developed roughly-textured grain surface at rates comparable to nonimplanted surfaces. Roughly textured surfaces developed more on some grains than others; more on mechanically polished surfaces (9-, 3-, 1-diamond and γ-alumina, in that order) than on electropolished surfaces; and more, at a given depth, with higher energy ions.

On Ti-implanted 304 steel, no grain relief appeared until more than 240 nm of material was removed, and no roughening until more than 300 nm. A Michelson interferogram in Fig. 3 shows a crater eroded to a depth of 170 nm; only the upper half of the substrate had been implanted with Ti (46×10^{16} ions/cm^2 at 190 keV). A magnified portion of the crater on the left shows no evidence of grain structure or roughening attributable to ion milling. The "polishing" effect seen on the Ti-implanted surface could only be achieved on nonimplanted 304 by ion milling a rotating substrate at low angles (60-70° off normal).

4. DISCUSSION

Ion milling erodes surfaces by the process of sputter removal of atoms from the outermost layers of bombarded surfaces. Grain relief develops because sputtering yields vary with crystalline orientation. Since sputtering rates are highly orientation dependent, grain relief can be avoided only by milling the surface from many directions (e.g., by rotating the substrate under fixed angle bombardment), by milling a substrate which has a single crystallographic orientation, or by milling an amorphous substrate.
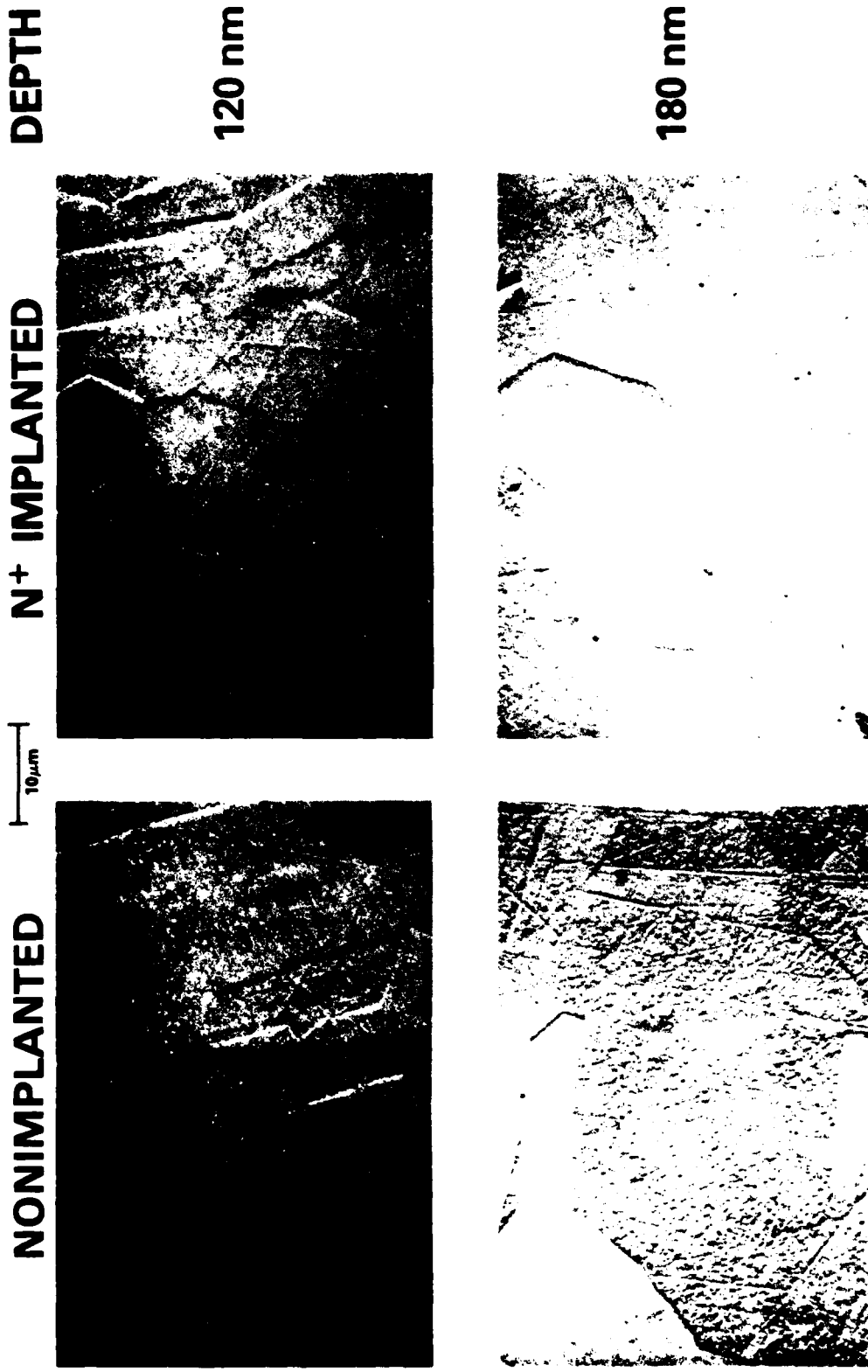
Fig. 2 — Optical micrographs of a 302 steel substrate (taken with oblique lighting) ion milled to depths of 120 nm and 180 nm. The right half of the substrate had been implanted with N ions to a fluence of $10^{17}/cm^2$
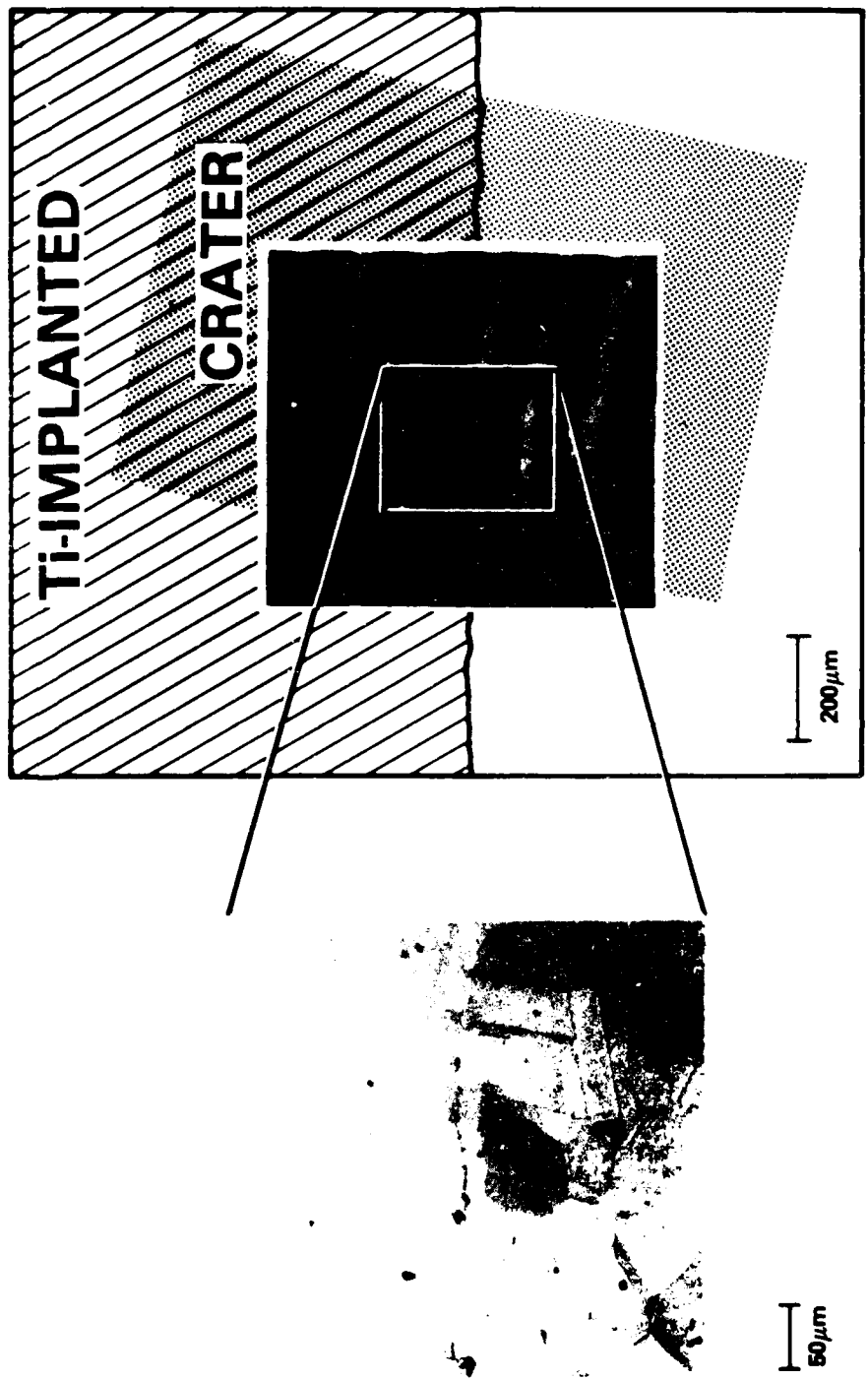
Fig. 3 — Optical micrographs of ion milled crater in 304 steel (Michelson on right, Nomarski on left). Crater depth was 170 nm.

200μm

50μm

R-054

In the case of Ti-implanted 304, there is inferential evidence that the surface is amorphous. Transmission electron microscopy has been performed on Fe (13) and an Fe alloy (AISI 52100 steel)(14) implanted with Ti to high fluences. Electron diffraction patterns were identical to those of amorphous Fe. In both cases, the amorphous surface was attributed to the anomalous presence of large amounts of C in the implanted layer. Ti-implanted 304 steel shows a Fe-Ti-C chemistry similar to that found in Ti-implanted Fe and 52100 steel (previously unreported result)(15).

Grain roughening of the kind shown in Figs. 2 and 3 is not well understood. Heavily textured 304 steel surfaces appear to have arrays of protrusions, a feature observed on other metallic surfaces subjected to ion bombardment (16,17). Nonuniform erosion of originally smooth surfaces has been attributed to a) partial coverage by "impurities" which have lower sputtering yields than the surrounding materials (18) or b) nonuniform sputtering of inhomogeneously strained material (16,19). In the present case, the latter explanation appears more likely since the degree of roughening was observed to depend on grain orientation whereas impurities distribution should be relatively insensitive to grain orientation. Inhomogeneous strains may have been introduced into the steel surface during mechanical polishing (20). If sputtering on the damage surface produced roughening, then this would explain the observed decrease in roughening with the use of finer (i.e., less damaging) polishing abrasives. Mattox and Sharp (21) have reported that increased texture developed during ion erosion on cold-worked 304 steel.

The absence of grain-surface roughening in N-implanted 302 or 304 steel is clearly a chemical effect, but one probably associated with microstructure as well. Three explanations can be given to account for more uniform erosion. One is that the N forms a reactive surface layer (several atom layers thick) on the ever-eroding steel surface. Chromium nitride has, in fact, been identified by Auger spectroscopy as a constituent of the Ar-eroded surface of N-implanted 304 steel (11). This thin surface layer may be amorphous or, more generally, may have a lattice mismatch with the underlying steel. Either structure might suppress anisotropic sputtering from the underlying lattice thereby allowing the grain surface to erode isotropically. A similar explanation was given by Hofer and Liebl (21) to account for the reduction of surface roughening on Cu-Ni layers by 11 keV N ion bombardment compared to 11 keV Ar ion bombardment at the same fluence. Tsunoyama, et al. (22) noted a similar effect on Fe sputtered by O ions compared to Ar ions.

A second explanation for uniform erosion is that N implantation introduces high levels of uniform stress which mask variations. Hartley (23) has demonstrated that ion implantation produce high stress levels in Fe. A uniformly strained lattice is expected for ions which

can form chemical bonds with the host atoms (e.g., N, C, or O ions). Nonuniform strains, however may result from inert ion implantation; not being tightly bound, implanted inert atoms tend to agglomerate as microscopic bubbles, thereby relieving local bombardment-induced stresses in the surrounding lattice (16). The differences in residual stress fields of surfaces implanted with reactive ions and inert ions may account for the differences in grain surface texture of N-implanted 304 steel vs. Ne- or Ar-implanted 304 steel.

A third explanation is that N-implantation stabilizes the 304 steel microstructure against transforming under stresses introduced during the ion milling process. Several authors (16,24) have suggested that roughly textured grains develop as a result of nonuniform strain levels generated by the bombarding ions. Although the models were meant to describe the effects of deeply penetrating high energy ions (> 10 keV/ion), Walls et. al. (25) have recently demonstrated that even low energy ions (1-5 keV) can generate similar types of strain fields (i.e., dislocations) in metal surfaces. Bombardment stresses would likely cause the unstable austenite to partially transform to martensite, as occurs in 304 steel during grinding or rolling (26). N, however, is a very efficient austenite stabilizer (27). Results of abrasive wear studies on N-implanted 304 steel were also accounted for by suggesting that N stabilized the austenitic phase against transforming to a more brittle martensite (6).

5. SUMMARY

Low energy Ar ion bombardment produced grain relief on austenitic 18Cr8Ni steels. Erosion rates averaged 0.17 ± 0.02 and 0.25 ± 0.02 nm/μA-min/cm^2 for 1 and 2 keV Ar-ion bombardment, but with intergranular heights varying from 20 to 40% of average erosion depth. N-implanted steels developed grain relief, but did not show the roughly textured grains found in nonimplanted and inert-ion implanted steels. Ti-implanted steels eroded without grain relief and without surface roughening.

TABLE 1

ION SPECIES, FLUENCES, AND ENERGIES FOR IMPLANTATION OF 18Cr8Ni STEELS

Ion	N^+	Ne^+	Ar^+	Ti^+
Fluence ($10^{16}/cm^2$)	2-100	10	10	46
Energy (keV)	40	55	100	190

REFERENCES

1. _Ion Implantation_ (Ed. J.K. Hirvonen, Academic Press, New York, 1980).

2. _Ion Implantation Metallurgy_ (Eds. C.M. Preece and J.K. Hirvonen, Metallurgical Society of AIME, Warrendale, PA., 1980).

3. M. Paulis in _Microstructural Science_, Vol. 3 (Eds. P.M. French, R.J. Gray and J.L. McCall, American Elsevier, New York, 1975) p. 453.

4. _Methods of Surface Analysis_, Vol. 1, Czanderna, A.W., Ed., (Elsevier Scientific Publ. Co., New York, 1975).

5. J.K. Hirvonen, C.A. Carosella, R.A. Kant, I.L. Singer, R. Vardiman, and B.B. Rath, Thin Solid Films 63, 5 (1979).

6. R.N. Bolster and I.L. Singer, Appl. Phys. Lett. 36, 208 (1980); also p. 116 in Ref. 2.

7. I.L. Singer, R.N. Bolster, and C.A. Carosella, Thin Solid Films 73 (1980) 283.

8. C.A. Carosella, I.L. Singer, R.C. Bowers, and C.R. Gossett, in _Ion Implantation Metallurgy_, p. 103 in Ref. 2.

9. J.K. Hirvonen, J. Vac. Sci. Technol. 15, 1662 (1978).

10. N.E.W. Hartley, Thin Solid Films 64, (1979) 177; also p. 321 in Ref. 1.

11. I.L. Singer and J.S. Murday, J. Vac. Sci. Technol. 17, 327 (1980).

12. A.S. Holik, in "Microstructural Science, Vol. 3", Ed. P.M. French, R.J. Gray, and J.L. McCall, American Elsevier (1975) p. 991.

13. J.A. Knapp, D.M. Follstaedt, and S.T. Picraux, _Ion Implantation Metallurgy, Op. Cit._, p. 152.

14. I.L. Singer, C.A. Carosella and J.R. Reed at 2nd Int. Conf. on Ion Beam Modification of Materials, Albany, NY July 1980.

15. Unpublished result.

16. R.S. Nelson and D.J. Mazey, Radiat. Eff. 18, 127 (1973).

17. R. Smith and J.M. Walls, Surface Sci. 80, 557 (1979).

18. G.K. Wehner and D.J. Hajicek, J. Appl. Phys. $\underline{42}$, 1145 (1971).

19. N. Hermanne and A. Art, Rad. Effects $\underline{5}$, 203 (1970).

20. L.E. Samuels, <u>Metallographic Polishing by Mechanical Methods</u>, (American Elsevier, New York, 1971).

21. W.O. Hofer and H. Liebl, Appl. Phys. $\underline{8}$, 359 (1975).

22. K. Tsunoyama, Y. Ohashi, T. Suzuki, and K. Tsuruoka, Jpn. J. Appl. Phys. $\underline{13}$, 1683 (1974).

23. N.E.W. Hartley, J. Vac. Sci. Technol. $\underline{12}$, 485 (1975).

24. N. Hermanne, Radiat. Eff. $\underline{19}$, 161 (1973).

25. R.D. Webber and J.M. Walls, Rad. Effects $\underline{45}$, 111 (1979).

26. K.G. Brickner and J.D. Defilippi in <u>Handbook of Stainless Steels</u>, (Eds. D. Peckner and I.M. Bernstein, McGraw Hill, New York, 1977) Chapter 20.

27. R.A. Lula and I.M. Bernstein, <u>Ibid.</u>, Chapter 14.

Section II.D

THE EFFECT OF ION IMPLANTATION ON FATIGUE LIFE IN TI-6AL-4V

R. G. Vardiman[1], and R. A. Kant[2]

[1]Alloy Transformation and Kinetics Branch
Material Science and Technology Division

[2]Materials Modification Analysis Branch
Condensed Matter and Radiation Technology Division
Naval Research Laboratory

THE EFFECT OF ION IMPLANTATION ON FATIGUE LIFE IN Ti-6Al-4V

R. G. Vardiman and R. A. Kant

Naval Research Laboratory
Washington, D. C. 20375

Abstract

The alloy Ti-6Al-4V has been implanted with Carbon and nitrogen ions. The microstructure produced by these implants is found to contain fine particles of TiC and TiN respectively. Rotating beam fatigue tests show improved fatigue life for both implants, with the superior carbon implantation giving a 20% increase in endurance limit and a factor of four to five lifetime increase at highter stresses over unimplanted material. A dose of 1×10^{17} at/cm^2 is required to obtain the maximum effect. Fatigue cracks have been observed to originate up to 150 μm below the surface, indicating a complex interaction between the implanted layer and the fatigue failure process.

Introduction

Most metals and alloys in structural applications have a limited lifetime because of one or more of the following causes: corrosion, wear, and/or fatigue. All of these phenomena are surface or near-surface in origin. The technique of ion implantation has been shown in recent years to have considerable effect on such phenomena. Substantial improvement in corrosion and wear resistance has been demonstrated in various ion implanted metals and alloys (1-3). A few studies have shown the potential of ion implantation for the improvement of fatigue life (2,4-5).

The present work was undertaken to examine the influence of ion implantation on the surface microstructure and fatigue life of a technologically important alloy. α-β processed Ti-6Al-4V was chosen because of its widespread application and the value of improving its fatigue properties.
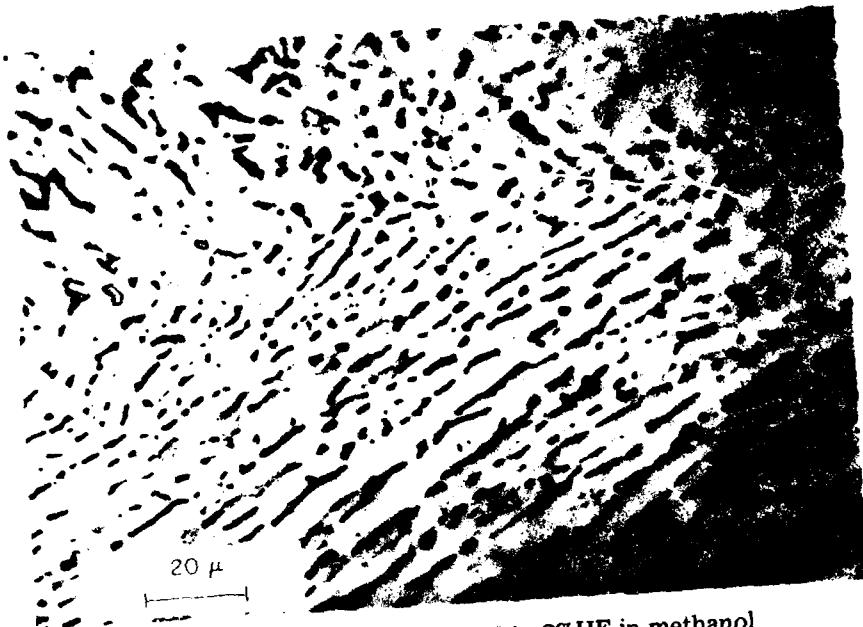
We have used carbon and nitrogen as the implanted species, since these have proved most effective in other mechanical property studies (1-5). The rotating beam test was used to determine fatigue lifetime. Samples were characterized by a variety of methods, including TEM, SEM, and Nuclear Reaction Analysis. The results show a substantial improvement in fatigue life, particularly for the carbon implant.

Experimental Techniques

The alloy composition is given in Table 1. The microstructure of the as-received material, as shown in Fig. 1, is typical of α-β processed (mill annealed) Ti-6Al-4V. The β grain size is of the order of a few microns, and the α grains typically contain more substructure than is visible in Fig. 1(b). The β grains are normally surrounded by the interface phase (7).

Element	Al	V	Fe	O	N	C	H
Wt.%	6.7	4.3	0.10	0.20	0.01	0.03	0.006

(a) Optical micrograph, etched in 2%HF in methanol

(b) TEM micrograph

Fig. 1 — Ti-6Al-4V, mill annealed, as received microstructure

Nitrogen was implanted as N_2^+ at 150 KeV, or 75 KeV per atom. Carbon likewise was implanted at 75 KeV.[2] Temperature of the fatigue samples during implantation was estimated not to exceed 100°C. The total dose for both species was 2×10^{17} at./cm^2, except where otherwise noted. The concentration profiles of the implanted nitrogen and carbon were measured by nuclear reaction analysis. The reactions used were ^{14}N (d,α_1) $^{12}C^*$[8], and ^{12}C ($^3He, \alpha_o$) ^{11}C (9). Mechanically polished discs 75 to 150 μm thick were used to prepare transmission electron microscope samples. Thinning was done with a single vertical jet of electrolyte impinging on a peripherally masked specimen. The electrolyte used was 5%H_2SO_4 in methanol, cooled to -50°C (10). To examine the implanted microstructures, the samples were thinned part way from only one side, then implanted on this polished side, and finally thinned to perforation from the other side. During implantation, the specimens were firmly mounted in a copper holder to avoid excessive temperature rises.

Rotating beam samples were used for fatigue testing, with a gage length of 1 in. and a minimum diameter of 0.25 in. Testing was done at approximately 30 Hz. Preliminary fatigue tests on electro-polished samples gave anomalously short lifetimes, so mechanically polished surfaces were used in all tests reported here. A 400 grit finish, with all radial scratches carefully eliminated, was chosen as satisfactory. No increase in fatigue life can be expected for a more finely polished surface finish (11). While a somewhat greater spread and lower peak in implant concentration occur for this surface finish (see Fig. 2), this should not affect our final results.

The fracture surfaces of the fatigue samples were examined by scanning electron microscopy, with particular attention to the origination point of the fatigue crack. By following surface striations it was usually not difficult to distinguish between surface and subsurface crack origination. Subsurface origin points could be determined to within roughly 25 μm or less.

Results

Nuclear Reaction Analysis - The nitrogen concentration profiles for two different surface finishes are shown in Fig. 2(a). The depth scale here should be regarded as approximate. LSS theory give a peak concentration depth of 141nm, in reasonable agreement with these profiles. The carbon peak position shown in Fig. 2(b) compares well with the predicted depth of 165nm.

Microstructures - The high dose levels used in this study produce a heavily damaged layer. Fig. 3 shows the dense, difficult to resolve tangle of dislocation found in TEM examination.

After nitrogen implantation, some electron diffraction patterns show diffuse rings as well as the titanium spots (Fig. 4, insert). Using a section of the two closely spaced inner rings for selected area diffraction dark field imaging, one finds a dispersion of small particles (Fig. 4). These are mostly 10 to 20 nm in size, and fairly evenly distributed. The diffraction rings indicate a non-coherent precipitate with a FCC structure. A rough measurement of the lattice parameter gives a value of 4.26+ .02A, very close to the value of 4.246A given in the literature for TiN (12). The phase Ti_2N may occur in the composition range of the implanted region, but no indication of it has been found in these samples.

(a) Nitrogen

(b) Carbon
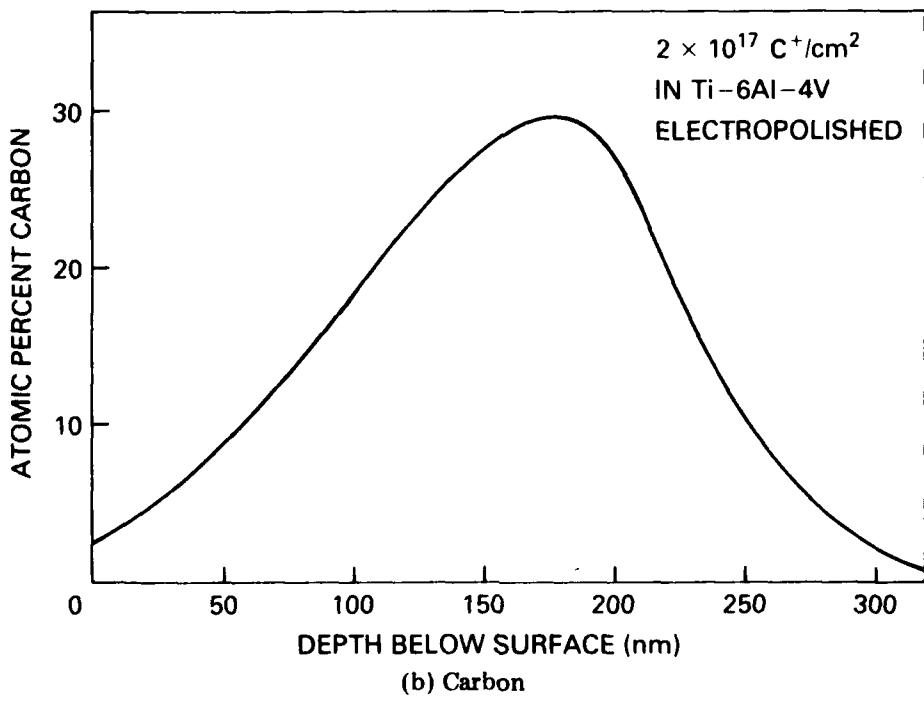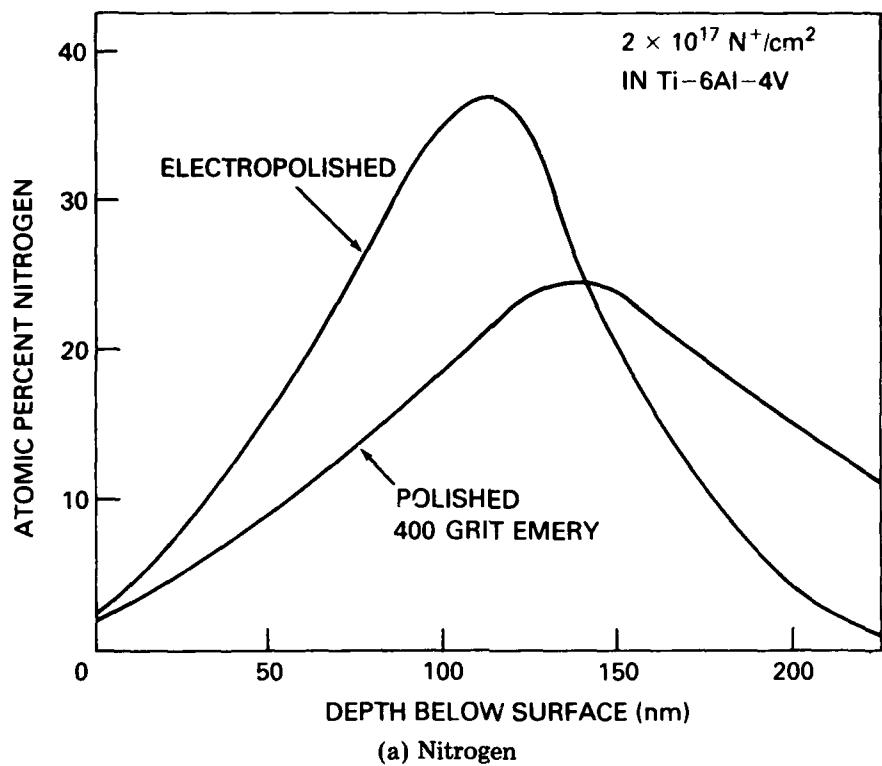
Fig. 2 — Nuclear reaction analysis concentration profiles of implants in Ti-6Al-4V

2000 Å
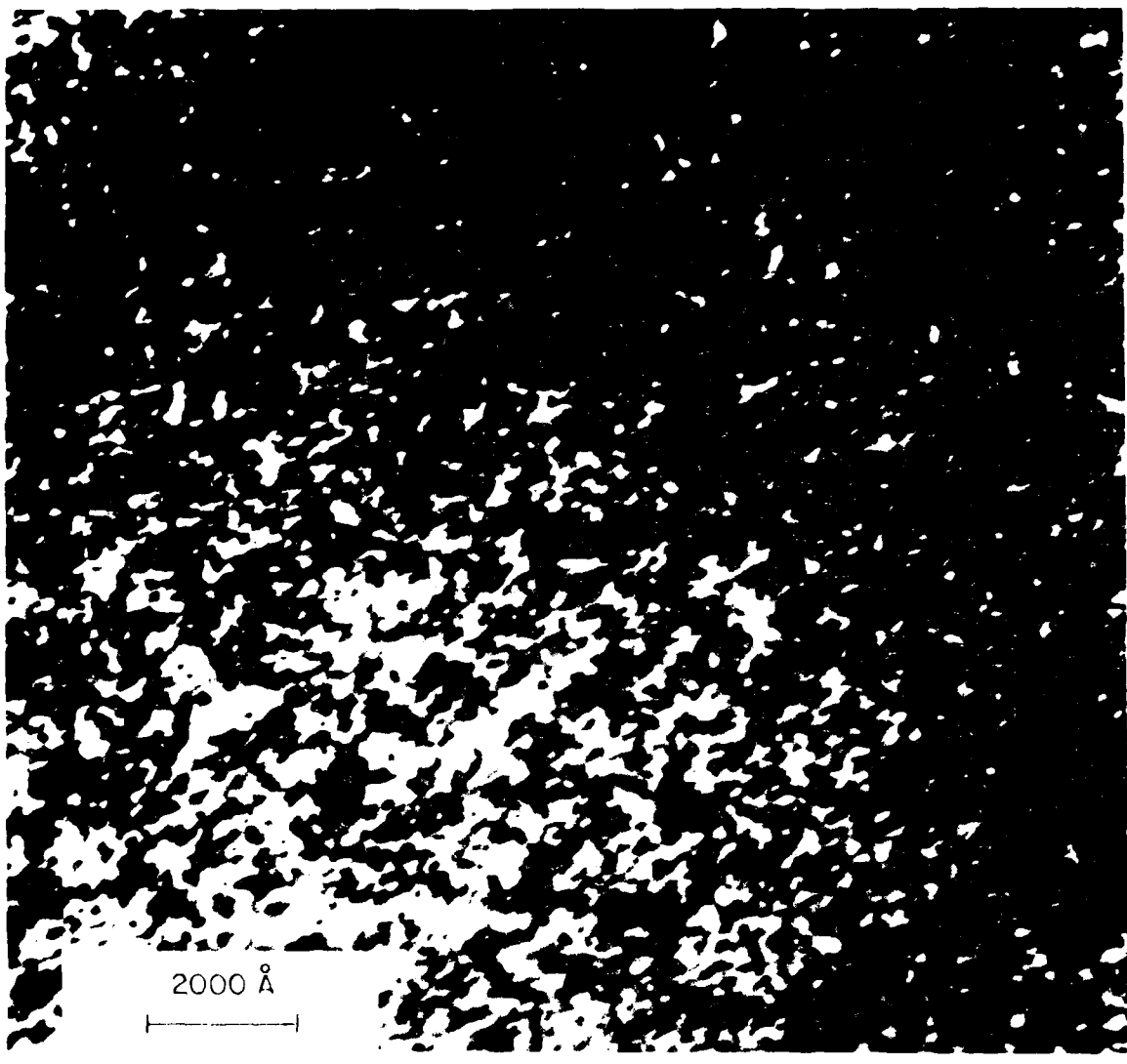
Fig. 3 — Ti-6Al-4V implanted with 2×10^{17} at/cm^2 of nitrogen, TEM micrograph, bright field

R-057
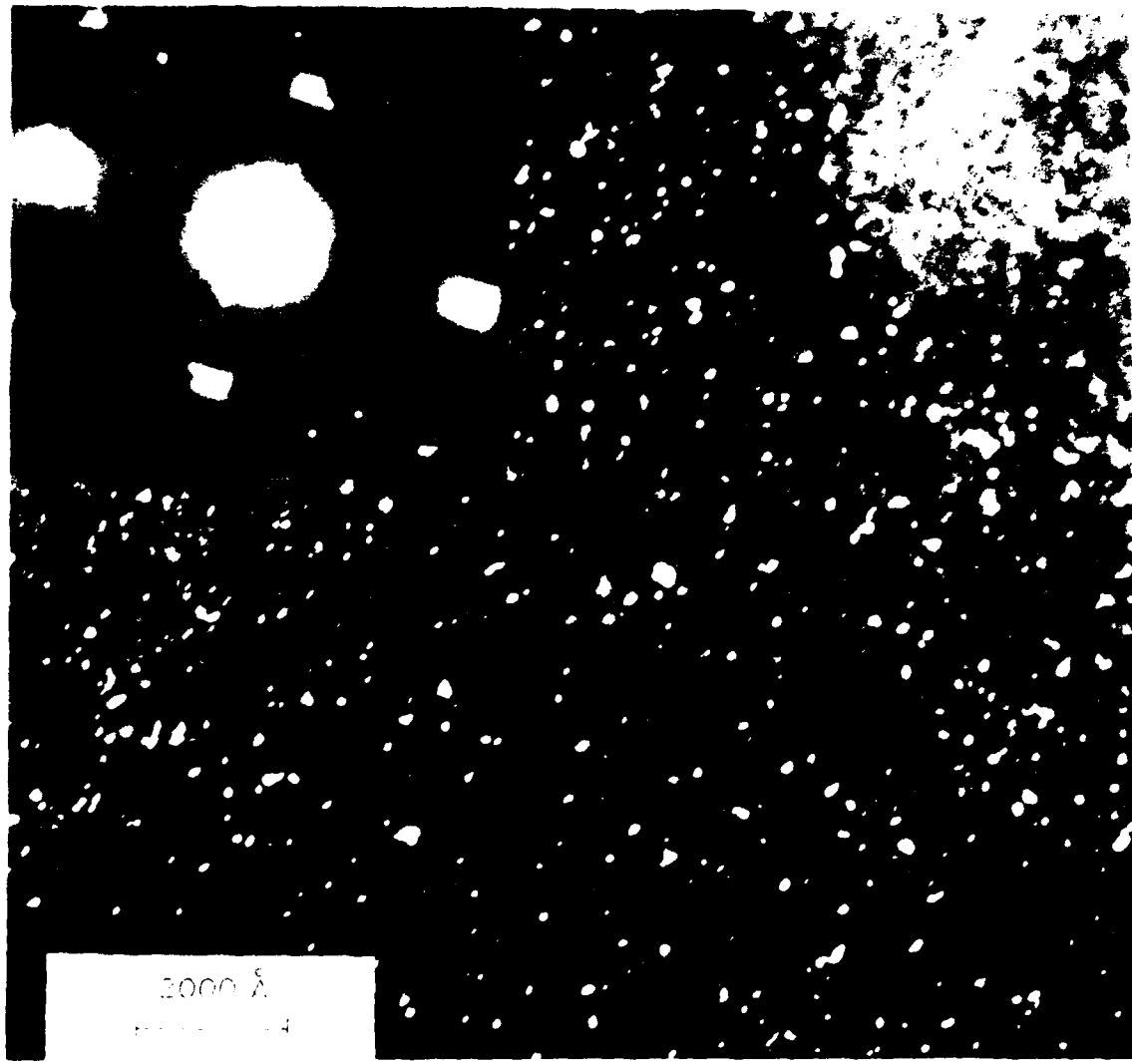
Fig. 4 — Ti-6Al-4V implanted with 2×10^{17} at/cm^2 of nitrogen. TEM micrograph, dark field. Insert, diffraction pattern showing diffuse rings used for dark field imaging.

Some samples were given a heat treatment of 4 hrs. at 500°C in a vacuum of 1×10^{-6} torr. No change in the damage due to implantation was apparent in the electron microscope. The diffraction rings of the TiN become somewhat sharper and stronger, and a small size increase in the precipitates occurred, to a maximum particle size of about 30 nm. The very modest changes in the second phase structure are consistent with the very low mobility of nitrogen in α-titanium (13).

Carbon implantation develops a microstructure similar to that found for nitrogen. The appearance of the damage structure is essentially identical. Electron diffraction shows a FCC ring pattern, with a lattice parameter of close to that of TiC. Foils implanted at different times show somewhat differing ranges of precipitate sizes, possibly due to variations in the degree of heat sinking obtained. In some cases the second phase particles were easily distinguished in bright field, and a typical foil is shown in Fig. 5(a). Dark field imaging could be done in the same manner as for the nitrides.

Heat treatment of carbon implanted samples in ultra high vacuum for 1 hr. at 400°C produced a decided increase in particle size, as shown in Fig. 5(b). Again, this is consistent with the much greater mobility of carbon than nitrogen in α-titanium (14).

TEM samples implanted with carbon doses of 7×10^{16} at./cm^2 and 3×10^{17} at./cm^2 were also examined. TiC particles were found in both cases. Maximum precipitate size was greater by perhaps 50% in the higher dose, and the density of particles appeared to be much greater. A quantitative estimate is difficult because of the particle size distribution and presence of damage. The difference is probably best shown in the electron diffraction patterns of Fig. 6, where for comparable conditions, the carbide diffraction rings are much stronger for the higher carbon dose.

Fatigue – Results of the fatigue life measurements are shown in Fig. 7. The unimplanted endurance limit of 73 ksi is increased approximately 10% by nitrogen implantation and 20% by carbon implantation. At stresses above 100 ksi the unimplanted lifetimes decrease sharply. The effect of nitrogen implantation nearly disappears at these stress levels while carbon implantation maintains a factor of 4 to 5 increase in lifetime even at the highest stresses measured.

Fatigue samples were given the same heat treatments as mentioned before for the TEM samples, 4 hr. at 500°C for the nitrogen implant, 1 hr. at 400°C for the carbon implant. No significant differences in fatigue lifetimes were found in either case. These data points are omitted in Fig. 7 for clarity: the carbon sample was tested at 91 ksi, the nitrogen sample at 85 ksi. Only small differences in fatigue life were found over non-heat treated implanted samples.

The effect of carbon dose on fatigue life is shown in Fig. 8. A dose of approximately 1×10^{17} at./cm is required to obtain full fatigue life improvement at 98 ksi, but higher doses give no further improvement. The small peak around 1×10^{17} is not fully verified, but is supported by a measurement at one other stress.
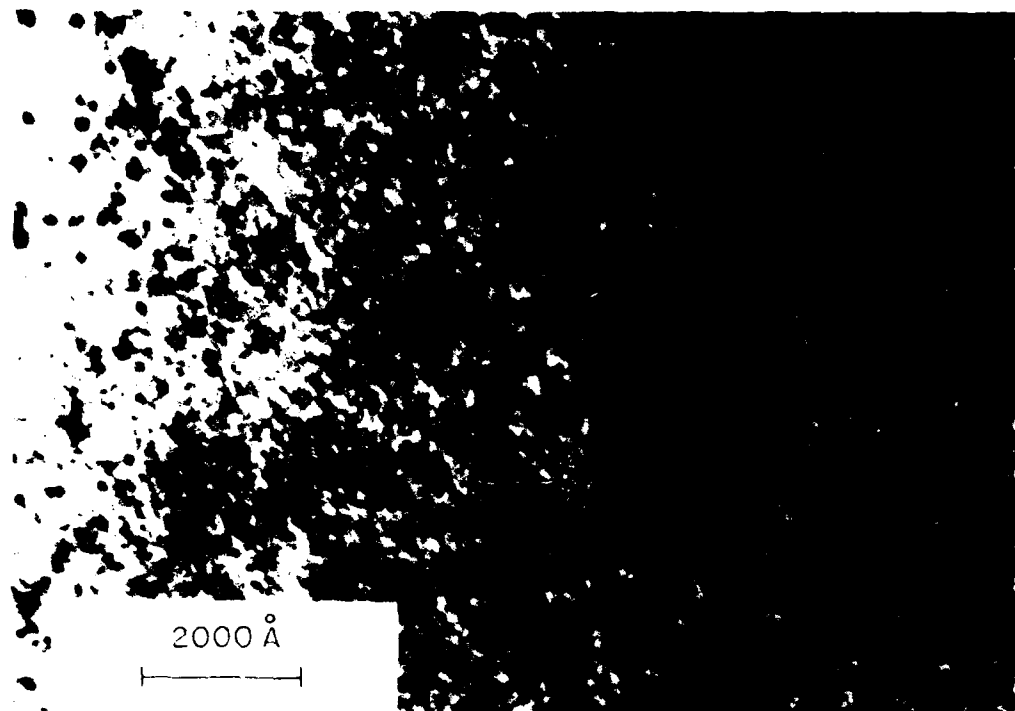
(a)
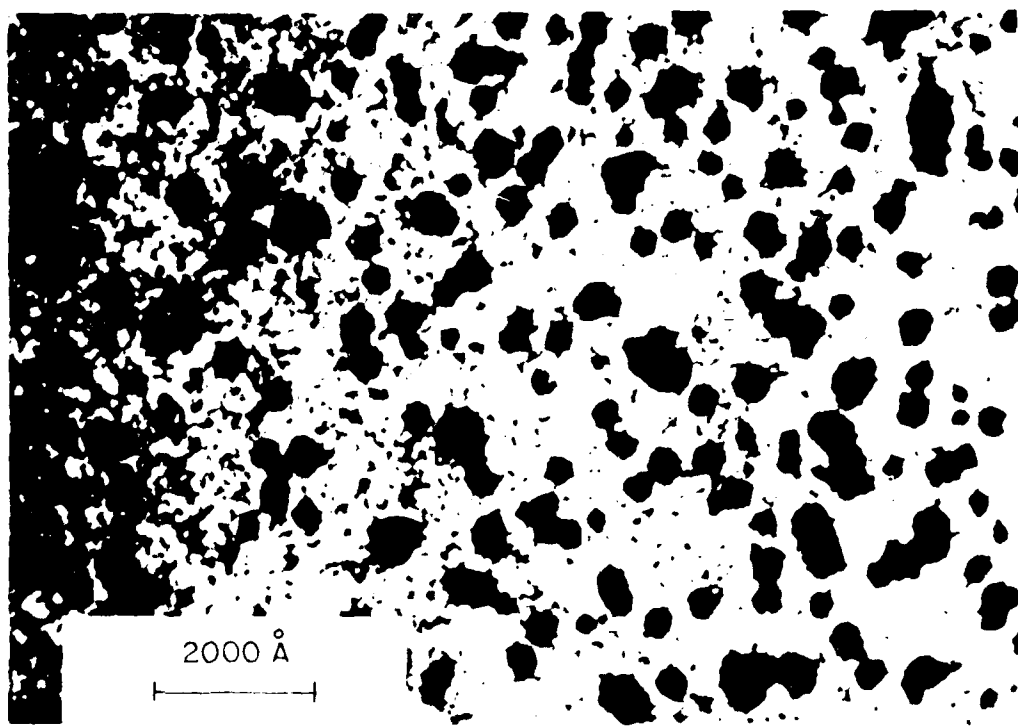
(b)

R-062

Fig. 5 — (a) Ti-6Al-4V implanted with 2×10^{17} at/cm^2 of carbon, TEM micrograph, bright field, (b) Ti-6Al-4V implanted with 2×10^{17} at/cm^2 of carbon, annealed 1 hr at 400°C, TEM micrograph

93
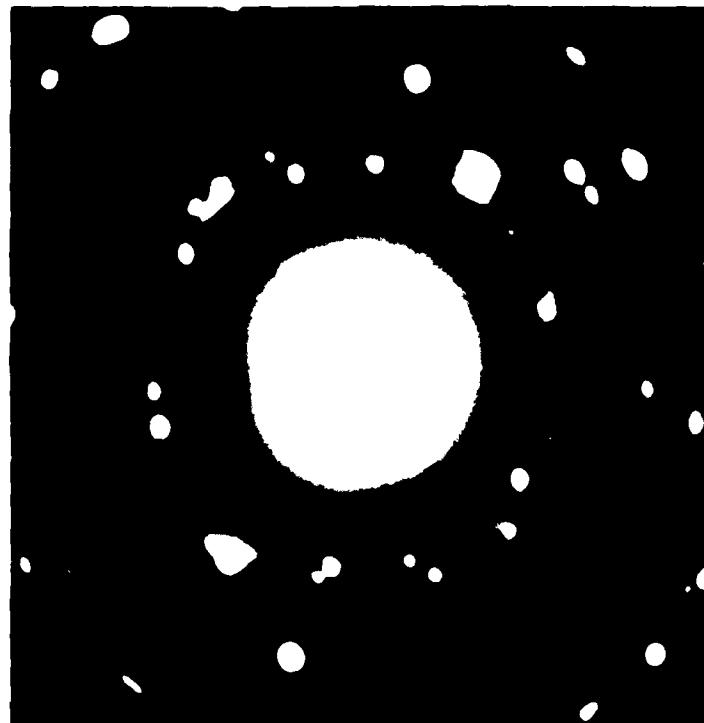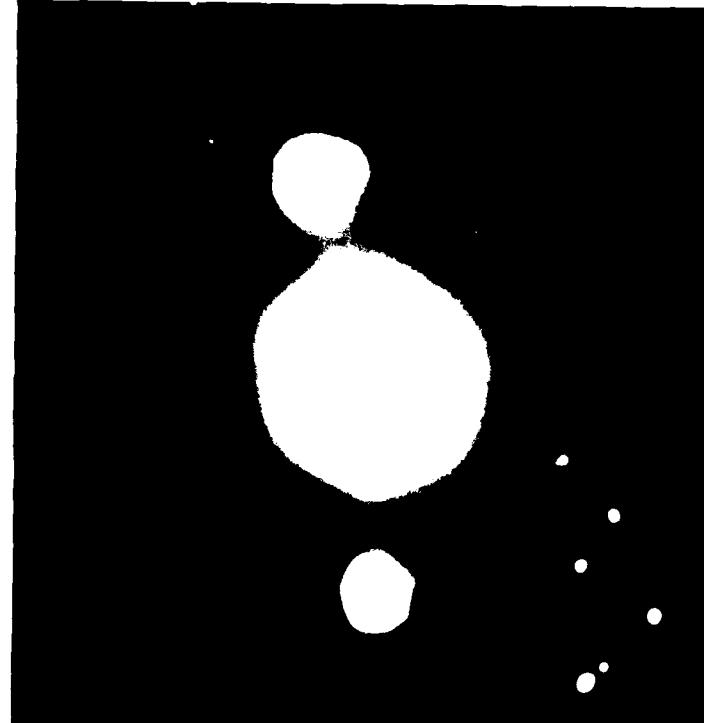
2 OF 2
AD A
102154

END
DATE
FILMED
8-81
DTIC

(a) 7×10^{16} at/cm^2

(b) 3×10^{17} at/cm^2

R-051

Fig. 6 — Electron diffraction patterns, Li-6Al-4V implanted with carbon

94
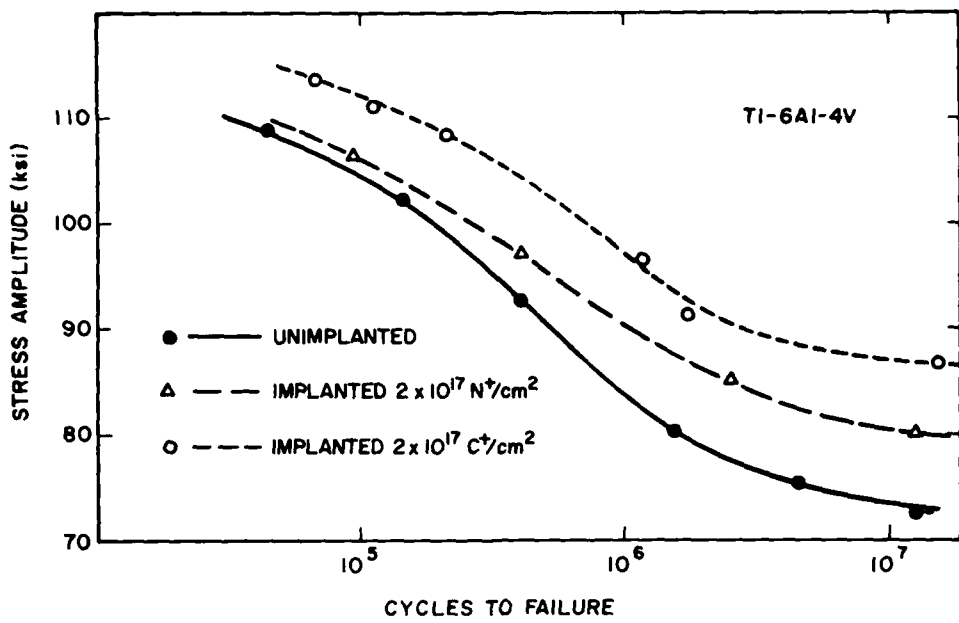
Fig. 7 — Cycles to failure vs. maximum stress, Ti-6Al-4V treated as indicated
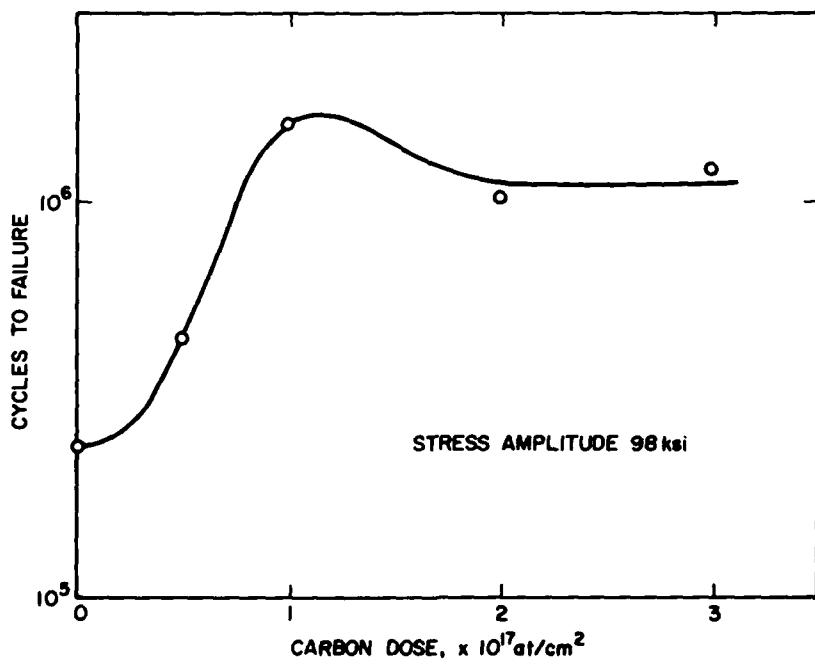
Fig. 8 — Cycles to failure vs. carbon dose, 98 ksi. maximum stress, Ti-6Al-4V

95

Fracture surfaces - It has been reported (15,16) that subsurface fatigue crack origins can occur in titanium alloys even in the absence of inclusions or other common stress concentrators. The subsurface origin does not appear to affect the fatigue lifetime, and occurs mainly in the longer lifetime tests (15). We have found subsurface crack origins in nearly all samples with a lifetime greater than 10^5 cycles, whether implanted or not, while those with a lifetime less than 10^5 cycles typically show a surface origination (Fig. 9). The subsurface origin points ranged in depth from 25 to 150 μm. In a few samples the origin was difficult to identify accurately, and some of these may be subsurface origins of less than 25 μm depth.
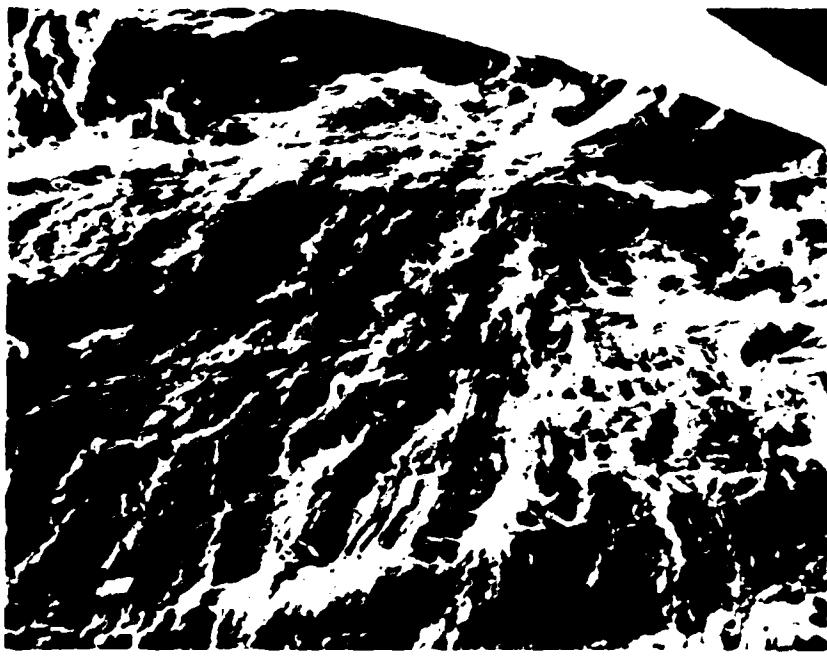
Discussion - It is perhaps surprising that an altered layer only a few tenths of a micron thick can have such a large influence on fatigue life. It was our original expectation that implantation would benefit fatigue life by creating a compressive stress, and by inhibiting the development of slip steps on the surface which could open into cracks. However, the extensive occurrence of fatigue crack origins at depths far below the implanted layer indicates a more complex interaction between the implanted layer and the fatigue process in the bulk.

It is obvious that the effect of implantation goes beyond the introduction of a compressively stressed surface layer. This is most easily illustrated by the difference in effect of carbon and nitrogen. Since an estimate of the percentage of implanted species tied up in precipitates indicates that a large proportion of both implants remains in solid solution, this should produce a hardening which would amount to embrittlement in a thicker layer. Segregation to dislocations can also be expected and carbon may be more effective in this respect since it has a much lower solubility and greater mobility than nitrogen. The effect of the precipitates is more problematical, as greater size and number of carbides produced both by heat treatment and by higher dose had negligible effect on fatigue life. Hu, et al (5) have interpreted fatigue life improvement in nitrogen implanted steel as due not to the nitride precipitates formed, but rather to the segregation of nitrogen to dislocations. This question is by no means settled, however, and further research is required to elucidate the basic mechanisms of fatigue life improvement due to ion implantation.

In conclusion, we have demonstrated increased fatigue life in the $\alpha - \beta$ processed Ti-6Al-4V alloy by ion implantation with both nitrogen and carbon. The larger effect is produced by carbon, with an increase of 20% in endurance limit, and lifetime increase by a factor of 4 to 5 at higher stresses. A dose of 1×10^{17} at/cm^2 of carbon is required for maximum effect with higher doses producing no further increase. Subsurface fatigue crack origins for lifetimes greater than 10^5 cycles point to a complex interaction between the implanted layer and the bulk. The presence of nitrides and carbides in the implanted layer has a questionable effect on the observed lifetime increases.
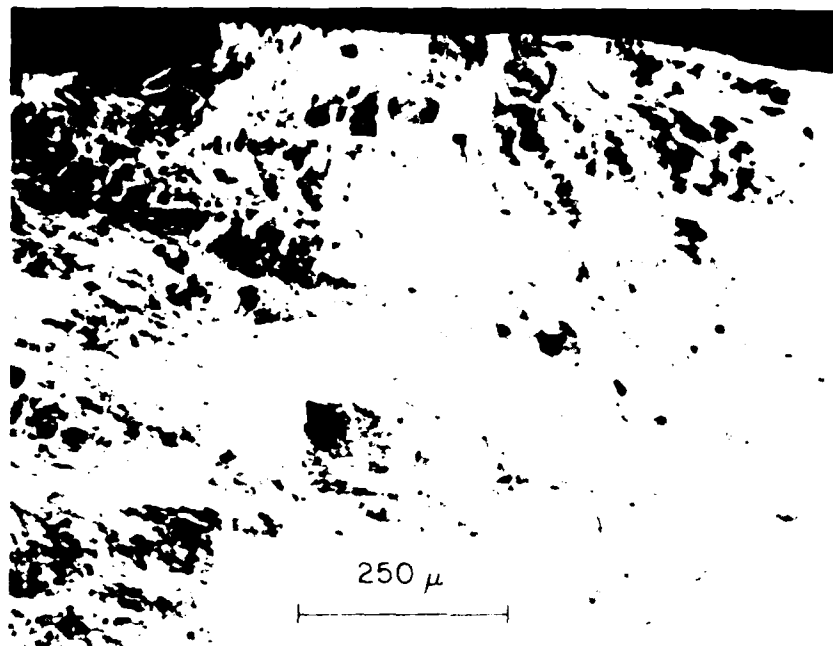
(a) High stress, short life showing surface crack origin

R-052

(b) Lower stress, longer life showing subsurface crack origin

Fig. 9 — Scanning electron micrograph of the fractured surfaces of Ti-6Al-4V fatigue samples

REFERENCES

1. G. Dearnaley and N.E.W. Hartley, Thin Solid Films 54, 215 (1978).
2. N.E.W. Hartley, "Applications of Ion Beams to Materials,"
   ed. G. Carter, J. S. Colligan, and W. A. Grant, Inst. Phys.
   Conf. Ser. No. 28 (1976) p. 210.
3. J.K. Hirvonen, Jour. Vac. Sci. and Tech. 15, 1662 (1978).
4. W.W. Hu, C.R. Clayton, H. Herman, and J.K. Hirvonen, Scripta
   Met. 12, 697 (1978).
5. W.W. Hu, H. Herman, C.R. Clayton, J. Kozubowski, R.A. Kant,
   J.K. Hirvonen, and R.K. MacCrone, "Ion Implantation Metallurgy,"
   eds. C.M. Preece and J.K. Hirvonen (TMS-AIME Warrendale, PA
   1980) p. 92.
6. A. Kujore, S.B. Chakbrabortty, E.A. Starke, Jr., and K.O. Legg,
   ibid, p. 132.
7. C.G. Rhodes and J.C. Williams, Met Trans. A, 6, 1670 (1975):
   C.G. Rhodes and N.E. Paton, ibid, 10, 209 (1979).
8. G. Amsel, J. P. Nadai, E. d'Artemare, D. David, E. Girard, and
   J. Moulin, Nucl. Instr. and Meth. 92, 481 (1971).
9. C. R. Gossett, Proc. of Fifth Int. Conf. on Ion Beam Analysis
   in Nuclear Inst. and Methods, to be published.
10. R.A. Spurling, Met. Trans. A, 6, 1660 (1975).
11. P.S. Maiya and D.E. Busch, Met. Trans. A, 6, 1761 (1975).
12. H.J. Beattie and F.T. Ver Snyder, Trans. ASM 45, 397 (1953).
13. J.P. Bars, E. Etchessahar, and J. Debuigne, Jour. Tess. Comm.
    Met. 52, 51 (1977).
14. A.I. Nakonschlikov and T.V. Pavlinor, Izv. Akad. Nauk. SSSR
    Metal. 2, 213 (1972).
15. D.F. Neal and P.A. Blenkinsop, Acta Met 24, 59 (1976).
16. J. Ruppen, R. Bhowal, D. Eylon, and Q.J. McEvily, "Fatigue
    Mechanisms," ed. I.T. Fong (ASTM-STP 675, 1979) p. 47.

Section III.A

ION IMPLANTATION OF BEARINGS FOR IMPROVEMENT OF CORROSION RESISTANCE

R. Valori[1] and G. K. Hubler[2]

[1]Naval Air Propulsion Center
Trenton, NJ

[2]Materials Modification and Analysis Branch
Condensed Matter and Radiation Technology Division
Naval Research Laboratory

Ion Implantation of Bearings for
Improvement of Corrosion Resistance

R. Valori - Naval Air Propulsion Center, Trenton, NJ
G. K. Hubler - Naval Research Laboratory, Washington, DC

ABSTRACT

A program is currently underway to use ion implantation to improve the tribological and corrosion characteristics of load bearing surfaces in both rolling element bearings and gears used in aircraft propulsion systems.

This paper describes that aspect of the program concerned with the use of ion implantation for surface alloying of bearing components in order to alleviate the problem of corrosion in costly M50 steel mainshaft aircraft engine bearings. Results to date indicate that implantation of selected ion species can significantly improve resistance to both generalized and localized (pitting) corrosion without adversely affecting bearing performance or fatigue endurance life.

INTRODUCTION

Ion implantation as a means of alloying the load bearing surfaces of gears and rolling element bearings used in Navy and aircraft propulsion systems, has the potential for solving costly problems relating to corrosion and premature surface failures.

Ion implantation is a process by which virtually any element can be injected into the near-surface region of any solid by means of a beam of high-velocity ions (usually tens to hundreds of keV in energy) striking a target mounted in a vacuum chamber. The bombarding ions lose energy in collisions with substrate atoms and come to a stop at depths of tens to thousands of angstroms in the host material. The major advantages of ion implantation over coatings and other methods of surface treatments are:

a. No change in dimensions or surface character which allows the implantation of existing bearings without further processing,

b. None of the interface bonding problems associated with coatings,

c. Material bulk properties remain the same,

d. Choice of alloying element is not limited by solid solubility or diffusion parameters.

Accordingly, ion implantation offers an attractive method of achieving corrosion resistance and improved tribological characteristics. Consequently the Naval Air Propulsion Center (NAPC) has established and is managing a program to investigate the use of ion implantation for:

100

a. Producing corrosion resistant alloys on M50 steel bearing surfaces,

b. Improving the tribological characteristics (wear, scoring, etc.) of bearing and gear surfaces.

The major effort to date and the work described herein is related to the first item listed. This is motivated by the fact that a major cause of bearing rejection at Naval Air Rework Facilities (NARF's) is corrosion pitting [1]. The estimated yearly cost for replacement of the expensive mainshaft bearings made of M50 steel is several million dollars for both the Navy and Air Force.

The program was designed to:

a. Determine optimum implantation parameters (ion energy, species and fluence) most effective for inhibiting corrosion in hardened M50 bearing steel using several types of corrosion tests as a measure of success,

b. Develop the methods of implanting all load bearing surfaces of both ball and roller bearings for subsequent testing,

c. Conduct full scale bench tests to insure that no deterioration in bearing performance or endurance life occurs as a result of implantation,

d. Determine the effectiveness of implantation in inhibiting corrosion of full scale bearings in service, in the long term storage, and in a test cell engine evaluation.

The Naval Research Laboratory is responsible for items (a) and (b). The NAPC and the Naval Air Rework Facility in North Island share responsibilities for items (c) and (d).

THE IMPLANTATION PROCESS

Ion implantation is not a coating technique. Implantation consists of forcibly injecting selected elemental ion species beneath the surface of materials by means of a high-energy ion beam from an accelerator (usually at tens to hundreds of kilovolts). This injection process produces an intimate alloy of the implanted and host elements without producing a sharp interface characteristic of most coatings and hence avoids the related adhesion problems. The resultant depth distribution and alloy composition depend on the energy and atomic number of the projectile as well as on the atomic number of the host. Typically, depths of 0.01 to 1.0 micrometers are achievable with concentrations of up to 50 atomic percent. It should be stressed that ion implantation is not a thermodynamical equilibrium process and that metastable alloys can be formed without regard for the conventional considerations of solid solubility and diffusivity; since any elemental species can be implanted into any other material. Heating of the implanted alloy to sufficiently high temperatures will, of course, ensure equilibrium conditions, but several durable metastable (or amorphous) phases with potentially interesting physical properties have been formed by implantation. Figure 1 summarizes many of these factors pertaining to ion implantation for materials modification. The ability to control and reproduce the ion beam parameters listed in Figure 1 is especially important to its large scale commercial usage for implanting (doping) semiconductor wafers with high reproducibility (typically less than 3% dose difference on different wafers or between different points on a single wafer).

101

ION IMPLANTATION PARAMETERS

IMPLANTED ELEMENTS — VIRTUALLY ANY ELEMENT FROM HYDROGEN
TO URANIUM CAN BE IMPLANTED.

ION ENERGIES — NORMALLY 2 TO 200 KeV. ENERGIES UP TO 5 MeV
MAY BE OBTAINED WITH THE VAN DE GRAAFF
ACCELERATOR.

ION RANGES — VARY WITH ION ENERGY, ION SPECIES AND
HOST MATERIAL RANGES NORMALLY 0.01 μm
TO 1.0 μm.

RANGE DISTRIBUTION — APPROXIMATELY GAUSSIAN. CHOICE OF ENERGIES
ALLOW TAILORED DEPTH DISTRIBUTION PROFILES.

CONCENTRATION — FROM TRACE AMOUNTS UP TO 50% OR MORE.

HOST MATERIAL — ANY SOLID MATERIAL CAN BE IMPLANTED.

SPECIAL EFFECTS — SPUTTERING, RADIATION DAMAGE, RADIATION
ENHANCED DIFFUSION.

Fig. 1 — The effect produced by ion implantation depends on a number of
factors or parameters. These parameters, together with typical ranges of
values, are shown here.

Figure 2 shows a schematic diagram of a typical research-type ion implantation system. As depicted, atoms are ionized in an ion source, accelerated to the desired energy, analyzed according to mass by a magnet to select the desired species, and then electrostatically raster scanned over the target to ensure dose uniformity of the implantation. The implanted dose (in terms of impurity atoms per unit volume) is obtained from the ion beam charge, the implanted target area, and the implanted species depth distribution.

Table I. Elemental Composition of M50 Tool Steel (% by Wt.)

Carbon	0.85
Manganese	0.25
Silicon	0.20
Phosphorous	0.015 (max. allowable)
Sulfur	0.010 (max. allowable)
Chromium	4.00
Vanadium	1.20
Iron	Remainder
Molybdenum	4.30

ION SPECIES SELECTED FOR EVALUATION

M50 (AMS 6491) is an alloy tool steel used extensively in mainshaft aircraft engines because of its excellent hot hardness characteristics, wear resistance and good contact fatigue life. However, its corrosion resistance is poor. Its elemental composition is shown in Table I. Ion species and combinations of species which were considered as good candidates for imparting corrosion resistance to M50 steel include Cr, Cr+Mo, Cr+Mo+N, Cr+P, Cr+B, Al, Ti, and Mo. The ion energies used ranged between 12.5 and 150 KeV with fluences betwen $1.0 \times 10^{16}/cm^2$ and $4 \times 10^{17}/cm^2$. The fluences used for Cr, Ti, and Al were sufficient to produce a 15 to 30 atomic percent concentration of the implanted elements in a region from the surface to a depth of about 800 nm. The choice of ions was determined by the well known corrosion behavior of the ions in bulk materials, i.e., chromium produces stainless steel when added to iron based alloys in concentrations greater than 12%, [2] Mo is known to improve pitting resistance in steels, [3] Ti and Al form stable corrosion resistant oxides, [2] P and B stabilize an amorphous phase when alloyed with iron, [4] and N has been shown to improve pitting resistance of steel [5].

CORROSION EXPERIMENTS

Several types of corrosion tests were used to ascertain the degree of improvement in corrosion resistance occuring as a result of ion implantation. To conduct these corrosion tests in actual bearings would have been expensive and time consuming. Therefore, tests were conducted on small M50 steel hardened specimens on an area of about 1 cm^2.

Two types of tests were performed. The first were qualitative field service simulation tests. Those ions which looked promising in simulation tests were further studied by electrochemical polarization and pitting tests. These are described below.
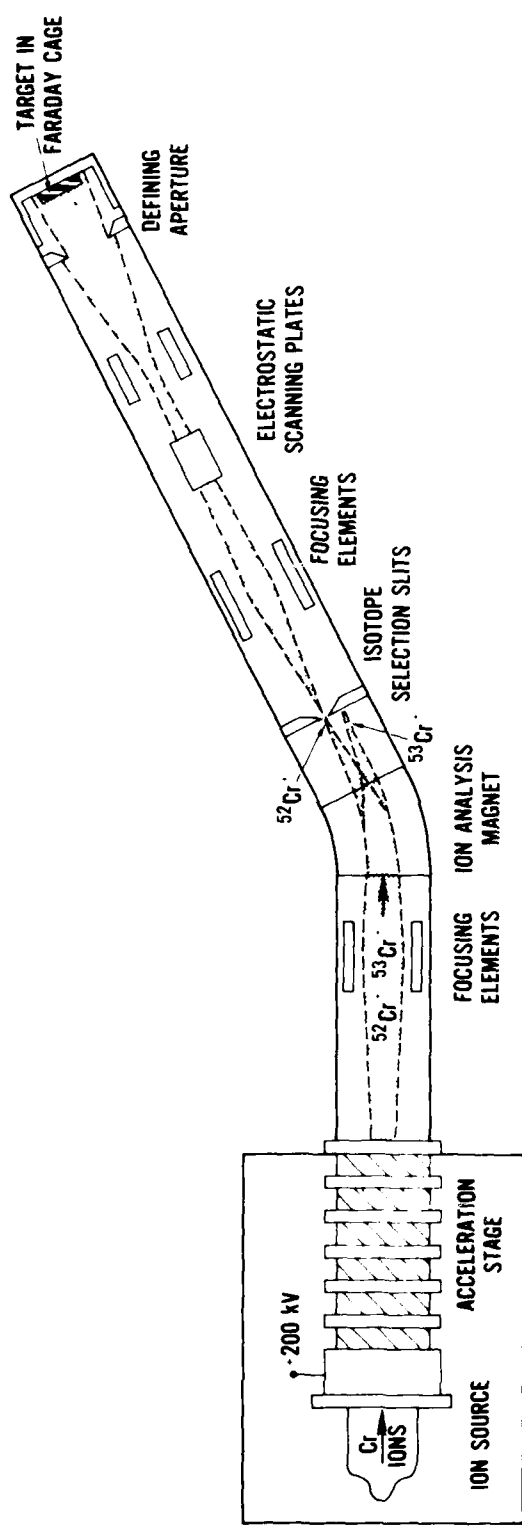
Fig. 2 — Schematic diagram of research-type ion implantation system

Simulation Tests

The tests used herein for simulating the corrosion mechanism which occurs in gas turbine engines was based in the findings of the test method developed by Brown and Feinberg [6]. They found that in a gas turbine engine bearing compartment; (a) corrosion usually occurred statically (i.e., bearing not running) at the conjunction of the bearing rolling element and the race, (b) the lubricant in the form of a miniscus was present at the corrosion site and (c) the lubricant showed typical contamination levels of 3 ppm (wt) of chloride and 600 ppm of water.

Figure 3 shows the arrangement of the simulated geometry corrosion test. The cylindrical surface resting on the flat side of the upright cylinder is intended to simulate the roller on race contact geometry of an actual bearing. The cylinders are .0095M (3/8") diameter M50 rods. The flats (about .006M tall) are cut from the rod and consecutively polished down to a mirror finish with a final (3 μ m) diamond paste. The cyliners were positioned in place and totally immersed for 2 hours in a ccntaminated neopentyl polyolester gas turbine engine lubricant conforming to specification MIL-L-23699. The oil was contaminated by adding three ppm (wt) of chlorides as ASTM DD665 synthetic seawater to oil and then adjusting the water content to a level of 600 ppm (wt.) by the addition of distilled water. The two parts were then removed from the oil and allowed to drip dry. A miniscus of contaminated oil was retained between the two parts as shown in Figure 3. This system was then exposed to alternate cycles of moist air at 60°C (8 hours) and 4°C (16 hours) for a period of several weeks.

The test shown in Figure 3 was done for several implanted ions and several time periods. Figure 4 shows optical photographs (10x magnification) of the corrosion inhibiting effectiveness of an implantation of Cr+Mo+N after a 7 week test (two samples at bottom) as compared to an unimplanted control specimens (two samples at top). The control specimens show severe corrosion. The attack generally occurs in two areas; e.g., a line of pits beneath the line of contact between the cylindrical and flat surfaces, and general corrosion in the thin layer of oil outside this region. A qualitative ordering of the improvement in corrosion resistance found in this simulated field test produced by implanting ions or combinations of ions from best to worst is: Cr+P, Cr+Mo+N, Cr, Ti, Cr+Mo, Al, M50.

Electrochemical Tests

Two independent electrochemical characterizations were done to study two types of corrosion behavior. Passivity tests in strong acids provide insight into general corrosion (rusting) behavior and pitting tests in chloride ion solutions give a measure of the resistance to localized corrosion (pitting).

The acid tests were done in 1 Normal H_2SO_4 at room temperature. Figure 5 shows potentiodynamic polarization scans (1 mV/S) for unimplanted M50 and for Cr, Mo, Ti, and Cr+Mo implants [7]. Notice that all implant samples show a reduction in the maximum current density when compared to the base line M50 curve. Lowering of the maximum current density indicates that the surface is more easily passivated and that improved corrosion resistance may be expected. These tests establish a qualitative ordering of the improvements to be expected in general corrosion behavior which is, from best to worst, Cr+Mo, Cr, Mo, Ti, unimplanted M50.

The chloride ion tests were in a pH6, 0.01, or 0.1 Molar NaCl, buffered solution. The buffer ensured that the pH was constant throughout the measurements. Figure 6

1. Test pieces (both M50 alloy steel) were placed in contact as indicated by the dotted line.
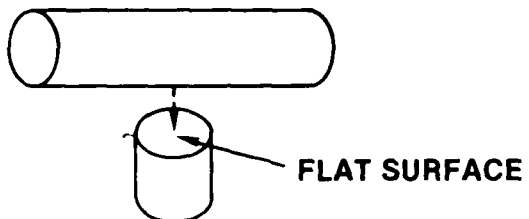
FLAT SURFACE

2. Both pieces in place were immersed in chloride-contaminated oil for 2 hrs., removed, and allowed to dry.

3. A meniscus of contaminated oil was retained between the two parts:

UPPER CYLINDER (end view)

Cl-CONTAMINATED OIL
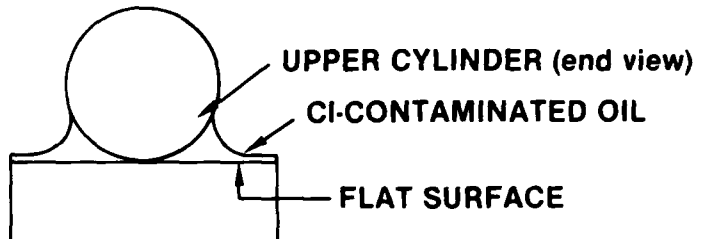
FLAT SURFACE

Fig. 3 — Laboratory-simulated field service test of corrosion of bearings

Con.   Con.

7 wks.

Cr+Mo+N   Cr+Mo+N
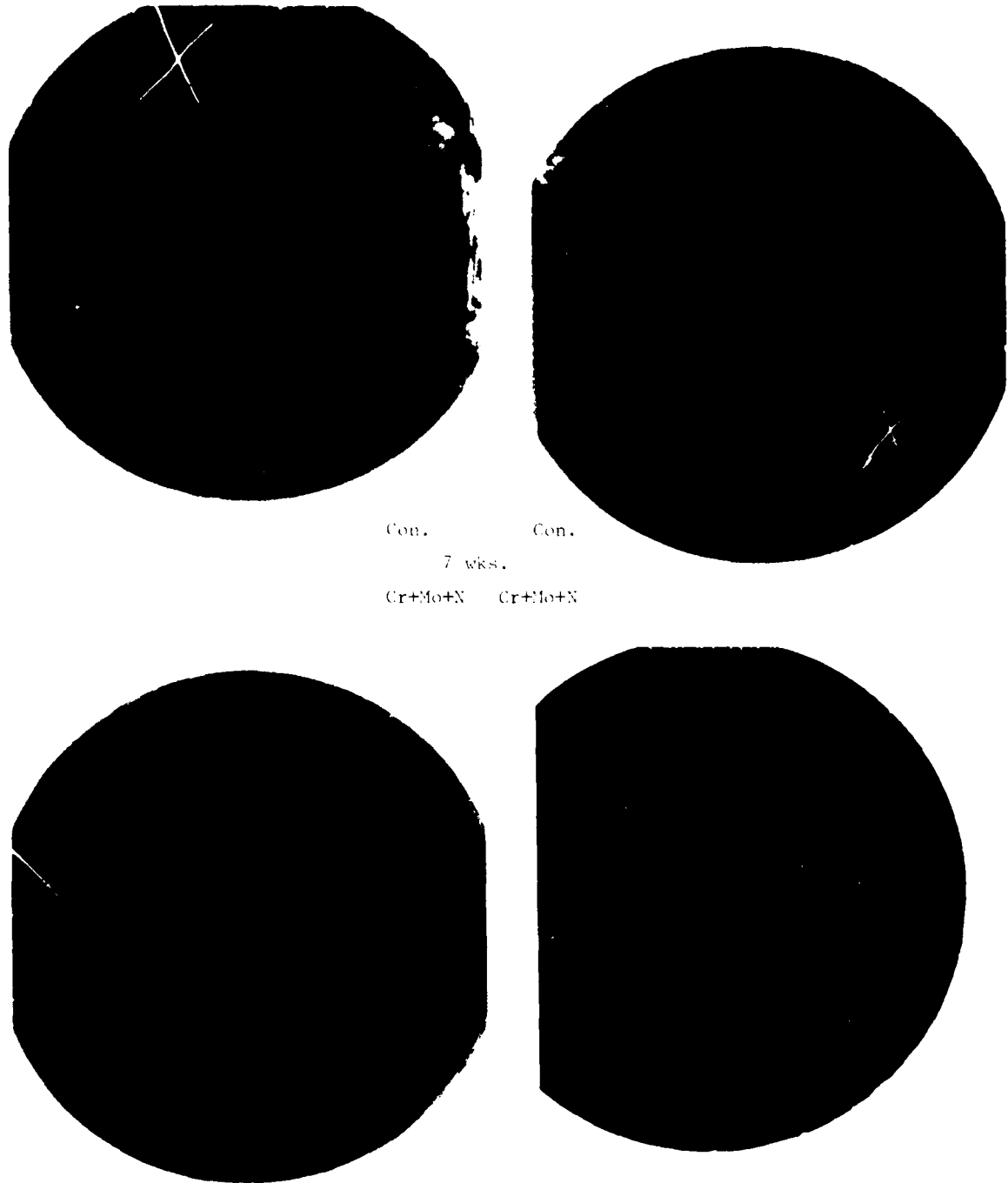
Fig. 4 — Optical photographs of the flat surfaces of M50 test samples after a
simulated field service test. The two unimplanted samples at the top show
pitting under the line of contact. The two Cr+Mo+N implanted samples at
the bottom show complete immunity. (Magnification 10X)
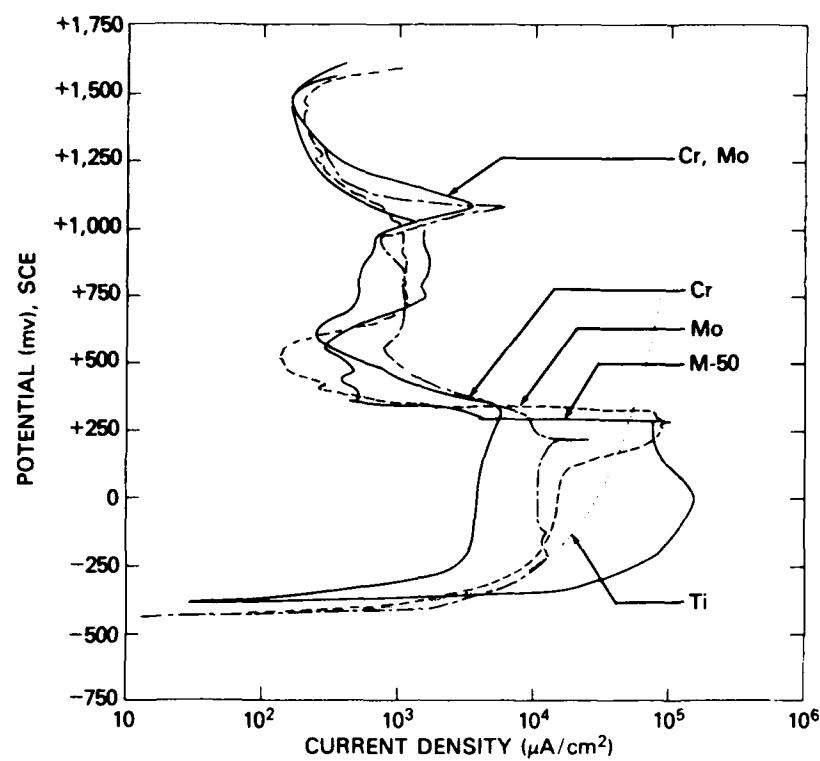
Fig. 5 — Potentio-kinetic anodic polarization data produced in hydrogen-saturated 1N H_2SO_4 for M50 steel, and for M50 steel implanted with titanium chromium, molybdenum and chromium + molybdenum
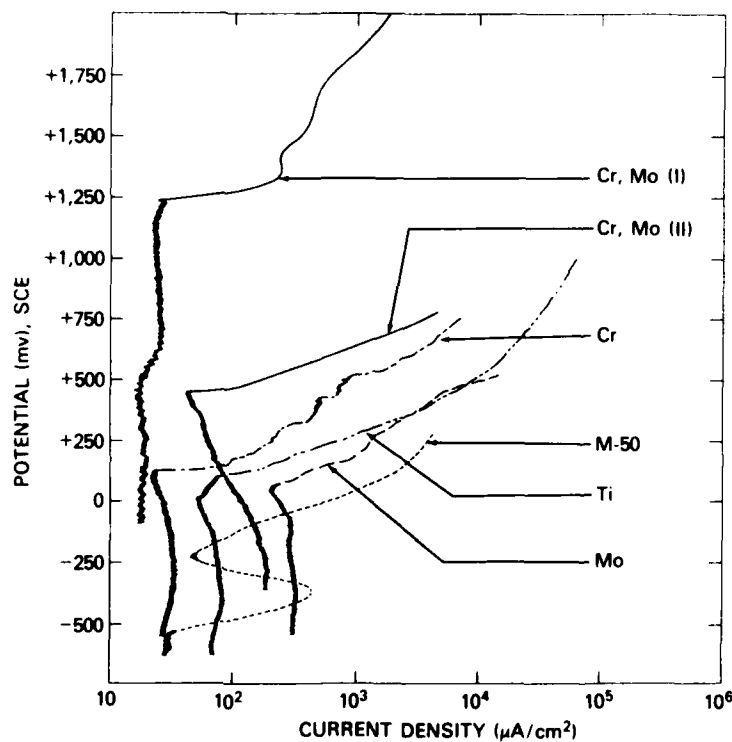

Fig. 6 — Potentio-kinetic anodic polarization data produced in buffer solution of pH6 containing 0.1 M NaCl for M50 steel, and for M50 steel implanted with titanium, chromium molybdenum and chromium + molybdenum

10č

presents potentiodynamic polarization scans (1 mV/S) for the 0.1M NaCl solution for several implants. The sailent characteristic of each curve is the breakdown potential, E_b, which characterizes the metals ability to withstand pitting attack (i.e., higher E_b indicates better protection). The breakdown potential is that voltage on the curve where there is a sudden increase in current density. The qualitative order of effectiveness is from best to worst, Cr+Mo, Cr+P, Cr, Mo, Ti. The pitting data in a 0.01M NaCl solution for several implant species was performed with two different pretreatments. In one case, the sample was polarized positively immediately upon immersion into the solution so that the air formed film was being tested for pitting. In the other case, the air formed film was removed by polarizing in the negative direction (H_2 charging) for 15 min., then scanned positively allowing a new passive film to form. The latter was the pretreatment for the 0.1M data as well. The former is more realistic since an air formed film would be expected to exist on actual bearings. These test results, for a number of tests similar to those shown in Figure 6, are summarized in columns 4 and 5 in table II and are discussed below.

Qualitative rankings for the data from the five different tests, (1) simulation tests, (2) 1-normal H_2SO_4 test (3,4) the 0.1M and 0.01M NaCl pitting test with cathodic charging, and (5) the 0.01M pitting test on air formed films, are compared in Table II. Cr and Cr+Mo are found effective in all tests. Chromium implants show good performance in all tests while Cr+Mo perform best in two tests. Cr+P performed best in the simulation tests and the 0.01M NaCl test. Therefore, Cr, Cr+Mo and Cr+P were selected for further examination in full scale rolling element bearings.

Table II. M50 Corrosion Test Results (Qualitative Ranking)

Sim.	IN H_2SO_4	0.1M NaCl (cath.)	0.01M NaCl (no cath.)	0.01M NaCl (cath.)
Cr+P	Cr+Mo	Cr+Mo	Cr+P	Cr
Cr	Cr .	Cr	Cr	Cr+P
Cr+Mo+N	Mo	Mo	Cr+Mo	M50
Ti	Ti	Ti	M50	Cr+Mo+N
Cr+Mo	M50	M50	Cr+Mo+N	Cr+Mo
M50				

Implantation Parameters

Ion(s)	Fluence ($\times 10^{17}$/cm^2)	Energy (keV)
Cr+	1.5-2.0	150
P	0.5-1.0	40
Cr	1.5-2.0	150
Cr+	1.5-2.0	150
Mo+	0.35-0.5	100
N	0.1	12.5
Ti	2.0	55-150
Al	0.6	50
	1.0	100

Table III. Bearings Selected for Implantation

Application	Type*	Bearing Size – mm			No. Brgs. Implanted	Ions	Function in Program
		O.D.	Bore	Rolling Element Size			
J79 Gas Turbine Engine Thrust Bearing	B	225	150	22.22 (Ball)	1	Cr+Mo	Performance and Field Evaluation
T58 Turboshaft Engine – No. 4 Bearing	R	68	40	7 long x 7 dia.	2	Cr+Mo	Performance and Field Evaluation
Modified T58 Bearing	R	68	40	7 long x 7 dia.	10 11	Cr+P Cr	Fatigue Endurance Testing
T63 Gas Turbine Engine Bearing No. 3 No. 6	 B R	 55 42	 30 25	 16 (Ball) 5 long x 6 dia.	 2 2	 Cr+P	T63 Engine Evaluation in a Test Cell with Contaminated Oil
Various Engine Gearbox Bearings	B&R	Various Sizes		–	0		Long Term Storage Tests

*B = Ball Bearing
 R = Roller

110

IMPLANTATION OF BEARINGS

Bearings selected for implantation are listed in Table III along with pertinent information on bearing size where applicable, and function in the overall program. Table III also identifies the bearings that have been implanted to date.

There are a number of practical problems to be considered for the successful implantation of the bearings. Obviously, all contacting surfaces must be implanted to protect against the formation of corrosion pits which can act as initiation sites for fatigue spalling. This entails implanting the active surfaces of the bearings (i.e., the inner race outer race and the total area of the rollers and the balls). In order to implant the bearings in a reasonable period of time, very high ion beam currents were developed and used. For Cr a typical beam current is 500 μA at 150 keV. This represents 75 watts of incident power which must be dissipated or the bearing will overheat, causing loss of hardness. Fortunately, M50 holds its hardness well in that it has been established that no loss of hardness occurs at temperatures of 800°F for 1000 hours [8]. This enables the heat dissipation to be handled in some cases by radiation losses alone.

During implantation, all the races were clamped tightly to a solid aluminum or brass plate and rotated at 1.5 rpm. Typically 60 revolutions are required to finish one race. In this manner, heat was transferred to the plate and both the plate and race then radiated the heat away.

For the races the beam was scanned vertically but not horizontally so that the beam irradiated the bearing races over the vertical extent of the race (1.5 cm for T58; 3 cm for J79) with a width of about 1 cm. Table IV shows the maximum temperature of each bearing component during implantation. The target chamber vacuum was typically less than 3 x 10^{-6} Torr during implantation and the target chamber was always vented to atmospheric pressure with dry nitrogen gas after the bearing components had cooled to at least below 550°F.

Table IV. Normal and Maximum Temperatures Reached by Bearing Components during Implantation

Component	Temperature ($^\circ$F)	
	T_{Normal}	$T_{Max.}$
J79 Inner race	400	500
J79 Outer race	400	500
J79 Ball	450	500
T58 Inner race	400	550
T58 Outer race	500	640
T58 Roller	390	650

The T58 rollers were implanted on the ends with the jig shown in Figure 7. A stainless steel frame held down to an aluminum block contains the rollers which are held tightly in place by a stainless bar pressed against the roller array by two screws. Beneath the rollers is a thin sheet of Mo. Cooling is accomplished by fastening the holder with three screws to a water cooled shaft. Indium foil pressed between the aluminum block and cooled shaft promotes heat conduction from the block. The materials of stainless steel and Mo were chosen to minimize any possible deleterious

111

79599(4)

Fig. 7 — Photograph of implantation jig used to implant 18 T-58 bearing roller ends. Stainless steel frame is turned over to implant opposite ends of rollers. The aluminum base is water cooled.
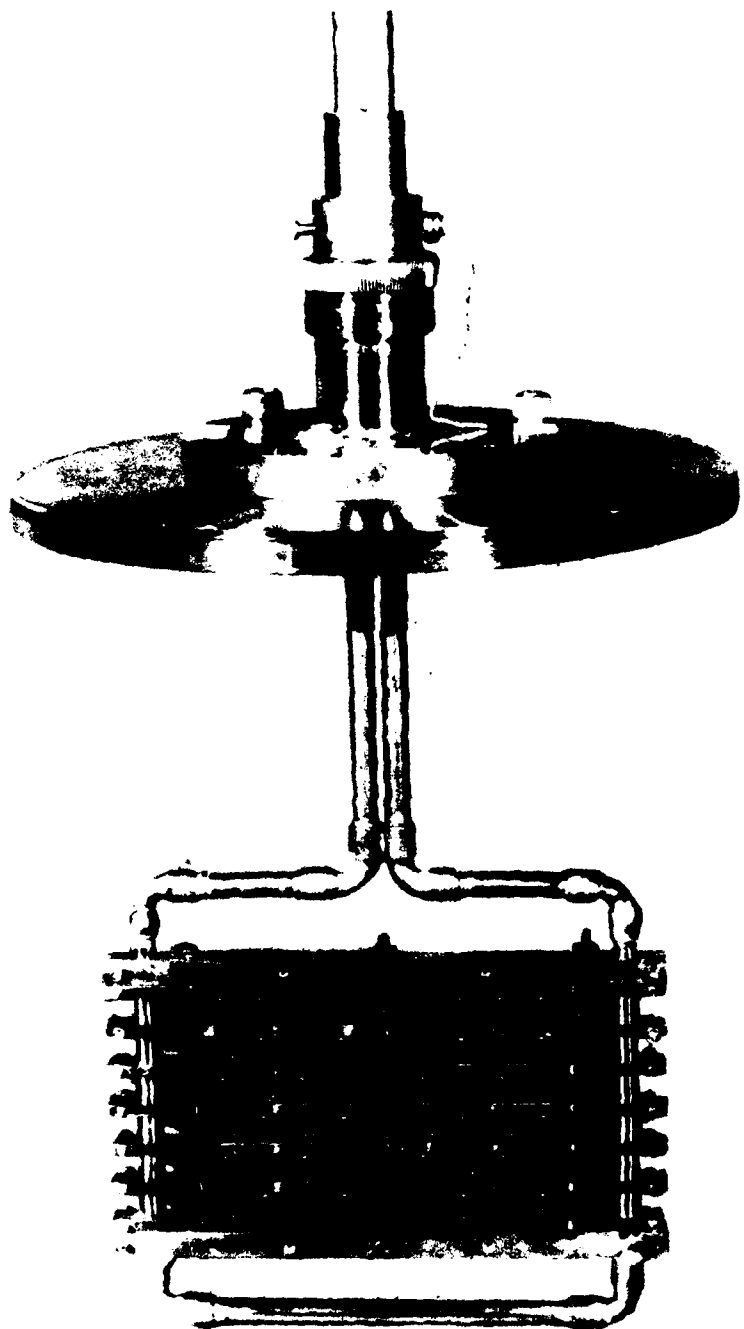
Fig. 8 — Photograph of implantation jig used to implant up to 48 T-58 rollers at one time. Quarter inch copper tubing provides water cooling and support for stainless steel bars that retain the rollers. Rollers are implanted in four rotations, 90° apart, for complete coverage of the circumference.

effects of sputtering of the holder material onto the bearings. Brass and aluminum, which conduct heat much better than stainless, unfortunately sputter very efficiently and would therefore non-uniformly coat the rollers with Cu, Zu and Al. Mo has a low sputtering coefficient and is innocuous in that the small amount of sputtered Mo contamination on the bearings would be expected to have a beneficial effect on corrosion resistance. Impurities sputtered onto the bearings from stainless steel are chiefly iron, chromium and nickel which are also compatible with the corrosion prevention purpose of the implanted layer. The sputtering coefficient for P on these materials is much smaller than for Cr and thus was not deemed a problem.

Roller circumferences were implanted in four steps with the jig shown in Figure 8. Stainless steel tubing supports stainless horizontal struts each of which hold 8 rollers. Water flowing through the tubing cools the struts which in turn hold and cool the rollers. The roller circumferences are implanted in a cubic geometry such that each of four "sides" receives the same fluence of particles. This results in a $\pm 15\%$ variation in fluence around the circumference of the roller. For Cr implants, the fluence varies between 1.5×10^{17} and $2.1 \times 10^{17}/cm^2$. We have observed that the corrosion inhibition effects of Cr implants between 1×10^{17} and $2 \times 10^{17}/cm$ fluences are equal by means of the simulation test mentioned previously. Therefore, the $\pm 15\%$ variation in fluence is not expected to be a problem. This observation is also consistent with the well known observation that an abrupt improvement in the corrosion resistance of steels occurs at a Cr concentration of 12%, so that if this criteria is met by the lowest fluence implant, additional Cr will not substantially further improve the corrosion resistance [2].

Figure 9 shows a planetary gear jig designed to implant up to 48 J79 balls in one operation. It is set up for 24 balls on a 0.19M diameter as shown in Figure 9. The balls are held in place by gravity in a stainless steel "golf tee" and each ball rotates 18 times for each rotation of the whole assembly. The beam is scanned horizontally and vertically over an area 22 mm high by 51 mm wide so that at any one time slightly more than 2 balls are being irradiated. The problem of temperature rise is solved by a 12 to 1 duty cycle wherein each ball is irradiated for about 3 seconds and allowed to cool (chiefly by radiation) for about 37 seconds.

The emissivity of the balls was determined by measuring the heating curve of a ball with a thermocouple attached to it in vacuum. Figure 10 presents the data for two different input powers of an Ar ion beam. From the equation in Figure 10 and knowing the input power and surface area of the ball, an emissivity of 0.25 is computed. From this information an equilibrium temperature of $390^\circ F$ for a $200\,\mu A$, 150 keV, beam was computed. The measured value under the stated implantation conditions of $425^\circ F$ is in satisfactory agreement with the calculated value. During implantation the temperature of the bearings was measured and continuously monitored by means of an infrared pyrometer sighted on the bearing through a quartz window in the implantation vacuum chamber.

The procedure for implanting the balls with Cr was to (i) implant in a rotating cylindrical geometry to a fluence of $1 \times 10^{17}/cm^2$, (ii) rotate the balls 90° with respect to the vertical direction and implant again to an additional fluence of $1 \times 10^{17}/cm^2$. This leaves the ball surface with two poles containing 2×10^{17} ions/cm^2, two poles containing 1×10^{17} ions/cm^2, and the remainder of the surface with fluences between these two values. This factor of the two nonunifomrity in fluence will not be deleterious for the same reasons as discussed for roller bearings. It is envisaged that under production conditions T58 bearings could be implanted at the rate of 4 per hour.

114

79599(10)

Fig. 9 — Photograph of planetary gear fixture used to implant 24 J-79 balls at one time (expandable to 48 balls). Stainless steel "golf tees" retain the balls and each ball rotates through the beam spot which remains fixed at the dimensions 7/8 in. tall by 2 in. wide. A ball rotates 18.5 times for each rotation of the platform.

300

200

100

T M50 BALL (°C)

$$a = W/\sigma A \left(T_b^4 - T_c^4\right)$$

× W = 1.35 WATTS
● W = 2.25 WATTS

a = EMISSIVITY
$A = 4\pi r^2 = 1.55 \times 10^{-3} m^2$
$\sigma = 5.67 \times 10^{-8} Wm^{-2}K^{-4}$
$T_c = T$ CHAMBER $= 293°K$
$T_b = T$ BALL (STEADY STATE)

10
0   50   100   150

TIME (min)
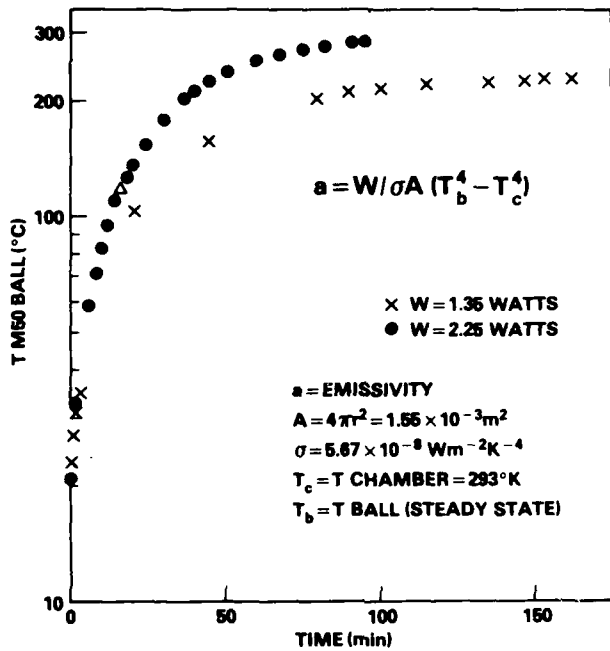
Fig. 10 — The increase in temperature as a function of time
of an M50 steel ball from a J-79 main shaft bearing for two
different values of the ion beam input power. From this data
the emissivity of the M50 ball is determined to be 0.25.

116

PERFORMANCE AND ENDURANCE TESTING OF FULL SCALE BEARINGS

One each of the J79 and T58 engine bearings (first two bearings listed in Table III), were performance tested for 400 hours at conditions simulating speed, load, and temperatures of actual operating engines.

In addition, 10 each of the modified T58 bearings (Table III) implanted with either Cr+P or Cr were fatigue endurance tested. Another group of 10 untreated bearings, also fatigue endurance tested, provided a baseline for comparison. All thirty bearings were made from a single lot of M50 steel and were manufactured at the same time. Differences in endurance life could therefore be attributed only to the implantation process since the material and manufacturing processes were statistically similar among the three groups.

The conditions for the performance and the endurance testing are given in Table V. Note that in the fatigue endurance testing the loads are much higher than would be expected in actual operation. This is done to accelerate fatigue spalling so that failures will be obtained in a reasonable period of time on a large number of bearings. For simplicity and reliability the machine rotating speed is usually kept low. Bearings in both performance tests successfully completed the scheduled 400 hour test without failure and were capable of continued operation. Fatigue test results for the fatigue endurance bearings are shown in Table VI. All bearings experienced a fatigue spall at the endurance life indicated (in hours) except where noted. The data from each group were assumed to be distributed as a Weibull function, which is a population distribution normally used to fit contact fatigue data [9]. For each group of data, Weibull distribution parameters, which are used for comparison between groups, were calculated using a least squares regression analysis. They are the L10 life, L50 life, and the Weibull slope (β) and listed in Table VI. These are defined as follows:

a. L10 life – The number of hours exceeded by 90% of the population,

b. L50 life – The number of hours exceeded by 50% of the population,

c. Weibull slope (β) – The slope of the computed Weibull line. This parameter indicates the amount of scatter in the data.

Using the method described in reference 9, a statistical comparison was made of the L10 and L50 lives of each implanted group against the baseline unimplanted group. The results show no significant difference in fatigue lives among any of the three groups. This is evident by the large amount of overlap in the 90 percent confidence intervals around the L10 and L50 Weibull parameters as shown in Table VI.

Energy dispersive X-ray analysis was conducted to ascertain the Cr content in the surface of one roller before and after endurance testing. The results are shown in the X-ray spectra of Figure 11 which includes an unimplanted roller for baseline comparison at the bottom, implanted and fatigue tested in the middle, and as-implanted at the top. It can be seen that after running for 420 hours, there is very little depletion of Cr in the roller surface.

Table V. Test Conditions for Performance and Fatigue Endurance Testing of Implanted Bearings

	Performance Tests		Fatigue Endurance Tests T58 Modified		
	J79 Brg.	T58 Brg.	Group 1	Group 2	Group 3
Implant	Cr+Mo	Cr+Mo	Cr+P	Cr	Untreated
Load Radial Thrust	900 lbs. 6922 lbs.	150 lbs. 0	– 	2800 lbs. 	–
Speed	7460 rpm	19,500 rpm	–	7000 rpm	–
Oil in Temp.	300°F	250°F	–	210°F	–
Oil Flow	1.45 gals/min	0.35 gals/min	–	0.25 gals/min	–
Length of Test	400 hours	400 hours	–	Until Failure	–
No. of Bearings Tested	1	1	10	10	10

Note: Lubricant – MIL-L-23699

118

Table VI. Results of Fatigue Endurance Tests (Hours to Failure)

	Cr+P	Cr	Untreated
	81.7	36.2	76.2
	92.6	94.4	86.9
	93.0	127.4	113.2
	100.1	132.8	177.6
	191.4	135.1	177.9
	191.7	150.9	221.9
	278.4	193.4	296.8
	351.8*	252.2	361.4*
	361.2	306.9*	383.8
	420.4*	399.3	394.3*
L_{10} Life	61.21	51.27	73.21
90% LCL	22.73	18.84	29.93
90% UCL	256.92	218.46	267.25
L_{50} Life	203.39	172.53	216.44
90% LCL	129.60	109.41	144.09
90% UCL	319.38	272.19	323.26
β	1.56	1.55	1.73

*Bearing test suspended prior to failure
LCL = Lower Confidence Limit
UCL = Upper Confidence Limit

119
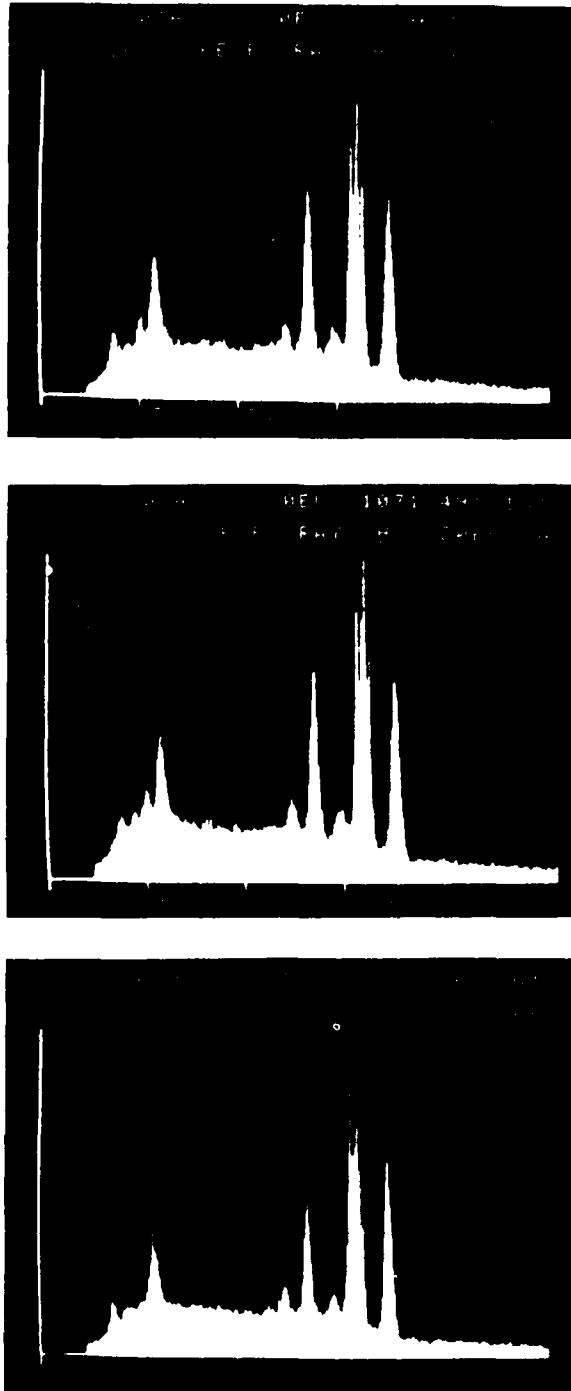
Fig. 11 — Energy dispersive x-ray spectra of M50 steel rollers from a T-58 main shaft bearing. Top — Cr+P implanted but not endurance tested. Middle — Cr+P implanted and after 420 hours of endurance testing. Bottom — not implanted and not endurance tested. The 3 spectra are normalized to the Fe K_β line for easy comparison. The Cr K_α line is considerably larger in the top and middle spectra than in the bottom spectrum.

R-063

120

FUTURE PLANS

Evaluation of ion implanted M50 bearings for corrosion protection will continue with:

a. In-service evaluation of the applications listed in Table III,

b. Testing of a T63 engine in a test cell with chloride and water contaminated oil. Two of the seven mainshaft engine bearings will be implanted with the Cr+P,

c. Storage testing of implanted bearings,

d. Full scale bearing corrosion tests as described in reference 6. Moreover, plans are currently underway to examine ion implantation for (1) improvement in scuffing resistance of spur gears and (2) corrosion resistances of advanced bearing and gear steels such as CBS600 and CBS1000M.

COST OF IMPLANTATION PROCESS

With currently available ion sources it is possible to produce currents of up to approximately 1 mA of Cr ions. This would correspond to a treatment time of about 16 sec/cm^2 to reach a fluence of (10^{17} atoms/cm^2). If an operating cost of $35/hour is assumed, these times correspond to costs of roughly $0.15/$cm^2$. Further development of ion sources that is underway should increase attainable ion currents to at least 10 mA and therefore lower costs.

CONCLUSIONS

Implantation of a single element (Chromium) or dual elements (Chromium plus Phosphorous or Molybedum) substantially improves resistance to both general and pitting corrosion in M50 steel. The improvements are strongly evident in three independent methods, i.e., (1) cylinder-on flat simulation (2) polarization in $1N-H_2SO_4$ and polarization in 0.1M or 0.01M NaCl solution.

Implantation jigs have been disigned and built which enable the inner and outer bearing race surfaces, rollers and balls to be implanted to adequate fluences for corrosion protection. The temperature of the bearing components may be adequately controlled during implantation so that there is no loss of hardness.

Twenty-three T58 bearings and one J79 bearing have been successfully implanted. The average time to implant one complete T58 bearing with Cr was about 3 hours beam time. This was under less than optimum production line conditions. It is estimated that this figure could be improved by a factor of about ten in a production line situation.

Implantation of the ion species evaluated does not adversely affect either bearing performance or fatigue endurance life.

REFERENCES

[1] J. S. Cunningham and M. A. Morgan, Review of Aircraft Bearing Rejection Criteria and Causes, Journal of the American Society of Lubrication Engineers, Volume 35, 8, pp. 435-441 August 1979.

[2] N. D. Tomashov, Theory of Corrosion and Protection of Metals, (the Macmillan Company, New York 1966).

[3] J. R. Ambrose, Corrosion, NACE, 34, 27 (1978).

[4] J. L. Whitton, W. A. Grant, and J. S. Williams, Proc. Int. Conf. on Ion Beam Modification of Materials, Budapest, Hungary (1978).

[5] J. E. Truman, M. J. Coleman, and K. R. Pirt, Br. Corros. J., 12, 236 (1977).

[6] C. Brown and F. Feinberg, Development of Corrosion Inhibited Lubricants for Gas Turbine Engines and Helicopter Transmissions, ASLE Preprint No. 80-AM-6C-3 presented at the 35th Annual Meeting, May 5-8, 1980.

[7] Y. F. Wang, C. R. Clayton, G. K. Hubler, W. H. Lucke, and J. K. Hirvonen, Thin Solid Films 63, 11 (1979).

[8] N. E. Anderson, Long-Term Hot-Hardness Characteristics of Five Through-Hardened Bearing Steels, NASA Tech. Paper 1397, AVRADCOM Tech. Rept. 78-16, October (1978).

[9] L. G. Johnson, The Statistical Treatment of Fatigue Experiments, Elsvier Publishing Co., Amsterdam, London, NY 1961.

Section III.B

THE CORROSION BEHAVIOR AND RUTHERFORD BACK-SCATTERING ANALYSIS OF PALLADIUM-IMPLANTED TITANIUM

G. K. Hubler[1] and E. McCafferty[2]

[1]Materials Modification and Analysis Branch
Condensed Matter and Radiation Technology Division

[2]Advanced Materials Technology Branch
Material Science and Technology Division
Naval Research Laboratory

THE CORROSION BEHAVIOUR AND RUTHERFORD BACK-SCATTERING ANALYSIS OF PALLADIUM-IMPLANTED TITANIUM*†

G. K. HUBLER and E. MCCAFFERTY

Naval Research Laboratory, Washington, DC 20375, U.S.A.

Abstract—The corrosion behaviour of Pd-implanted Ti in boiling 1M H_2SO_4 has been investigated by means of high resolution Rutherford backscattering (RBS) profiles of the Pd concentration as a function of corrosion time, and by electrochemical methods consisting of corrosion potential vs time curves and potentiostatic polarization data. Employing ion-implanted Xe as a surface 'marker', absolute corrosion rates were determined by RBS analysis and compared to corrosion rates determined from the polarization curves. The rate of Ti dissolution is found to be reduced by about three orders of magnitude for Pd-implanted samples. The corrosion potential-time curves and high resolution RBS data both show that soon after immersion, the Pd surface concentration rises to 20 at. % because of preferential dissolution of Ti and that the Pd is retained in the surface for corrosion times of up to 9 h. The steady state corrosion potential of implanted samples is close to that of pure Pd and 800 mV anodic with respect to the corrosion potential of pure Ti. The protection is explained by the fact that the mixed electrode potential is more noble than the critical potential for passivity of Ti, resulting in a markedly reduced dissolution rate.

INTRODUCTION

THE CORROSION of metals is caused by chemical or electrochemical reactions occurring within the first few atomic layers of the surface. One method of corrosion control is to introduce, by alloying, elements which improve the thermodynamic stability of the surface or promote the formation of passive films. A disadvantage of this method is that elements which improve corrosion resistance may not be those which give the desired structural properties of the material. Ion implantation of metals offers the capability of modifying the surface chemically without affecting bulk physical or mechanical properties because implantation depths are typically only 1–1000 nm. Other attractive features of the ion-implantation method and additional background have been given by Ashworth and co-workers.[1]

Results in the literature pertaining to the effect of ion implantation on the aqueous corrosion of metals has been directed toward iron and its alloys. Ashworth *et al.* found that Cr implanted into Fe to surface concentrations of up to 6% Cr produced the same corrosion resistance as bulk 6% content alloys.[2] In addition, it was found that ion-implanted Ta was better than Cr in improving the corrosion resistance of Fe.[3] The Ta in Fe system had not been previously studied in bulk alloys because of the vanishingly small solid solubility of Ta. Covino and co-workers[4,5] studied Cr and Ni implanted into Fe and obtained similar results.

*Manuscript received 19 December 1978.

†Paper presented at the Meeting on 'Ion Implantation and Ion Beam Analysis Techniques in Corrosion' held at the University of Manchester Institute of Science and Technology in the Corrosion and Protection Centre, 28–30 June 1978.

This paper reports on the corrosion behaviour and characterization of Pd-implanted titanium in boiling 1M H_2SO_4. It is well known that small amounts of Pd in bulk alloys (0.1 at.%) produce a dramatic reduction in the corrosion rate of titanium in boiling acids.[6,7]

The present investigation utilizes electrochemical techniques in conjunction with high resolution Rutherford backscattering measurements. Employing ion-implanted Xe as a surface 'marker', absolute corrosion rates were determined by Rutherford backscattering (RBS) analysis. These rates were in good agreement with the corrosion rates determined from the polarization curves and by colorimetric measurements of dissolved Ti. The rate of Ti dissolution is shown to be reduced by about three orders of magnitude for Pd-implanted samples. The protection is explained by retention of surface Pd producing a mixed corrosion potential which is above the critical potential for passivity of Ti, resulting in a markedly reduced dissolution rate.

Preliminary results of this investigation have been published elsewhere.[8,9]

EXPERIMENTAL METHOD

In order to obtain unambiguous high-resolution depth information concerning the ion-implanted palladium, it is necessary to prepare smooth and clean titanium surfaces. Therefore, careful attention was given to the preparation of the original titanium surfaces by means of a mechanical polishing procedure. Samples of 5 mm thickness were cut from the titanium rod (99.97% pure, 1.0 cm diameter) and were vacuum mounted in epoxy leaving one exposed surface to be polished. The exposed face was abraded with 240, 320, 400 and 600 grit silicon carbide polishing papers, followed by a mechanical polish with 6 μm diamond paste on cloth. A final polish with 0.05 μm γAl_2O_3 particles in a 5% oxalic acid solution[10] resulted in a mirror finish surface in which no scratches or surface features could be detected on a scanning electron microscope (SEM) at magnifications up to 10,000 times.

Surfaces polished in this manner were implanted with Pd to a fluence of $1 \cdot 10^{16}$ ions cm^{-2} at an energy of 90 keV. This fluence resulted in a near-gaussian shaped concentration profile centred at a depth of 24 nm. The concentration at the gaussian peak was 4 at.%. Some samples were also implanted with Xe to a fluence of 3.5×10^{15} ions cm^{-2} at 90 keV. The Xe concentration profile was similar to the Pd profile but with a factor of three lower peak concentration. The Xe atoms provided a 'marker' in RBS analysis with which to register the amount of Ti removed from the front surface. It is assumed that the Xe atoms dissolve into solution as they are uncovered. The amount of Ti removed is measured as a shift toward the surface of the RBS Xe profile. (Of course, physically the surface moves in the direction of the Xe atoms as the Ti dissolves.) The behaviour of Pd-implanted, and Pd-plus-Xe-implanted samples was identical in both RBS and electrochemical measurements.

High resolution RBS profiles were obtained with a 2.5 MeV α-particle beam produced by the NRL 5MV Van de Graaff accelerator. Particles backscattered by the target at an angle of 135 were detected in a position-sensitive detector placed in the focal plane of a 50.8 cm by 180 double-focusing magnetic spectrometer. This particle detection system provides an energy resolution of 0.80% which results in a system depth resolution of about 4 nm. Details of the RBS techniques and the magnetic spectrometer detection system may be found elsewhere.[11]

Electrochemical measurements were made using a single-compartment cell fitted with a condenser. The cell was also fitted with standard taper ports for insertion of the sample electrode, auxiliary electrode, and a second, smaller condenser through which aliquots of the solution were pipetted for colorimetric analysis of dissolved titanium by the hydrogen peroxide method.[12]

Electrode potentials were measured versus the mercury/mercurous sulphate electrode using a Luggin-Haber capillary. Heat conduction through the capillary was sufficient to maintain the external reference electrode at 95°, as compared to the cell temperature of 100°. The Hg/Hg_2SO_4 electrode was utilized because it has been shown to be a reliable reference electrode at those temperatures.[13] All electrode potentials in this paper are reported relative to the Hg/Hg_2SO_4 reference electrode. (Potentials are converted to the NHE scale by adding 0.66V.)

Before use, the electrochemical cell and all component glass parts were cleaned with a H_2SO_4 HNO_3 mixture and were washed thoroughly with tap and then distilled water. Solutions of 1M H_2SO_4 were made from the reagent grade chemical and distilled water prepared in a Barnstead still.

EXPERIMENTAL RESULTS

Samples co-implanted with Pd and Xe were immersed in boiling 1M H_2SO_4 for various times, removed from the solution, and profiles of the Pd and Xe concentrations measured. Figure 1 shows profiles for an as-implanted sample corroded for the
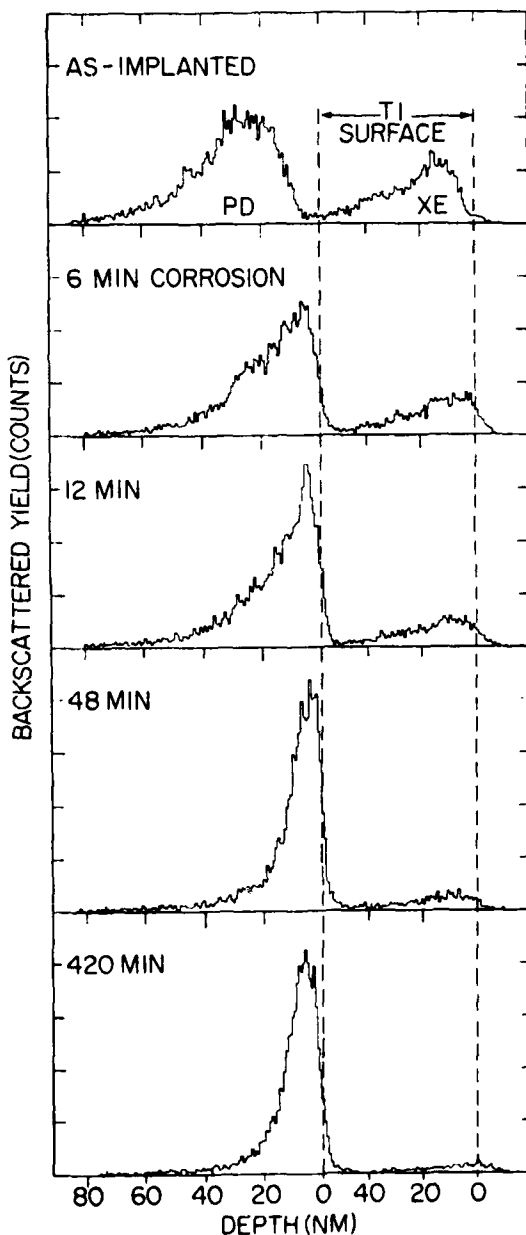

FIG. 1. The energy spectrum of α particles backscattered from ion-implanted Pd and Xe in pure Ti metal for an as-implanted sample, and after four different times of immersion in boiling 1M H_2SO_4. Particle energy is converted into a depth scale on the abscissa.

times of 6, 12, 48 and 420 min. The Ti surface with respect to the Pd and Xe profiles are shown as vertical dashed lines in the figure. After 6 min a significant shift of both the Pd and Xe profiles is evident. After 12 min the Xe signal has diminished and the Pd has clearly redistributed. For longer corrosion times the Xe signal continues to diminish while the Pd profile shows that Pd builds up on the surface to a concentration of about 20 at.%. The total area beneath the Pd profile for all corrosion times is constant to within the ± 5% error in the measurement indicating that no Pd has
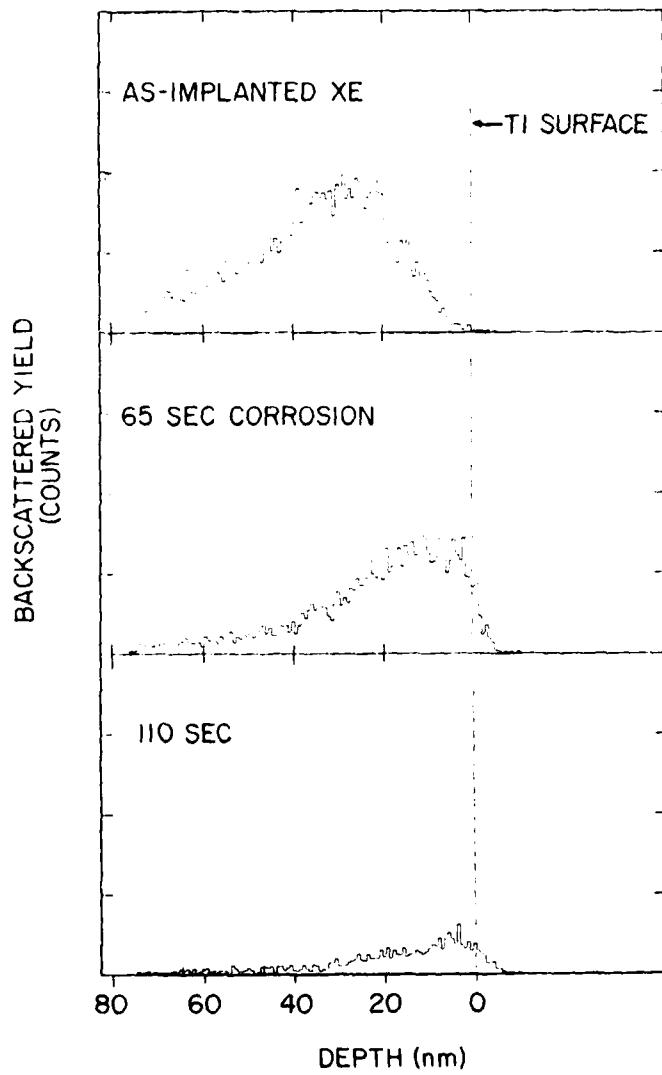
FIG. 2. The energy spectrum of α particles backscattered from ion-implanted Xe in pure Ti metal for an as-implanted sample (top), after immersion in boiling 1M H_2SO_4 for 65 s (middle), and 110 s (bottom). Particle energy is converted into a depth scale on the abscissa.

127

been removed from the surface. The continual reduction of the Xe signal with cor-
rosion time, however, indicates that Ti is being dissolved. Note that after 420 min,
some Xe still remains in the sample.

Figure 2 shows similar profiles for samples implanted with Xe only. Fifty per cent
of the Xe is removed after 65 s, 90% is removed after 110 s and 100% removed after
240 s.

Profiles of implanted samples that were annealed at 101°C for several hours showed
that there is no bulk diffusion of Pd or Xe at this temperature. Therefore, the in-
creased surface concentration of Pd and the loss of Xe occur due to the dissolution
process and cannot be attributed to diffusion effects.

Implanted Pd is retained at the surface for at least 9 h, the longest test performed
to date. Longer tests were precluded because of the failure of the epoxy moulds. This
retention time was verified by colorimetric analysis of dissolved titanium as a function
of immersion time. As seen in Fig. 3, a negligible amount of titanium was lost from
the Pd-implanted sample until after immersion for 8 h.
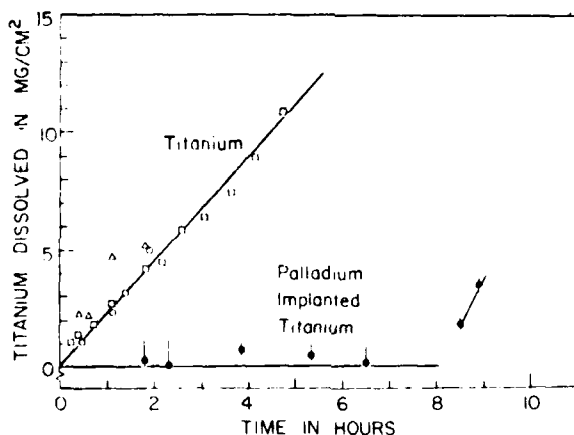
FIG. 3. Corrosion–time curves for titanium and palladium-implanted titanium in
boiling 1M H_2SO_4, as measured by colorimetric analysis of dissolved titanium. The
sharp increase in dissolved titanium after approximately 8 h was caused by failure of
the epoxy mould.

Figure 4 shows electrode potentials for pure titanium, pure palladium, and
palladium-implanted titanium as a function of immersion time in boiling (100°C) 1M
H_2SO_4. The time-axis is plotted logarithmically for illustration purposes only. The
steady-state open-circuit corrosion potential of palladium was approximately 1000 mV
more noble than that of pure titanium. The steady-state corrosion potential of
implanted sample was much closer to that of pure palladium than of pure titanium.

In the first few minutes of immersion, the implanted samples show a rapid transi-
tion in time from a corrosion potential near that of pure Ti to a potential close to
pure Pd. The initial part of this transition is shown in Fig. 5. After 1 min in the
case of two of the implanted samples and after 1.5 min for a third, the electrode
potential was − 1.0 V vs Hg/Hg_2SO_4 and tending toward the potential of pure
titanium. In the next few seconds in each case, however, the electrode reversed toward
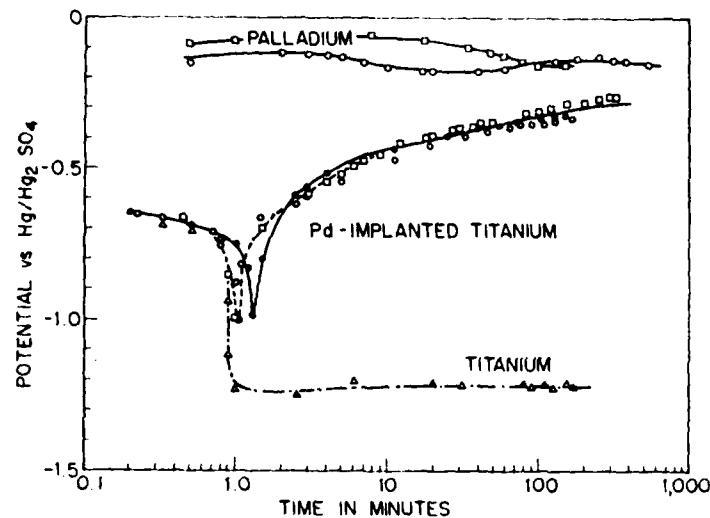
FIG. 4. Open circuit corrosion potentials as a function of immersion time in boiling 1M H$_2$SO$_4$ for pure titanium, pure palladium, and palladium-implanted titanium. The different symbols refer to replicate experiments.
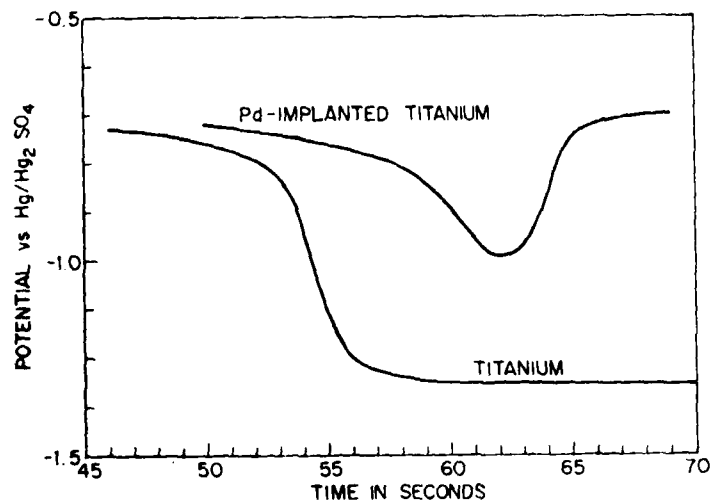

FIG. 5. Initial portions of the electrode potential–time curves for titanium and palladium-implanted titanium in boiling 1M H$_2$SO$_4$.

the noble direction as the Ti-rich surface dissolved away to expose a new surface region containing an increased concentration of Pd. According to the RBS data, the surface concentration of Pd is initially less than 0.1 % in as-implanted samples, rises to 5 % after 6 min, 10 % after 12 min and saturates at about 16 % after 48 min.

129

Figure 6 shows potentiostatic anodic polarization curves for pure titanium, pure palladium, and palladium-implanted titanium in boiling $1M$ H_2SO_4. All curves were
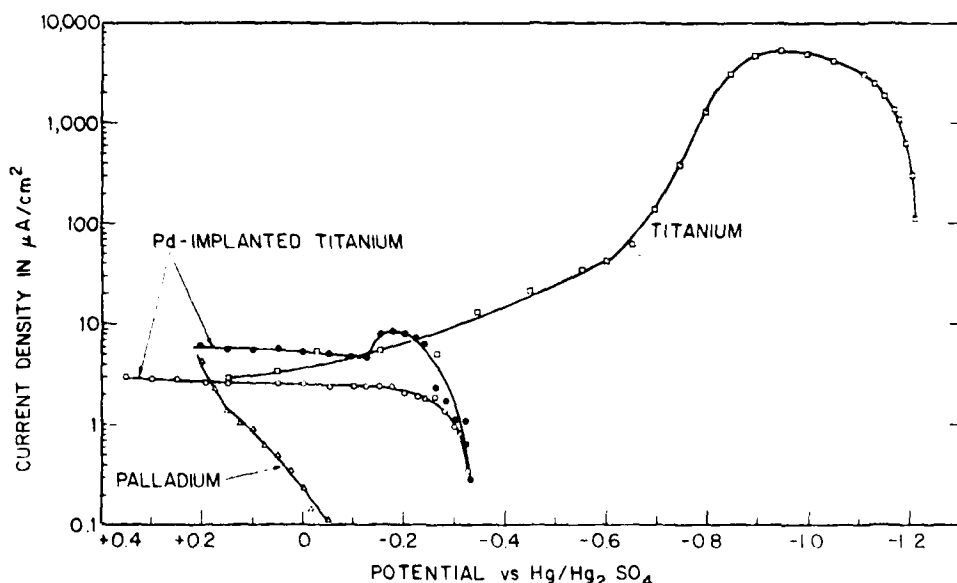
FIG. 6.   Anodic polarization curves for titanium, palladium, and palladium-implanted titanium in boiling $1M$ H_2SO_4.

determined after steady-state open circuit potentials were first established (2–2.5 h immersion). For a given potential, the anodic current was usually constant within 5–10 min. The anodic curve for pure titanium shows the normal active-passive behaviour which has been typically observed.[6,7,14] Well-defined Tafel slopes were not observed in the active region but the corrosion rate at the open-circuit potential, as determined by the colorimetric analysis data in Fig. 3, is 3.7 mA cm^{-2}, on the basis that the overall anodic reaction is Ti $\rightarrow$ Ti^{3+} + $3e^-$.[14] The implanted samples display a passive current density of 2–6 μA cm^{-2}. The approach to the passive current plateau is very rapid, so that there is probably not too much error by assuming that the passive current is also the corrosion current at the open-circuit potential of the implanted sample. Thus, implantation with Pd lowers the corrosion rate of Ti by a factor of about 1000.

Anodic current densities for pure Pd are less than the values for the implanted samples for electrode potentials more negative than 0.2 V vs Hg/Hg_2SO_4. At potentials more positive than + 0.2 V, the corrosion rate of the implanted sample is less than that of pure Pd, as seen in Fig. 6. Using the Pourbaix diagram[15] for palladium at 25°C as an approximate guide, at zero pH Pd is polarized from a region of immunity into one of corrosion for potentials more positive than 0.81V vs NHE (0.15V vs Hg/Hg_2SO_4).

Corrosion rates were also determined in a novel manner from the RBS profiles in
Figs 1 and 2. Figure 7 shows the amount of Ti removed from the implanted sample
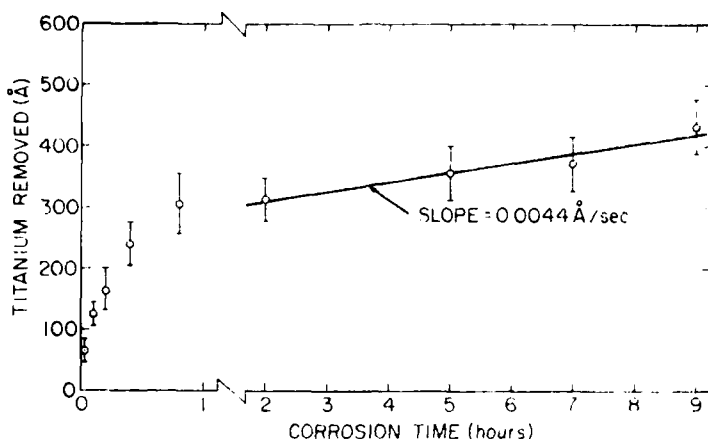
Fig. 7. Rutherford backscattering measurements of the thickness of Ti removed
from a Pd-implanted Ti sample as a function of corrosion time in boiling 1M H_2SO_4.

as a function of corrosion time, as measured by energy shifts in the Xe profiles.
These measurements are obtained in the following manner. It is assumed that the
shape of the Xe profile is modified only by the removal of Xe atoms from the surface
as the surface moves inward. The shift in energy of the remaining Xe profile with
respect to the initial profile is converted into a thickness of material removed by
means of the well known energy loss rate (dE/dx) for He ions in titanium. For
example, 2.5 MeV He ions incident on the sample that are scattered by a Xe atom
and are subsequently detected have an effective $dE/dx = 0.9$ keV nm^{-1}. If an energy
shift of 10 keV is measured in the Xe profile, the thickness of material removed, t, is
t = 10 keV/0.9 keV nm^{-1} = 11.1 nm. By this method, the Ti corrosion rate is deter-
mined by the slope of the curve in Fig. 7, which is seen to be very large at small
corrosion times, but for corrosion times greater than one hour becomes constant at
0.44 pm s^{-1}. This value may be considered the steady-state corrosion rate because the
Pd profiles in Fig. 1 indicate that the Pd redistribution is complete for times greater
than about one hour. Also, the open circuit corrosion potential is also nearly constant
at this time, as seen in Fig. 4. The rate of Ti removal of 0.44 pm s^{-1} corresponds to a
corrosion current density of 1.2 μA cm^{-2}, in reasonable agreement with the values
measured by the polarization method. The values are listed in Table 1.

TABLE 1.   CORROSION RATES FOR TITANIUM AND PALLADIUM-IMPLANTED TITANIUM
IN BOILING 1M H_2SO_4

| Sample | Corrosion rate | | Method of determination |
	Corrosion current density	Rate of titanium removal	
Titanium	3.7 mA cm^{-2}	1.4 nm s^{-1}	Colorimetric analysis of solution
	6.0 mA cm^{-2}	2.2 nm s^{-1}	RBS profiles
Pd-implanted	2–6 μA cm^{-2}	0.74–2.2 pm s^{-1}	Polarization curves
titanium	1.2 μA cm^{-2}	0.44 pm s^{-1}	RBS profiles

The behaviour of Xe-only implanted samples is shown in Fig. 8. The circles are for samples which were at room temperature when inserted itno the boiling acid. There is an incubation period of 30–60 s during which there is negligble removal of Ti. This incubation is probably caused by two effects. First, some time is required to remove the native oxide film from the metal surface; and secondly, the sample mass (i.e. epoxy + Ti) requires time to warm up from room temperature to 101 C, the boiling temperature of 1M H_2SO_4. The latter effect can be minimized by preheating the samples in boiling distilled water and quickly transferring the sample to the acid solution. The procedure reduced the incubation time to ca. 20 s, as shown by the crosses in Fig. 8. However, preheating the sample quite possibly introduces another variable in that the native oxide may thicken during the preheating. Also the thickening of air-formed oxides occurs as the result of ion implantation in Fe[16] and may occur for Ti as well. However, the slope of the solid line in Fig. 8 is 2.2 nm s^{-1}, in good agreement with the value of 1.4 nm s^{-1} determined by colorimetric analysis of dissolved titanium. When the same slope is drawn for the case of insertion at room temperature, the incubation period is seen to be 50 s, in good agreement with the delay time required in Fig. 4 for Ti to approach its steady state corrosion potential.
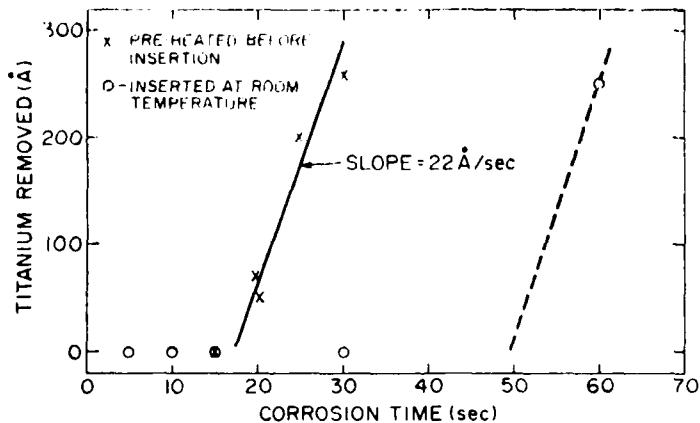

Fig. 8.   Rutherford backscattering measurements of the thickness of Ti removed from pure Ti samples as a function of corrosion time in boiling 1M H_2SO_4.

DISCUSSION

The corrosion resistance of the Pd-implanted surface alloy in boiling 1M H_2SO_4 is comparable to that of bulk Pd–Ti alloys. Table 2 shows that the corrosion rate of the ion-implanted system is actually less than the corrosion rates of the bulk alloys, most likely due to the greater surface concentration of Pd in the ion-implanted case. Table 2 also shows that the corrosion rate of unimplanted titanium agrees favourably with the results of previous investigators.

Electrochemical measurements and Rutherford backscattering analyses indicate that the improvement with the implanted sample is due to initial preferential dissolution of titanium with subsequent build-up and retention of surface palladium. The role of Pd is to provide cathodic sites for the hydrogen evolution reaction. As

TABLE 2. COMPARISON OF EXPERIMENTAL CORROSION RATES IN BOILING 1M H_2SO

| Investigator(s) | Pd content | Corrosion rate in nm s^{-1} | | |
		Ti	Pd-Ti alloy	Pd-implanted Ti
Tomashov et al.[7]	0 wt.%	7.7		
Tomashov et al.[7]	0.1		0.22	
Tomashov et al.[7]	2.0		0 049	
Cotton[17]	0	1.9		
Stern and Bishop[18]	0	3.2		
Stern and Bishop[18]	0.22		0.054	
Stern and Wissenberg[6]	0	3.2		
Stern and Wissenberg[6]	0.08		0.13	
Stern and Wissenberg[v]	0.44		0.036	
This study	0	1.4–2.2		
This study	1.8 μg cm^{-2}			0.0005–0.0022

the surface concentration of Pd increases, so does the cathode/anode area ratio. The electrochemical behaviour of the composite electrode is determined by the intersection of the polarization curves for hydrogen evolution on the cathodic Pd sites and dissolution of Ti on the anodic sites.

The observed mixed potential of −0.35 V resides in the passivation region of Ti, resulting in a markedly reduced dissolution rate. This mechanism was first proposed for noble metal alloying of bulk titanium by Stern and Wissenberg.[6]

According to the Rutherford backscattering analyses, the concentration of Pd at the surface is increased to ca. 20% by the initial preferential dissolution of Ti. A measurement by X-ray photo-electron spectroscopy (XPS) on a sample after a 5 h immersion showed about equal amounts of Pd and Ti on the surface, implying a Pd surface coverage of 50%. In addition, it was determined that the Ti was in the form of an oxide with the oxygen being 3–4 times more abundant than Ti. There is good qualitative agreement between the two measurements of surface coverage of Pd. Quantitative agreement is precluded by uncertainties involved in each measurement technique. For example, computer simulations of RBS energy spectra show that with a 4 nm depth resolution, a 5 nm thick 20% Pd coverage cannot be distinguished from a 0.5 nm thick 50% coverage overlying a 4.5 nm thick 16.7% coverage.

A further complication in measuring the anode/cathode area ratio arises from the different effective surface areas of the implanted versus unimplanted samples. Figure 9 shows optical photographs and micrographs taken with the scanning electron microscope (SEM). The optical photographs (top) were exposed by scattered light from the sample surface, resulting in dark images for the mirror finish surfaces (implanted samples before and after corrosion). The bright image from the unimplanted, corroded sample (middle) shows that the surface is very rough because of the large amount of diffuse scattering. The surfaces are shown in more detail by their corresponding SEM micrographs (bottom). The two implanted samples are smooth and featureless, while the unimplanted sample surface is very granular and pitted. The effective surface area of the unimplanted sample is somewhat larger than for the implanted, smooth surfaces. A reasonable estimate is that the surface roughness is two or three times that of the implanted sample.

Corrosion of titanium in boiling I molar H_2SO_4

As implanted (10^{16} Pd/cm^2)

Unimplanted
8 minute corrosion

Implanted (10^{16} Pd/cm^2)
48 minute corrosion

R-059
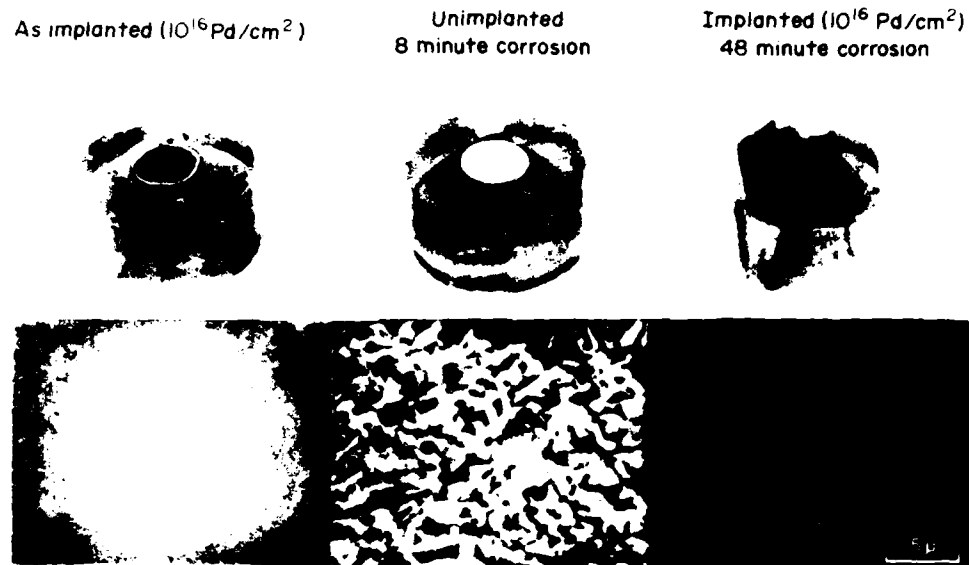
FIG. 9. Photographs of epoxy mounted Ti samples (top) and their corresponding SEM micrographs (bottom). All samples were initially polished to a mirror finish. The photographs detected mostly diffusely scattered light and indicate that the centre sample has a very rough surface.

134

Figure 10 shows the cathodic polarization curve for hydrogen evolution on bulk palladium and portions of the anodic polarization curve for bulk titanium. These curves are computed on the basis of equal areas of Pd and Ti, and show the total current which would be realized for the two electrochemical processes occurring on an implanted sample having a 50% Pd enrichment. Allowing a surface roughness factor of 2-3 for the anodic Ti curve, the two curves intersect at an electrode potential of -0.42 to -0.46 V, and a corrosion current density of $2.3–6.0$ μA cm^{-2}. These values are not too different from the corrosion potential (-0.26 to -0.35 V) and corrosion rates ($2–6$ μA cm^{-2}) of the implanted sample. Thus, the electrochemical behaviour of the implanted sample can be reasonably interpreted by the mixed potential corrosion theory.

No evidence of intermetallic surface compounds of Ti and Pd was found upon examination of the implanted surface using glancing angle electron diffraction.
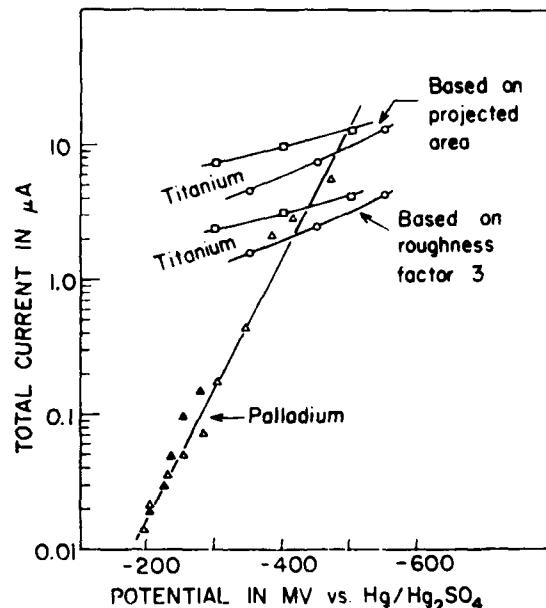
FIG. 10. The cathodic polarization curve for hydrogen evolution on Pd and portions of the anodic polarization curve for Ti in boiling 1M H$_2$SO$_4$. Both curves are calculated on the basis of equal electrode areas of Pd and Ti. (Duplicate experimental runs are shown for each curve.)

CONCLUSIONS

The active dissolution of titanium in boiling 1M H$_2$SO$_4$ is reduced by there orders of magnitude when implanted with 1.8 μg cm^{-2} of Pd in a thin surface layer, and the corrosion protection lasts for at least 9 h. The mechanism of corrosion protection is explained by the fact that Pd residing on the surface creates a highly local galvanic couple whose corrosion potential is between that of pure Pd and pure Ti, and is more noble than the critical potential for passivity of Ti. This corroborates the mechanism proposed by other workers of Ti–Pd alloy systems.

A method of determining absolute corrosion rates by measuring energy shifts of an implanted Xe 'marker' in RBS maesurements gave results in good agreement with electrochemical methods.

Both RBS and potential vs time measurements show that initially the Pd is buried beneath the surface, and preferential dissolution of Ti redistributes Pd until a high surface concentration is obtained ($\gtrsim 20\%$). The approximately equal areas of anode and cathode material are then responsible for the noble value of the corrosion potential of implanted samples.

REFERENCES

1. V. ASHWORTH, W. A GRANT and R. P. M. PROCTOR, *Corros. Sci.* **16**, 661 (1976).
2. V. ASHWORTH, D. BAXTER, W. A. GRANT and R. P. M. PROCTER, *Corros. Sci.* **16**, 775 (1976).
3. V. ASHWORTH, D. BAXTER, W. A. GRANT and R. P. M. PROCTER, *Corros. Sci.* **17**, 947 (1977).
4. B. S. COVINO, JR., B. D. SARTWELL and P. B. NEEDHAM, JR., *J. electrochem. Soc.* **125**, 366 (1978).
5. B. S. COVINO, JR., P. B. NEEDHAM, JR. and G. R. CONNER, *J. electrochem. Soc.* **125**, 370 (1978).
6. M. STERN and H. WISSENBERG, *J. electrochem. Soc.* **106**, 759 (1959).
7. N. D. TOMASHOV, R. M. ALTOVSKY and G. P. CHERNOVA, *J. electrochem. Soc.* **108**, 113 (1961).
8. G. K. HUBLER and E. MCCAFFERTY, *Reports of NRL Progress*, May (1978) p. 28.
9. E. MCCAFFERTY and G. K. HUBLER, *J. electrochem. Soc.* **125**, 1892 (1978).
10. L. E. SAMUELS, *Metallographic Polishing by Mechanical Methods*, p. 122, Pitman Press, London (1967).
11. G. K. HUBLER, J. COMAS and L. PLEW, *Nucl. Instrum. Meth.* **149**, 635 (1978).
12. E. B. SANDELL, *Colorimetric Determination of Traces of Metals*, p. 868, Interscience, New York (1959).
13. R. L. EVERY and W. P. BANKS, *Electrochem. Technol.* **4**, 275 (1966).
14. E. J. KELLEY, *Proceedings of the Fifth International Congress on Metallic Corrosion*, Tokyo, 1972, p. 137, National Association of Corrosion Engineers, Houston (1974).
15. M. POURBAIX, *Atlas of Electrochemical Equilibria*, p. 360, Pergamon Press, Oxford (1966).
16. V. ASHWORTH, W. A. GRANT, R. P. M. PROCTER and T. C. WELLINGTON, *Corros. Sci.* **16**, 393 (1976).
17. J. B. COTTON, *Platin. Metals Rev.* **11**, 50 (1967).
18. M. STERN and C. R. BISHOP, *Trans. A.S.M.* **52**, 239 (1960).

Section III.C

EFFECT OF HELIUM, IRON, AND PLATINIUM IMPLANTATION
ON THE ABSORPTION OF HYDROGEN BY IRON

M. Zamanzadeh[1], A. Allam[1], H. W. Pickering[1] and G. K. Hubler[2]

[1]Department of Materials Science and Engineering
The Pennsylvania State University
University Park, Pennsylvania 16802

[2]Materials Modification and Analysis Branch
Condensed Matter and Radiation Technology Division
Naval Research Laboratory

Effect of Helium, Iron, and Platinum Implantation on the Absorption of Hydrogen by Iron

M. Zamanzadeh, A. Allam, and H. W. Pickering*

Metallurgy Section, Department of Materials Science and Engineering, The Pennsylvania State University, University Park, Pennsylvania 16802

and G. K. Hubler

Naval Research Laboratory, Washington, D. C. 20375

ABSTRACT

A preliminary study was made of the effect of certain elements implanted in iron on the absorption of hydrogen by Ferrovac-E iron. Using the permeation technique, it was found that the location of implanted Pt, as modified by selective dissolution of iron from the surface, affects the kinetics of the hydrogen evolution reaction and, hence, of the hydrogen absorption process. The rate of hydrogen absorption decreased with increase in Pt concentration on the surface in both $0.1N$ NaOH and $0.1N$ H_2SO_4. A catalytic mechanism is proposed to explain the marked reduction in hydrogen permeation. There are no significant differences in the permeation behavior of unimplanted and helium- or iron-implanted iron membranes in $0.1N$ NaOH. The experimentally observed Tafel slope, the permeation-(charging) potential relationship, and the permeation-(charging) current relationship indicate a coupled discharge-recombination mechanism of hydrogen evolution on He-, Fe-, or Pt-implanted iron. At higher cathodic overpotentials in $0.1N$ NaOH, corresponding to potentials more -negative than $-1.0V$ (SHE), another mechanism of hydrogen evolution is indicated. Selective dissolution of iron from the Pt-implanted Fe surface layer may involve some platinum and iron interdiffusion according to Rutherford backscattering analyses.

Hydrogen absorption greatly reduces the mechanical properties of structural alloys. A number of investigators have studied the possibility of reducing hydrogen absorption by coatings (1-4). Besides functioning as barriers to hydrogen entry, coatings may also reduce hydrogen absorption through their effect on the kinetics of the hydrogen evolution reaction and, hence, of the hydrogen absorption process. Chatterjee et al. (4) provided experimental evidence for the catalytic mechanism of decreasing hydrogen entry into iron. They found that discontinuous electrodeposited coatings of Pt, Ni, or Cu on iron are effective in reducing hydrogen entry into the membrane. The ion implantation technique is another method for altering the surface chemically and, thus, the mechanism and kinetics of the hydrogen evolution reaction, without affecting bulk physical or mechanical properties.

Ashworth and co-workers (5) were among the first to report the effect of implantation on the polarization behavior of iron. They found that there are no significant differences between the polarization behavior of unimplanted and argon-implanted iron beyond that due to changes in surface roughness associated with the implantation process. Other implanted elements in iron, such as chromium and lead, were shown to influence the polarization behavior (6, 7).

This paper reports the results of initial studies directed at evaluating the effect of implantation on hydrogen permeation. No other studies of hydrogen permeation of implanted membranes are known to be reported in the literature. Specifically, the results provide insight on:

1. Whether, and to what extent, implanted platinum, helium, or iron reduce hydrogen permeation through iron.

2. The effect of the nature and proximity to the surface of the implanted species on the mechanism and kinetics of the hydrogen evolution reaction and, hence, of the hydrogen absorption process.

3. The effect of implantation on (effective) hydrogen diffusivity which may be related to trapping characteristics.

The rationale behind choosing Pt for implantation is that Pt is one of the best electrocatalysts for the hydrogen evolution reaction. In order to sort out any effects due to the implantation process, itself, the inert element, He, and the substrate element, Fe, were also chosen for comparison.

Experimental Procedure

The hydrogen permeation measurements were carried out on Ferrovac-E iron. The Fe membranes were prepared by cold-rolling wafers cut from a master ingot to the required thickness (0.365 mm). After polishing to 600 grit, they were degreased using benzene and methanol in a soxhlet apparatus, and then annealed for 2 hr at $1273°K$ ($1000°C$) in an argon-filled silica capsule. The latter treatment produced an etched surface. One side of some of these membranes was exposed to beams of Fe^+, He^+, or Pt^+ ions at fluences and energies given in Table I. The samples were implanted in a vacuum of 10^{-4} Pa (10^{-6} Torr) and were in close proximity to a cold surface at liquid nitrogen temperatures ($77°K$) which minimized carbon contamination. The temperature of the samples during implantation did not exceed $323°K$. The implanted samples were stored in an evacuated desiccator. Prior to the permeation runs, the Pt content on the surface of the Pt-implanted membranes was increased by selective dissolution of iron via immersion in 1M H_2SO_4 for 20 sec. This amount of etching produced no change in surface morphology observable by light or

Table I. Energies and fluences of implanted ions in iron membranes

Ion	Energy, keV	Fluence, ions/cm²
Fe	150	1×10^{17}
Pt	100	1.5×10^{16}
He	25	1.6×10^{17}

1688

scanning electron microscopy. Permeation measurements were also made after subsequent 10 sec immersions in 0.1N H_2SO_4. Sulfuric acid is known to selectively remove iron from a Fe-Pt solid solution (8).

Electrolyte solutions were prepared from conductivity water (doubly distilled) prepared by the method of Powers (9) and reagent grade chemicals. Final purification was made by pre-electrolyzing the solutions in an external cell prior to admitting them to the permeation cell.

The technique of Devanathan and Stachurski (10) was used to measure the permeability of hydrogen through a membrane while evolving hydrogen off the implanted surface. In this method, a thin metallic membrane is electrolytically charged with hydrogen on the implanted side, while on the other exit side the hydrogen, which has diffused through the membrane, is anodically oxidized. The orifice of the cell and, thus, the charging area was 0.785 cm². The measured anodic current is a direct measure of the hydrogen flux through the membrane for conditions at the exit surface, which included a thin palladium coating and an oxidizing potential of 0.018V (SHE). These are the same conditions found previously to be suitable for oxidizing all of the hydrogen arriving at the anodically polarized surface (4). The reported values are the measured values after correction for the residual current which is typically less than 1 μA cm⁻². The potential of the charging surface was measured using an Hg/Hg_2SO_4 reference electrode in 0.1N H_2SO_4 and an Hg/HgO reference electrode in 0.1N NaOH, and that of the exit surface using an Hg/HgO reference electrode in 0.1N NaOH. Both chambers of the cell were deaerated by bubbling oxygen-free nitrogen through the solutions. The permeation measurements were performed under conditions of cathodic protection. Details of the cell and circuitry are reported elsewhere (4).

The permeation data were obtained as follows. The Fe- and He-implanted iron membranes were precharged at $i_c = 0.10$ mA cm⁻² for 45 min by which time a quasi-stationary permeation current was established. The Pt-implanted membranes were similarly precharged at 1 mA cm⁻² (~15 min in 0.1N NaOH and ~7 min in 0.1N H_2SO_4). The membranes were then charged galvanostatically in 0.02 mA cm⁻² steps in 0.1N NaOH or in 0.2 mA cm⁻² steps in 0.1N H_2SO_4 in descending and then ascending directions. Each charging current was maintained for about 4 min by which time a quasi-stationary permeation current was established. This procedure has been found to give constant and reproducible permeation transients dependent only on the charging conditions for a given specimen.

Some of the concentration profiles after implantation were measured by means of high resolution Rutherford backscattering of alpha particles with a depth resolution of 4 nm. For this measurement, the surface to be implanted was first polished to a mirror finish with 6 μm diamond paste. Details of this method may be found elsewhere (11, 12).


Fig. 1. Hydrogen permeation transients for an He-implanted Fe membrane and for a Pt-implanted Fe membrane after a 20 sec dissolution in 1M H_2SO_4. $i_c = 0.1$ mA cm⁻² in 0.1N NaOH.

Results

Table II shows that the steady-state hydrogen permeation fluxes, i_e, and electrode potentials at the charging side, E, in 0.1N NaOH are the same for unimplanted Fe membranes and identical membranes implanted with He or Fe. These values and the transients themselves are also typical for these samples after various periods of immersion in sulfuric acid.

The permeation transients prior to steady state were also the same within the experimental error for these membranes; the half-rise time ($t_{1/2}$) was 5.5 ± 1.0 sec. Typical permeation transients are shown in Fig. 1. The effective diffusivity, calculated using the expression (13, 14)

$$D = \frac{0.138 \, L^2}{t_{1/2}}$$

where L is the membrane thickness, is $D = 3 \times 10^{-5}$ cm² sec⁻¹. This value is in good agreement with literature values for well-annealed iron (15) and is also essentially the value obtained by extrapolation of high temperature diffusion data to room temperature (16). The experimentally observed Tafel slope is −122 ± 5 mV (Fig. 4). This value is the same as that re-

Table II. Variation of the steady-state hydrogen permeation flux and of the electrode potential at the charging side with the charging current density for an unimplanted Fe membrane and for an identical membrane implanted with He or Fe. Charging solution was 0.1N NaOH

| Charging current density, mA/cm²	Steady-state permeation rate and electrode potential of the charging side					
	Unimplanted Iron		He-implanted Iron		Fe-implanted Iron	
	i_e, μA/cm²	$-E_c$, V(SHE)	i_e, μA/cm²	$-E_c$, V(SHE)	i_e, μA/cm²	$-E_c$, V(SHE)
0.1	1.77	1.005	1.78	1.005	1.65	1.00
0.08	1.50	0.990	1.44	0.989	1.45	0.990
0.06	1.32	0.975	1.27	0.974	1.27	0.975
0.04	1.02	0.960	1.02	0.960	1.01	0.950
0.02	0.70	0.910	0.74	0.910	0.67	0.910

Fig. 2. **Rutherford backscattering** profiles of implanted Pt in Fe as a function of time of immersion of the implanted sample in 1M H₂SO₄ at room temperature. Depth of resolution is 4 nm (40Å).

ported for hydrogen evolution on Fe in 0.1N NaOH (17).

Figure 2 shows distribution profiles of Pt implanted in Fe after different amounts of dissolution in 1M H_2SO_4 at room temperature. After 20 sec immersion in the acid, the peak concentration of Pt is closer to the surface and the area under the curve is essentially unchanged, indicating that only iron is dissolved during this initial dissolution period; and the tail of the profile extends further into the alloy as measured from either the peak or the original surface position (not shown), suggesting Pt diffused into the alloy (during and/or following dissolution) to a distance roughly equal to the distance the surface has receded.[1] The (average) Pt concentration within a surface region of about 4 nm thickness as measured by Rutherford backscattering is *significantly higher* (~3% by weight) than in the as-implanted case (≲0.1%).

Profiles obtained after a second 20 sec dissolution period in 1M H_2SO_4 show that the Pt content is much less and nearly at background levels (Fig. 2), which indicates that most of the Pt is lost from the mem-

[1] This follows since the profile width is about the same before and after the initial 20 sec immersion. An estimate is 10 nm after 2v sec based on published corrosion rates (>10⁻³ A cm⁻² at 298°K) of steel in sulfuric acid (18).

brane during this second dissolution process. Permeation measurements were mainly done, therefore, after an initial 20 sec exposure of the Pt-implanted membranes to 1M H_2SO_4.

Figure 3 shows a linear dependence of the steady-state permeation current density on the square root of the charging current density with the curve passing through the origin for an unimplanted Fe membrane and for a Pt-implanted Fe membrane following a 20 sec immersion in 1M H_2SO_4. This is taken as an indication of a diffusion-controlled hydrogen permeation process (17, 19). The permeation transient for the latter membrane is shown in Fig. 1. The hydrogen permeability is less at all charging currents for the Pt-implanted, than for the unimplanted, iron membranes. Pt profiles which were not modified by selective iron dissolution were found to have an insignificant effect on the hydrogen evolution and permeation kinetics.

The electrode potentials for hydrogen evolution on the Pt-implanted membrane (after immersion in acid) are invariably more noble than those on the unimplanted membrane, Fig. 4. The Tafel slope is −122 ± 5 mV for both unimplanted and Pt-implanted iron. The relations between permeation and the electrode potential of the charging surface for unimplanted and Pt-implanted Fe membranes are given in Fig. 5 for the 0.1N NaOH charging solution. The slopes of the straight segments of the curves of both the unimplanted Fe and Pt-implanted Fe membranes are −255 ± 5 mV. About the same slope is also obtained in the 0.1N H_2SO_4 charging solution over a wide range of overpotential for both charging surfaces, Table III.

As with the Pt content of the surface (Fig. 2), both the measured electrode potential of the Pt-implanted surface and the permeation rate of hydrogen through the Pt-implanted membrane during hydrogen charging are functions of the pretreatment immersion time in, and concentration of, sulfuric acid. Figure 6 shows variations in potential and permeation as a function of additional 10 sec immersion periods (following the initial 20 sec immersion) in a diluted sulfuric acid. The trends of i_s decreasing and E increasing in a more oxidizing direction hold for an additional 40 sec immersion in 0.1N H_2SO_4. Then, a reversal of the electrochemical parameters occurs.

Discussion

The electrocatalytic activity of a surface for the hydrogen evolution reaction can be estimated from the overpotential required to evolve hydrogen at a given current density—the lower the overpotential or the more noble the electrode potential, the more catalytic the surface. Figure 4 and Table III show the electrode potentials measured in alkaline- and acid-charging solutions. It is seen that the electrode potential for the hydrogen evolution reaction is more noble on Pt-implanted than on unimplanted surfaces. It follows
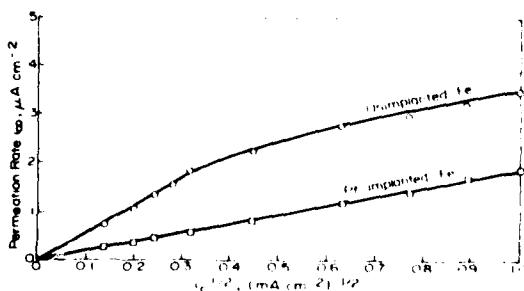

Fig. 3. Steady-state permeation rate i_s as a function of the square root of the charging current density i_c for an unimplanted Fe membrane and a Pt-implanted and acid-treated Fe membrane. Charging solution was 0.1N NaOH.
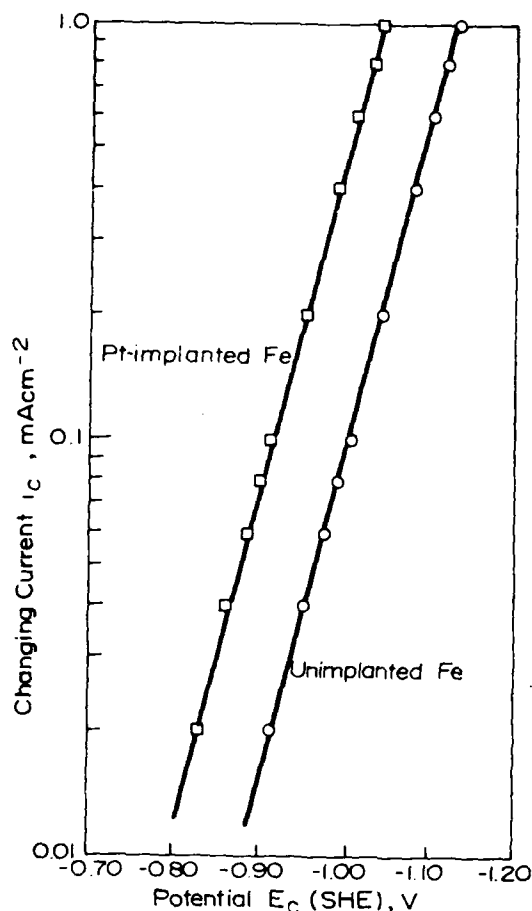
Fig. 4. The polarization curve in the Tafel region for hydrogen evolution in 0.1N NaOH on an unimplanted iron (○) and a Pt-implanted Fe membrane following a 20 sec immersion in 1M H₂SO₄ (□).


Fig. 5. Steady-state permeation rate $i_∞$ as a function of the potential of the charging surface of the membrane, E_c. Charging solution was 0.1N NaOH.

Rutherford backscattering (Fig. 2). A correspondence of the electrochemical and the backscattering data also holds at longer pretreatment immersion times when a reversal in the trends of E_c and $i_∞$ corresponds to a loss of Pt from the surface. Thus, it would seem

that the degree of hydrogen coverage, θ, and the permeability of hydrogen should be less for Pt-implanted, than for unimplanted, iron membranes (20, 13, 4) in accord with the permeation results in Fig. 3 and 5.

The above reasoning also explains the decrease of the steady-state permeation and the more positive electrode potential with increasing pretreatment immersion time (Fig. 6), i.e., acid attack initially increases the Pt content of the surface as was shown by

Table III. Variation of the steady-state hydrogen permeation flux and of the electrode potential of the charging side with the charging current density for an unimplanted Fe membrane and for a Pt-implanted Fe membrane. Charging solution was 0.1N H₂SO₄

| Charging current density, mA/cm²	Steady-state permeation rate and electrode potential of the charging side			
	Unimplanted iron		Pt-implanted iron	
	$i_∞$, μA/cm²	$-E_c$, V(SHE)	$i_∞$, μA/cm²	$-E_c$, V(SHE)
1.0	22.0	0.425	16.2	0.407
0.8	20.0	0.415	14.5	0.395
0.6	17.5	0.400	12.5	0.380
0.4	14.2	0.380	10.5	0.360
0.2	10.2	0.345	7.5	0.325
0.1	7.2	0.310	5.5	0.290

Fig. 6. Steady-state permeation rate (□) and charging potential (○) as a function of additional immersion periods in 0.1N H₂SO₄ beyond the initial 20 sec immersion in 1M H₂SO₄ of the Pt-implanted surface. Charging current was 0.6 mA cm⁻² in 0.1N H₂SO₄.

141

that as the surface recedes and overtakes the Pt profile, the Pt concentration on the surface reaches a level for which accumulation of Pt into particles, followed by detachment, occurs. Such is known to happen when an alloy contains low percentages ($\lesssim 1\%$) of a noble metal in solid solution (21), and is in accord with industrial experience, especially during electrolytic refining of copper containing small amounts of gold. The reversal in the trends of E_c and i_a occurs at shorter immersion times for higher concentrations of sulfuric acid (Fig. 2 vs. Fig. 6). This is in accord with a faster rate of attack in the more concentrated acid, and thus a faster rate of recession of the surface. That continued dissolution of the membrane eventually leads to Pt loss from the surface (Fig. 2) is supported by the approach after long times of the i_a and E_c values to those for unimplanted Fe membranes.

In summary, the mechanism by which implanted Pt reduces hydrogen absorption by iron is related to the different catalytic tendencies of Pt and Fe for the hydrogen evolution reaction. In this case, the hydrogen evolution reaction occurs more readily (lower overvoltage required) on Pt than on Fe (sites); thus, the coverage of hydrogen on the composite Pt-Fe surface is lower and, consequently, so also is the absorption rate. Thus, these results indicate that for implantation in iron to be effective for reducing hydrogen absorption, implants should have a higher exchange current density for hydrogen evolution than that for the substrate metal. The data also show for Pt implants that modifications of the implantation profile, which increase the concentration of the implant in the outermost surface layer, increase evolution and decrease absorption of hydrogen.

The Rutherford backscattering data here and elsewhere (11) give some indication that a limited amount of interdiffusion of the alloy components occurs during (and/or after) selective dissolution (of the iron). While this has yet to be shown to be the actual explanation of the backscattering profiles obtained before and after the initial (20 sec) dissolution period (Fig. 2), the explanation itself is reasonable for certain conditions of anodic dissolution which generate vacancies as analyzed elsewhere (21-25).

The data in Table II for He- and Fe-implanted iron show that there are no significant differences in the polarization or permeation behavior between unimplanted and He- or Fe-implanted iron. Furthermore, the Tafel slopes are also the same. Thus, the implantation process, itself, does not modify the mechanism of, or the catalytic character of the surface for, the hydrogen evolution reaction. Ashworth *et al.* (5), also found that once the air-formed oxide is removed, the polarization behavior of unimplanted and argon-implanted iron is nearly the same. A delay in the permeation-kinetics, on the other hand, might have been expected for the implanted membrane since the implantation process, itself, introduces defects to about the depth of the profile. In recent ion beam studies of deuterium-implanted iron Myers *et al.* (26) found that the activation energy of a deuterium trap produced by the implantation process is 0.81 eV, that slow release from the traps occurs between 300° and 400°K, and that either implanted deuterium or iron creates the traps. The presence of effective hydrogen traps can, in principle, be indicated by a comparison of the permeation rise times for unimplanted and implanted membranes. That the half-rise times in the present measurements were the same within the experimental error may be attributed to (i) modifications of the nature or density of the traps during the long (~ 9 month) delay between the implantation process and the permeation measurements, (ii) filling of the traps with hydrogen from other sources during the above-mentioned delay, and/or (iii) a lack of sensitivity in the measurement. Experiments are currently underway in an attempt to resolve this issue.

Some of the data obtained in this work are of the type normally used for evaluation of the mechanism of the hydrogen evolution reaction. It has been shown elsewhere (13, 19, 20) that if hydrogen evolution occurs via a coupled discharge-recombination mechanism, as is the case for iron, the following relations are obtained at low hydrogen coverages, Θ, for rate-controlling diffusion through the membrane

$$i_a \, \alpha \, i_c^{1/2} \qquad [1]$$

$$\frac{\partial \eta}{\partial \ln i_c} = -\frac{2RT}{F} = -120 \, \text{mV} \qquad [2]$$

$$\frac{\partial \eta}{\partial \ln i_a} = \frac{\partial \eta}{\partial \ln \Theta} = -\frac{4RT}{F} = -240 \, \text{mV} \qquad [3]$$

where η is the overpotential for hydrogen evolution, F the Faraday, R the gas constant, and T the temperature. In this investigation it was found that the steady-state permeation current is directly proportional to the square root of the charging current density (Fig. 3 and Table II) for Fe-implanted, He-implanted, and unimplanted iron membranes in accord with Eq. [1]. Furthermore, the Tafel slope (Fig. 4) is -122 ± 5 mV and $\partial \eta / \partial \ln i_a = -255 \pm 5$ mV (Fig. 5) in reasonably good agreement with Eq. [2] and [3], respectively. At higher cathodic overpotentials in 0.1N NaOH, corresponding to potentials more negative than -1.0V (SHE), there appears to be a change in the mechanism of hydrogen evolution for the unimplanted and Fe- and He-implanted membranes to slow discharge-fast electrochemical desorption, as indicated by an increase in $\partial \eta / \partial \ln i_a$, Fig. 5 (17, 20).

For Pt-implanted Fe, as modified by the 20 sec immersion the Tafel slope is -122 ± 5 mV and $\partial \eta / \partial \ln i_a = -255 \pm 5$ mV, and the steady-state permeation varies linearly through the origin with the square root of the charging current density. Thus, it is concluded that the mechanism of hydrogen evolution for Pt-implanted Fe is also coupled discharge-chemical desorption in both the 0.1N NaOH and 0.1N H_2SO_4 solutions within the overpotential range studied. The Tafel slope reported in the literature for hydrogen evolution on Pt surfaces is in two different ranges, either -110 to -130 mV in NaOH solutions (27-30) or about -30 mV in H_2SO_4 solutions (29) for ultra-clean systems. Tafel slopes greater than -30 mV in H_2SO_4 have, however, been observed in the presence of impurities (31).

Conclusions

Implantation by the ion beam technique can be used to reduce hydrogen entry into iron. This was shown using the (model) system of Pt implanted into Fe. Pt is known to greatly reduce hydrogen entry into iron via a catalytic effect of the hydrogen evolution reaction when the Pt is present on the surface (4). The effectiveness of implanted Pt was greatly increased by controlled selective dissolution of iron which increased the surface concentration of Pt. There are no significant differences in the permeation behavior of unimplanted and He- or Fe-implanted Fe specimens.

The experimentally observed Tafel slope, the permeation-charging potential relationship, and the permeation-charging current relationship indicate a coupled discharge-recombination mechanism of hydrogen evolution on Fe-, He-, or Pt-implanted Fe surfaces in 0.1N NaOH or 0.1N H_2SO_4 charging solutions.

REFERENCES

1. M. A. Figelman and A. V. Shreider, *J. Appl. Chem. (USSR)*, **31**, 1175 (1958).
2. T. Matsushima and H. H. Uhlig, *This Journal*, **113**, 555 (1966).
3. H. P. Tadrif and H. Marquis, *Can. Metall. Q.*, **1**, 153 (1962).
4. S. S. Chatterjee, B. G. Ateya, and H. W. Pickering, *Metall. Trans.*, **9A**, 389 (1978).
5. V. Ashworth, W. A. Grant, R. P. M. Procter, and T. C. Wellington, *Corros. Sci.*, **16**, 393 (1976).
6. V. Ashworth, D. Baxter, W. A. Grant, and R. P. M. Procter, *ibid.*, **16**, 775 (1976).
7. V. Ashworth, W. A. Grant, R. P. M. Procter, and E. J. Wright, *ibid.*, **18**, 681 (1978).
8. H. W. Pickering and P. J. Byrne, *This Journal*, **120**, 608 (1973).
9. R. W. Powers, *Electrochem. Technol.*, **2**, 163 (1969).
10. M. A. V. Devanathan and Z. Stachurski, *Proc. Roy. Soc. A*, **270**, 90 (1962).
11. G. K. Hubler and E. McCafferty, *Corros. Sci.*, To be published.
12. J. K. Hirronen and G. K. Hubler, "Ion Beam Surface Layer Analysis," Vol. 1, O. Meyer, G. Linker, and F. Käppeler, Editors, p. 457, Plenum, New York (1976).
13. J. McBreen, L. Nanis, and W. Beck, *This Journal*, **113**, 1218 (1966).
14. J. O'M. Bockris, in "Proceedings of International Conference on Stress Corrosion Cracking and Hydrogen Embrittlement of Iron Base Alloys,"

p. 286, Firminy, France, June 1973.
15. T. R. Radhakrishan and L. L. Shreir, *Electrochim. Acta*, **12**, 889 (1967).
16. O. D. Gonzalez, *Trans. Met. Soc. AIME*, **239**, 229 (1967).
17. J. O'M. Bockris, J. McBreen, and L. Nanis, *This Journal*, **112**, 1025 (1965).
18. W. Whitman, R. Russel, C. Welling, and J. Cochrane, *Ind. Eng. Chem.*, **15**, 672 (1923).
19. J. McBreen and M. A. Genshaw, in "Proceedings of the International Conference on Fundamental Aspects of Stress Corrosion Cracking," R. W. Staehle, A. J. Forty, and D. van Rooyan, Editors, p. 51, NACE (1969).
20. M. A. V. Devanathan and Z. Stachurski, *This Journal*, **111**, 619 (1964).
21. H. W. Pickering, *ibid.*, **117**, 8 (1970).
22. H. W. Pickering and C. Wagner, *This Journal*, **114**, 698 (1967).
23. H. W. Pickering, *ibid.*, **115**, 143 (1968).
24. J. E. Holliday and H. W. Pickering, *ibid.*, **120**, 470 (1973).
25. H. W. Pickering, "Darken Conference: Physical Chemistry in Metallurgy," R. M. Fisher, R. A. Oriani, and E. T. Turkdogan, Editors, pp. 353–373, U.S. Steel Corporation, Pittsburgh, Pa. (1976).
26. S. M. Myers, S. T. Picraux, and R. E. Stoltz, *J. Appl. Phys.*, To be published.
27. S. Schuldiner, *This Journal*, **107**, 426 (1954).
28. I. A. Ammar and S. Darwich, *J. Phys. Chem.*, **63**, 983 (1959)
29. J. O'M. Bockris and S. Srinivasan, *Electrochim. Acta*, **9**, 31 (1964).
30. C. M. Shepherd and S. Schuldiner, *This Journal*, **115**, 1124 (1968).
31. J. O'M. Bockris, I. A. Ammar, and A. K. M. S. Huq, *J. Phys. Chem.*, **61**, 879 (1957).

Section III.D

CORROSION RESISTANT AISI 52100 BEARING SURFACES BY IMPLANTATION

G. K. Hubler,[1] J. K. Hirvonen,[1] C. R. Clayton,[2]

Y. F. Wang,[2] J. Budnick,[3] and H. Hayden[3]

[1]Materials Modification and Analysis Branch
Condensed Matter and Radiation Technology Division
Naval Research Laboratory

[2]Department of Materials Science and Engineering
State University of New York
Stony Brook, New York 11794

[3]Physics Department
University of Connecticut
Storrs, Connecticut 06268

145

Corrosion Resistant AISI-52100
Bearing Surfaces by Ion Implantation

J. K. Hirvonen and G. K. Hubler
Naval Research Laboratory
Washington, DC 20375

K. W. Chan and C. R. Clayton
State University of New York at Stony Brook
Stony Brook, NY 11794

INTRODUCTION

AISI 52100 alloy is one of the most widely used bearing alloys in Navy systems. It is a through-hardened martensitic steel possessing high hardness and good wear resistance. Its elemental composition is given below.

52100 Tool Steel Composition (% by Wt)

C	0.96
Mn	0.36
Si	0.22
P	0.01
S	.012
Cr	1.36
Fe	remainder

There is a widespread bearing corrosion problem in Navy aircraft propulsion systems. It is found in all engines, independent of the bearing alloy used, and is common to engines in intermittent service and various types of storage. The rejection rate of used bearings is 30%-50% and is a major reason for rejection at the NARF's. The corrosion is typified by localized pitting along the contact region between the rollers and races. The corrosion pits may act as initiation sites for fatigue spalling which can lead to catastrophic engine failure. Another serious field problem is that replacement bearings have a short shelf life and must be reworked every 90 days, such that a majority of the bearings reconditioned at Naval Air Rework Facilities (NARF's) are recycled bearings from the shelf, not bearings to be reworked from used aircraft engines.

Preliminary 6.1 work at NRL showed that the corrosion resistance of 52100 could be significantly improved by the implantation of Cr. The following describes the NAVAIR funded program for the development of anticorrosion ion implantation treatments for 52100 bearing surfaces.

SAMPLE PREPARATION, IMPLANTATION TREATMENTS, AND CORROSION TESTS

Numerous corrosion tests were deemed necessary to ascertain if changes in corrosion resistance occured as a result of ion implantation. To conduct these tests in actual bearings would have been expensive and time consuming. Therefore, small samples were prepared from 3/8" diameter AISI 52100 rods so that electrochemical

polarization tests could be conducted on surfaces of about 1 cm^2 in area. Flats (1/8" to 1/4" tall) were cut from the rod by means of a water cooled SiC cut-off wheel and polished to a mirror finish with diamond paste (1 μm). Alumina polishing was initially used but was replaced with the diamond polish because numerous alumina inclusions remained in the polished surfaces.

Implantation Conditions

Ion	Fluence (x10^{17}/cm^2)	Energy (KeV)
Cr	2.0	150
Cr+	2.0	150
Mo	0.35	100
Cr+	2.0	150
P	0.5	40
Ta	1.0	150
Mo	0.5	100

The choice of implanted ions was determined by the well known corrosion behavior of the ions in bulk materials, viz., (i) Chromium produces stainless steel when added to iron based alloys in concentrations greater than 12%, (ii) Mo is known to improve pitting resistance in steels, (iii) Ta forms stable corrosion resistant oxides, and (iv) P and Ta stabalize an amorphous phase when alloyed with iron.

It has been well established that measurements of the pitting potential by electrochemical polarization in chlorine-contaminated solutions gives a measure of the pitting resistance of an alloy. Before presenting polarization curves, a brief review of the physical processes occuring at a corroding surface is given using the oversimplified schematic in Figure 1.

Corrosion consists of metal being consumed either by dissolution or by oxidation at the metal surface. The metal dissolves as a cation at an anodic site and charge neutrality is maintained by the reduction of hydrogen at a cathodic site on the metal surface where hydrogen gas is evolved. Almost all corrosion problems encountered in practice involve this reaction. This picture immediately suggests that we can prevent corrosion by inhibiting either the anodic or cathodic process. For example, cathodic protection consists of placing the metal at about -1 Volt with respect to ground so that electrons are furnished to the metal surface from an external circuit, instead of from dissolving metal ions. In addition, implantation of an elemental species (such as Pb) which poisons the cathodic reaction has been shown to greatly reduce the corrosion rate of iron.

More commonly, corrosion resistance is the result of the anodic process being inhibited by the formation of an insoluble oxide film on the surface which inhibits metal cation transport, electronic charge transport, or both through the passive film. As long as the oxide film is stable in the solution, the surface is said to be passivated. Chlorine

aqueous environment
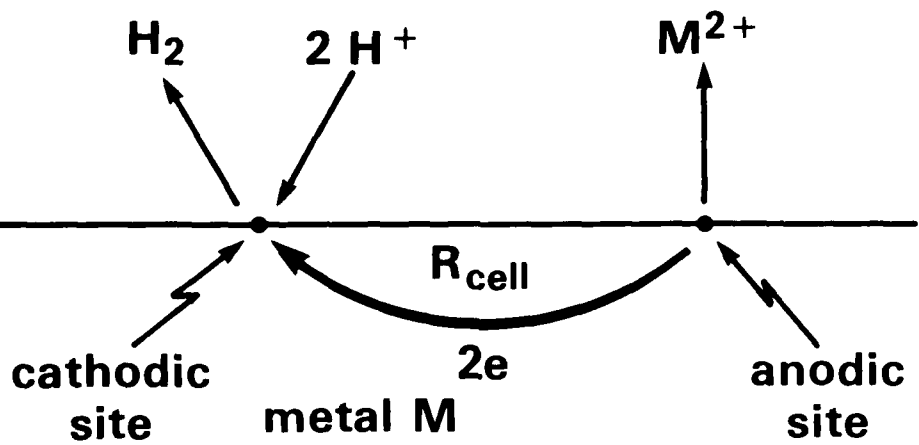
Figure 1
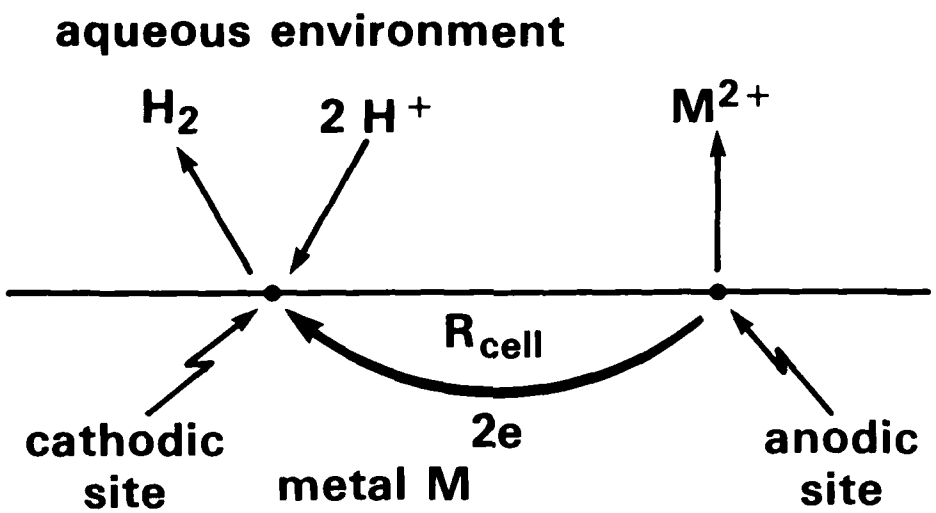
Figure 1

polarization tests could be conducted on surfaces of about 1 cm^2 in area. Flats (1/8" to 1/4" tall) were cut from the rod by means of a water cooled SiC cut-off wheel and polished to a mirror finish with diamond paste (1 μm). Alumina polishing was initially used but was replaced with the diamond polish because numerous alumina inclusions remained in the polished surfaces.

Implantation Conditions

Ion	Fluence (x10^{17}/cm^2)	Energy (KeV)
Cr	2.0	150
Cr+	2.0	150
Mo	0.35	100
Cr+	2.0	150
P	0.5	40
Ta	1.0	150
Mo	0.5	100

The choice of implanted ions was determined by the well known corrosion behavior of the ions in bulk materials, viz., (i) Chromium produces stainless steel when added to iron based alloys in concentrations greater than 12%, (ii) Mo is known to improve pitting resistance in steels, (iii) Ta forms stable corrosion resistant oxides, and (iv) P and Ta stabalize an amorphous phase when alloyed with iron.

It has been well established that measurements of the pitting potential by electrochemical polarization in chlorine-contaminated solutions gives a measure of the pitting resistance of an alloy. Before presenting polarization curves, a brief review of the physical processes occuring at a corroding surface is given using the oversimplified schematic in Figure 1.

Corrosion consists of metal being consumed either by dissolution or by oxidation at the metal surface. The metal dissolves as a cation at an anodic site and charge neutrality is maintained by the reduction of hydrogen at a cathodic site on the metal surface where hydrogen gas is evolved. Almost all corrosion problems encountered in practice involve this reaction. This picture immediately suggests that we can prevent corrosion by inhibiting either the anodic or cathodic process. For example, cathodic protection consists of placing the metal at about -1 Volt with respect to ground so that electrons are furnished to the metal surface from an external circuit, instead of from dissolving metal ions. In addition, implantation of an elemental species (such as Pb) which poisons the cathodic reaction has been shown to greatly reduce the corrosion rate of iron.

More commonly, corrosion resistance is the result of the anodic process being inhibited by the formation of an insoluble oxide film on the surface which inhibits metal cation transport, electronic charge transport, or both through the passive film. As long as the oxide film is stable in the solution, the surface is said to be passivated. Chlorine

147

ions in solution cause the passive film to breakdown locally forming deep pits at random points on the surface in a way which is poorly understood.

The polarization curve is an experimental means of isolating the anodic and cathodic processes occuring microscopically between groups of atoms on a corroding surface. Just as in cathodic protection, if a negative voltage is applied to the sample, the anodic processes are stopped because electrons are supplied by the external circuit and cathodic processes are examined in detail. Conversely, a positive voltage disables the cathodic processes as electrons are consumed by the external circuit and the anodic processes where metal ions go into solution proceed at their own rate.

One final point regarding Figure 1 is that the microstructure can play an important role in the corrosion process both in the bulk material and in the film that forms. Two phase alloys will set up galvanic couples between differing regions of elemental composition resulting in anodic dissolution of one of the phases. Carbides and grain boundaries are always very effective cathodes, and surface roughness can alter the activity of a surface by altering the number of chemically active sites. Also, if a surface is truly amorphous, it might be expected that with no phase boundaries or grain boundaries that the corrosion resistance would be very good.

The chloride ion tests presented here were in a pH6, 0.01 Molar NaCl, buffered solution. The buffer ensured that the pH was constant throughout the measurements. The salient points of these measurements are illustrated in the idealized curves in Figure 2. The solid line in the upper portion of the figure represents the potentiodynamic scan (1 mV/s) that is obtained with no Cl ions added to the solution. From open circuit voltage (i.e., the sample potential with respect to a standard electrode with no externally applied potential), the potential is scanned in the positive direction producing a constant but small current flow. In this region, the rate of metal dissolution is very low and the metal is said to be passivated. At higher potentials the sharp rise in current is caused by pitting or transpassive behavior, the latter not being important to this discussion. Adding chloride ions produces the dashed curve. The Cl ions locally attack the passive film producing pits where metal ions are actively dissolving and causing increased current flow. The breakdown potential E_b characterizes the metals' ability to withstand pitting attack. The bottom portion of the figure demonstrates the desired result of surface treatment (e.g., to drive the breakdown potential back toward more positive values). The difference in breakdown potentials for implanted versus unimplanted samples is a measurement of the pitting behavior of metals.

POTENTIODYNAMIC POLARIZATION MEASUREMENTS

The 52100 samples were mounted on an epoxy mount, and were potentiodynamically scanned in the anodic direction in a 0.01M buffered (pH = 6) NaCl solution. The scan rate used was 1 mV/sec. One set of ion implanted samples were potentiodynamically scanned following immersion, while another set was cathodically charged to remove the preexisting air-formed film. Ta and Cr+P implantations were carried out to promote amorphicity in the surface alloy and, therefore, to improve pitting resistance by removing surface imperfections such as grain boundaries. Cr+Mo was implanted together following successful results obtained with M50 bearing steel. In this case the synergistic behavior of Cr and Mo found in conventionally alloyed steels was being exploited.

149
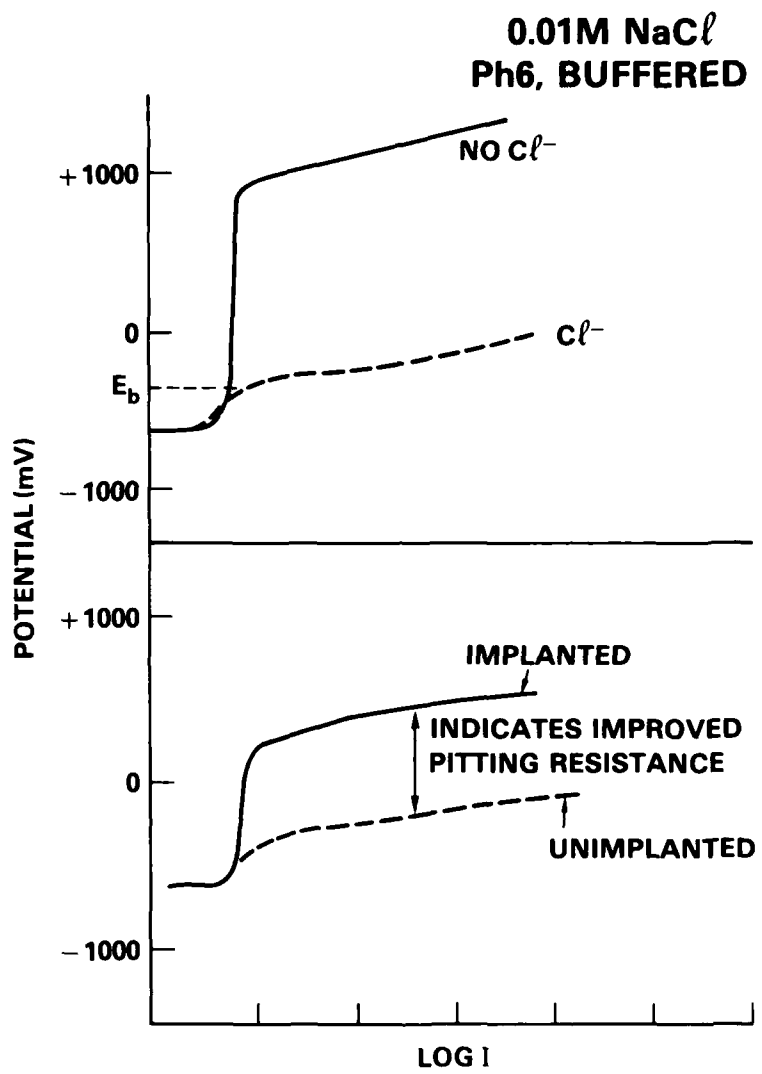
Fig. 2 — Idealized potentiodynamic polarization scans (current versus voltage characteristic) for a ferrous alloy in a buffered pH6 solution at room temperature. The upper set of curves demonstrate the effect of adding Cl⁻ ions to the solution. E_b defines the pitting potential where a sharp increase in current results when pits form on the surface. The lower set of curves demonstrate the desired result of ion implantation, i.e., force the pitting potential toward higher values.

Table 1 summarizes the pitting data of the ion implanted 52100 steel. Figs. 3 and 4 show the actual potential versus Log Current Density plots for the samples analyzed. The rank order of resistance to pitting for the implantation treatments are as follows:

WITH CATHODIC TREATMENT   52100 < Mo < Cr < Cr+Mo < Cr+P < Ta

WITHOUT CATHODIC TREATMENT   52100 < Cr* < Cr+Mo < Mo < Cr+P < Ta.

*{It should be noted that the early breakdown of Cr 52100 shown in Fig. 4 was the result of crevice corrosion between the sample and the epoxy mount.}

The benefit of not removing the air-formed film prior to analysis, is that the breakdown potential measured is more accurately reflecting the behavior of the bearing in practice. During operation the bearing will undoubtedly form relatively higher temperature oxide films which will tend to be richer in the passivations which have been added by ion implantation. Hence, it is to be expected that the oxide films formed during operation will promote even greater passivity.

Ta produced the best improvement in pitting potential, and deserves a more in-depth analysis of the surface alloy and passive film structure, in order to evaluate the possibility of improving the corrosion resistance further, by modifying the implantation parameters. It is tempting to attribute the large improvements in the pitting potential of Cr+P and Ta implanted samples to the creation of amorphous surface layer similar to those produced by P and Ta implantation into Fe. This hypothesis awaits further microstructural characterization which is now in progress.

Auger depth profiles of unimplanted samples as well as Cr-, Cr+P-, and Ta-implanted samples are presented respectively in Figs. 5, 6, 7, and 8. These depth concentration profiles are obtained by monitoring the intensity of the Auger electron transition signal for a particular element of interest while sputter etching away the surface with a 2 keV beam of argon ions. The amount of material sputter eroded is assumed proportional to the sputtering time and represents a depth scale. The depth scale can be calibrated by measuring the crater depth at the end of the measurement or by using a more depth-sensitive technique such as nuclear reaction profiling done at NRL. For example, the Cr distribution of Cr implanted 52100 (Fig. 6) is similar to that obtained by the nuclear reaction analysis technique at NRL. The combination of these techniques provides high sensitivity as well as good depth resolution.

The profiles obtained in these ways allow the determination of the implanted species concentration for different implantation parameters (i.e., dose and energy) such that optimal anticorrosion conditions can be selected.

SIMULATION TESTS

The tests used herein for simulating the corrosion mechanism which occurs in gas turbine engines was based on the findings of the test method developed by Brown and Feinberg at NSRDC. They found that in a gas turbine engine bearing compartment; (a) corrosion usually occurred statistically (i.e., bearing not running) at the conjunction of the bearing rolling element and the race, (b) the lubricant in the form of a miniscus was

151

Table 1

52100 Pitting Data* in 0.01 M Buffered (pH = 6) NaCl Solution

*Scan Rate: 1 mV/Sec.

Sample	Cathodic Treatment	Open Circuit Pot. (mV)	Breakdown Pot. (mV)	Passive Current Density ($\mu A/Cm^2$)	Comments
52100 Unimplanted	45 min. at 25 mA	-675	-648	23	Slightly dull, tiny pits, (similar to Mo).
2E17 Cr 150 Kev	"	-764	-50	12	Surface shiny, scattered visible pits.
3.5E16 Mo 100 Kev	"	-682	-612	10	Surface dull, tarnished around the metal-epoxy interface.
2E17 Cr 150 KeV 3.5E16 Mo 100 KeV	"	-61	+0.0	20	Tarnished & Possibly rusted islands on surface.
1E17 Ta 150 KeV	"	-474	+225	20	Big tarnished pits visible.
2E17 Cr 150 KeV 1E17 P 40 KeV	30 min. at 5 mA	-642	0	30	Small visible pits.
52100 Unimplanted	none	-678	-608	47	Half of surface covered with tarnished rust. No visible pits seen.
2E17 Cr 150 KeV 3.5E16Mo100 KeV	"	-143	+20	12	Extremely shiny. No visible pits seen.
1E17 Ta 150 KeV	"	-146	+325	21	A few tarnished islands around the pits.
3.5E16 Mo 100 KeV	"	-550	+75	12	Surface quite shiny.
2E17 Cr 150 KeV 1E17 P 40 KeV	none	-196	+175	10	Big visible pits, surface shiny.
2E17 Cr 150 KeV	none	-283	-205	200	Possible crevicing at sample and Epoxy interface.
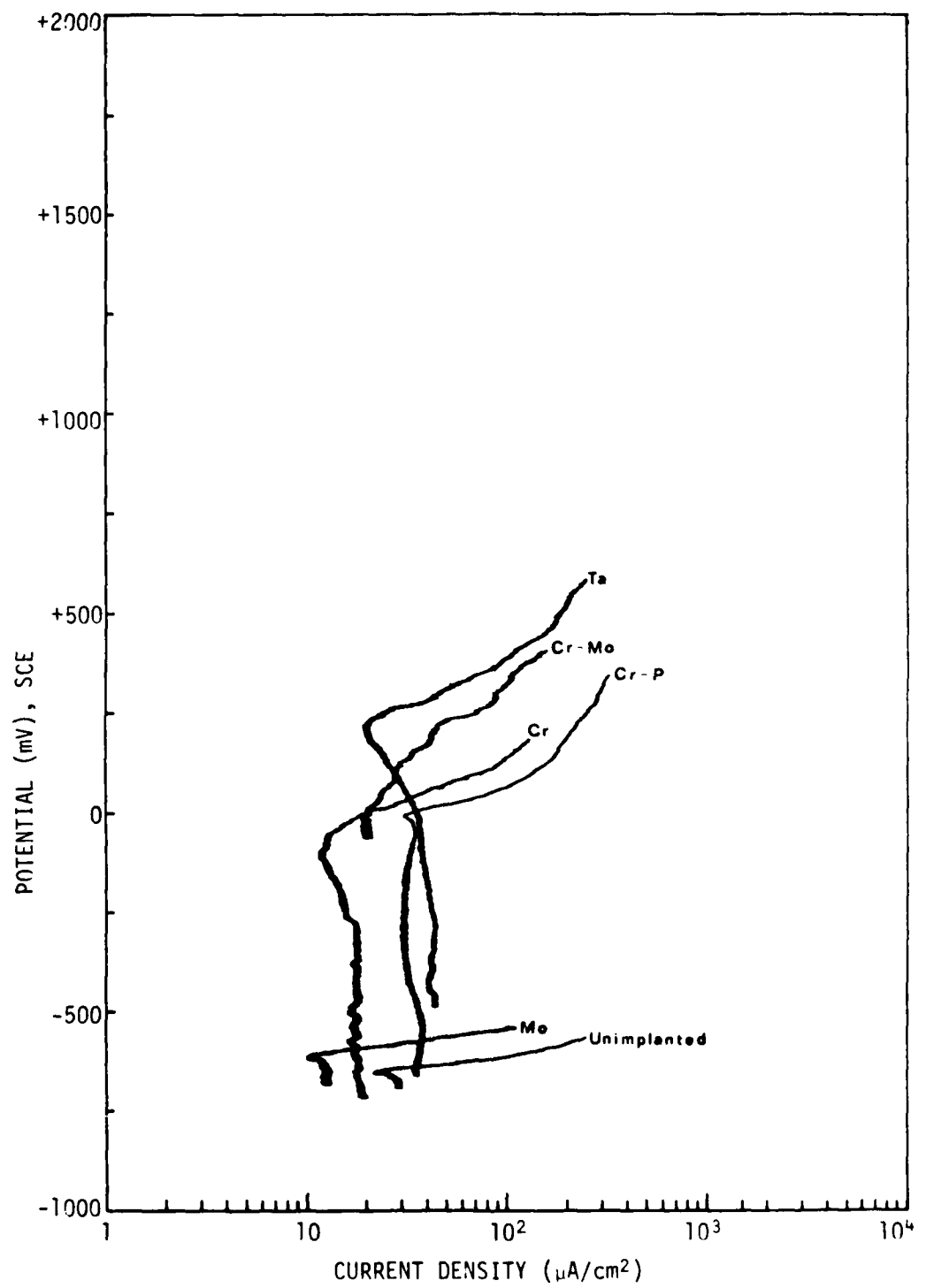
Fig. 3 — Anodic polarization curves of implanted 52100 bearing steel in 0.01 M NaCl
solution buffered at pH 6 with cathodic pretreatment

153
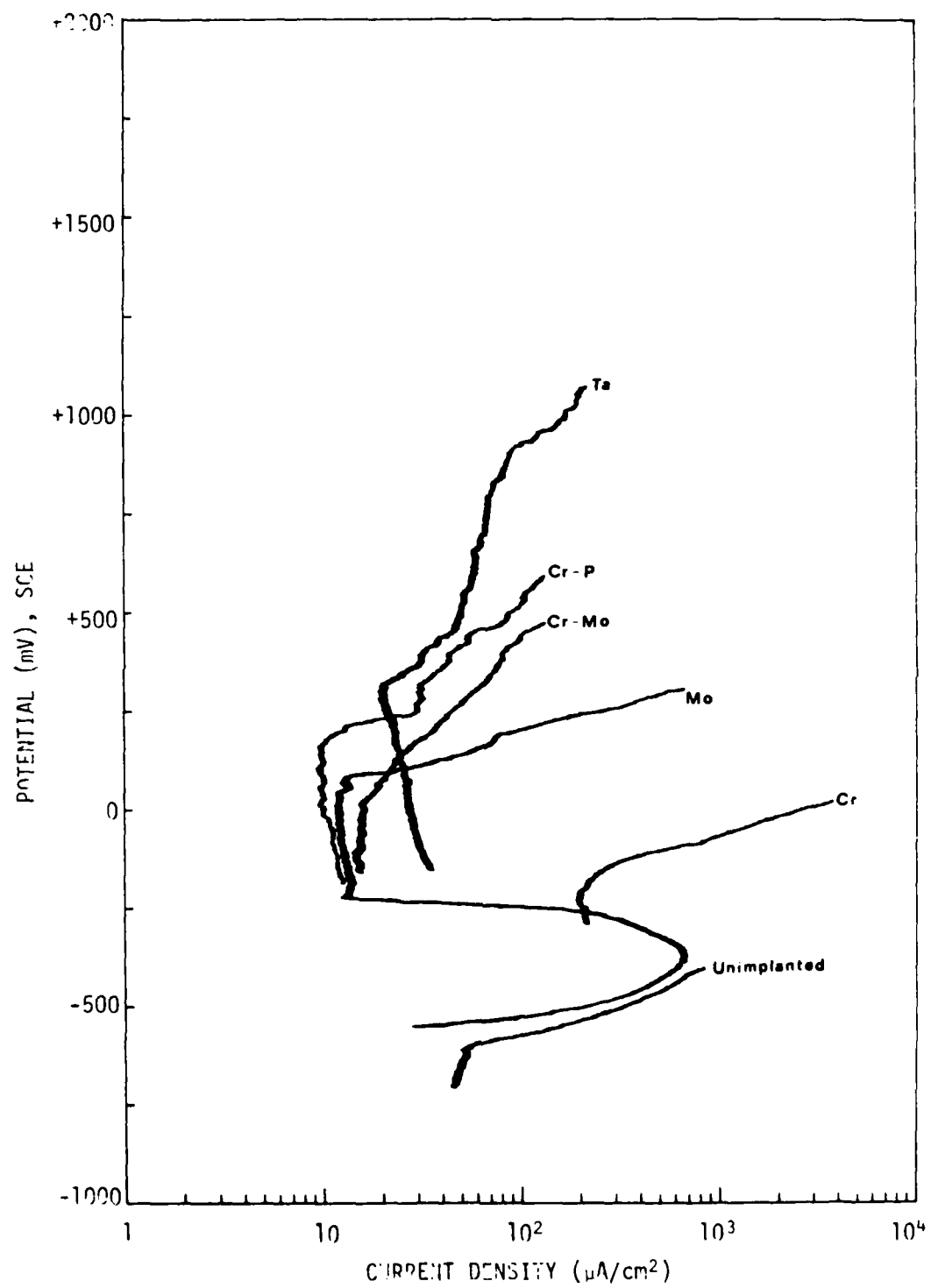
Fig. 4 — Anodic polarization curves of implanted 52100 bearing steel in 0.01 M NaCl
solution buffered at pH 6 without cathodic pretreatment
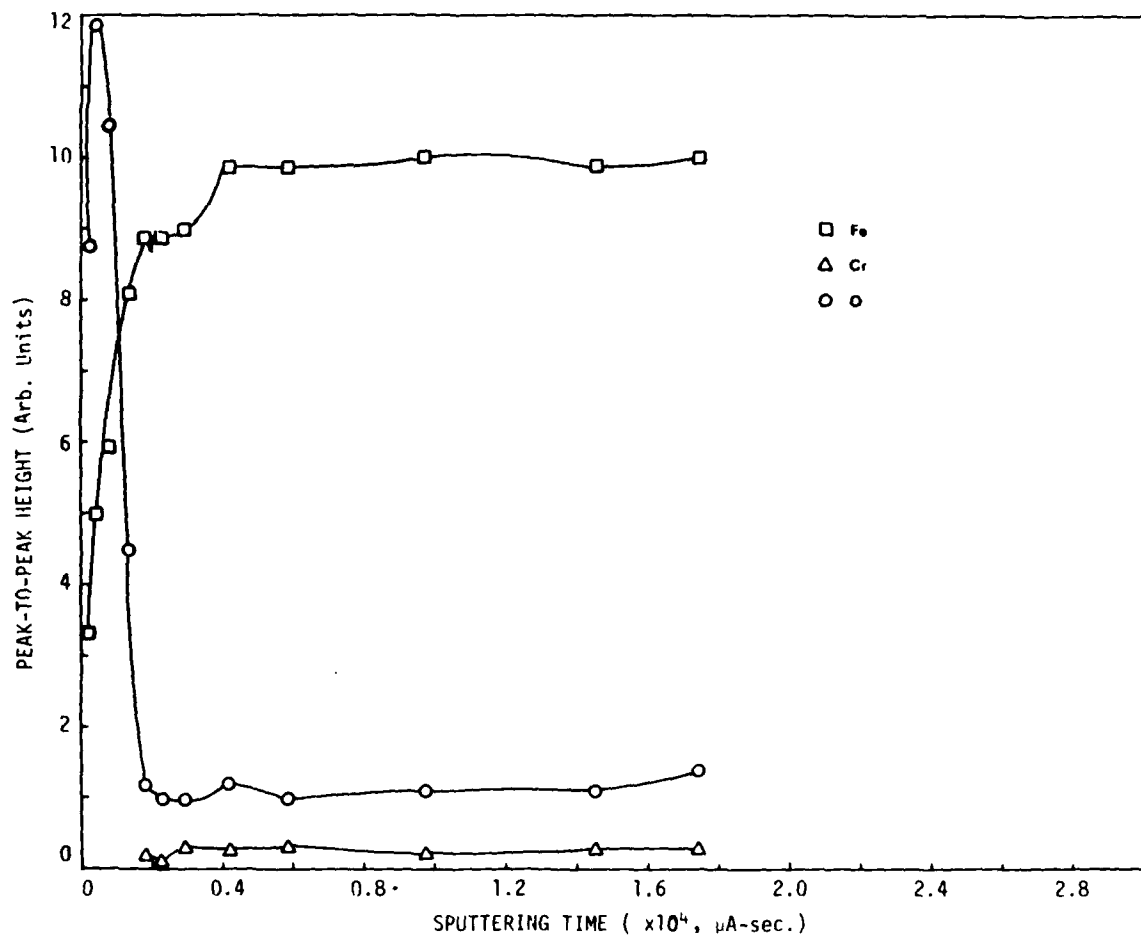
Fig. 5 — Auger depth profile of Fe, Cr, O in unimplanted 52100 bearing steel
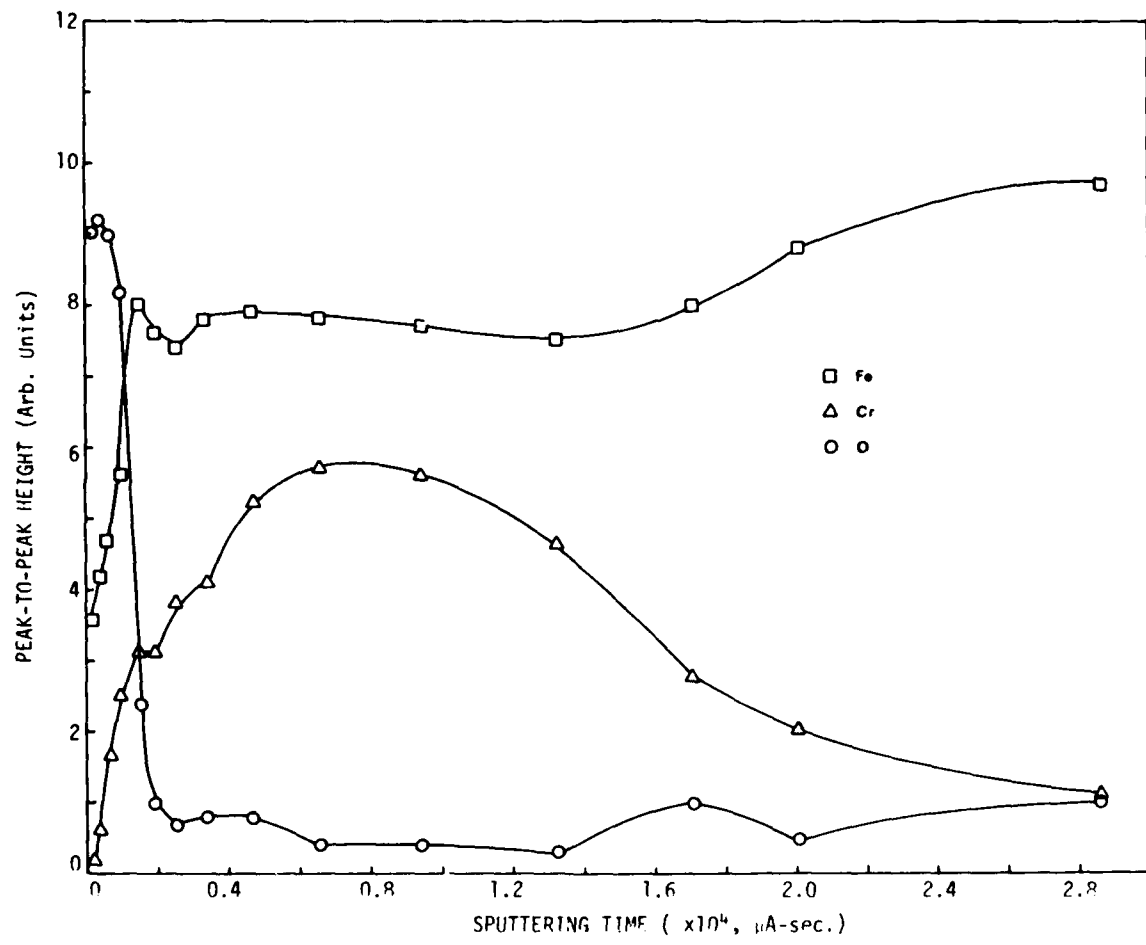
Fig. 6 — Auger depth profile of Fe, Cr, O in Cr implanted 52100 bearing steel

156

*PH x4
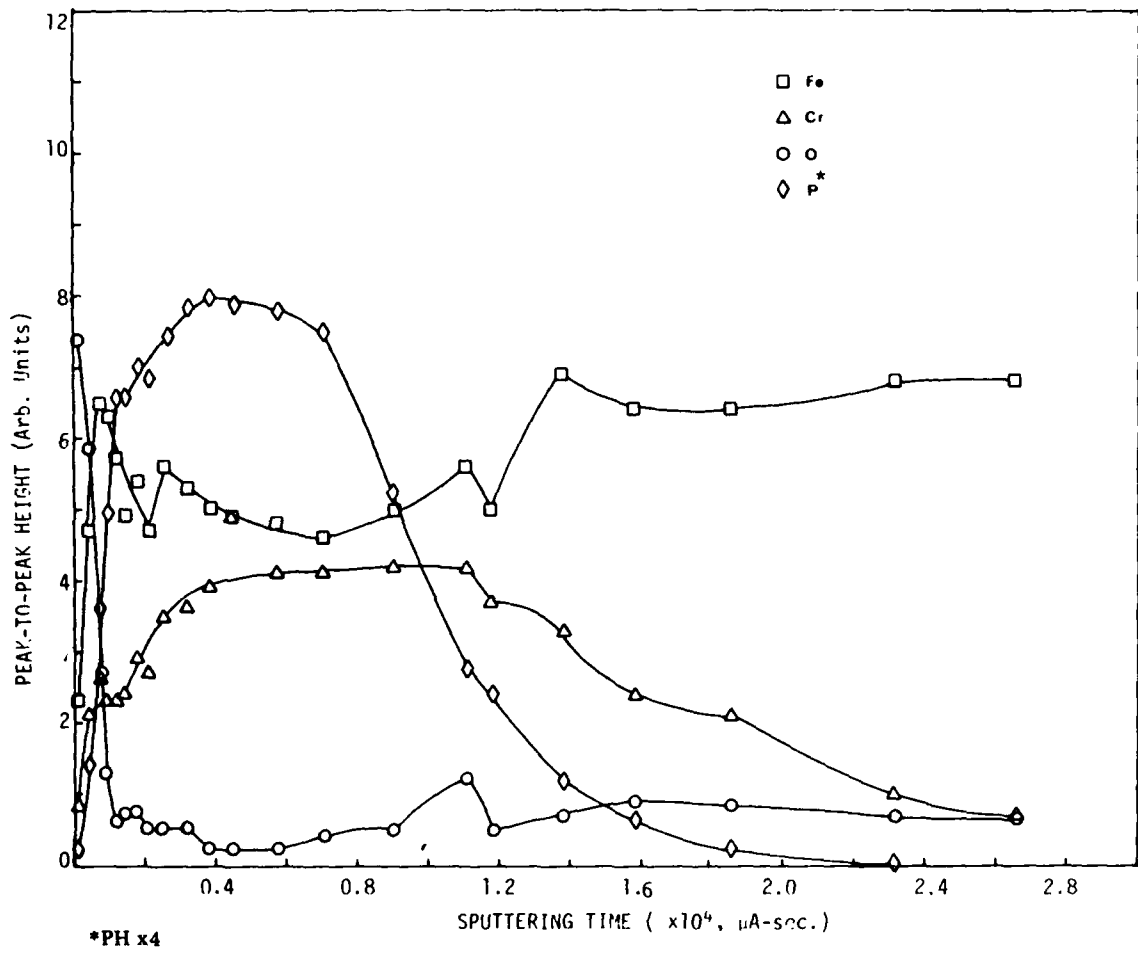
Fig. 7 — Auger depth profile of Fe, Cr, O and P in Cr-P implanted 52100 bearing steel

157
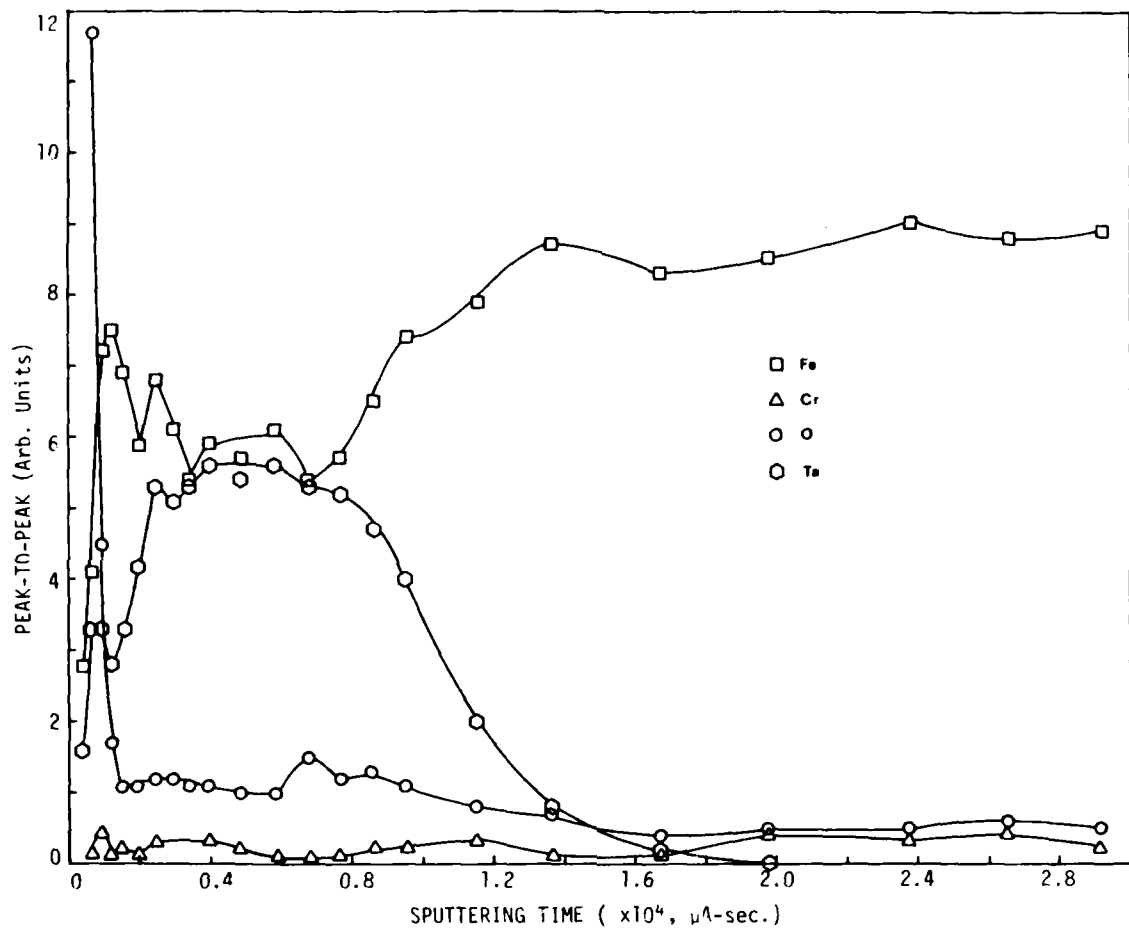
Fig. 8 — Auger depth profile of Fe, Cr, O and Ta in Ta implanted 52100 bearing steel

158

present at the corrosion site and (c) the lubricant showed typical contamination levels of 3 ppm (wt) of chloride and 600 ppm of water.

Figure 9 shows the arrangement of the simulated geometry corrosion test. The cylindrical surface resting on the flat side of the upright cylinder is intended to simulate the roller on race contact geometry of an actual bearing. The cylinders are .0095m (3/8") diameter 52100 rods. The flats (about .006m tall) are cut from the rod and consecutively polished down to a mirror finish with a final (3 μ m) diamond paste. The cylinders were positioned in place and totally immersed for 2 hours in a contaminated neopentyl polyolester gas turbine engine lubricant conforming to specification MIL-L-23699. The oil was contaminated by adding three ppm (wt) of chlorides as ASTM DD665 synthetic seawater to oil and then adjusting the water content to a level of 600 ppm (wt.) by the addition of distilled water. The two parts were then removed from the oil and allowed to drip dry. A miniscus of contaminated oil was retained between the two parts as shown in Figure 9. This system was then exposed to alternate cycles of moist air at 60°C (8 hours) and 4°C (16 hours) for a period of several weeks to simulate an engine during intermittent use.
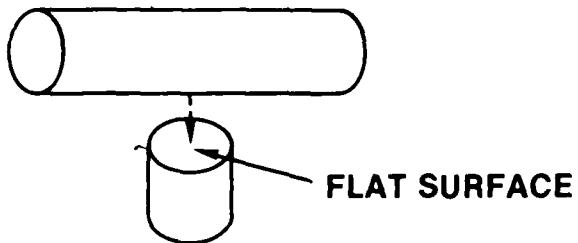
In almost all cases the control specimens showed severe generalized corrosion in this test which tended to obscure the localized (pitting) corrosion. This is in contrast to tests made on M50 bearing alloy which contains more chromium and has a significantly higher resistance to corrosion than 52100. Figures 10 and 11 shows optical photographs (70x magnification) of the corrosion inhibiting effectiveness of an implantation of a Cr and a Cr+Mo implantation after a 4 week test (Fig. 10) as compared to an unimplanted control specimens (Fig. 11). It can be observed that the implanted 52100 samples all showed a dramatic improvement in corrosion resistance in this test simulating field service conditions.

ION BEAM INTERMIXING (INTEGRATED COATINGS)

Recently, it has been shown that it is possible to intermix a vacuum deposited layer of metal with its underlying substrate by means of passing an energetic beam of ions through the layer into the substrate. This process may represent an alternative to direct high-dose implantation. For example, it may be possible to evaporate 1-2 microinches (25-50 mm) of Cr on 52100 and integrate it into the substrate by another suitable beam and enhance the corrosion resistance without encountering any adhesion properties that many coatings have.

Preliminary studies have already been carried out to evaluate the use of ion intermixing to produce highly corrosion resistant surface alloys on 52100 steel. Anodic polarization curves of Cr vapor deposited film on 52100, and Cr intermixed with 52100 (Xe→Cr, 398 KeV, 3 x 10^{16} ions cm^{-2}) are presented in Fig. 12. The data is also summarized in Table 2. One would expect vapor deposited Cr to behave as Cr metal, however, in this case Cr vapor deposited 52100 had a lower breakdown potential. The Cr metal only brokedown in the transpassive region. In examining the surface of the vapor deposited surface pits were observed. This was found to result from ultrasonic cleaning of the bearings prior to deposition. In the cleaning process cavitation erosion produced the pits, which later became imperfectly coated with Cr, which in turn led to localized corrosion. This result is surprising since bearings are generally very resistant to cavitation erosion.

159

1. Test pieces (52100 alloy steel) were placed in contact
   as indicated by the dotted line.

   FLAT SURFACE

2. Both pieces in place were immersed in chloride-contaminated
   oil for 2 hrs., removed, and allowed to dry.

3. A meniscus of contaminated oil was retained between the
   two parts:

   UPPER CYLINDER (end view)

   Cl-CONTAMINATED OIL
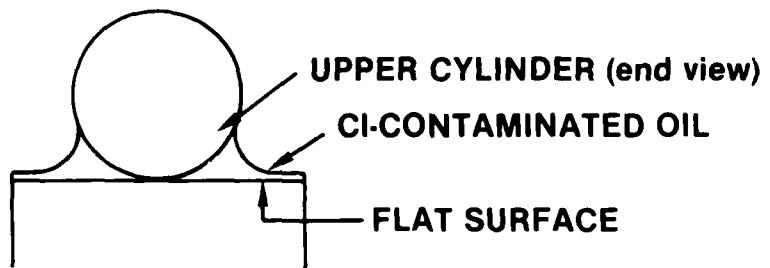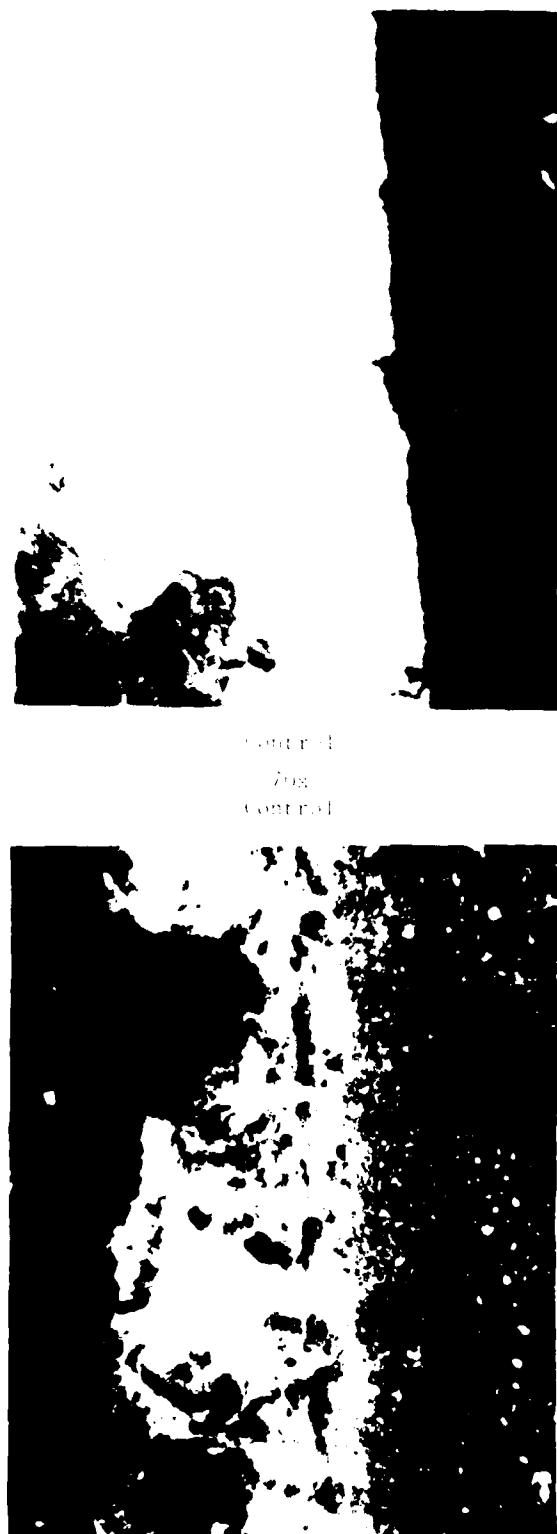
   FLAT SURFACE

   Fig. 9 — Schematic of field service simulation test for pitting corrosion
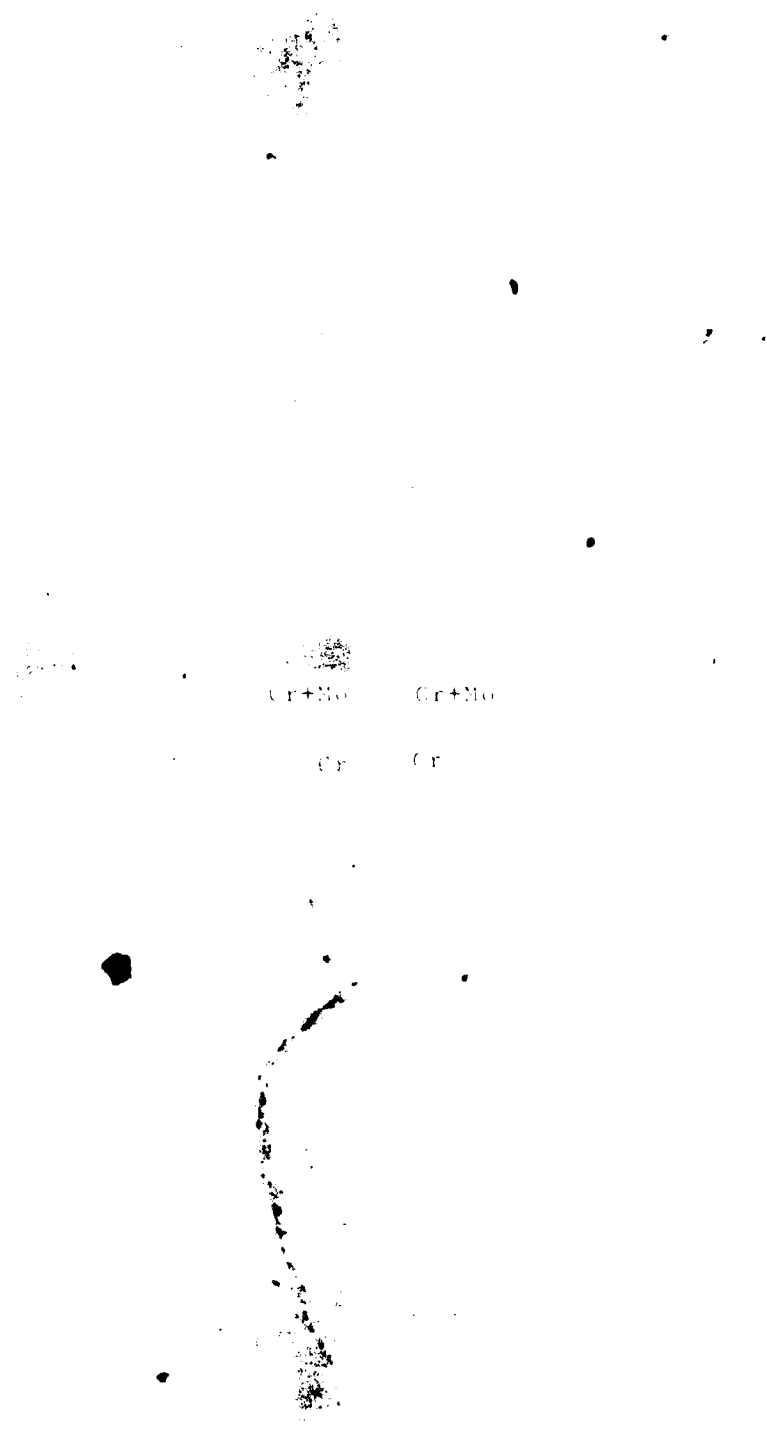
R-061

Fig. 10 — Optical micrographs (70X) of the surfaces of 52100 steel polished flats after 4 weeks exposure to the corrosion test outlined in Fig. 9. The two upper samples were implanted with Cr+Mo and the two lower samples with Cr. Note the good resistance to general corrosion when compared to two unimplanted control samples shown in Fig. 11.

161

Fig. 11 — Optical micrographs (70X) of the surfaces of two 52100 steel flats after 4 weeks exposure to the corrosion test outlined in Fig. 14. Note the high degree of general corrosion on these unimplanted samples as compared to the Cr- and Cr+Mo-implanted samples in Fig. 10.

R-046

162
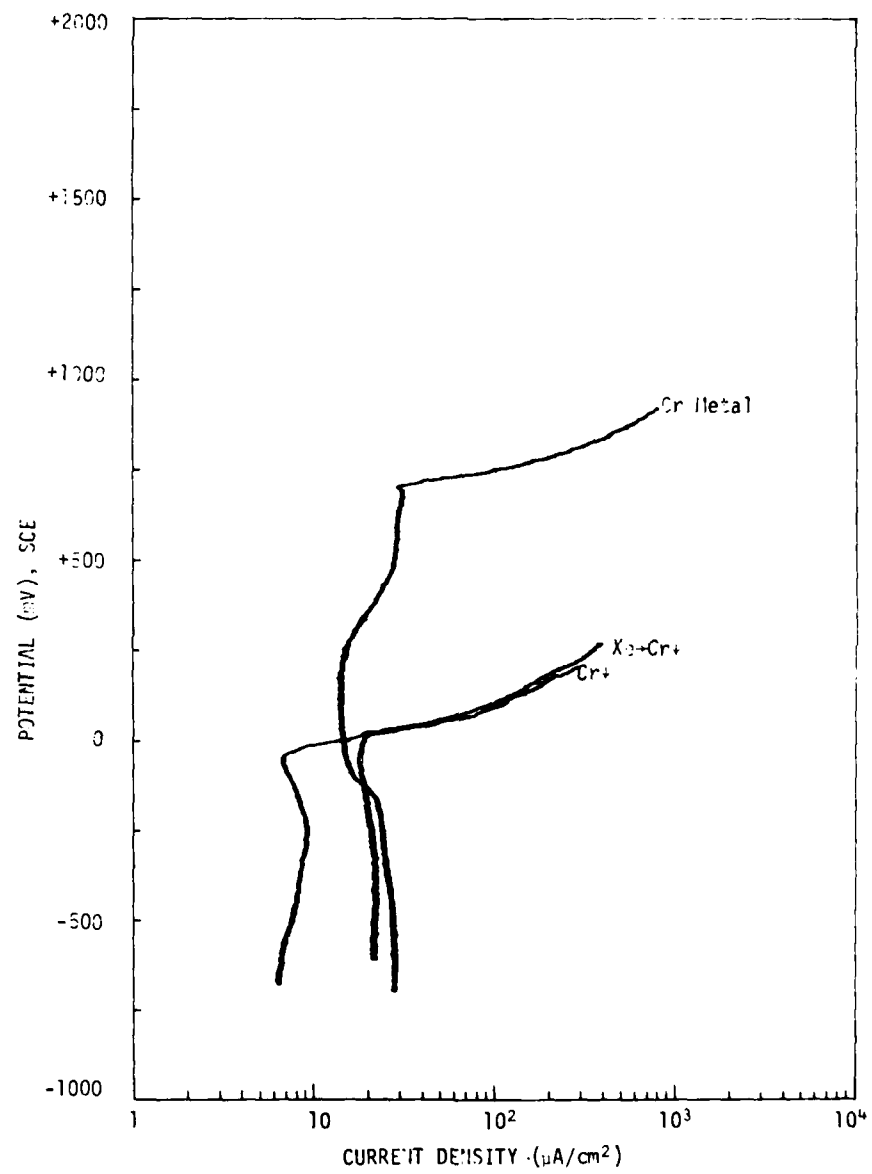
Fig. 12 — Anodic polarization curves of Cr metal, 125 Å Cr↓ vapor deposit film on 52100 and Cr↓ intermix with 52100 bearing steel in 0.01 M NaCl solution buffered at pH 6 with cathodic pretreatment

163

Table 2

52100 Pitting Data* in 0.01 M Buffered (pH=6) NaCl Solution

*Scan Rate: 1 mV/Sec.

Sample	Cathodic Treatment	Open Circuit Pot. (mV)	Breakdown Pot. (mV)	Passive Current Density ($\mu A/Cm^2$)	Comments
Cr + (125Å)	30 min. at 5 mA	-585	+25	17	A few small pits on surface.
Xe → Cr + (125Å)	30 min. at 5 mA	-655	-40	7	Small pits on surface.
Cr metal	90 min. at 5 mA	-685	+700	14	Metal becomes transpassive.

This preliminary experiment showed that under the conditions used for intermixing, and with the current imperfections in the Cr film, the pitting resistance of the intermixed alloy was comparable to a high dose Cr implantation. Auger depth profiles for Cr, Fe, and O for the Cr-vapor deposited and the intermixed Cr (Xe→Cr/52100) samples have been measured. The mixing effect is more readily seen by comparing Figs. 13 and 14. The relatively abrupt interface of the vapor deposited coating at Fig. 13 gives way to a smooth interfacial transition in Cr content in the case of the Xe implanted sample of Fig. 14. Furthur studies of this promising technique are underway.
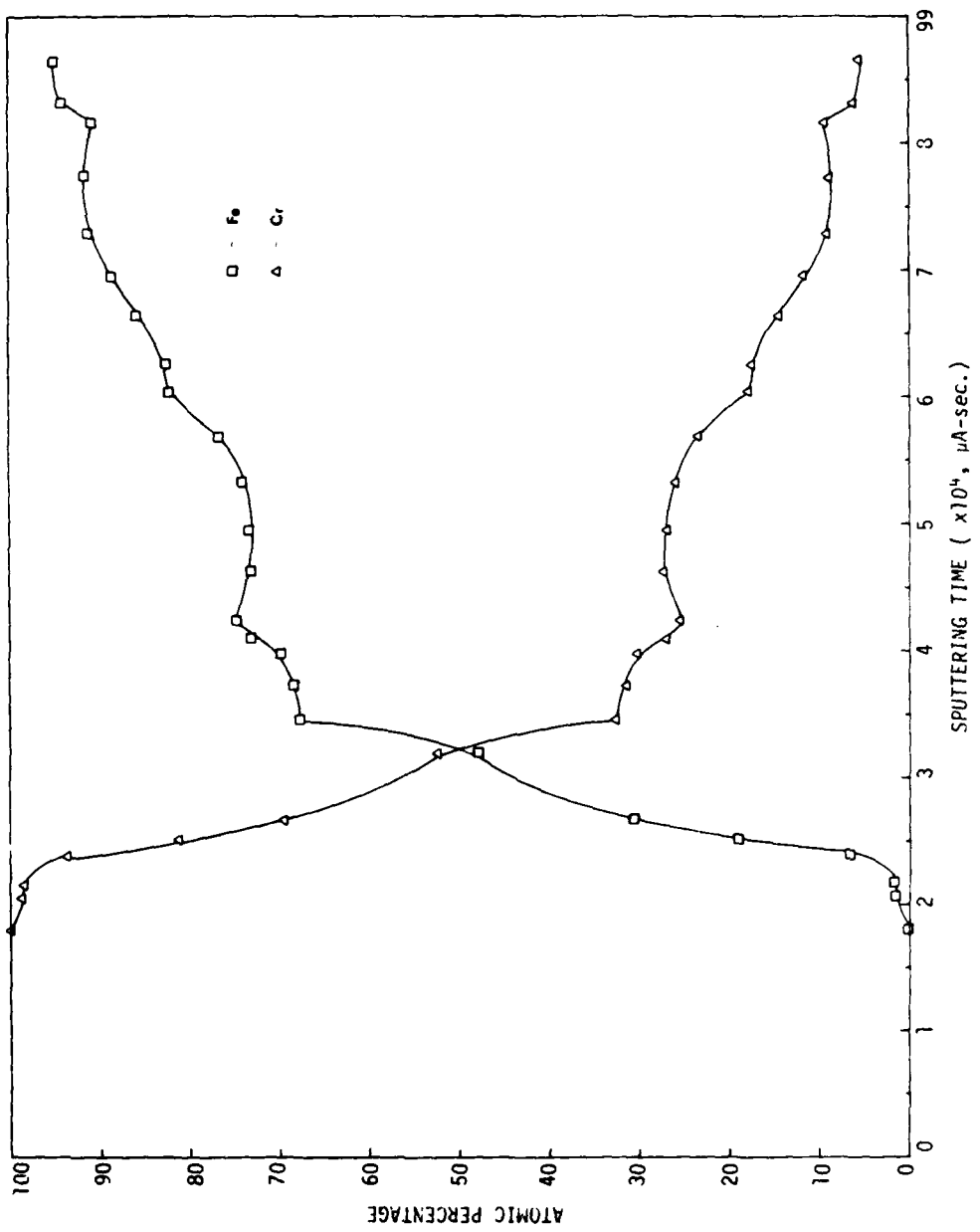
Fig. 13 — Auger depth concentration profile of Fe and Cr in Cr vapor deposit on 52100 bearing steel

166
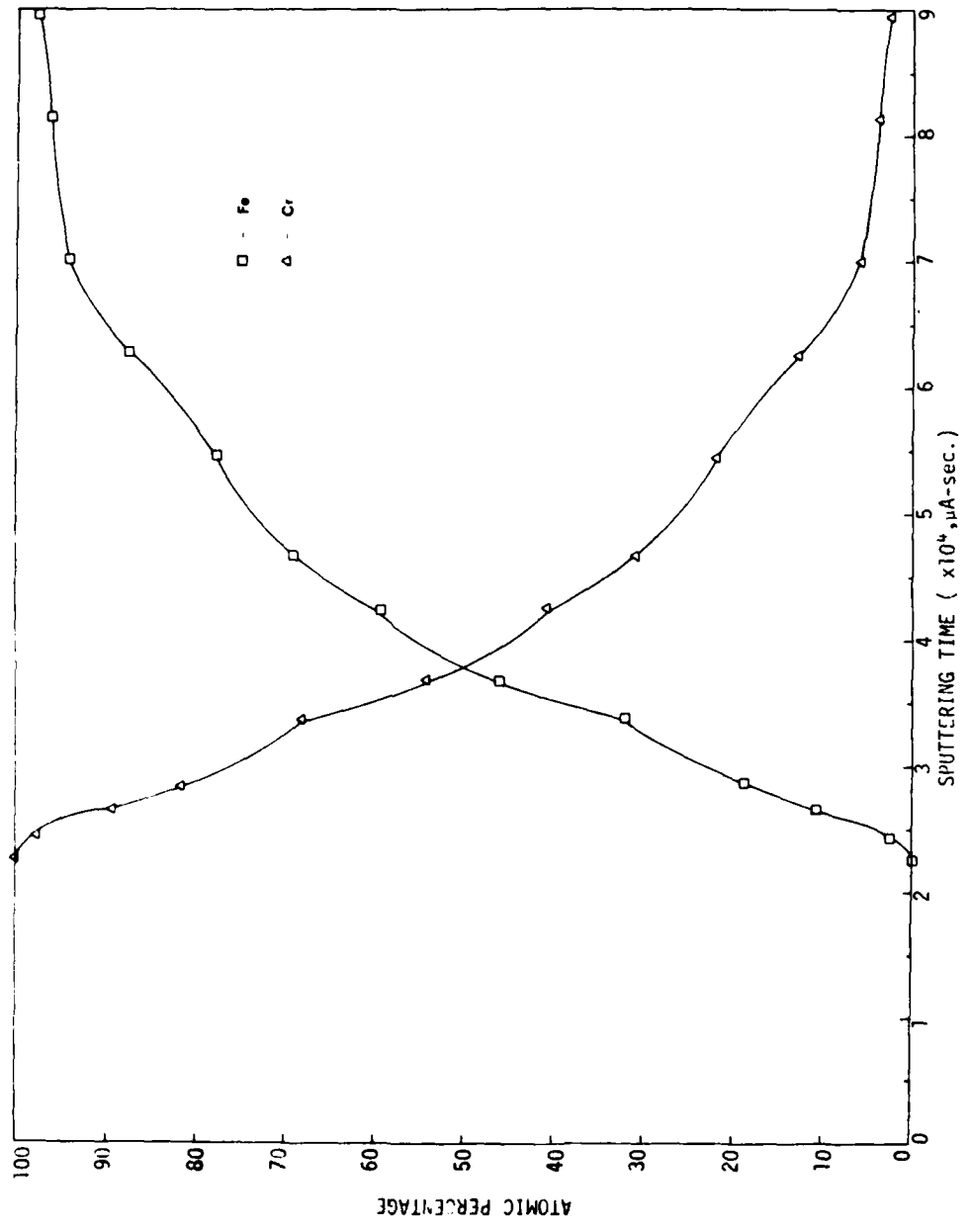
Fig. 14 — Auger depth concentration profile of Fe and Cr in Cr intermix with 52100 bearing steel

167

Section IV.A

OPTICAL EFFECTS RESULTING FROM DEEP IMPLANTS
OF SILICON WITH NITROGEN AND PHOSPHORUS

G. K. Hubler[1], P. R. Malmberg[1], C. A. Carosella[1] and T. P. Smith III[1]

W. G. Spitzer[2], C. N. Waddell[2] and C. N. Phillippi[3]

[1]Materials Modification and Analysis Branch
Condensed Matter and Radiation Technology Division
Naval Research Laboratory

[2]Physics and Materials Science Departments
University of Southern California
Los Angeles, California 90007

[3]U. S. Air Force Materials Laboratory
Dayton, Ohio 45433

PRECEDING PAGE BLANK-NOT FILMED

OPTICAL EFFECTS RESULTING FROM DEEP IMPLANTS OF SILICON WITH NITROGEN AND PHOSPHORUS†

G. K. HUBLER, P. R. MALMBERG, C. A. CAROSELLA, and T. P. SMITH, III

U.S. Naval Research Laboratory, Washington, DC, U.S.A. 20375.

W. G. SPITZER and C. N. WADDELL

University of Southern California, Los Angeles, CA, U.S.A. 90007.

C. N. PHILLIPPI

U.S. Air Force Materials Laboratory, Dayton, OH, U.S.A. 45433.

Single crystal silicon has been implanted with nitrogen and phosphorus ions at MeV energies to fluences between 10^{16} and 1.6×10^{18} ions/cm². Infrared transmission and reflection spectra in the range of 1.25 to 40 μm were measured for as-implanted samples and after various annealing treatments. Interference fringes were observed in the IR spectra which are produced by the interference of light which has been multiply reflected between the front surface and the buried layers. By detailed theoretical analyses of the interference fringe structure, we obtained refractive index profiles, which, under suitable interpretation, provide accurate measurements and several quantities of interest. These quantities are the range and straggling of the implanted ions, the depth of disordered layers, and the width of the order-disorder transition. Mechanisms for the refractive index changes which have been identified include amorphization of the implanted silicon, bulk compositional change in the buried layer, localized vibrational mode dispersion, and free electron dispersion. Experimental results and theoretical predictions are presented, demonstrating each of these mechanisms.

INTRODUCTION

The face of single crystal silicon slices have been implanted with nitrogen ions at energies of 1.4, 1.5, and 3.2 MeV and for fluences between 0.25 and 1.55×10^{18} ions/cm². During implantation the substrates were held at a temperature of 700°C. Interference fringes were observed in the infrared transmission and reflection spectra which are produced by the interference of light multiply reflected between the front surface and the buried implanted layers. By using a multilayer thin-film interference computer code to analyze the interference fringes, refractive index profiles are obtained which can be directly related to the projected range and straggling of the implanted nitrogen. Dispersive effects due to localized vibrational modes of silicon nitride formed in the buried layer are also included in the analysis.

Implantation of the (111) faces of single crystal silicon were also made with 2.7 MeV phosphorus ions to fluences between 10^{16} and 10^{17} ions/cm² with the substrate temperature maintained at $-78°C$. Analysis of the interference fringes from these samples gave measurements of the refractive index of amorphous silicon, the thickness of the amorphous layer, and the width of the amorphous to crystalline transition. After annealing a prominent interference fringe pattern arises at low frequencies. A theoretical prediction of these interference fringes was obtained by assuming that the activated phosphorus donor electrons interact with the light as a damped, free-electron plasma.

Implantations were made using NRL 5-MV Van de Graff accelerator. Nitrogen implanted samples were heated by the 5 watts of power of the ion beam and maintained at 700 C by varying the configuration of heat shielding surrounding the sample and by varying the beam current. Phosphorus implanted samples were heat sunk with a

81

thin layer of vacuum grease to a brass holder that was maintained at a temperature of −78°C. The ion beams were raster scanned to ensure uniform implants over a 0.5 cm² area. The silicon slices were 0.38 mm thick and had a resistivity of 10 Ω-cm for the nitrogen implants, and 0.25 mm thick and < 1000 Ω-cm for the phosphorus implants.

NITROGEN IMPLANTATION SILICON

A number of authors[1][5] have reported on the formation of silicon nitride by the implantation of nitrogen into silicon. These implants were with beam energies of <280 keV, usually at room temperature, and subsequent annealing was used to promote silicon nitride formation. Although several different methods were used to study the resulting silicon nitride layers, the most direct indicator was the formation of an absorption band in the infrared at about 900 cm^{-1}. In the present work, ions of MeV energies were used to produce deeper, thicker layers and the implant was made with the sample hot to encourage the immediate formation of silicon nitride.

Figure 1 shows the transmission spectrum for a sample implanted to a fluence of 1.25 × 10¹⁸ ions/cm² at an energy of 1.5 MeV and the same spectrum for an unimplanted sample. Note that there is a strong absorption band near 900 cm^{-1}, which indicates that some silicon nitride formation has occurred, and that at higher wave numbers there are very prominent interference fringes.

Analysis of Non-Dispersive Region

Others have also noted interference fringes resulting from ion implantation. In particular

Crowder *et al.* used the spacing between fringes to determine depths of disordered silicon layers produced by low energy implantation.[6] Kachare *et al.* obtained interference fringes for GaAs and GaP implanted with nitrogen and phosphorus[7] and measured the refractive index of the disordered layers as well as the thickness by fitting the data to a thin-film interference model. Hubler *et al.* have studied the N, Si, and P implants in Si.[8,9]

The interference fringes of Figure 1 are not due to a disordered surface layer because the high temperature during the implantation maintained the crystalline structure, but instead are due to a buried layer with an index of refraction, n, less than that of silicon. To model the buried layer, the assumption was made that the refractive index profile has a gaussian shape to match that of the implanted nitrogen ions. To permit calculation of the fringes with a multilayer thin-film method, this region was approximated by dividing it into 80 uniform-property layers, each with an index of refraction given by a point on a gaussian curve. A computer code to calculate transmission (T) and reflection (R) for this model was written using the thin-film equations of Heavens.[10] For the non-dispersive region the absorption may be neglected (e.g. extinction coefficient $k = 0$). Thus the only variable parameters are the projected range, R_p, standard deviation of the projected range, ΔR_p, and the decrease in the refractive index at the peak of the gaussian. Fitting of data was made by varying

FIGURE 1 Infrared transmission spectrum of silicon sample implanted with 1.25 × 10¹⁸ N cm² at 1.5 MeV, and comparison spectrum for an unimplanted sample
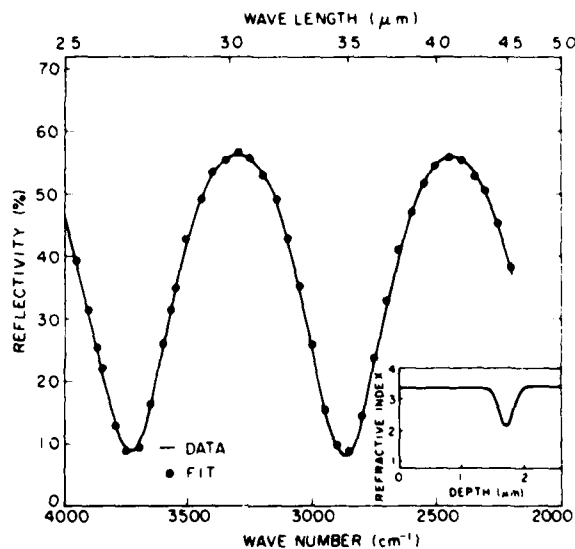

FIGURE 2 Reflection spectrum for same sample as in Figure 1 with calculated fit superimposed (smooth curve). The insert shows index of refraction profile to yield this fit

these three parameters by means of a non-linear least-squares method.

The quality of fits that can be obtained is illustrated in Figure 2 for a sample which had the back surface lapped to eliminate rear surface reflections and had been annealed at 1000°C for one hour in a partial pressure of oxygen and stripped in HF. The data were fitted by the refractive index profile shown in the insert for a refractive index minimum $n = 2.1$ at $R_p = 1.72\,\mu m$ and $\Delta R_p = 0.11\,\mu m$.

Similar fits for the transmission spectra of several samples are given in Figure 3. Note that the amplitude of the fringes increases with fluence, and that,
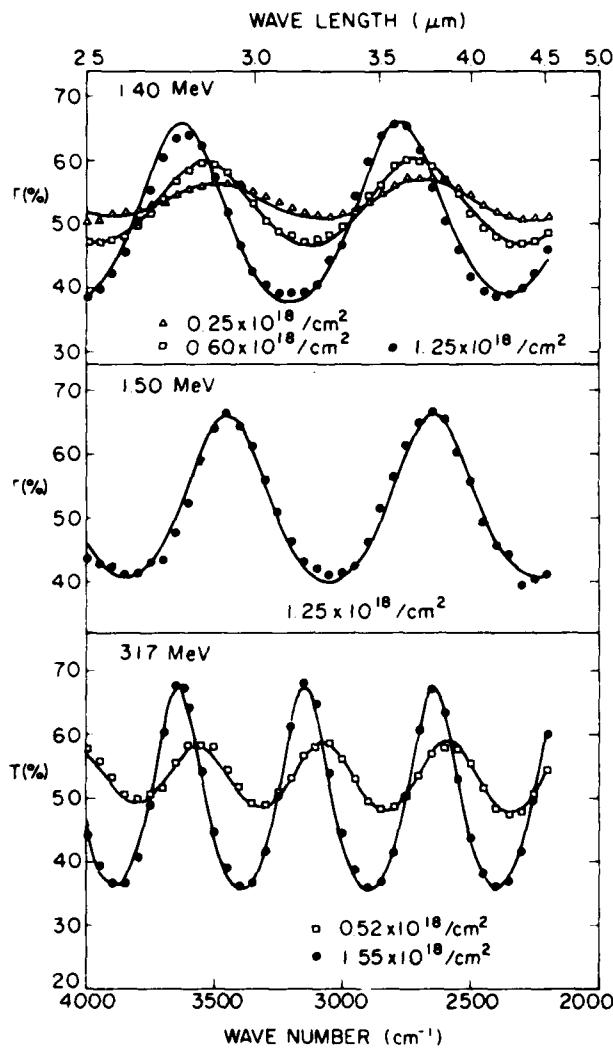
as expected, the spacing between fringes decreases as the depth of the layer increases.

These fits give a precise measurement of the projected ranges of the implanted nitrogen and the values obtained are about $40\,\%$ below the values given in the tabulation by Gibbons et al.[11] A measurement of projected range for one sample using Rutherford backscattering gave a result in good agreement with the optical method.

Analysis of Dispersive Region

At wave numbers less than about 1500 cm^{-1}, the periodicity of the interference fringes in Figure 1 becomes irregular indicating that the dispersive effects of the silicon nitride are no longer negligible. Therefore, to be able to use the thin-film interference code, the optical constants n and k must be computed from classical dispersion theory. We assume for the buried layer a collection of damped oscillators, the oscillator being the silicon-nitrogen molecule. The necessary quantities to calculate are the conductivity, σ, and dielectric susceptibility, α, which are given as a function of frequency, ν, by Seitz.[12] The frequency dependent dielectric constant is given by $\varepsilon = \varepsilon_0 + 4\pi\alpha$ where ε_0 is the high frequency dielectric constant. By using the expressions, $n^2 - k^2 = \varepsilon$ and $nk = \sigma\nu$, n and k are computed for each layer in the gaussian profile approximation—it is assumed that the concentration of oscillators follows the gaussian nitrogen ion concentration.

Three parameters for each resonance were varied to give fits to the data. These are the resonant frequency, ν, the damping constant, γ, and the oscillator strength, ρ (proportional to the number of active oscillators per unit volume). An example

FIGURE 3 Transmission for six samples varying fluence and energy with superimposed fits (smooth curves).
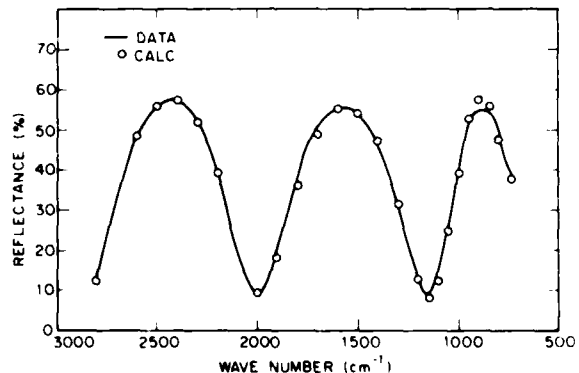

FIGURE 4 Reflectance spectrum (line) for same sample as in Figure 2 including the dispersive region. The circles are calculated values using classical dispersion theory

of this kind of calculation is shown in Figure 4. Two oscillator frequencies were required to give a reasonable fit to the reflection data in the region around 900 cm^{-1}. The parameters for oscillators 1 and 2 were $v_1 = 850$ cm^{-1}, $v_2 = 900$ cm^{-1}, $\gamma_1 = \gamma_2 = 0.20$ and $\rho_1 = \rho_2 = 0.22$.

PHOSPHORUS IMPLANTATION OF SILICON

The IR reflectance from a silicon sample implanted under conditions stated previously is presented in Figure 5. This sample was also coarse lapped on the rear surface to eliminate reflections. The crosses are the data and the solid curve is the result of a fit in which three parameters were varied. The parameters are, along with their fitted values: $R_d = 2.5$ μm, the depth of the amorphous layer; $\sigma_d = 0.035$ μm, the standard deviation of the half-gaussian used to connect the amorphous refractive index with the crystalline value; and n_d, the refractive index of the amorphous material. The refractive index profile is shown in the insert for a frequency of 4000 cm^{-1}

The slight rise in the average value of reflectance with increasing wave number is due to the dispersion of silicon and was accounted for by the model. The decrease in amplitude of the interference fringes with increasing wave number is sensitive to the parameter σ_d which governs the sharpness of the amorphous-layer crystal interface. Also shown are the data (circles) for an unimplanted sample and a model calculation (line) using the crystalline refractive index.

Figure 6 presents reflectance data for the same sample after annealing at 600 C for 5 hours. The prominent interference fringes at low frequencies are caused by reflection from the buried conducting layer which may be treated theoretically as a damped, free-electron plasma.[13] To obtain the calculated curve in Figure 6, the dispersion relations for a damped plasma were inserted into the thin-film interference code. The plasma frequency which enters into the dispersion relations is proportional to the square root of the free-electron density which is taken to be a gaussian distribution.

The solid curve is not a fit but a preliminary
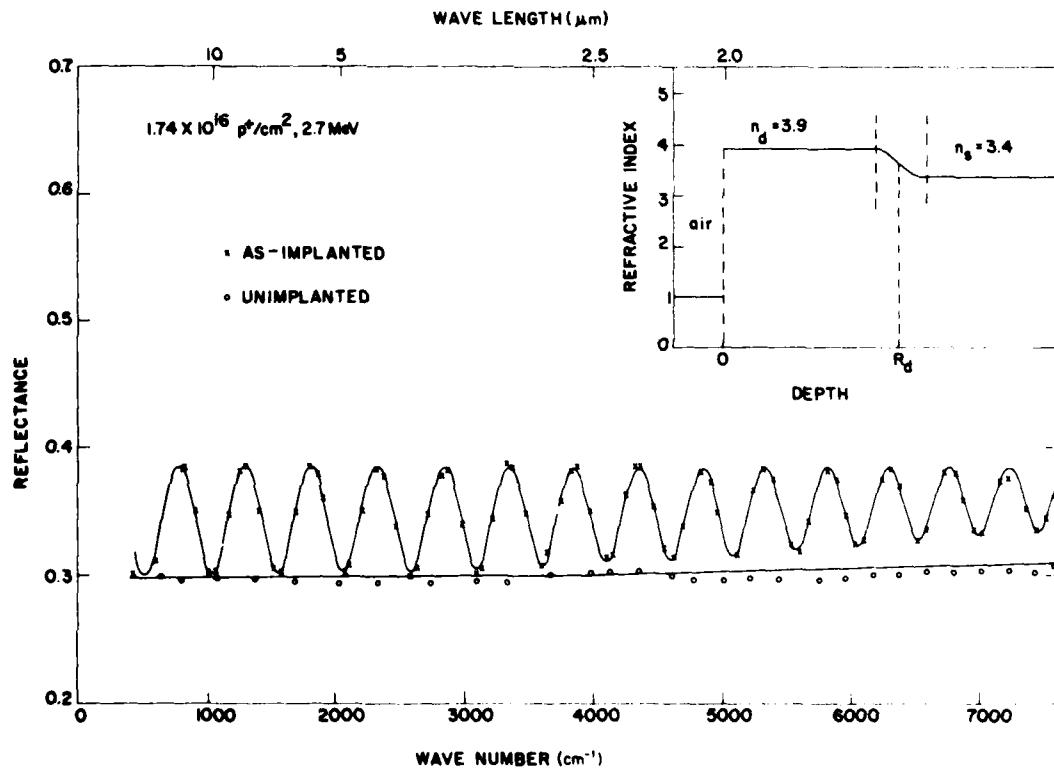
FIGURE 5   Reflectance spectrum for silicon implanted with phosphorus. A fit using refractive index profile of the insert is given by the solid line.

WAVE LENGTH (μm)
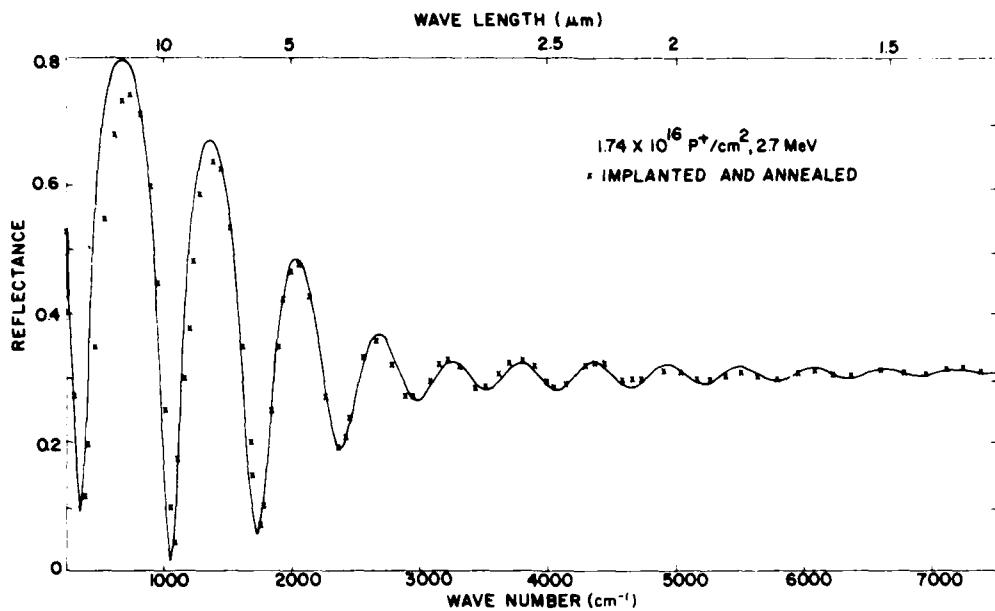
FIGURE 6 Reflectance spectrum for same sample as figure 5 after annealing. Method for obtaining prediction given by solid line is described in text.

prediction. By varying the parameters for the plasma, we anticipate that much improved fits will be obtained.

The parameters used for this predicted curve were $R_p = 2.1$ μm. $\Delta R_p = 0.22$ μm. and the carrier concentration at the peak of the gaussian = 0.7 × 10^{20} cm^3. The small amplitude fringes at high frequency provide information on the residual damage in the implanted region after annealing. To predict these fringes, it was necessary to include a narrow, disordered-region at the depth of the original amorphous-layer/crystalline interface.

CONCLUSION

It may be said that interference fringes in infrared transmission and reflection spectra resulting from implantation of silicon with nitrogen and phosphorus can be matched very well by fitting with theoretical models which employ a multilayer thin-film interference code. Accurate measurements of projected ranges of the implanted ions may thereby by deduced, as well as refractive index profiles resulting from ion implantation. Predictions of the model for localized vibrational mode dispersion and free electron dispersion are likewise in good agreement with the IR data.

REFERENCES

1. G. H. Schwuttke, Air Force Cambridge Research Laboratories Report AFRCL-70-0459, Bedford, Massachusetts (July 1970).
2. J. A. Borders and W. Beezhold, *Ion Implantation in Semiconductors*, edited by I. Ruge and J. Graul, (Springer-Verlag, New York, 1971), p. 241.
3. R. A. Kruze, D. I. Tetelbaum, E. I. Zorin, F. V. Shitova, and P. V. Pavolv, *Iz. Ak. Nark SSSR*, Neorgan. Mat. 11, 1381 (1975).
4. N. A. Genkina, P. V. Pavlov, F. V. Shitova, T. A. Kruze, and E. I. Zorin, *Iz. Ak. Nark SSSR*, Neorgan. Mat. 11, 1988 (1975).
5. F. L. Edelman, D. N. Kuznetov, L. V. Lezheiko, and E. V. Lubopytova, *Rad. Eff.*, 29, 13 (1976).
6. B. L. Crowder, R. S. Title, *Ion Implantation*, edited by F. H. Eisen, L. T. Chadderton, (Gordon and Breach, 1971), p. 87.
7. A. H. Kachare, W. G. Spitzer, J. E. Fredrickson, and F. K. Euler, *Jour. Appl. Phys.*, 47, 5374 (1976).
8. G. K. Hubler, C. N. Waddell, W. G. Spitzer, R. G. Wilson, S. Prussin, and J. K. Fredrickson, *J. Appl. Phys.*, 50, 3294 (1979).
9. G. K. Hubler, P. R. Malmberg, and T. P. Smith, *J. Appl. Phys.*, 50, 7147 (1979).
10. O. S. Heavens, *Optical Properties of Thin Solid Films*, (Academic Press, New York, 1955).
11. J. F. Gibbons, W. S. Johnson, and S. W. Mylroie, *Projected Range Statistics In Semiconductors and Related Materials*, 2nd Edition (Dowden, Hutchison Andross, Stroudsburs, Pennsylvania, 1975).
12. F. Seitz, *The Modern Theory of Solids*, (McGraw-Hill, New York, 1940), Chap. 17.
13. W. G. Spitzer, C. N. Waddell, G. H. Narayanan, J. F. Fredrickson, and S. Prussin, *Appl. Phys. Lett.*, 30, 623 (1977).

174

Section IV.B

PULSED ELECTRON BEAM IRRADIATION OF ION-IMPLANTED
COPPER SINGLE CRYSTALS

J. K. Hirvonen[1], J. M. Poate[2], A. Greenwald[3] and R. Little[3]

[1]Materials Modification and Analysis Branch
Condensed Matter and Radiation Technology Division
Naval Research Laboratory

[2]Bell Laboratories
Murray Hill, New Jersey 07947

[3]SPIRE Corporation
Bedford, Massachusetts 01730

175

Pulsed electron beam irradiation of ion-implanted copper single crystals

J. K. Hirvonen

Naval Research Laboratory, Washington, D.C. 20375

J.M. Poate

Bell Labs, Murray Hill, New Jersey 07974

A. Greenwald and R. Little

SPIRE Corporation, Bedford, Massachusetts 01730

The effect of an intense, pulsed electron beam on high-dose implanted Cu single crystals has been studied. Rutherford backscattering and channeling have been used to obtain the depth concentration profiles and lattice locations of the implanted species (Au, Ag, and Ta) before and after pulsed electron beam irradiation. Channeling and secondary electron microscopy measurements show that the Cu surface melts during pulsed irradiation followed by an epitaxial lattice growth resulting in (i) a redistribution of the implanted species, (ii) some species (e.g., Au and Ag) remaining on lattice sites, and (iii) Ta leaving substitutional sites.

This letter describes the effect of pulsed electron beam irradiation on surface alloys produced by high-dose implantation in single-crystal Cu. There is much current interest in the use of pulsed heat sources(laser and electron beams) for treatment of surfaces.[1] The metallurgical behavior of surface layers can be conveniently studied by the location of implanted species before and after a transient heat treatment. While many implanted semiconductors have been studied by the technique, there appears to be only one reported measurement of the laser irradiation of an implanted metal.[2]

Ion implantation has been previously employed to produce both equilibrium and metastable surface alloys in Cu single crystals. Since Cu has received considerable attention as an implantation host, it is desirable to study the system under pulsed irradiation. Electron beams offer an effective means of studying transient heating of Cu crystals since considerable difficulties are experienced in coupling lasers to polished Cu. This is presumably due to the very high reflectivity and conductivity of Cu. We employed an electron beam with a mean energy of approximately 25 keV, a pulse duration of 100 nsec and a deposited energy of 2 cal/cm² (8.2 J/cm²). Details of this process have been described elsewhere.[1] Heat-flow calculations were performed for the beam energy deposition conditions described above. The calculations show that the Cu melts to a depth of approximately 4 μm and that the surface stays molten for a period of approxi-
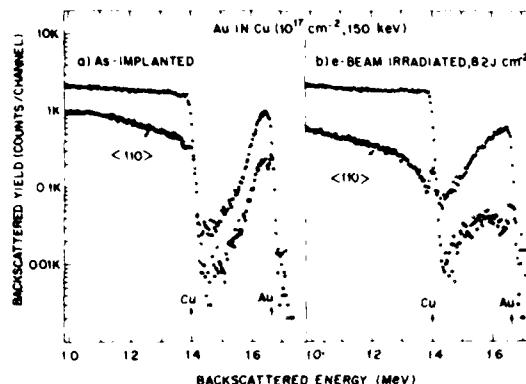
FIG 1 Rutherford backscattering spectrum of 1 8-MeV incident He⁺ ions after high-dose Au implantation into single-crystal copper both before (a) and after (b) electron beam irradiation. The upper curves (closed circles) are unaligned (random) spectra and the lower curves (open circles) are (110) aligned channeling spectra


FIG. 2. Secondary electron microscopy pictures of Au-implanted Cu surfaces both before (a) and after (b) electron beam irradiation. (a) shows the boundary between the implanted (lower left) and unimplanted (upper right) regions. (b) shows the smooth epitaxially regrown layer after electron beam irradiation, with a copper surface ball included for comparison.

mately 750 nsec. The liquid interface regrows with a velocity of approximately 10 m/sec and the quench rate of the molten surface layer is about 10^9 K/sec. Initial experiments demonstrated that the deposited energy needed to produce surface melting in copper was appreciably higher than that needed for silicon, presumably due to the higher thermal conductivity of the single-crystal copper.

Figure 1 shows the channeling and backscattering spectrum of Au implanted into single-crystal Cu [crystal normal 5° from (110)] to a peak concentration of approximately 5% obtained using a 1.8-MeV incident He⁺ ion beam and an annular solid state detector positioned at a mean angle of 175°. After electron beam irradiation, two significant features arise. First, the crystallinity of the Cu surface region has been markedly improved as evidenced by a significant decrease in the channeling yield. Second, the Au has remained substitutional but has diffused significantly into the host matrix. For example, the width (FWHM) of the Au peak in the unirradiated samples corresponds to about 480 Å whereas after irradiation the width increases to 840 Å. A movement of 360 Å in 750 nsec implies a diffusivity of about 2×10^{-5} cm²/sec, which is in accord with published values of metallic liquid-state diffusivities.[4]

The effect of the pulsed irradiation is graphically demonstrated in the secondary electron microscopy SEM picture of the Au-implanted Cu taken both before and after electron beam irradiation. Figure 2(a) shows the boundary between the implanted and unimplanted Cu surface. The sputter-induced surface ripples in the implanted region are believed to be due to disloction structures lying parallel to the surface of the Cu.[5] Figure 2(b) shows the same region after electron irradiation. The surface is now completely flat except for a surface Cu ball included for comparison. These balls are few in numbers and are believed to originate from local hot spots. We believe the SEM and channeling indicates that epitaxial regrowth has taken place from the liquid phase.

It is not surprising that Au remains substitutional after
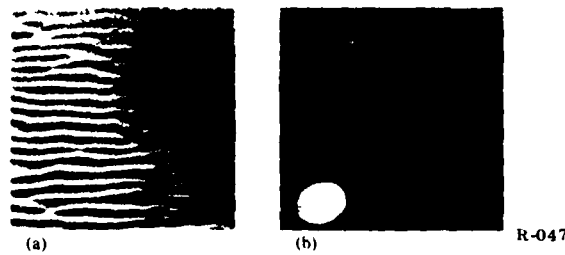
pulsed irradiation since Au and Cu form substitutional solid solutions for all compositions. The Ag-Cu system, however, ordinarily shows very limited solid solubility. Earlier experiments have shown that implantation of Ag into Cu results in highly substitutional lattice positions[6] and when such Ag-implanted samples are irradiated with pulsed electron beams the Ag remains highly substitutional in a metastable solid solution. Metastable solid solutions of Ag-Cu were first produced by Duwez et al. in the first splat cooling experiments.[7] In those experiments the quench rates were approximately 10^6 K/sec whereas quench rates in the present experiment are calculated to be about 10^9 K/sec.

An even more extreme example of elements having limited solubility is given by TA and Cu. They are virtually insoluble, even in the liquid phase. However, Ta implanted Cu again demonstrates high substitutionality at low doses. For example, Fig. 3(a) shows the backscattering spectra for Ta implanted into Cu to a concentration of approximately 5 at. %. The observed attenuation of the implanted Ta indicates that it is highly substitutional following implantation. Following pulsed irradiation, however, the Ta shows no significant sign of long-range order (substitutionality) in the
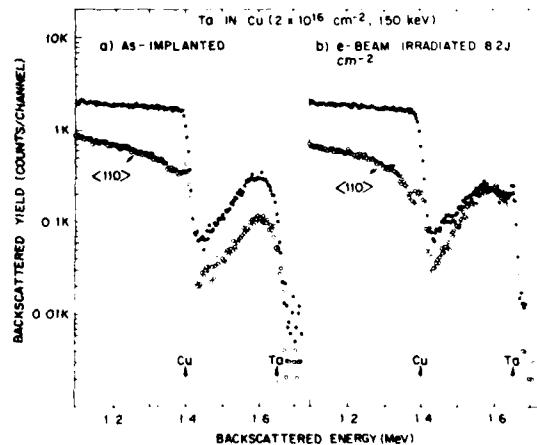

FIG. 3. Rutherford backscattering spectrum of 1 8-MeV incident He⁺ ions after high-dose Ta implantation into single-crystal copper both before (a) and after (b) electron beam irradiation. The upper curves (closed circles) are unaligned (random) spectra and the lower curves (open circles) are (110) aligned channeling spectra.

177

channeling spectrum [Fig. 3(b)]. These results indicate that the quench rate is not sufficient to retain the implanted Ta in substitutional lattice positions. The implanted Ta, however, comes off of substitutional lattice sites along with some redistribution of the concentration profile. This change of lattice site can be explained either by the formation of Ta precipitates in the liquid or solid phase. Since Ta is immiscible in both the liquid and solid phase it is not expected to show significant zone refining to the surface. Higher-dose implantations of Ta in Cu (10^{17} Ta/cm^2) produces an extremely thin surface Ta-Cu alloy which has previously been found to be amorphous.[6] Electron irradiation of this layer causes enrichment of the Ta at or near the surface with an accompanying recovery of the Cu crystallinity. However there is no evidence of Ta substitutionality.

Attempts were also made to use pulsed electron beams to alloy films of vacuum-deposited Ag, Au and Ta with an underlying Cu single-crystal substrate. These deposited films all showed severe adhesion problems upon irradiation with only a small fraction ($< 10\%$) of the film remaining on the Cu substrate, with no significant interaction with the underlying substrate.

In conclusion, following the pulsed electron beam irradiation of implanted copper a high degree of subtitutionality is found for Au (an element having an inherently high solubility) and for Ag (an element which forms metastable solid

solutions). Ta, an element immiscible in Cu, comes out of solution and presumably precipitates. These differences in behavior are thought to be associated with the difference of the effective quench rates associated with (i) ion implantation ($\sim 10^{14}$ K/sec) and (ii) regrowth from the melt ($\sim 10^9$ K/sec). The deposited thin-film results also point to the usefulness of employing ion implantation rather than deposited coatings for studying intermetallic interactions under such rapid thermal treatments.

[1] *Laser-Solid Interactions and Laser Processing*—1978, edited by S.D. Ferris, H.J. Leamy, and J.M. Poate (American Institute of Physics, New York, 1979).

[2] G. Della Mea and P. Mazzoldi, in Ref. 1, p. 212.

[3] A.C. Greenwald and R.G. Little, Solid State Technol. 22, 143 (1979).

[4] T.E. Faber, *Theory of Liquid Metals* (Cambridge University, Cambridge, England, 1972).

[5] D.J. Mazey, R.S. Nelson, and P.A. Thackeray, J. Mater. Sci. 3, 26 (1972).

[6] A.G. Cullis, J.A. Borders, J.K. Hirvonen, and J.M. Poate, Philos. Mag. B 37, 615 (1978).

[7] P. Duwez, R.H. Willens, and W. Klement, Jr., J. Appl. Phys. 31, 1136 (1960).